Modelling Neuromuscular Circuits In Vitro

Crossley, Martin Richard

Awarding institution:
King's College London

Modelling Neuromuscular Circuits *In Vitro*

By

Martin Crossley

A thesis submitted to King's College London for the degree of

Doctor of Philosophy

MRC Centre for Developmental Neurobiology

King's College London

July 2015

In dedication to my parents, Michael and Anne;

my first and most important teachers.

It ain't what you don't know that gets you into trouble. It's what you know for sure that just ain't so.

- Mark Twain

Abstract

The survival of complex organisms depends on their ability to interact with their environment through precise control of motor behaviours. This is achieved via specialised synapses called neuromuscular junctions (NMJs) found between motor neurons (MNs), projecting from the hindbrain and spinal cord, and skeletal muscle in the periphery. Current evidence suggests that pathological changes at the NMJ precede many neuromuscular disorders. Studying neuromuscular circuits is therefore critical to improving our understanding of this system and advancing therapies for many currently incurable diseases. One key strategy for discovering new treatments are pharmacological screens, however performing these on NMJs *in vivo* is challenging, with limited opportunities for experimental manipulation or long-term observation.

Recent advances in stem cell biology present an exciting opportunity to produce *in vitro* models of neuromuscular circuits, with improved accessibility, reproducibility and scalability. This thesis describes and validates a model for neuromuscular circuit development and NMJ formation and maturation. Mouse ESC lines were generated to enable the production of spinal MNs and skeletal muscle. Patch-clamp experiments revealed that murine embryonic stem cell-derived motor neurons (ESC-MNs) mature electrically over a period of 3 weeks, progressing from an immature, non-spiking character to a mature phenotype capable of firing high frequency trains of action potentials. This behaviour was recapitulated via photostimulation using a stably integrated Channelrhodopsin-2 (ChR2) transgene.

To investigate the functional properties of ESC-MNs, an ESC line was established expressing a doxycycline-inducible *Myod1* transgene. Following *Myod1* induction these cells form multinucleated skeletal myotubes in vitro. Co-cultures of ESC-MNs and myotubes show immature but functional synapses, with contractile activity directed by light stimulation via ChR2. Long-term in vitro culture was assessed using an alternative muscle target from the chick model system. Co-culture of ESC-MNs with chick primary skeletal muscle leads to maturation of NMJs, and spontaneous as well as light-evoked muscle contractions. These co-cultures represent an accessible model for studying NMJ development and function, as well as providing a potential assay to screen genetic or pharmacological therapies for muscular and MN diseases.

Acknowledgements

I have more people to thank than can be reasonably managed here, however I wish to extend special thanks to a few key individuals without whom this work would not have been possible.

Firstly, deepest thanks to my primary supervisor Ivo Lieberam, who has been there every step of the way to discuss ideas, troubleshoot problems and critique data. I have thoroughly enjoyed my time in your lab, and have probably learnt more in passing conversation with you than years of study could provide! I'll never forget our discussions (ranging from dinosaur evolution to cocktail making!) or the occasional spot quiz. You have been a great mentor and scientific role model, and I'm confident the skills and knowledge I have gained with you will serve me well in my future career.

Thanks also to my secondary supervisor Juan Burrone, who besides teaching me everything I know about electrophysiology is also the most reliable centre-midfield you could hope to have on a Thursday lunchtime! Your advice and guidance has been crucial throughout, and it has been a great pleasure working (and playing!) with you.

Special mention to my colleague and friend Carolina Barcellos-Machado, who has been my anchor in the storm more times than I can remember. Your unwavering support and patience has kept me going through thick and thin, and your open friendship made the lab a great place to work. Thanks for everything, the next whiskey is on me!

To my friends and housemates – Thanks for bearing with me! Liam, Laura and especially my comrade-in-arms Danielle, thanks for being there both at work and at home, and making every day one that I look forward to starting. Will, Thom and our 4th musketeer Chris, thanks for the years of fun and adventure – here's to many more to come you scrubs! Thanks also to my unofficial housemates John, Patrick and Mil – I appreciate your patience with my constant invasions, I'm glad I got to meet you all, and I can't wait to visit your next residence!

Finally, huge thanks to my parents, Michael and Anne, my brother Sam, and my partner-in-crime Srish, for their constant emotional and intellectual support, guidance and love. My parents have believed in me more than I believed in myself at times, and that has made the difference on more than one occasion. Sam, you are my oldest and closest friend; I think it is easy to forget how lucky I am to be able to say that. Srish, where would I be without you? Probably somewhere without socks. You've been with me every day of this wild ride, counting down to the very last page, and you've made every single day better. Thank you all for everything, I literally couldn't have done it without you.

Table of Contents

Table of Figures

Table of Tables

Abbreviations

Abbreviation	Meaning
3D	3 Dimensional
AChR	Acetylcholine Receptor
ADFN	Neural differentiation medium without serum
ADFNK	Neural differentiation medium
ANS	Autonomic Nervous System
AsNAs	Astro-neural aggregate
BDNF	Brain Derived Neurotrophic Factor
BMP	Bone Morphogenic Protein
BSA	Bovine Serum Albumin
CEE	Chick Embryo Extract
ChR2	Channelrhodopsin-2
CNS	Central Nervous System
CPM	Chicken Primary Muscle
DAPI	4',6-Diamidino-2-Phenylindole
DMEM	Dulbecco Modified Eagle Medium
DNA	Deoxyribonucleic Acid
DPBS	Dulbecco's Phosphate-Buffered Saline
EB	Embryoid Body
ESC	Embryonic Stem Cell
F-12	Nutrient Mix F-12
FBS	Fetal Bovine Serum
FGF	Fibroblast Growth Factor
GDNF	Glial Derived Neurotrophic Factor
GFAP	Glial Fibrillary Acid Protein
GFP	Green Fluorescent Protein
hESC	Human Embryonic Stem Cell
HMC	Hypaxial Motor Column
iPCR	Inverse Polymerase Chain Reaction

Abbreviation	Meaning
iPSCs	Induced Pluripotent Stem Cells
KCL	Kings College London
KO-DMEM	Knockout Dubelcco's Modified Eagle Medium
KOSR	Knock Out Serum Replacement
LMC	Lateral Motor Column
MACS	Magnetic Associated Cell Sorting
MEF	Mouse Embryonic Fibroblasts
mESC	Mouse Embryonic Stem Cells
MMC	Medial Motor Column
MN	Motor Neuron
NEAA	Non-Essential Amino Acids
NMJ	Neuromuscular Junction
PBS	Phosphate-Buffered Saline
PCR	Polymerase Chain Reaction
PDGF	Platelet derived growth factor
PFA	Paraformaldehyde
PNS	Peripheral Nervous System
PGC	Preganglionic Column
PSC	Pluripotent Stem Cell
qPCR	Quantitative Polymerase Chain Reaction
RNA	Ribonucleic Acid
RT	Room Temperature
SAG	Sonic hedgehog Agonist
SC	Stem Cell
SD	Standard Deviation
SEM	Standard Error Of The Mean
Shh	Sonic hedgehog
RA	Retinoic Acid

Chapter I

Introduction

One of the most consistent and important features of the animal kingdom is the ability to interact with and respond to the external environment. Current thinking suggests that the nervous system initially arose for this purpose, allowing gradually more complex behaviours to evolve that conferred a survival advantage on the organism (Ghysen, 2003). Potentially the earliest and most important behaviour to arise was that of movement, driven by the action of motor neurons on contractile muscle cells via a specialised synaptic connection called the neuromuscular junction (NMJ) (Miller, 2009). This neuromuscular circuitry is responsible in humans for everything from locomotion to breathing, and dysfunction of this system can lead to devastating and often lethal disorders. Understanding the development and function of neuromuscular circuits is therefore of vital importance to both basic science and modern medicine.

This thesis describes the development of mouse embryonic stem cell lines used to generate spinal motor neurons and skeletal muscle in order to model neuromuscular circuit development and neuromuscular junction formation. As directed differentiation of stem cells into desired terminally differentiated cells typically requires recapitulation of the signalling events that occur *in vivo* during development, a good understanding of the developmental genetics of the tissue(s) being studied is necessary. This introduction will cover the developmental biology of spinal motor neurons and skeletal muscle before discussing basic stem cell biology and some of the strategies used in this study to model and analyse neuromuscular circuits and synapse formation.

1.1 Motor Neurons

A motor neuron is defined as a CNS neuron which projects its axon out of the CNS where it synapses onto peripheral targets. Motor neurons (MNs) are extremely important for animal life, as all behaviour relies on efficient and precise MN activity and connectivity with muscle tissue and other peripheral targets; these behaviours range from basic reflexes to avoid damage to the body through to essential life functions such as breathing and swallowing.

While often referred to as a single group, there is actually vast diversity among "motor neurons", with distinct gene expression profiles, molecular signatures and muscle targets. This diversity is required to enable the independent innervation of the large number of distinct muscle groups found in most animals; humans for example have over 300 bilateral paired muscles, while a typical vertebrate limb contains up to 50 individual muscles (Dasen and Jessell, 2009; Kanning et al., 2010). The precise control of inputs to MNs and their outputs to their target muscle is essential for the fine, coordinated motor control seen in complex behaviour, and much evidence suggests that the developmental subtype identity of a MN determines its innervation pattern and connectivity (Landmesser, 2001; Milner and Landmesser, 1999). Understanding the specification of MN subtypes is therefore vital to understanding motor networks and function.

1.1.1 Subtype diversity

The first major distinction between MNs is that of branchial, visceral and somatic MNs (Stifani, 2014). Branchial MNs are located in the brainstem, and innervate the head and neck musculature via the cranial nerves (Chandrasekhar, 2004). Visceral MNs comprise a component of the autonomic nervous system (ANS), which is further subdivided into the sympathetic and parasympathetic systems. Sympathetic MNs are located in the preganglionic column of the spinal cord, and innervate the sympathetic chain ganglia and the adrenal medulla. Parasympathetic MNs on the other hand are located mainly in the brain stem and sacral spinal cord, and innervate peripheral ganglia found near major organs including the heart, lungs,

kidneys, bladder and pancreas. Somatic MNs are found in the ventral horn of the spinal cord and in hindbrain nuclei, and their axons project out of the central nervous system (CNS) into the periphery along the spinal nerves, where they form specialised synapses called neuromuscular junctions (NMJs) with skeletal muscles (Wu et al., 2010).

Somatic MNs can be further subdivided into four groups called motor columns, identified by their position within the spinal cord. Each column innervates a set group of muscle targets. The medial motor column (MMC) runs along the entire length of the spinal cord, and MMC MNs innervate dorsal axial muscles of the back and torso (Agalliu et al., 2009; Fetcho, 1987). The lateral motor columns (LMC) meanwhile are only found at limb levels, with brachial LMC MNs innervating the forelimbs and lumbar LMC MNs innervating the hindlimbs (Landmesser, 1978). The hypaxial motor columns (HMC) are only present at cervical and thoracic levels and innervate the ventral axial muscles including the intercostal and abdominal wall muscles (Gutman et al., 1993). The final group, the preganglionic column (PGC), are found at thoracic levels, and innervate sympathetic chain ganglia of the peripheral nervous system (PNS) (Prasad and Hollyday, 1991). This rostrocaudal organisation is shown below in figure 1.1.

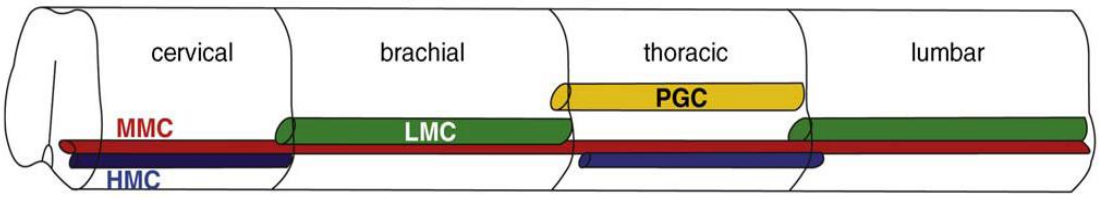

Figure 1.1 The organisation of spinal motor columns. Columnar identity dictates the general muscle target of a motor neuron and the location of its cell body. Medial motor column (MMC) neurons innervate dorsal axial muscles, hypaxial motor columns (HMC) innervate intercostal and abdominal wall muscles, lateral motor columns (LMC) innervate the muscles of the limbs and preganglionic column (PGC) motor neurons innervate sympathetic ganglia. (Adapted from Peljto and Wichterle, 2011.)

The LMC, which has been studied most extensively, is further subdivided into medial and lateral divisions which innervate ventral (typically flexor) and dorsal (typically extensor) limb muscles (Kania and Jessell, 2003; Tosney and Landmesser, 1985). These divisions are themselves

segregated into motor pools, and all MNs within one motor pool project to a single target muscle. The motor pools form a rough topographic map of the limb, with rostral and proximal muscles innervated by rostral pools, while caudal and distal muscles are innervated by caudal pools (Hollyday and Jacobson, 1990; Landmesser, 1978).

Individual MNs can also be grouped in three classes dependent on their muscle fibre targets, morphology and function: alpha (α), beta (β) and gamma (γ) (Kanning et al., 2010). The largest and most common MN subtype are αMNs, which synapse onto the contractile extrafusal skeletal muscle fibres and are responsible for eliciting muscle contraction. Gamma MNs are smaller, and synapse onto the proprioceptive intrafusal muscle fibres of the muscle spindle, where they can modulate the sensitivity of the sensory neurons innervating the spindle to stretch forces (Hunt and Kuffler, 1951; Proske and Gandevia, 2009). Beta MNs remain poorly characterised, and despite innervating both intrafusal and extrafusal muscle fibres (via axon collaterals), their function remains unclear (Kanning et al., 2010; Manuel and Zytnicki, 2011). The final level of MN subtype diversity is seen within αMNs, which can be subdivided based on the functional properties of the motor unit they form with their muscle target into slow-twitch fatigue resistant (αS), fast-twitch fatigue-resistant (αFR) and fast-twitch fatigable (αFF). The functional properties of these motor units are largely determined by the metabolic and molecular characteristics of their muscle target, which will be discussed in section 1.2.1. Most motor pools contain a mixture of all these MN subtypes and while the final contractile properties of the muscle are determined by the ratio of these different classes, transitions from one fibre type to another have been observed *in vivo* due to changes in neuronal activity, physical demand or hormonal signals (Friese et al., 2009; Pette and Staron, 2000; Staron, 1997).

1.1.2 Subtype specification

While αMNs can transition between fast-twitch and slow-twitch identities as a result of external influences throughout adult life, the specification of spinal motor columns and pools is

genetically determined during development and the factors that regulate this process have been well characterised. As stem cell differentiation often closely recapitulates signalling cascades and genetic programmes that drive development in the embryo, understanding the developmental biology of spinal MNs is vital to advancing the field of regenerative medicine and enabling the creation of better cellular models of MNs for research.

The spinal cord is patterned by the combined actions of diffusible morphogens that establish concentration gradients along the dorsoventral and rostrocaudal axes of the embryo. MN progenitors, like all cells of early neural tube, establish a specific positional identity determined by these signals, restricting them to a specific motor column and pool, thereby also defining their axonal projection pattern and muscle target.

1.1.2.1 Dorsoventral patterning

Dorsoventral (DV) patterning of the neural tube is largely driven by a counter-gradient of sonic hedgehog (Shh) and bone morphogenic proteins (BMPs). Shh is initially secreted by the notochord, a mesodermal structure running ventral to the neural tube. Shh from the notochord diffuses dorsally into the ventral neural tube, where it establishes a new Shh producing region termed the floor plate (Echelard et al., 1993). BMP proteins are initially secreted by the dorsal epidermis lying adjacent to the neural tube, and as with Shh, this signalling results in the formation of the roof plate in the dorsal neural tube, which itself produces the TFG-β family members BMP4 and BMP7 (Wilson and Maden, 2005). These BMP proteins drive the expression of other TFG-β proteins in the dorsal neural tube, including Dorsalin and Activin (Liem et al., 1997). Concurrent to these opposing morphogen gradients, the somites and paraxial mesoderm lateral to the neural tube secrete fibroblast growth factors (FGFs) and retinoic acid, which have important roles in promoting neural progenitor proliferation (Ulloa and Briscoe, 2007). This early patterning is summarised in figure 1.2.

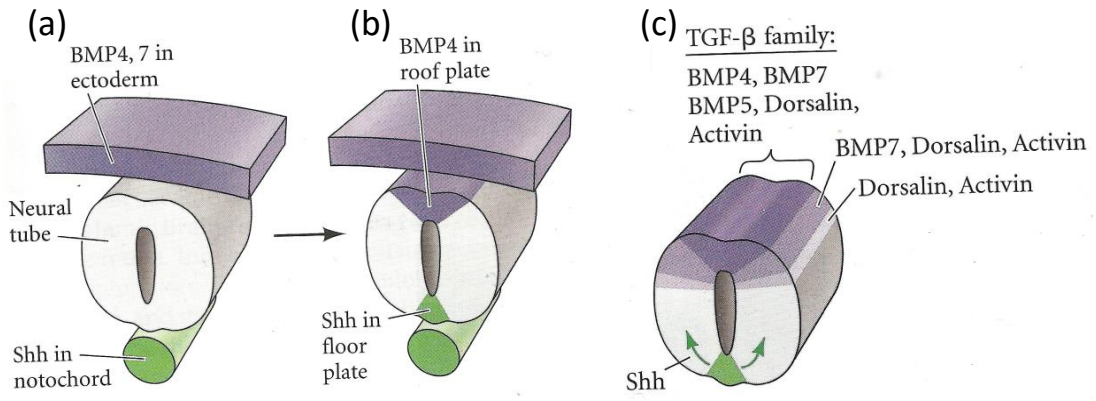

Figure 1.2 Early patterning of the neural tube. (a) The notochord secretes Shh which diffuses to the ventral neural tube, while the dorsal ectoderm secretes BMP 4 and 7 which diffuse to the dorsal neural tube. **(b)** The floor plate is induced in the ventral neural tube by Shh, while the roof plate is induced in the dorsal neural tube by BMP proteins. **(c)** The floor and roof plates secrete Shh and TGF-β proteins respectively, setting up two morphogen gradients to pattern the neural tube along the dorsoventral axis. (Adapted from Gilbert *et al.,* 2006).

The gradients of Shh and BMP signalling on cells within the developing neural tube results in a dorsoventral gradient of Gli activity, a zinc finger protein family which induces the expression of multiple basic helix-loop-helix (bHLH) and homeodomain transcription factors (TFs) (Dessaud et al., 2008; Jacob and Briscoe, 2003). Downstream TFs can be divided into class I and class II genes, which are repressed by Shh signalling or require it respectively (Briscoe and Ericson, 2001). These homeodomain TFs work in mutually antagonistic pairs that are induced or repressed by Shh activity, and each pair has different response thresholds. Together, these properties result in the ventral or dorsal expression boundaries of each TF delineating specific TF expression regions, converting the initially smooth gradient of Shh/BMP and Gli acitivity into restricted progenitor zones spread along the DV axis. Each progenitor zone therefore expresses a specific subset of genes, ultimately determining the fate of cells in that zone (Briscoe et al., 2000). The boundaries between progenitor zones are further refined and sharpened due to the mutually antagonistic activity of Shh and the BMPs themselves, improving the contrast of progenitor zone patterning (Liem et al., 2000).

The motor neuron progenitor zone (pMN) is established in the ventral neural tube, and is characterised by the expression of the bHLH protein Olig2, the class I TFs Nkx6.1 and Nkx6.2, and the class II TF Pax6 (Novitch et al., 2001; Vallstedt et al., 2001). Following a period of progenitor proliferation, these cells exit the cell cycle and initiate MN differentiation driven by the expression of downstream homeodomain TFs including Hb9, Isl1/2 and Lhx3, as shown in figure 1.3. These proteins define the generic MN identity prior to subdivision into specific motor columns and pools (Arber et al., 1999; Pfaff et al., 1996; Sharma et al., 1998).

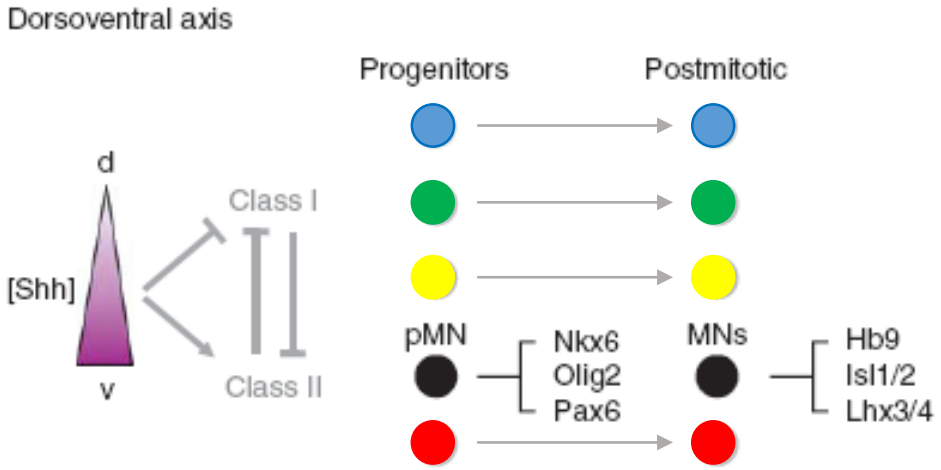

Figure 1.3 Specifying generic motor neuron identity A gradient of Shh along the dorsoventral axis of the spinal cord induces the expression of specific transcription factors in neural progenitors. Class I (repressed by Shh) and class II (require Shh) transcription factors are mutually repressive, refining and delineating particular differentiation fate zones. The stable expression of Nkx6, Olig2 and Pax6 in motor neuron progenitors leads to the expression of Hb9, Isl1/2 and Lhx3/4, which define motor neuron identity. (Adapted from Dasen *et al.,* 2009).

1.1.2.2 Rostrocaudal patterning

Rostrocaudal (RC) patterning of the spinal cord occurs alongside DV patterning and establishment of MN identity, and is responsible for segregating post-mitotic MNs into motor columns, and also influences motor pool organisation later in development (Dasen et al., 2003). As with DV patterning, RC patterning is also mediated by the differential expression of homeodomain proteins in response to gradients of diffusible signalling molecules. In the case of RC patterning, it is the Hox proteins that direct cell fates, and their expression is induced in

response to varying levels of fibroblast growth factor (FGF), retinoic acid, Wnt and TGF-β family signalling (Bel-Vialar et al., 2002; Diez del Corral and Storey, 2004; Nordström et al., 2006).

The initial inductive factor for Hox gene expression is FGF signalling, and the main source of FGFs in the spinal cord is the node (Henson's node in the chick), a key signalling structure at the caudal end of the neural tube. As development proceeds, the body grows via extension of the tail bud (and node) caudally. This growth results in the caudal neural tube being exposed to high levels of FGFs for extended periods of time, while more rostral regions receive weaker and shorter FGF signalling, creating a gradient along the RC axis (Dubrulle and Pourquié, 2004; Liu et al., 2001). Previous work has shown that while all Hox genes can be induced by FGF signalling, they have varying response thresholds, resulting in the expression of high-threshold Hox genes at caudal levels and low-threshold Hox genes at rostral levels (Bel-Vialar et al., 2002; Dasen et al., 2003). Interestingly, this results in the expression of Hox genes along the RC axis that is co-linear to their chromosomal arrangement, with genes at the 3' end of the cluster being expressed at rostral levels and 5' genes expressed at caudal levels (Kmita and Duboule, 2003; Lemons and McGinnis, 2006). This process establishes Hox gene expression ranging from 3' Hox5 paralogs found at brachial levels, Hox8 and 9 paralogs at thoracic levels and 5' Hox10 paralogs at lumbar levels (Fig. 1.4).

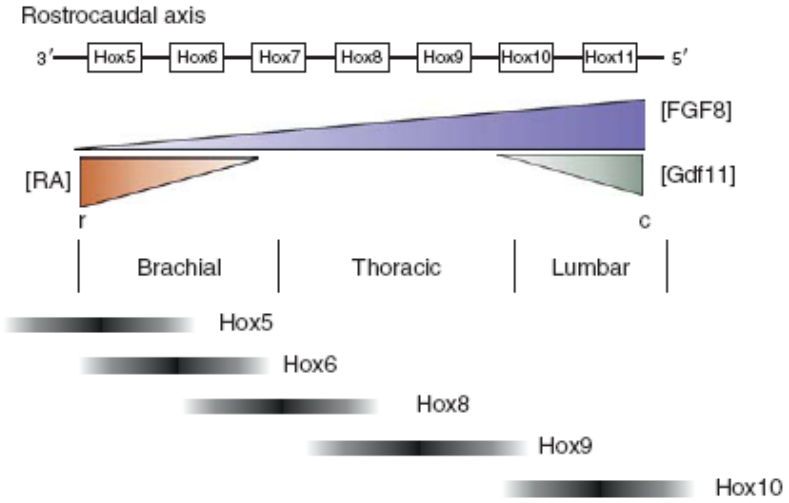

Figure 1.4 Patterning the rostrocaudal axis. An FGF gradient along the rostrocaudal axis induces the co-linear expression of *Hox* genes in the spinal cord. Retinoic acid (RA) acts at rostral levels (r) and Gdf11 acts at caudal levels (c) to further regulate *Hox* expression (Adapted from Dasen *et al.,* 2009).

The TGF-β family member Gdf11 is also expressed caudally, and appears to synergise with FGF signalling in lumbar and thoracic levels to promote expression of Hox8-10 paralogs (Liu, 2006; McPherron et al., 1999). Retinoic acid on the other hand, expressed by the somites and paraxial mesoderm, is found at high levels in the rostral neural tube, and antagonises FGF signalling. As with DV patterning, this counter-gradient leads to better defined fate zones with sharper boundaries at brachial levels (Diez del Corral and Storey, 2004). Further distinction between expression zones is generated by the cross-repressive interactions of the Hox proteins themselves, as Hoxc9 has been shown to represses more anterior (or 3') Hox genes, while posterior Hox genes are epigenetically silenced by recruitment of Polycomb Group (PcG) complexes (Dasen and Jessell, 2009; Dasen et al., 2003; Jung et al., 2010). This is reminiscent of the mutual antagonism of class I and class II TFs in DV patterning discussed previously, and reveals a general mechanism of gradient patterning to define fate zones during development.

The expression of Hox genes instructs MN columnar identity, so that the limb-innervating brachial and lumbar LMCs are associated with Hox6 and Hox10 paralogs respectively, while thoracic PGC MNs express Hox9 paralogs (Choe et al., 2006; Dasen et al., 2003; Liu et al., 2001). This is supported by experiments manipulating Hox gene expression; for example, ectopic expression of Hoxc9 at brachial levels converts presumptive LMC MNs to a PGC fate, while ectopic expression of Hoxc6 or Hoxd10 in the thoracic neural tube converts presumptive PGC and HMC MNs to an LMC fate (Dasen et al., 2003; Shah et al., 2004). This fate conversion can also be induced by addition of exogenous FGFs at the rostral end of the neural tube during development, leading to ectopic Hoxc9 expression and PGC MN identity (Dasen et al., 2003).

Interestingly, this fate conversion results in altered axonal projection patterns, in addition to changes in gene expression and molecular profiles. For example, brachial MNs converted to a PGC fate project to the sympathetic chain ganglia rather than limb musculature, while thoracic MNs converted to an LMC fate project to the limbs (Dasen et al., 2003; Shah et al., 2004). This finding indicates that motor axon guidance is initially intrinsically specified by Hox gene

expression. The Hox genes also influence motor pool organisation, discussed in the following section.

1.1.2.3 Motor pool specification

Most work on motor pool specification has been carried out on brachial LMC neurons that project into the forelimbs. While ectopic expression of Hox proteins can cause a motor column identity switch that results in axonal projection to the new target, transposition of LMC MNs to ectopic locations results in accurate axonal pathfinding to the limb musculature, indicating that motor pool identity is at least partially intrinsically specified (Landmesser, 2001). A key candidate for this intrinsic specification is again the Hox family of transcription factors, as expression of Hox4-8 paralogs is seen in the developing brachial LMC in a rostral to caudal pattern, similar to the expression found in the neural tube earlier in development (Dasen et al., 2005). Due to the mutually repressive interaction between Hox5 and Hox8 paralogs, defined Hox expression zones are established, with rostral motor pools expressing *Hoxa5* and *Hoxc5*, while more caudal pools express *Hoxc8*.

This rostrocaudal organisation is reflected in the axonal projection of LMC motor pools, as rostral motor pools innervate anterior and proximal muscles, while caudal motor pools innervate posterior and distal muscles (Hollyday and Jacobson, 1990; Landmesser, 1978). This pool-specific identity is driven by the expression of downstream TFs, such Runx1, which is dependent on Hox5 activity and is expressed in rostral motor pools, and Pea3 and Scip, expressed in caudal motor pools requiring Hox8 activity (Dasen and Jessell, 2009; Dasen et al., 2005).

However, unlike spinal motor columns, which are generally arranged end-to-end along the rostrocaudal axis with little overlap, as many as ten distinct motor pools can occupy the same RC level within the spinal cord (Dasen and Jessell, 2009). This arrangement reveals that Hox gene expression alone cannot account for motor pool identity, as MNs from distinct motor pools would be exposed to the same gradient of signalling factors and express the same initial Hox

proteins. Work on the brachial LMC has revealed that motor pool specification actually occurs in two phases; initial competency to adopt a rostral or caudal motor pool fate is established by Hox gene expression, followed by local or peripheral target-derived signalling refining motor pool identities (Haase et al., 2002; Livet et al., 2002; Machado et al., 2014).

The best characterised peripheral signal in motor pool specification is glial-cell line derived neurotrophic factor (GNDF), which is expressed at various points along the LMC trajectory, including the plexuses, the mesoderm and skeletal muscles of the limb, particularly the cutaneous maximus (CM) and latissimus dorsi (LD) (Dudanova et al., 2010; Haase et al., 2002; Kramer et al., 2006; Lin et al., 1998; Livet et al., 2002). In mutant mice lacking functional GDNF signalling, the motor pools that would innervate these two muscles are disorganised, with the MNs malpositioned in the spinal cord and a dramatic decrease in innervation and axon branching at both the CM and LD. Supporting the role of GDNF in establishing these motor pool identities, Pea3 expression is greatly reduced in the absence of GDNF signalling, and the phenotype of these mice is indistinguishable from Pea3 KO mice (Haase et al., 2002; Lin et al., 1998; Livet et al., 2002).

GDNF influences motor pool differentiation by inducing Pea3 expression in competent MNs via the Ret receptor present on the axons of MNs innervating the CM and LD muscles (Kanning et al., 2010). The Pea3 TF then influences MN clustering in the spinal cord via regulation of type II cadherin expression, as well other functions including final muscle target selection, dendrite morphology and connectivity with the CNS (Haase et al., 2002; Livet et al., 2002; Pecho-Vrieseling et al., 2009; Price et al., 2002; Vrieseling and Arber, 2006).

MN differentiation and development is therefore a complex, multi-stage process requiring a combination of varied extrinsic and intrinsic factors interacting in a precise spatiotemporal sequence to produce the diversity of neuronal subtypes necessary for precise control of refined motor behaviours. While gradients of signalling molecules in the early embryo establish

homeodomain protein expression that confers basic MN identity to cells in the ventral neural tube, complete differentiation relies on interactions with peripheral tissues, including the final skeletal muscle targets. Certain features of skeletal muscle maturation are also dependent on functional innervation by MNs, therefore understanding the development of both these tissues is crucial to the development of *in vitro* models of the neuromuscular system.

1.2 Muscle

1.2.1 Subtype diversity

The purpose and function of MNs is tightly bound to that of muscle, and effective communication between these two highly specialised tissues. Muscle tissue is vital to survival in virtually all extant animal species, with rare exceptions in evolutionarily primordial animals such as sponges and larval stages of Cnidaria and Ctenophora (Burton, 2008; Seipel and Schmid, 2005, 2006). To achieve the multiple and varied roles that muscle serves, there is substantial subtype diversity, parallel to MN diversity. The largest division in muscle subtypes is determined by their mode of activity and function; skeletal muscle, cardiac muscle and smooth muscle. Cardiac and smooth muscle are involuntary, requiring no conscious control for their activity, while skeletal muscle is predominantly voluntary (with some exceptions e.g. respiratory muscles), requiring conscious behaviour to contract. Cardiac muscle contracts continuously and rhythmically even in the absence of neuronal input, and is completely fatigue resistant, providing the ideal properties required for heart function, driving the systemic and pulmonary circulatory systems (Sonnenblick and Stam, 1969). To achieve the synchronous contractility necessary for a ventricular or atrial systole, cardiomyocytes are physically joined by intercalated disks to form large syncytia, providing mechanical support and rapid transmission of electrical activity between cells via gap junctions (Sarantitis et al., 2012).

Smooth muscle also forms syncytia, however without the presence of intercalated disks which give cardiac muscle its branched structure. Smooth muscle also does not display sarcomeres, the repeating units of myosin and actin filaments which give the distinctive banding seen in both

cardiac and skeletal muscle (Cooke et al., 1987; Small, 1995). Smooth muscle is responsible for the control of the vascular system, being found in the walls of arteries and veins, and is also found in the bladder, skin and gastrointestinal, reproductive and respiratory tracts, among others. Smooth muscle typically contracts in a tonic fashion, with slow sustained activity, which can produce waves of contraction as seen in peristaltic waves in the oesophagus during swallowing or the intestines during digestion (Diamant, 1997; Huizinga and Lammers, 2009).

Skeletal muscle, the subtype investigated in this study, is mainly responsible for locomotion and posture, and makes up most of the muscles of the body wall and limbs, accounting for around 40% of the body mass of an average adult male human, or 35% for a female (Marieb and Hoehn, 2010). It carries out its function by attachment to the skeleton via tendons, enabling movement of the limbs and spinal cord via voluntary contraction. Individual skeletal myoblasts fuse together during development to form long, multinucleated myofibres, which are then innervated by a single motor neuron (which may also innervated multiple other myofibres), to form a functional motor unit. Many muscle fibres align with each other, joined by connective tissue including a basement membrane, to form a complete muscle, containing multiple motor units (Sanes, 2003).

Skeletal muscle is also called striated muscle, due to the presence of regularly arranged myofibrils containing units made of opposing myosin and actin filaments, called sarcomeres, which are visible as bands on the surface of myofibres (Clark et al., 2002). A schematic showing the basic sarcomere structure is shown in figure 1.5. Skeletal muscle is further subdivided based on the isotypes of myosin heavy chain expressed by the myofibre, which also determine its functional properties (Burke et al., 1973; Pette and Staron, 2000). At least seven myofibre types can be identified in humans, however four main groups predominate (Staron, 1997). Type I fibres, also called slow-twitch, express myosin heavy chain 1β, have an oxidative metabolism and are highly resistant to fatigue but contract slowly with relatively little force. Type I fibres are innervated by slow-twitch fatigue resistant alpha MNs (αS).

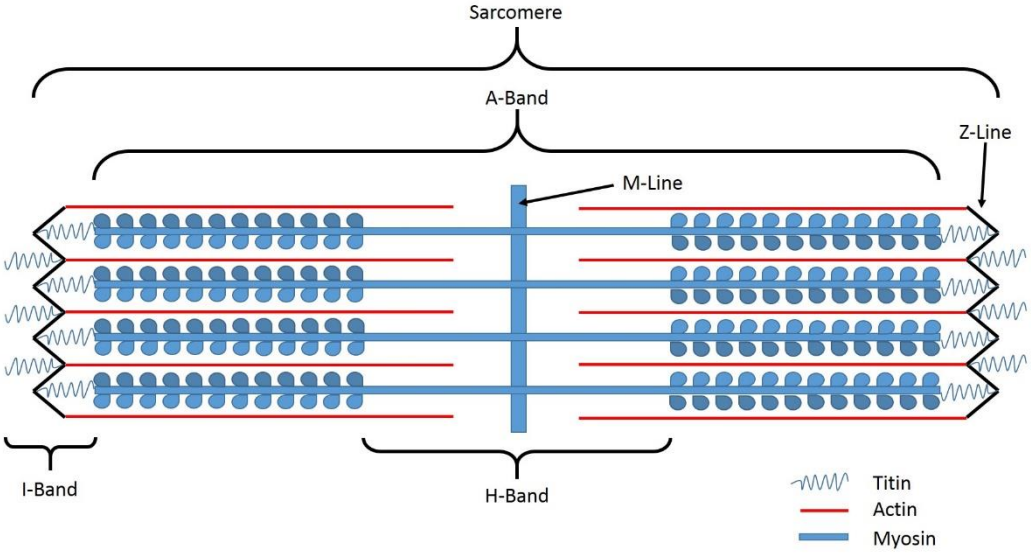

Figure 1.5 Basic sarcomere structure. Skeletal myofibrils have a banded appearance due to the parallel alignment of multiple protein fibres, arranged into repeating units called sarcomeres. A sarcomere consists of parallel arrays of actin thin filaments opposed to myosin thick filaments, which slide past each other during contraction. The edges of a sarcomere are defined by the Z-line, in which actin and titin fibres are anchored. The M-line defines the centre of a sarcomere. The visible bands observed under a microscope have been named according to their light-polarising properties, as the I-band is isotropic, while the A-band is anisotropic. (Clark et al., 2002).

Fast-twitch fibres can be type IIa or type IIb/x. Type IIa fibres express myosin heavy chain IIa, are similarly resistant to fatigue with a mixed glycolytic/oxidative metabolism, but are capable of contracting quickly with medium force and synapse with αFR MNs. Type IIb/x myofibres express myosin heavy chain IIx, and have a mostly glycolytic metabolism during activity resulting in a motor unit capable of fast contractions that produce a large force, while having low resistance to fatigue. These fibres are innervated by αFF MNs. Finally, intrafusal fibres, innervated by gamma MNs, are proprioceptors, providing feedback on limb position and stretch forces rather than generating contractile force (Burke et al., 1973; Hunt and Kuffler, 1951; MacIntosh et al., 2006). These relationships are shown below in figure 1.6. While this categorisation is useful, there are in fact multiple hybrid fibre types, and even transitions from one fibre type to another are possible *in vivo* due to changes in neuronal activity, physical demand or hormonal changes (Pette and Staron, 2000; Staron, 1997). Most skeletal muscles contain a continuum of fibre subtypes, and variations in the relative number of each class of motor unit determine the final contractile properties of the muscle (Friese et al., 2009).

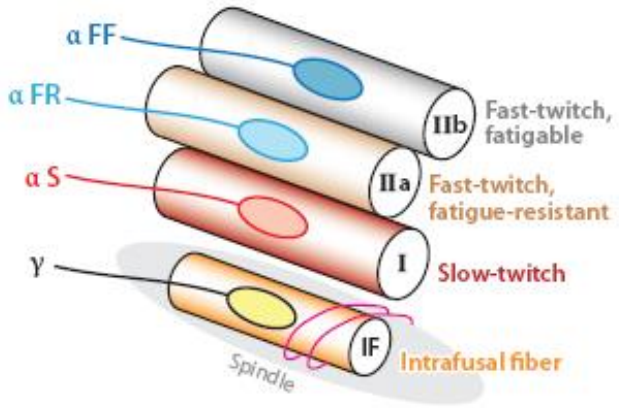

Figure 1.6 Muscle fibre diversity. Muscle fibres are divided according to their myosin heavy chain isotype expression and metabolism. Type IIb/x muscle fibres are innervated by fast-twitch fatigable (αFF) alpha neurons, type IIa fibres are innervated by fast-twitch fatigue-resistant (αFR) MNs, and type I muscle fibres are innervated by slow-twitch fatigue resistant (αS) MNs. (Adapted from Kanning *et al.,* 2010)

1.2.2 Myogenesis

1.2.2.1 Somitogenesis and homeoproteins

While the metabolic and functional properties of skeletal myofibres may not be genetically determined, the specification and generation of muscle tissue during development – myogenesis – is under highly regulated multi-level genetic control. All skeletal muscle in vertebrates is derived from mesodermal progenitors, with the vast majority of trunk and limb muscle tracing its origin back to the somites, regions of segmented paraxial mesoderm found either side of the embryonic neural tube (Tajbakhsh and Buckingham, 2000). The somites are initially composed of two compartments; the sclerotome which generates the vertebrae and ribcage, and the dermomyotome which produces myogenic and endothelial progenitors and contributes to the dermis and connective tissue of the trunk (Ben-Yair et al., 2003; Olivera-Martinez et al., 2000; Wilting et al., 2000). As development progresses, the dermomyotome undergoes further segmentation, whereby myogenic progenitors collect at the epithelium of the dermomotome and begin to delaminate from the edges (“lips”) of this structure to form the myotome, which is situated ventral to the dermomyotome (Gros et al., 2004). These delaminating cells give rise to the primary myotome and are post-mitotic, expressing Mrf4 and Myf5, the first muscle regulatory factors (MRFs) to be expressed, key genes involved in driving

myogenic differentiation. Subsequent waves of myogenic progenitors from the dermomyotome contribute to the growth of the myotome, and unlike the primary myotome, continue to proliferate and generate the majority of fetal and postnatal muscle as well as derived populations such as satellite cells, the adult stem cell population of skeletal muscle (Gros et al., 2005; Kahane et al., 2007; Relaix et al., 2005).

The specification of cells in the dermomyotome to the myotome or other mesodermal fates appears to be strongly influenced by the expression of the paired domain and homeodomain-containing transcription factors Pax3 and Pax7 (Bober et al., 1994; Tremblay and Gruss, 1994). Pax3 positive cells are found in the central dermomyotome, and lineage tracing studies have shown this population gives rise to the proliferative myogenic progenitors of the myotome. Mouse splotch mutants, lacking functional Pax3, show impaired muscle development, lacking limb and some trunk musculature (Bajard et al., 2006). While Pax7 knockouts (KOs) have a much more subtle defect mainly affecting the somatic muscle progenitor cells (satellite cells), Pax3/7 double KO mice lack all trunk and limb musculature, with the only skeletal muscle present being derived from the post-mitotic primary myotome (Relaix et al., 2005; Seale et al., 2000). While Pax3 directly influences the expression of downstream MRFs, it is also vital for muscle progenitor delamination from the dermomyotome and later migration from the myotome into the limb buds (Bajard et al., 2006; Bober et al., 1994). The control of delamination from the dermomyotome is regulated by the tyrosine kinase receptor Met and its ligand, scatter factor/hepatocyte growth factor (SF/HGF). The gene encoding Met, c-met, is a known target of Pax3, and mouse mutants for c-met also display muscle-less limbs similar to Splotch mutants, due to failure of the dermomyotome to delaminate (Bladt et al., 1995; Dietrich et al., 1999; Epstein et al., 1996). Also important in the formation of the myotome is asymmetric cell division in the dermomyotome, where asymmetric cellular distribution of N-cadherin is implicated in distinction between myogenic (high N-cadherin) and dermal cell fate, and asymmetric distribution of the Notch antagonist Numb is associated with delaminating myogenic

progenitors (high Notch) versus cells of the dermomyotome (Cinnamon et al., 2006; Holowacz et al., 2006).

The expression of the Pax genes is in turn dependent on homeoproteins genetically upstream in somitogenesis, the Six proteins and their co-factors Eya and Dach (Grifone et al., 2007). Overexpression of combinations of Six1, Eya2 and Dach2 lead to upregulation of Pax3, while Six1 or Six1/Six4 double KOs die at birth with multiple muscle defects (Grifone et al., 2005; Heanue et al., 2002). These mutants display apoptosis of myogenic progenitors from the somites combined with aberrant migration and reductions in downstream MRFs including *Mrf4, Myod1* and *Myogenin*, possibly as a result of downregulation of Pax3 (Buckingham, 2006). Another factor involved in progenitor migration especially in the limbs is the chemokine stromal-derived growth factor 1 (SDF-1) and its G-protein-coupled transmembrane receptor CXCR4 (Yusuf et al., 2006). The receptor is expressed in migrating myogenic progenitors, while SDF-1 is found in the limb bud mesenchyme, and mutants display defects in limb muscle formation (Vasyutina et al., 2005; Yusuf et al., 2005). Both SDF-1 and SF/HGF also appear to suppress further progenitor differentiation during this migratory phase to the limb buds, and continued myogenic differentiation requires the down-regulation of Pax proteins and is dictated by downstream MRFs, including most importantly Myod1 and Mrf4.

1.2.2.2 Myogenic regulatory factors

Myod1 was first identified over 20 years ago for its ability to convert cultured fibroblasts to a myogenic fate *in vitro,* and was also found to cause myogenic conversion in multiple primary cell types (Choi et al., 1990; Lassar et al., 1986; Weintraub et al., 1989). Three related genes were soon discovered, *Mrf4, Myf5* and *Myogenin*, and together they make up the myogenic regulatory factor (MRF) gene family that is critical for muscle development (Weintraub et al., 1991). While some functional redundancy is observed between these factors, careful dissection of the regulatory network controlling myogenesis has revealed distinct roles for these genes,

often related to temporal or spatial expression patterns as much as protein sequence (Berkes and Tapscott, 2005).

The MRFs belong to the basic helix-loop-helix (bHLH) family of transcription factors (TFs), due to their tertiary protein structure, and each contains a conserved basic DNA binding domain which recognises the DNA sequence CANNTG, called the E box (Blackwell and Weintraub, 1990). The E box DNA motif is found in the promoters and enhancers of many muscle specific genes, giving the MRFs their myogenic activity (Lassar et al., 1989). While sharing this common mechanism, differences in spatial and temporal expression *in vivo,* as well as association with multiple different co-factors and regulators, result in slightly different activities. *Myf5* is first expressed in the dorso-medial region of the somites, which give rise to epaxial (trunk) muscles, while *Myod1* is expressed slightly later in the dorso-medial somite, giving rise to hypaxial muscles (Kablar et al., 1998). Mutation of one of these TFs alone does not result in loss of any major muscle groups, with compensatory upregulation in the remaining MRF indicating a large degree of redundancy (Braun et al., 1992; Rudnicki et al., 1992). However, homozygous loss of both *Myod1* and *Myf5* results in loss of all skeletal muscle, and while double KO mice are born alive, they are immobile and die shortly after birth (Rudnicki et al., 1993). *Myogenin* on the other hand appears to be more important for terminal myoblast differentiation, both due to its later onset of expression and as murine *Myogenin* KOs do have myoblasts, but have poorly developed skeletal muscle (Hasty et al., 1993; Nabeshima et al., 1993). The final member of the MRF family, *Mrf4,* appears to be involved in both early myogenic specification and later terminal differentiation. This role is supported by early (E9) and later (E16) periods of *Mrf4* expression in mice corresponding to muscle specification and terminal differentiation phases, as well as rescue of *Myogenin* KOs by *Mrf4* expression at the *Myogenin* promoter and rescue of muscle loss in *Myf5:Myod1* double KOs in which *Mrf4* is unaffected (Kassar-Duchossoy et al., 2004; Zhu and Miller, 1997). A schematic summarising the core myogenic regulatory factor network is presented in figure 1.7 below.

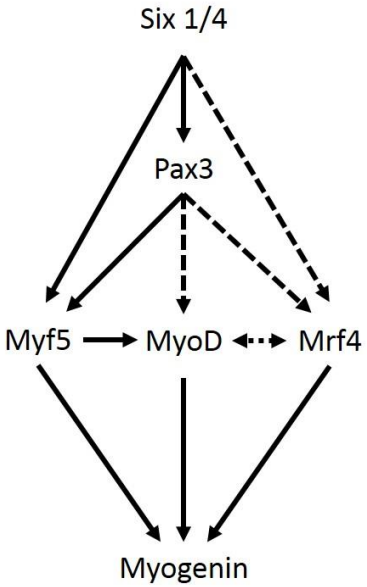

Figure 1.7 The myogenic regulatory factor network. Myogenesis is initiated in the developing somites by expression of the homeodomain proteins Six 1 and 4, which in turn induce expression of Pax 3. Pax 3 induces expression of key MRFs including Myf5 and MyoD. At later stages of myogenesis, Myogenin expression is induced by the upstream MRFs, enabling terminal differentiation. Solid black arrows indicate known interactions at the transcriptional level, while dashed arrows indicate indirect genetic interactions. (Adapted from Bismuth and Relaix, 2010).

Some of the difference in functional effects of the MRFs is dependent on their interactions with co-factors. MRFs are capable of forming homodimers and heterodimers with other factors, and one group of bHLH transcription factors called the E proteins appear particularly important for promoting myogenesis. E proteins efficiently bind E box sites found at myogenic promoters, and studies have shown members of the E protein family including E2-2, HEB and E12/E47 can form heterodimers with any of the MRFs; however preference for certain pairings is apparent even *in vitro* (Blackwell and Weintraub, 1990). Similar to the MRFs, E proteins also show significant redundancy, as single KOs of each of the E proteins does not result in loss of skeletal muscle (Berkes and Tapscott, 2005).

1.2.2.3 Myogenic co-factors

Another important class of myogenic transcription factors are the myocyte enhancer factor 2 (Mef2) proteins (Black and Olson, 1998). There are four alternatively spliced Mef2 gene products in vertebrates, Mef2A-D, and they are generally expressed very widely during development, with the exception of Mef2C, which is found only in muscle, brain and spleen tissue (Martin et al., 1993, 1994). These TFs belong to the MADS (MCM1, agamous, deficiens, serum response factor) box containing family, and bind a DNA motif found in many muscle-specific gene promoters (Gossett et al., 1989). The Mef2 binding site is often situated close to an E box in myogenic

promoters and enhancer regions, and indeed Myod1 and Mef2 have been shown to interact directly *in vitro* to synergistically activate transcription of downstream targets (Molkentin et al., 1995; Wasserman and Fickett, 1998). Additionally, Mef2A overexpression in cultured cells can cause conversion to the myogenic lineage via interaction with Myod1 (Kaushal et al., 1994). Like the other myogenic factors mentioned, there appears to be some functional redundancy between Mef2 members, as skeletal myogenesis appears normal in the absence of Mef2B, C and D, while the role of the Mef2 TFs is thought to be in mediating terminal myogenic differentiation, as expression of these proteins occurs following *Myogenin* expression (Edmondson et al., 1994; Estrella et al., 2015; Lin et al., 1997).

The MRFs are also negatively regulated by other bHLH TFs, including most notably the Id family as well as Twist, MyoR and Mist-1. The Id (Inhibitor of DNA binding) family is expressed by four different genes in mice and humans, Id1, Id2, Id3 and Id4 (Benezra et al., 1990; Lasorella et al., 2014; Riechmann et al., 1994). Id proteins inhibit myogenesis in a dominant negative manner by forming heterodimers with E proteins, sequestering them from interacting with the MRFs. As Id proteins do not contain a basic region, they cannot bind DNA, and thus prevent E protein binding to myogenic promoters, inhibiting myogenesis (Norton et al., 1998). Like Id proteins, Twist inhibits myogenesis by binding E proteins and sequestering them from the MRFs, however Twist also contains a basic region, which allows it to also form heterodimers with Mef2 TFs (Spicer et al., 1996). Unlike Id and Twist, MyoR and Mist-1 bind MRFs directly via interactions at their basic region. While MRF/MyoR and MRF/Mist-1 heterodimers are capable of binding E boxes at gene promoters, these complexes are unable to initiate transcription, thereby dominantly negatively regulating the MRFs and myogenic differentiation (Lemercier et al., 1998; Lu et al., 1999).

Further control of myogenesis is provided by epigenetic regulators including histone acetylases (HATs), histone deacetylases (HDACs) and chromatin remodelling agents such as the SWI/SNF complexes (Berkes and Tapscott, 2005). For example, the HAT p300 is found in complexes with Myod1 in differentiating C2C12 myotubes, and p300 is necessary for muscle-specific gene

expression (Puri et al., 1997). While HATs typically promote gene expression, HDACs tend to repress transcription, and indeed interactions between HDAC4 and HDAC5 with Mef2 proteins inhibit expression of myogenic genes containing Mef2 promoters (Lu et al., 2000; McKinsey et al., 2001). The involvement of SWI/SNF complexes in myogenesis is demonstrated by the requirement of BRG1 and BRM for Myod1-mediated gene expression, and it is likely that these SWI/SNF factors are recruited to myogenic loci by Myod1, as supported by co-immunoprecipitation of Myod1, P300 and BRG1 from C2C12 myotubes, a well-established myoblast cell line (de la Serna et al., 2001; Simone et al., 2004; Yaffe and Saxel, 1977). Additionally, the SWI/SNF protein BAF60 appears instrumental to Myod1 function, as inhibition of this subunit by preventing p38 signalling prevents recruitment of SWI/SNF to myogenic promoters, inhibiting Myod1 activity (Simone et al., 2004). Indeed recent attempts to generate skeletal muscle from human embryonic stem cells have reconfirmed the importance of BAF60, as forced expression of BAF60C with Myod1 commits human ES cells to the myogenic lineage, without the need for mesodermal directed differentiation (Albini et al., 2013).

Finally, an emerging theme in control of differentiation across multiple cell lineages in development is regulation by micro RNAs (Ambros, 2004; Bartel, 2004). Micro RNAs (miRNAs) are typically ~22 nucleotide single-stranded RNA molecules produced via cleavage of pre-miRNA transcripts by the cytoplasmic processing enzyme Dicer (Lund and Dahlberg, 2006). They function via complementary binding to specific mRNA sequences, thereby negatively regulating that mRNA by targeting it for degradation or inhibiting translation. As with other lineages, miRNAs are emerging as a major regulator of myogenesis, with three miRNAs in particular, miRNA-206, miRNA-1 and miRNA-133, being key to skeletal muscle development and having muscle-specific expression patterns (Luo et al., 2013). While a detailed explanation of the function of specific miRNAs is beyond the scope of this introduction, miRNAs have been implicated in regulating multiple stages of myogenesis, from initial cell fate commitment and

exit of the cell cycle to MRF and Mef2 regulation and even in myoblast fusion and fibre sub-type decisions (Chen et al., 2010; Hirai et al., 2010; Naya and Olson, 1999; van Rooij et al., 2009).

1.2.3 Functional maturation of the neuromuscular system

Once motor neurons and muscle are formed in the developing embryo, and motor axons have been correctly guided to their specific muscle targets, the next stage in development of the neuromuscular system is the formation and maturation of the specialised synapse between these cells, the neuromuscular junction (NMJ). This process occurs around E12-E13.5 in rodents, and requires signalling and activity from both the presynaptic motor axon terminal and the post-synaptic muscle end plate (Sanes and Lichtman, 1999). There is also increasing evidence that perisynaptic Schwann cells (PSCs) or terminal Schwann cells, a PNS glial-cell type found associated with NMJs, are important regulators of NMJ function and maturation, revealing this to be a complex and dynamic process (Darabid et al., 2013; Reddy et al., 2003).

Prior to arrival of motor axons at skeletal muscles, muscle fibres show some level of pre-patterning, with clusters of ionotropic acetylcholine receptors (AChRs) forming at the centre of myofibres (Yang et al., 2001). This neuron-independent pre-patterning has been shown to influence the location of mature NMJs *in vivo,* and while it is independent of neurally derived factors including agrin, it is dependent on the Muscle specific tyrosine kinase (MuSK) (Kim and Burden, 2008; Vock et al., 2008; Yang et al., 2001). Once motor axons reach these pre-patterned sites, poly-innervated NMJs are formed, with many MNs competing to synapse with the same muscle fibres at the same synapses (Tapia et al., 2012; Wyatt and Balice-Gordon, 2003). While functional signalling can occur at these immature NMJs, maturation of both the pre- and post-synaptic compartments is necessary for controlled and efficient muscle activity (Darabid et al., 2014).

1.2.3.1 Post-synaptic maturation

Post-synaptic maturation is characterised by an increase in the number and clustering of AChRs on muscle fibres, and this is largely driven by interactions between the proteoglycan agrin and its receptor MuSK. Genetic studies on agrin and MuSK have revealed the importance of these factors to NMJ formation and maturation, as defects in NMJ synaptogenesis are seen in KO mice of both genes. MuSK is a transmembrane tyrosine kinase receptor that is concentrated at the post-synaptic endplate and co-localises with AChRs, while agrin is secreted into the extracellular space by motor axon terminals (as well as other sources) where binding triggers MuSK autophosphorylation, leading to increased AChR clustering at the endplate (Burgess et al., 1999; DeChiara et al., 1996; Valenzuela et al., 1995). Agrin KO mice show multiple defects in NMJ development, particularly after neuronal innervation, with AChRs failing to cluster and instead being uniformly spread out across the sarcolemma, as well as impaired arborisation and overgrowth of MN axons (Gautam et al., 1996). MuSK KO mice show a similar impairment in AChR clustering, however this is even more severe than in agrin KOs, with loss of even the neuronal-independent AChR pre-patterning (DeChiara et al., 1996).

Another transmembrane protein, low-density lipoprotein receptor-related protein 4 (LRP4), is also important to AChR clustering both before and after innervation. LRP4 serves as an agrin co-receptor for MuSK, and mice lacking LRP4 have a similar phenotype to MuSK KOs (Weatherbee et al., 2006). Additionally, LRP4 association with MuSK appears to be the critical step in MuSK activation, as this can cause AChR pre-patterning and clustering even in the absence of agrin (Kim et al., 2008).

The downstream activity of MuSK is mediated partly by its recruitment of proteins of the post-synaptic density (PSD), including neuregulin receptors and rapsyn. Rapsyn is capable of clustering AChRs at the post-synaptic endplate, and rapsyn KOs show a lack of AChR clustering, instead having AChRs uniformly spread across their muscle fibres, similar to MuSK KOs (Gautam et al., 1995). Neuregulin receptors on the other hand are not directly involved in AChR clustering,

but instead influence AChR gene transcription and protein production (Jo et al., 1995; Sandrock et al., 1997). This is of particular interest, as the nuclei of syncytial myofibres display differential gene expression profiles, with sub-synaptic nuclei transcribing much higher levels of AChR mRNA than non-synaptic nuclei (Burden, 1993). Supporting this hypothesis, mice lacking the neuregulin-1 protein or its tyrosine kinase receptors ErbB2 or ErbB3 show aberrant development of NMJs, and overexpression of ErbB2 in murine muscle *in vivo* causes impaired synaptogenesis and a diffuse distribution of AChRs reminiscent of agrin KOs (Ponomareva et al., 2006; Riethmacher et al., 1997; Wolpowitz et al., 2000). While neuregulin signalling has a clear influence on NMJ formation and maturation, it is not clear if this is a direct effect, or possibly mediated via PSCs, as these glia are absent in mice lacking neuregulin-1, ErbB2 or ErbB3, and a further study showed that MN or muscle derived neuregulin-1 is not required for AChR clustering (Jaworski and Burden, 2006; Riethmacher et al., 1997; Wolpowitz et al., 2000).

Other important influences on post-synaptic maturation include the effect of matrix metalloproteinases (MMPs) and even acetylcholine itself. Interestingly, acetylcholine signalling appears to negatively regulate AChR clustering in an activity-dependent negative feedback loop, opposing the clustering effects of agrin/MuSK and rapsyn while reducing AChR expression (Misgeld et al., 2005). This effect is even strong enough to partially rescue agrin KO mice, as double KOs for both choline acetyl-transferase (CHaT) and agrin show relatively normal AChR clustering (Misgeld et al., 2005). This activity is thought to prevent or disassemble ectopically located AChR clusters that do not oppose a MN terminal that also supplies clustering signals such as agrin (Darabid et al., 2014). MMPs influence synaptic maturation via controlling levels of agrin in the extracellular matrix. MMP3 has been shown to cleave agrin, and MMP3 KO mice have increased levels of agrin at NMJs and a higher density of AChRs (VanSaun and Werle, 2000; VanSaun et al., 2003). MMP3 activity may be mediated by PSCs, as it has a perisynaptic localisation, co-localising with PSC processes *in vivo* (VanSaun and Werle, 2000; VanSaun et al., 2003).

1.2.3.2 Pre-synaptic maturation

Pre-synaptic maturation is characterised not only by synapse elimination at multiply-innervated NMJs, but also increased neurotransmitter vesicle clustering at the active zone, more active zones per synapse and changes in calcium channel subtype and distribution. Many factors influencing these changes have been identified, and can largely be split into two main groups: extracellular matrix (ECM) proteins and secreted growth factors.

ECM proteins important to pre-synaptic maturation include laminin and collagen family members, which are vital to early and later NMJ maturation respectively. Laminins are multidomain heterotrimeric glycoproteins produced by muscle that contain one α, one β and one γ chain to form a single functional unit (Aumailley et al., 2005). There are multiple isoforms of each laminin chain, and laminin β2 seems particularly important for NMJ maturation, as it is included in all synaptically-localised laminins, and mice lacking this subunit have fewer and smaller active zones with poorly clustered neurotransmitter vesicles and impaired functional properties (Knight et al., 2003; Noakes et al., 1995). This influence is mediated by laminin β2 binding to pre-synaptic calcium channels, which clusters calcium channels at the active zone, in turn leading to recruitment of other active zone components such as bassoon (Chen et al., 2011; Nishimune et al., 2004; Singhal and Martin, 2011). Type IV collagen α subunits are also important for pre-synaptic vesicle clustering, with α2 chains contributing to embryonic development, while α3 and α6 chains are predominantly involved in postnatal maturation (Fox et al., 2007). Muscle derived collagen XIII appears vital for both pre- and post-synaptic maturation, as mice deficient for this protein show reduced AChR clustering, incomplete adhesion of pre- and post-synaptic sites, and invasion of PSC processes into the synaptic cleft (Latvanlehto et al., 2010).

Fibroblast growth factor (FGF) signalling is also important to early stages of NMJ development, as revealed by mice lacking the presynaptic FgfR 2B receptor, which show reduced vesicle clustering in MN terminals and poor NMJ maturation (Fox et al., 2007). The main FGFs responsible for this signalling are muscle-derived Fgf7, 10 and 22 (Chen et al., 2011; Fox et al.,

2007). Other muscle-derived growth factors important for NMJ maturation include GDNF (Glial-cell-derived neurotrophic growth factor) and BDNF (Brain-derived neurotrophic growth factor), however these factors influence MN survival and synapse elimination rather than subcellular changes and specialisations. GDNF promotes MN survival, and overexpression of the muscle isoform delays synapse elimination resulting in NMJs innervated by multiple axons (Henderson et al., 1994; Nguyen et al., 1998). While mature BDNF (mBDNF) has similar effects to GDNF, BDNF is first produced as pro-BDNF, which has been shown to promote synapse elimination (Je et al., 2013). The proteolytic cleavage of pro-BDNF to form mBDNF may be carried out by MMPs including MMP3 which is localised to the perisynapse along with PSCs, indicating that this may be another mechanism through which PSCs influence NMJ maturation (Darabid et al., 2014; Je et al., 2013).

1.2.3.3 Activity dependent maturation

Once the pre- and post-synaptic specialisations necessary to form a synapse are established, further maturation to form a mature NMJ is necessary, and a major contributing factor to this process is neuronal activity at the synapse. As mentioned previously, synapses initially form with multiple MN terminals making contact with a single post-synaptic end plate, however precise and controlled motor activity requires each muscle fibre to be innervated by a single MN (Wyatt and Balice-Gordon, 2003). During post-natal development, presumptive axon terminals compete to occupy the synapse in a highly dynamic, activity-dependent fashion that results in a single MN innervating each muscle fibre (Walsh and Lichtman, 2003). This competition between axon terminals appears to be based on strength or efficacy of activity, as MNs lacking choline acetyl-transferase (ChAT), the enzyme responsible for acetylcholine synthesis, cannot compete with MNs possessing the enzyme for synaptic connections, and are preferentially eliminated (Buffelli et al., 2003).

While the strength of activity is important for synapse elimination, the pattern of activity also influences this competition. MN activity measured by electrophysiology *in vivo* reveals a gradual

shift from initially synchronous firing at early post-natal stages (P0-P4) to more and more asynchronous activity at later stages during the synapse competition phase (P4-P10), and finally complete asynchrony by the end of synapse elimination (P14) (Buffelli et al., 2002; Personius and Balice-Gordon, 2001). This is supported by experiments showing that artificially imposing asynchronous activity on competing terminals promotes synapse elimination, while imposing synchronous activity delays or prevents elimination (Favero et al., 2012). Terminals that have more activity also fire out of synchrony with weaker terminals more often, strengthening the selection of the active terminal over its competitors (Favero et al., 2012). Differences in firing rate or strength may be detected by the muscle end plate or potentially by PSCs, which have been shown to compete with MN axons for contacts on the synapse, can detect different firing activity from separate axonal inputs, and are responsible for removing retraction bulbs (the "losing" axon terminal) from the proximity of the muscle (Bishop et al., 2004; Darabid et al., 2013; Smith et al., 2013). The activity of PSCs at the maturing NMJ have also been linked to morphological changes in the structure of the synapse from an immature oval shape to a characteristic "pretzel shape" seen in mature NMJs, due to their association with MMP3 expression and the change in morphology of these cells to a highly branched structure in a timeframe corresponding to NMJ maturation (Brill et al., 2011). It is also likely that this morphological change is activity-dependent, as it occurs during the synaptic competition phase of development, and a key driver of this transformation is the loss of AChRs from the post-synaptic membrane, which may result from acetylcholine signalling from the terminal bouton (Marques et al., 2000; Misgeld et al., 2005). This may be mediated muscle-expressed laminins acting in an autocrine role, as topological maturation fails to proceed in murine double mutants of laminin α4 and α5, and are delayed in mice lacking laminin α4 (Nishimune et al., 2008). This role of laminin appears to be mediated by laminin-dependent clustering of dystroglycan on the post-synaptic muscle membrane, revealing the complex bi-directional signalling and

interdependent mechanisms occurring at both pre- and post-synaptic partners to coordinate NMJ formation and maturation (Nishimune et al., 2008).

1.3 Stem Cells

Stem cells are characterised by two key properties; they are capable of indefinite self-renewal, and they can differentiate into one or more specialised cell types of the organism in response to the right stimuli. There are four broad categories of stem cells, which include embryonic stem cells (ESCs), adult or somatic stem cells (SSCs), induced pluripotent stem cells (iPSCs) and cancer stem cells (CSCs) (Alvarez et al., 2012). While all stem cells are capable of differentiation into specialised cell types, the potency of each type of stem cell differs, ranging from totipotent to unipotent. A totipotent stem cell is capable of producing every cell type found in the body, as well as all extra-embryonic tissues such as the placental trophectoderm, and is represented by the zygote post-fertilisation of an egg (Rossant and Cross, 2001). Pluripotent stem cells, which includes ESCs, embryonic germ cells and iPSCs, are capable of producing all cells of the body, but cannot produce extra-embryonic tissues. Multipotent, oligopotent and unipotent stem cells are typically restricted to one cell lineage, or even a single cell type as in the case of unipotent stem cells. This last category includes most SSCs, including muscle satellite cells, neural stem cells and mesenchymal stem cells.

The majority of work using stem cells has traditionally been carried out with murine ESCs (mESCs) due to their well-defined culture conditions and relatively fast cell cycle; however the medical potential and ethical advantages of human iPSCs has rapidly expanded research on this stem cell subtype in recent years. While all of the work detailed in this thesis utilises mESCs, an understanding of the defining features of each type of stem cell is valuable, particularly as future extensions to this work could incorporate the use of human stem cells, especially human iPSCs.

1.3.1 Stem cell subtypes

1.3.1.1 Embryonic stem cells

Embryonic stem cells (ESCs) are obtained by enzymatic dispersion of the inner cell mass of a pre-implantation blastocyst, and are capable of indefinite self-renewal as well as differentiating into any cell from all three germ layers of the body, excluding extra-embryonic tissues. Mouse ESCs grow in culture as round, compact colonies that are dependent on leukaemia inhibitory factor (LIF) to maintain pluripotency independent of FGF signalling (Pera and Tam, 2010). LIF, produced by the endometrium during implantation *in vivo*, maintains pluripotency and self-renewal by phosphorylating STAT3 via its receptor, Gp130, expressed on the surface of ESCs (Niwa et al., 1998; Stewart et al., 1992; Williams et al., 1988).

The first ESCs were obtained from murine blastocysts, and were initially cultured on layers of chemically arrested mouse embryonic fibroblasts (MEFs) to maintain pluripotency (Evans and Kaufman, 1981; Martin, 1981). The first human ESCs were successfully cultured from human blastocysts in 1998, yet efficient generation of hESCs wasn't achieved until 2004 (Cowan et al., 2004; Thomson et al., 1998). However, while these hESCs appear pluripotent and capable of self-renewal, they require stimulation of FGF/activing pathway for growth, are LIF independent, have a flatter colony morphology, and cannot be passaged by enzymatic dissociation into single cells. These features more closely resemble mouse peri-implantation epiblast-derived SCs, which are partially primed to differentiate into particular lineages, rather than true "naïve", LIF-dependent ESCs (Brons et al., 2007; Nichols and Smith, 2009; Tesar et al., 2007). Recent advances in defining precise cultures conditions has led to the identification of small molecules that inhibit MEK and FGFR/GSK3 that are able to revert hESCs to a more naïve state. This protocol, called 2i or 3i conditions in reference to the number of inhibitors used, enables culture of hESCs independent of FGF signalling, while requiring LIF, resulting in round compact colonies as seen with mESCs (Ying et al., 2008).

The switch from naïve ESCs to primed epiblast-like stem cells (EpiSCs) appears to be dictated by epigenetic changes normally occurring during early blastocyst development (Nichols and Smith, 2009). Significant differences in DNA methylation, X chromosome inactivation, histone modification and chromatin structure between EpiSCs and ESCs have been identified which prime the cells to specific lineages while altering responses to external signalling (Bibikova et al., 2008; Guenther et al., 2010). Changes in miRNA expression and alternative splicing of key genes such as at the Dlk1-Dio3 locus have also been identified between ESCs and EpiSCs, and are known to be important in lineage commitment (Liu et al., 2010; Ng and Surani, 2011; da Rocha et al., 2008). Another major difference is that while both ESCs and EpiSCs are capable of teratoma (a tumour containing cells from all three germ layers) formation when injected into an adult animal, only ESCs are capable of generating chimeras with germ line transmission after integration into the blastocyst, a trait of vital importance in creating transgenic animals (Buehr et al., 2008; Pera and Tam, 2010). The establishment of naïve SCs from multiple species presents many opportunities both for efficient genetic engineering and research of developmental biology as well as generating specific differentiated cell types *in vitro* for surgical grafting or cell based assays.

1.3.1.2 Induced pluripotent stem cells

While mESCs have several advantages over hESCs for basic research, including faster differentiation and a shorter cell cycle, hESCs are by definition more relevant to human development and disease. However, hESCs are suffer from multiple ethical concerns, in some regions preventing their use in research entirely, mainly due to the creation of these cell lines resulting in the destruction of potentially viable human embryos. The development of induced pluripotent stem cells has resolved this issue, allowing the production of fully pluripotent human SCs from human somatic cells, by “reprogramming” differentiated cells back to a pluripotent state.

The first advances towards this goal were made with somatic cell nuclear transfer (SCNT), a technique where a donor somatic cell nucleus is injected into an enucleated recipient oocyte, resulting in the reprogramming of the donor nucleus to a pluripotent state. This technique famously allowed the creation of the first cloned animal, Dolly the sheep, however many draw backs including low efficiency, poor reproducibility and the inheritance of the mitochondria from the oocyte limited its uptake (Wilmut et al., 1997).

The next major breakthrough in induced pluripotency came in 2006, with the transfection of four key pluripotency genes, Oct4, Klf4, Sox2 and cMyc, into mouse fibroblasts, causing reprogramming into induced pluripotent stem cells (iPSCs) (Takahashi and Yamanaka, 2006). This was quickly replicated with human fibroblasts to generate human iPSCs, providing a source of pluripotent human SCs free from ethical complications (Takahashi et al., 2007). These cells were shown to have pluripotency equal to ESCs initially via the generation of chimeric mice containing iPSC derived cells in all three germ layers (Okita et al., 2007). Following this, fully iPSC derived mice were generated in a tetraploid complementation paradigm, where a tetraploid blastocyst, normally incapable of producing a viable embryo, is "rescued" by injection of pluripotent stem cells. While tetraploid cells can produce the extraembryonic tissues, only the iPSCs can contribute to the embryo, proving their pluripotency (Zhao et al., 2009).

Improvements on the original technique including the use of non-integrating plasmids as opposed to viral integration of the reprogramming factors (which can have unpredictable integration site related effects), and removal of cMyc (which can lead to increased tumour formation), have improved the safety and reliability of iPSC technology in recent years (Okita et al., 2008; Si-Tayeb et al., 2010). An additional advantage of iPSCs is the opportunity to produce patient-derived cell lines, carrying disease-specific mutations, accelerating the generation of *in vitro* models of the disease and opening the door to personalised medicine based on results from each patient's own iPSC lines (Burkhardt et al., 2013; Chamberlain et al., 2010; Moretti et al., 2010).

1.3.1.3 Somatic and cancer stem cells

Somatic stem cells (SSCs) are uni- or multipotent stem cells found in all postnatal tissues of the body. Like ESCs, they are capable of indefinite self-renewal as well as differentiation into specialised cell types that comprise the tissue they are resident in. The function of these cells is to maintain tissue homeostasis, as well as responding to signals elicited by damage to enable repair and regeneration of a tissue following injury (Voog and Jones, 2010).

All SSCs express some common stem cell markers, including Oct4, Klf4 and Sox2, and each type of SSC also expresses markers specific to its lineage, such as CD271 in bone marrow SCs and CD105 in subcutaneous fat SCs (Zapata, 2013). Most somatic stem cells described to date are regulated by a specialised microenvironment called the stem cell niche, which comprises specialised cell types that regulate the proliferation of the SSCs in response to external signalling events, typically via close proximity to a vascular supply. Stem cell niches have been described in many tissues, including the intestinal epithelium, skin, bone marrow, brain and muscle (Gómez-Gaviro et al., 2012; Moore and Lemischka, 2006; Yin et al., 2013). Most SSCs are maintained in a quiescent state in the niche, with periodic phases of proliferation and differentiation induced to maintain tissue homeostasis, particularly in high-turnover tissues such as the intestinal epithelium or skin.

While SSCs can be cultured and expanded *in vitro*, and have been successfully differentiated, for example from pancreatic SCs into insulin-producing β cells, these cultures are often time-consuming and differentiation has a low efficiency (Ramiya et al., 2000). These drawbacks, possibly related to the normally quiescent nature of these cells *in vivo,* in addition to issues in harvesting sufficient numbers of cells from adult tissues, limit the use of these SCs in regenerative medicine applications or disease modelling. New approaches aimed at manipulating the niche itself with small molecules, biologics or biomaterials may enable endogenous SSC amplification and regeneration, and could represent a viable alternative regenerative strategy for some diseases (Lane et al., 2014).

Cancer stem cells are cells found within tumours or leukaemias that display traits characteristic of physiological SCs including expression of telomerase and pluripotency markers like Sox2, a relatively slow rate of division, and lack of differentiation markers (Alvarez et al., 2012). While initially suspected to be SSCs that accumulated mutations leading to uncontrolled proliferation, a more recent hypothesis is that these cells are cancer cells that have acquired these SC characteristics later, providing increased resistance to radio- or chemotherapy treatments that efficiently kill more rapidly proliferating cancer cells (Borovski et al., 2011).

While all these stem cell types represent areas of active research today, further discussion of their properties is beyond the scope of this introduction. All the work presented in this thesis was carried out using murine ESCs, as the culture of these cells has been well established, and the faster proliferation and differentiation rates compared to human SCs is a significant advantage for proof of principle studies such as this. Another advantage offered by use of ESCs is the relative ease of genetic modification and clonal selection to create stable transgenic cell lines carrying genes of interest. This strategy can be used to introduce anything from fluorescent reporter proteins to known disease mutations, or even inducible transcription factors, enabling greater control over developmental and functional processes in ESC-derived cells. As ESCs are capable of producing cells from all three germ layers, directing their differentiation towards the desired cell type(s) is an important consideration for their use in *in vitro* modelling. A discussion of the directed differentiation and genetic modifications used in this study is presented in the following section.

1.3.2 Directed differentiation

Initial efforts to culture stem cells *in vitro* were focused on establishing media and conditions that were capable of maintaining stem cells (ESCs) in an undifferentiated, proliferative state. This is due to the fact that ESCs will undergo spontaneous differentiation if they do not receive specific signals maintaining them in the undifferentiated state. If cultured in suspension *in vitro*, ESCs will form embryoid bodies (EBs), spherical three-dimensional aggregates that recapitulate

aspects of early embryogenesis, and can express markers of all three germ layers (Itskovitz-Eldor et al., 2000; Kurosawa, 2007). If injected into immune-deficient mice, pluripotent stem cells will form a teratoma, a tumour composed of cell derivatives from all three germ layers, and in fact teratoma formation is often used as a test or benchmark for the pluripotency of stem cell lines (Aleckovic and Simón, 2008; Przyborski, 2005).

Once ESCs could be maintained in an undifferentiated state *in vitro*, the next challenge was to control their differentiation into specific cell lineages of interest for use in research and potentially cell therapy and regenerative medicine. Much progress has been made in this area, with protocols developed to produce cells including contractile cardiomyocytes, various hematopoetic cell types, hepatocytes, pancreatic beta cells that secrete insulin and various cells of the neural lineage including dopamine and motor neurons as well as astrocytes and oligodendrocytes (Irion et al., 2008; Murry and Keller, 2008). For this work, we developed and optimised protocols for the production of motor neurons and their supporting glia, as well as their target tissue, skeletal muscle. The production of these cell lineages are discussed below.

1.3.2.1 Motor neurons

One of the first and most reproducible protocols for directed differentiation is that for motor neurons, first developed in the Jessel lab for mESCs and later adapted to work for hESCs (Li et al., 2005; Wichterle et al., 2002). Directing differentiation towards a spinal motor neuron fate relies on similar signalling pathways to those found *in vivo* during spinal cord development, with the key factors being retinoic acid (RA; produced by the somites and paraxial mesoderm *in vivo*) and sonic hedgehog (Shh; produced by the notochord and floorplate *in vivo*). As the spinal cord is patterned along the dorsoventral and rostrocaudal axes in response to gradients of Shh and RA respectively, supplying these signalling molecules to differentiating ESCs *in vitro* at specific concentrations results in a ventral spinal cord identity that gives rise to spinal motor neurons. For mouse ESCs, differentiation is initiated with chemical dissociation of ESC colonies followed by EB suspension culture. Activation of RA and Shh signalling for three days during EB

development results in roughly 30% of cells acquiring a MN identity, as determined by expression of Hb9 and Islet1, characteristic markers of post-mitotic MNs (Wichterle et al., 2002).

While RA is relatively simple to synthesise, Shh is a protein, and preparations of purified Shh are relatively expensive and can have varying bioactivity. This potential variability can be avoided by use of small molecule agonists such as sonic hedgehog agonist (SAG), also reducing the cost of differentiation, an important factor to be considered in the case of scaling-up production for clinical purposes (Wichterle et al., 2002). Additionally, while up to 30% of cells may become post-mitotic MNs, many contaminating and proliferative cells remain in the EB after differentiation. MNs must therefore be sorted from contaminating cell types if a pure MN population is desired, and proliferative cells must be eliminated, especially for clinical use, as these could pose a serious risk of tumour formation if grafted *in vivo*.

1.3.2.2 Glia

Some of the "contaminating" cells in EBs subjected to the MN differentiation protocol are likely to be CNS glia, as the same signalling molecules and pathways give rise to glia in regions overlapping the MN progenitor zone (pMN) at later time points in the developing spinal cord *in vivo* (Rowitch and Kriegstein, 2010). As glial cell production typically occurs after neurogenesis *in vivo*, and astrocytes are known to be produced in ventral neural tube overlapping the pMN domain, continued culture of EBs subjected to the MN differentiation should lead to the production of ventral spinal astrocytes (Kessaris et al., 2001). Indeed, immunostaining EBs subjected to MN differentiation for glial fibrillary acidic protein (GFAP), a key glial cell marker particularly prominent in astrocytes, reveals the presence of substantial numbers of astrocytes generated by these conditions (Bryson et al., 2014).

In addition to astrocytes, spinal oligodendrocytes are also produced in high quantities from the pMN zone at later developmental time points *in vivo* (Rowitch and Kriegstein, 2010). While astrocyte production does not appear to require further factors, oligodendrocyte precursor

proliferation and maturation *in vivo* relies on FGF and platelet derived growth factor (PDGF) (Baron et al., 2000; Rogister et al., 1999). Efforts to produce oligodendrocytes from ESCs have recapitulated this signalling *in vitro*, resulting in relatively efficient production of oligodendrocyte precursors that express PDGFR-α and NG2, markers of this lineage, and subsequent removal of PDGF and FGF stimulation facilitates maturation into oligodendrocytes that express high levels of myelin basic protein (MBP), a marker of mature oligodendrocytes (Glaser et al., 2005; Izrael et al., 2007; Nishiyama et al., 2009).

1.3.2.3 Muscle

While the differentiation of ESCs into multiple ectodermal and endodermal lineages has been well characterised, including protocols to generate spinal MNs and glia documented in this study, the generation of mesodermal tissue, and particularly skeletal muscle, has remained elusive. This may be partly explained by the lack of paraxial mesoderm formation during EB differentiation, the major developmental source of skeletal muscle *in vivo*. Some success has been achieved using RA signalling to expand the myogenic progenitor population by recapitulating elements of *in vivo* myogenesis, or post-EB differentiation cell sorting by flow cytometry for PDGFRα and vascular endothelial growth factor receptor-2 (VEGFR-2) to enrich for paraxial mesoderm progenitors (Ryan et al., 2012; Sakurai et al., 2008). However, these approaches have low efficiency and do not produce defined cell populations. While attempts to induce skeletal muscle differentiation using external signalling factors have had limited success, alternative strategies driving myogenic differentiation using transgenic approaches have produced more encouraging results.

The forced expression of Pax3 and/or Pax7 in mouse and human pluripotent SCs has been shown to enhance paraxial mesoderm formation during differentiation, and generates a population of cells that are capable of engraftment into host skeletal muscle fibres, restoring muscle functionality in dystrophic mice (Darabi et al., 2008a, 2011a, 2012). An alternative approach has been to drive ectopic expression of MRFs, with particular focus on Myod1, due to its ability to

induce myoblast formation in multiple cell types, and even to force conversion of primary fibroblasts, chondroblasts and retinal pigmented epithelium to the myogenic lineage (Choi et al., 1990; Iacovino et al., 2011). Inducible *Myod1* transgene expression in pluripotent SCs results in the efficient production of skeletal myoblasts, and engraftment of induced cells into dystrophic mice revealed functional incorporation into host musculature with graft derived dystrophin expression evident (Ozasa et al., 2007; Tanaka et al., 2013).

In this study we took a similar approach to those described above, generating a mESC line containing a *Myod1* transgene under an inducible tetracycline response element (TRE). This cell line allows inducible *Myod1* expression, driving induced cells towards a skeletal myogenic fate during EB differentiation.

1.3.3 Stem cells in research

The stem cell field has great potential for revolutionising the future of both basic research and clinical medicine, and the discovery of iPSCs has circumvented initial ethical concerns surrounding the use of ESCs. While exciting, it is the combination of stem cell technology with other disciplines and techniques, such as development, genetics, pharmacology and surgery that will ultimately provide the greatest benefits. For example, many successful differentiation protocols rely on a thorough understanding of *in vivo* development, recapitulating signalling pathways driving endogenous gene expression. Some of the techniques and applications of stem cells most relevant to this study are presented below.

1.3.3.1 Genetic modification

One of the greatest strengths of pluripotent SCs is the ability to introduce stable genetic modifications relatively quickly and easily to create transgenic cell lines. As ESCs or iPSCs can be expanded from single clonal colonies that can be screened for a desired mutation/insertion, the reproducibility of experiments using genetically modified cell lines is much higher than transient transfection into primary or cultured cell lines. Stable transfection also enables long-term

studies of gene function or cell development, whereas transient transfection can only be used to observe short-term effects.

Genetic modification can be used in multiple scenarios, with possibly the most common being introduction of a reporter construct for a certain cell fate or lineage, or fluorescent proteins to facilitate imaging or lineage tracing studies. An example of this use in this study is the introduction of a GFP gene under the control of an Hb9 promoter in mESCs, enabling visual identification of MN differentiation. Creation of transgenic animals with ESCs containing these modifications allows visualisation of the *in vivo* development of the lineage or cell type of interest, while also helping visualise the effects of experimental manipulations pertinent to that cell type (Wichterle et al., 2002). Fusing a fluorescent protein to a protein of interest can also be used to visualise protein or organelle sub-cellular localisation, for example generation of transgenic animals containing an AChR-GFP fusion protein has been used to visualise NMJ formation and development *in vivo*, giving novel insights into this dynamic process (Gensler et al., 2001; Yampolsky et al., 2010). Fusing other short peptide sequences to target proteins can enable immunocytochemistry or modify protein expression, for example using a short myc-tag to facilitate labelling using anti-myc antibodies, or addition of a nuclear localisation sequence (NLS) or membrane trafficking sequence to force nuclear or membrane localisation respectively.

Genetic modification can also be used to insert genes with a specific function either in normal physiology or development, or alternatively with a disease related phenotype or mutation. In the case of pluripotent SCs, this can be used to direct cellular differentiation, as in the case of skeletal muscle differentiation presented here, where an inserted TRE::*Myod1* construct enables inducible expression of *Myod1*, driving myogenesis without the need for further external signalling factors. Another example from this study that demonstrates the value of stable genetic modification is the introduction of an optogenetic channel into ESCs, resulting in stable expression of Channelrhodopsin-2 (ChR2) in ESC-derived MNs (Nagel et al., 2003). This modification enables non-invasive control of ESC-derived MN activity via blue-light stimulation

of ChR2, leading to membrane depolarisation and action potential firing (Boyden et al., 2005). Optogenetics combined with reporters of activity such as genetically encoded calcium indicators (GECIs) should allow the non-invasive stimulation and reporting of neuronal activity in ESC-derived populations, facilitating studies of network dynamics, activity driven behaviours such as muscle contraction, or even enabling external control of grafted ESC-derived neurons *in vivo*.

Gene targeting and editing technologies, such as homologous recombination (HR) and zinc-finger nucleases (ZFNs), or the more recently developed techniques of TAL effector nucleases (TALENs) and CRISPR, provide opportunities for more precise and refined genomic modification (Fontes and Lakshmipathy, 2013; Li et al., 2014). These techniques can be used to create cell lines with gene KO's, insert known disease-causing mutations into endogenous genes to develop accurate pluripotent SC based models of disease, or even correcting patient-specific mutations in iPS cell lines in rescue experiments to investigate the influence of individual mutations. Using gene targeting to insert transgenes into a known genomic locus can also reduce variability and improve the reliability of experiments using modified cell lines.

1.3.3.2 Stem cell therapy

As pluripotent SCs are capable of indefinite self-renewal as well as having the potential to differentiate into any cell type, they present a great opportunity for treatment of otherwise incurable diseases by transplantation of healthy SC-derived cells into a patient. Degenerative diseases that result in gradual loss of specific cell types over time, or disease or injury resulting in damage to a particular organ could be treated by replacement of endogenous tissue(s) with grafted stem cell-derived tissue, fulfilling the endogenous role in the patient.

The transplantation of pluripotent SCs differentiated into the hematopoietic lineage will provide a reliable source of blood products for transfusion as well as enabling treatment of many blood-related diseases, such as immune deficiencies or reestablishment of hematopoietic SC niches following irradiation in the case of radiotherapy. Application of genetic modification could allow

the treatment of genetic diseases also, such as sickle cell anaemia (Hanna et al., 2007; Rideout et al., 2002). Generation of pancreatic beta cells provides an alternative, scalable source of transplant material for treatment of diabetes, and PSC-derived hepatocytes could be used in treating liver disease or injury, and even genetically modified to correct enzyme deficiencies or specific metabolic disorders (Asgari et al., 2013; Schulz et al., 2012).

The differentiation of PSCs into multiple neural and glial lineages also presents an opportunity to treat CNS disorders, including potential treatments for currently incurable degenerative conditions such as multiple sclerosis, Parkinson's disease and Huntington's disease (Benraiss and Goldman, 2011; Lindvall, 2012; Wang et al., 2013). Motor neuron diseases present a more difficult target for cell-based therapies due to the precise connectivity required between CNS and peripheral targets, however multidisciplinary approaches using technologies including optogenetics may present an alternative method to drive motor activity, and our lab recently presented an encouraging proof-of-principle of this approach (Bryson et al., 2014).

PSCs also represent an opportunity to treat muscular disease and injury, including the currently incurable muscular dystrophies. While muscle satellite cells represent the best target population for muscle regeneration, myogenic progenitors derived from human iPSCs have been shown to successfully integrate into mouse host muscle tissue, and restore dystrophin immunoreactivity and muscle function in dystrophic mice (Arpke et al., 2013; Darabi et al., 2012). Genetic correction of murine and human patient derived iPS cells to introduce a functional dystrophin gene has also been demonstrated, with successful transplantation of corrected cell after differentiation to restore muscle function (Filareto et al., 2013; Tedesco et al., 2012).

1.3.3.3 Disease modelling

While stem cell based therapies involving transplantation offer an alternative strategy for treating many difficult or incurable disorders, stem cell technology also presents another valuable opportunity; *in vitro* disease modelling, which is the focus of this thesis. The *in vitro*

differentiation of large numbers of defined, terminally differentiated cells facilitates the scalable production of cell—based assays for research, with the added benefits of fast and efficient genetic modification. The inherent scalability of PSCs makes them particularly applicable to large-scale pharmacological screening assays, as large quantities of differentiated cells can be produced. In addition, the potential for using patient-derived cells allows the generation of reliably faithful models of *in vivo* disorders, opening the door to personalised medicine while also increasing the confidence in the results obtained using these cultures.

One area this may be particularly useful is in modelling neuromuscular circuits, including the development and maturation of the NMJ. Multiple recent studies into both amyotrophic lateral sclerosis (ALS) and spinal muscular atrophy (SMA), the two most common motor neuron diseases, have shown that distinct pathological changes are observed at the NMJ, often before the appearance of clinical symptoms (Fischer et al., 2004; Frey et al., 2000; Gould et al., 2006a; Kong et al., 2009; Murray et al., 2008). In fact, complete rescue of motor neuron death in a mouse model of ALS by deletion of the pro-apoptotic gene *Bax* did not prevent NMJ breakdown, and only slightly affected the progression of the disease (Gould et al., 2006a). These findings suggest that it is in fact the pathophysiology at the NMJ that is important for understanding the disease, rather than the later and possibly consequent events on the motor neurons themselves, highlighting the importance of understanding this structure. However, studying NMJs *in vivo* is technically difficult, requiring invasive biopsies only allowing observation of fixed points in time, and with extremely limited experimental manipulation (Thomson et al., 2012). These factors reveal the value of a defined, reproducible and expandable *in vitro* model of NMJs for functional analysis, disease modelling and pharmacological screening.

1.4 Aims and Objectives

The aim of this study was to establish a reproducible *in vitro* model of neuromuscular circuit formation and neuromuscular junction development using murine embryonic stem cells, to enable functional characterisation of ESC-derived optogenetic MNs and skeletal myoblasts and provide a potential assay for pharmacological screening and investigation of neuromuscular disease mechanisms.

To this end, I developed and characterised a MACS-sortable murine ESC line containing a stably expressed channelrhodopsin-2 transgene. A MACS-sortable murine ESC line containing an inducible *Myod1* transgene was also generated to enable production of skeletal myoblasts, and these cell lines were functionally characterised *in vitro*. Co-cultures of ESC-derived MNs with ESC-derived and primary chick skeletal muscle were optimised and assessed for functional activity and morphological maturation, with particular emphasis on neuromuscular junction formation.

Chapter II

Materials and Methods

2.1 Materials

2.1.1 Standard reagents for molecular biology

- **Lysogeny Broth (LB):** (Sigma)
- **LB Agar:** (Sigma)
- **Ampicillin:** (Sigma) Working concentration of 50µg/ml.
- **Kanamycin:** (Sigma) Working concentration of 50µg/ml.
- **Hygromycin:** (Sigma) Working concentration of 50µg/ml.
- **1% Agarose gel:** (Sigma) 500mg agarose in 50ml 1x TAE buffer.
- **TAE buffer:** 40mM Tris-Acetate, 1mM EDTA

2.1.2 DNA Constructs

Plasmid	*Vector*	*ES Cell Line*
CAGs::Myod1	pTol2	Yes
p2Lox-Myod1	p2Lox	Yes
Myogenin::CD14	pTol2	Yes
p2Lox-Myf5	p2Lox	-

Figure 2.1 Table of DNA constructs. Constructs were designed by I.Lieberam and produced by M.Crossley.

2.1.3 Cell Culture Media and Reagents

Sterile PBS:	(Sigma) Phosphate buffered saline, pH 7.3
HBSS:	(Life Technologies) Hank's Balanced Salt Solution
Trypsin:	(Life Technologies) 0.25% Trypsin
AccuMax dissociation buffer:	(Millipore)
Recovery™ Cell Culture Freezing Medium:	(Life Technologies)
Matrigel:	(BD Biosciences)
5-Fluoro-2'-deoxyuridine (FDU):	(Sigma)
Lipofectamine 2000:	(Life Technologies)
Opti-MEM:	(Life Technologies)
Paraformaldehyde:	4% in PBS, with 15% Sucrose (Sigma)
VectorShield:	(Vector Laboratories)
Mouse Embryonic Fibroblast Cell Media:	DMEM (Life Technologies) 10% Fetal Bovine Serum (Hyclone) 1% Penicillin/Streptomycin (Life Technologies)

Mouse Embryonic Stem Cell Media:	DMEM (Life Technologies)
	15% Fetal Bovine Serum (Hyclone)
	1% Penicillin/Streptomycin (Life Technologies)
	1% Non-essential amino acids (Life Technologies)
	1% Nucleosides (Chemicon)
	2mM L-Glutamine (Life Technologies)
	0.1 mM 2-mercaptoethanol (Sigma)
	1000 u/ml LIF (Chemicon)
	0.01% FGFR inhibitor (1:10,000, Stemolecule)
	0.2% Plasmocin (1:500, InvivoGen)
Motor Neuron Media (ADFNK):	Advanced DMEM/F12 (Life Technologies) in a 1:1 ratio with Neurobasal medium (Life Technologies)
	10% Knock-out serum replacement (Life Technologies)
	1% Penicillin/Streptomycin (Life Technologies)
	2mM L-Glutamine (Life Technologies)
	0.1mM 2-mercaptoethanol (Sigma)

Primary Hippocampal Media:	Neurobasal media (Life Technologies)
	2% B27 (Life Technologies)
	1% Glutamax (Life Technologies)
	1% Penicillin/Streptomycin (Life Technologies)
	[2% Foetal Calf Serum {Attachment} (Life Technologies)]
Myoblast Media:	DMEM (Life Technologies)
	10% Fetal Bovine Serum (Hyclone)
	1% Penicillin/Streptomycin (Life Technologies)
	2mM L-Glutamine (Life Technologies)
Myotube fusion Media:	DMEM (Life Technologies)
	2% Fetal Bovine Serum (Hyclone)
	1% Penicillin/Streptomycin (Life Technologies)
	2mM L-Glutamine (Life Technologies)
Chick Primary Muscle Media (CPMM):	DMEM (Life Technologies)
	10% Horse Serum
	5% Chick Embryo Extract

	1% Penicillin/Streptomycin (Life Technologies)
MACS Buffer:	D-PBS without calcium (Life Technologies)
	0.5% BSA (Life Technologies)
	5U/ml trypsin-free DNase I (Sigma)
Hybridoma Media:	IMDM (Life Technologies)
	10% Fetal Bovine Serum (Hyclone)
	1% Penicillin/Streptomycin (Life Technologies)
	1% L-Glutamine

2.2 Methods

2.2.1 Molecular biology

2.2.1.1 DNA Restriction Endonuclease Digestion

Roughly 1µg of plasmid DNA was mixed with the relevant 10x restriction endonuclease buffer (New England BioLabs; NEB) to a final concentration of 1x in nuclease-free water. Bovine serum albumin (NEB) was added as necessary dependant on the enzymes used (see NEB catalogue). The reaction was incubated at 37°C for 1-2 hours, and products where then run on an electrophoresis gel.

2.2.1.2 DNA Electrophoresis and Extraction

All DNA samples were run in a 1% agarose gel in TAE Buffer containing 0.5µg/ml ethidium bromide to visualise the DNA under ultraviolet illumination. Samples were diluted in 6x Orange loading dye to a final concentration of 1x, and run at 100V alongside a 2-Log DNA ladder (New England Biolabs). Images of the final gel were taken using a digital camera and UV illuminator. Desired products were cut from the gel with a surgical blade, and DNA was extracted using a "Gel Extraction Kit" (Qiagen) following the manufacturer's instructions.

2.2.1.3 Plasmid ligation

Linearised products were mixed with linearised vector DNA in a 3:1 molar ratio, to a final volume of 5µl with 1µl T4 DNA ligase (Promega). This reaction was mixed with 5µl of 2x Rapid ligation buffer (Promega), and incubated at room temperature for 1 hour. Ligated DNA was either used immediately for transformation or stored at -20°C for future transformation.

2.2.1.4 Bacterial Transformation, Selection and Plasmid Purification

The 10µl ligation product was added to 100µl chemically competent DH5α bacteria, prepared in advance using the Zymo Research Transformation Kit according to manufacturer's instructions,

on ice for 1 hour. The bacteria were then heat shocked at 42°C for 45 seconds in a pre-heated water bath, and allowed to recover on ice for 2 minutes. After recovery, 1ml of warmed LB was added, and incubated in a bacterial shaker at 37°C for 1 hour. The sample was then spread on 10cm LB agar plates containing relevant antibiotics and incubated overnight at 37°C to allow selection of transformed clonal colonies.

Selected colonies were further cultured in 5ml LB suspension with antibiotics at 37°C overnight in a bacterial shaker. Plasmid DNA was purified using Qiagen Mini Prep kits as per manufacturer's instructions. Clones containing the desired product were often further cultured in 50ml LB overnight at 37°C and purified using a Qiagen Midi Prep kit to achieve a higher concentration and purity of DNA plasmid. Concentrations were determined using a Nanodrop spectrophotometer.

2.2.1.5 Polymerase Chain Reaction (PCR)

25µl of 2x PCR Ready Mix (Thermo Scientific) was mixed with 1µg of template DNA and 5µM of forward and reverse primers, made up to a final volume of 50µl with nuclease-free water. This reaction mixture was loaded into a PCR thermocycler with the following settings:

1.	Denaturing	-	95°C	1 minute
2.	Denaturing	-	95°C	1 minute
3.	Annealing	-	60°C	1 minute
4.	Extension	-	72°C	1 minute
5.	Final Extension	-	72°C	5 minutes

Repeated x30

2.2.1.6 Inverse PCR Mapping

Genomic DNA was harvested from 1 million ESCs using the DirectPCR Lysis Reagent for cells (Viagen Biotech) following the manufacturer's instructions. Briefly, cell samples were centrifuged at 3000 RCF for 5 minutes. The supernatant was discarded, while the

pellet was resuspended in 200µl of DirectPCR Lysis Reagent supplemented with 0.2mg/ml Proteinase K (Sigma), and then incubated at 55°C for 5 hours.

Lysed samples were then heated to 85°C for 15 minutes and then stored at -20°C. Genomic DNA was obtained from lysates by addition of NaCl to a concentration of 250nM, with 0.7 volume isopropanol to promote precipitation. Samples were then centrifuged at 3000 RCF at 4°C for 2 minutes, and the opaque pellets were washed once in 70% ethanol prior to resuspension in 50µl water and concentration determined by nanodrop.

For inverse PCR, 500ng of genomic DNA was digested with AluI or DPNII using appropriate buffers in a volume of 20µl at 37°C for 1 hour, and then 430µl of water was added and the sample heat inactivated at 70°C for 15 minutes. This was allowed to cool to 16°C before adding 50µl 10x T4 DNA Ligase buffer and 2µl T4 DNA ligase and incubated overnight at 4°C to allow self-ligation. DNA was precipitated by adding 50µl 3M sodium acetate, 350µl 100% ethanol and 1µl glycogen and centrifuging at 3000 RCF for 10 minutes at 4°C. Precipitated DNA was washed with 70% ethanol and resuspended in 20µl water.

10µl of this sample was used for the primary PCR reaction with 25µl of 2x PCR Ready Mix (Thermo Scientific), 5µM of forward and reverse primers (see table 2.1), made up to a final volume of 50µl with nuclease-free water. This reaction mixture was loaded into a PCR thermocycler with the following settings:

1.	Denaturing	-	95°C	1 minute
2.	Denaturing	-	95°C	30 seconds
3.	Annealing	-	57°C	30 seconds
4.	Extension	-	72°C	1 minute
5.	Final Extension	-	72°C	5 minutes

Repeated x30

2µl of this PCR reaction was used for the secondary PCR reaction with 1µM of the nested forward and reverse primers (see table 2.1), using the same conditions as for the first PCR. A 1% agarose gel was used to analyse 10µl of the second PCR reaction, and bands were excised, extracted and purified (see Chapter 2.2.1.2). These were then cloned into the pGEM-T easy vector for amplification in competent. DNA extraction from transformed DH5α was carried out using a Qiagen Miniprep kit following the manufacturer's instructions (see Chapter 2.2.1.4). Plasmid DNA was then sent for sequencing using the M13F and M13R primers (Source Bioscience). Analysis of sequences was performed using the MacVector software.

Tol2 (small construct)

Tol2L_in1	DpnII	GATGCGGGAAGAGGTGTATTAGTC
Tol2L_in2		CGTGAGCAGAGACTCCCTGGTG
Tol2L_out		CTGTGAGAGGCTTTTCAGCACTG
Tol2R_in	AluI	TTGGTAATAGCAAGGGAAAATAGAATG
Tol2R_out1		ACAGTCAATCAGTGGAAGAAAATGG
Tol2R_out2		TGGAAGAAAATGGAGGAAGTATGTG

Figure 2.2 Table of inverse PCR primers. Primers were designed against sequences at the ends of the tol2 recognition sequence, to minimise integrated DNA sequencing and enable use of the same primers across multiple cell lines. A nested primer approach was taken to reduce non-specific product amplification.

2.2.2 Cell Culture and Transfection

2.2.2.1 Creation of Stable Embryonic Stem Cell Lines

All DNA constructs were introduced into embryonic stem cells (ESCs) via electroporation. Approximately $5x10^6$ ES cells were electroporated with 20µg DNA (3:1 transposase:transgene) in a Biorad X-cell Gene Pulser (240V, 500µF, infinite resistance, in a 4mm cuvette) and then cultured on mouse embryonic fibroblasts. After 24 hours of recovery relevant antibiotics were added, and surviving clones were picked for screening and expansion after 7-10 days under selection. The inducible *Myod1* lines were selected based on a spindle-shaped morphology and expression of muscle specific genes, such as myosin heavy chain. Final lines were selected for high expression of the desired transgene in a specific and uniform manner, in addition to good morphology and continued antibiotic resistance.

2.2.2.2 COS-7 Cell Transfection

COS-7 cells were cultured in DMEM (Life Technologies) with 15% FBS (HyClone), 1x Penicillin/Streptomycin (Life Technologies) and 2mM L-Glutamine (Life Technologies) in T-75 culture flasks (Corning). Before transfection, the cells were dissociated with 0.25% trypsin (Sigma) for 15 minutes at 37°C, counted with a haemocytometer, and plated on permanox slides (Nunc Lab-Tek) at a density of 100,000 cells per well and incubated at 37°C overnight. Immediately prior to transfection, 2µg of the required construct was mixed with 0.5µg of pEGFP-C1 (provided by Dr. I.Lieberam) as a transfection reporter, alongside a transfection control of 2.5µg of pEGFP-C1. These mixtures were then mixed 1:1 with 2% lipofectamine-2000 (Life Technologies) in Opti-MEM (Life Technologies) for 15 minutes at room temperature, and 200µl of the lipofectamine-2000/DNA mix was then applied to the appropriate wells overnight at 37°C. COS cells transfected with optogenetic constructs were dissociated with 0.25% trypsin (Sigma) and plated on 18mm coverslips 24 hours post-transfection for patch clamping.

2.2.2.3 Mouse Embryonic Fibroblasts

Non-mitotically inactivated mouse embryonic fibroblasts were purchased from Millipore. One vial containing 5-6x10^6 cells was removed from liquid nitrogen, thawed in a 37°C water bath and resuspended in 5ml of mouse embryonic fibroblast (MEF) medium. After centrifugation the cells were evenly distributed between 6x 90mm Nunc™ tissue culture plates and cultured in a tissue culture incubator at 37°C in MEF medium until confluent.

2.2.2.4 Mitotic inactivation and Freezing of MEFs

Once the MEFs were confluent, the MEF media was replaced with MEF media + 10µg/ml Mitomycin C (Sigma) for 2 hours at 37°C to mitotically arrest the cells. The MEFs were then washed with sterile PBS three times before being dissociated with 0.25% trypsin at 37°C for 10 minutes. Dissociated cells were collected in sterile 50ml Falcon tubes (Fischer Scientific) and the trypsin was inactivated with MEF media prior to centrifugation. The cell pellet was then resuspended in Recovery™ Cell Culture Freezing Medium (Life Technologies) and quickly aliquoted into freezing vials (Star Labs) in various volumes according to future experimental requirements. These vials were put into a Mr. Frosty™ Freezing Container (Thermo Scientific) and stored at -80°C overnight. The following day the vials were transferred to liquid nitrogen storage for future use.

2.2.2.5 Embryonic Stem Cell Culture

Embryonic stem cells (ESCs) were grown on Mitomycin C-inactivated mouse embryonic fibroblasts in ES media in Nunc™ tissue culture plates. Stem cells were passaged onto new plates with fresh mouse embryonic fibroblasts when 80-90% confluent.

2.2.2.6 Freezing

ES cell cultures for expansion and freezing were cultured in a 6-well Nunc™ tissue culture plate to 80-90% confluency before being washed three times with sterile PBS and

dissociated with 0.25% trypsin at 37°C for 10 minutes. Dissociated cells were collected in sterile 15ml Falcon tubes (Fischer Scientific) and the trypsin was inactivated with MEF media prior to centrifugation. The cell pellet was then resuspended in Recovery™ Cell Culture Freezing Medium and quickly aliquoted into freezing vials each containing ¼ of the original cell number. These vials were put into a Mr. Frosty™ Freezing Container (Thermo Scientific) and stored at -80°C overnight. The following day the vials were transferred to liquid nitrogen storage for future use.

2.2.2.7 Motor Neuron Differentiation

ES cell colonies were dissociated after reaching 80-90% confluency in culture on mouse embryonic fibroblasts ("Day 0"), and cultured as embryoid bodies (EBs) in suspension culture in motor neuron media (ADFNK). After 2 more days ("Day 2"), the media was replaced and supplemented with 1µM retinoic acid (Sigma) and 0.5µM Sonic Hedgehog Agonist (HhAg1.3, Curis Inc.) to induce a ventral cervical spinal motor neuron fate (as in Wichterle *et al.,* 2002), and cultured for an additional 3 days before Magnetic Activated Cell Sorting (MACS) to obtain purified ESC-derived motor neurons ("Day 2+3").

2.2.2.8 Astrocyte Differentiation

To obtain astrocytes the protocol for differentiating motor neurons was followed until "Day 2+3", at which point the EBs were dissociated, counted using a haemocytometer and plated on Matrigel-coated 90mm Nunc™ tissue culture plates at $1x10^6$ cells per plate in 10ml ADFNK. These cells were maintained in this format for 7 days ("Day 2+10"), only replacing the ADFNK every 2 days. The adherent cultures were then dissociated for MACS on "Day 2+10" to obtain purified ESC-derived astrocytes.

2.2.2.9 Induced Myoblast Differentiation

"iMyoD C4" ES cell colonies were dissociated after reaching 80-90% confluency in culture on mouse embryonic fibroblasts ("Day 0"), and cultured as embryoid bodies in Myoblast media. After 2 days ("Day 2"), the EBs were collected and transferred to matrigel-coated tissue culture plates, where 10ug/ml Doxycycline was added to fresh Myoblast media to induce the expression of the *Myod1* transgene under the control of the tetracycline response element (TRE). The cells were cultured in this medium for 4 days ("Day 2+4"), with a full media exchange after 2 days, before dissociation with 0.25% trypsin and either plating or MACS.

2.2.2.10 Primary Muscle Preparation

Fertilised chick eggs were incubated at 37°C for 10 days before the surface of the eggs was sprayed with 70% ethanol, a window was opened using surgical scissors and the embryos were decapitated using forceps. The torso was placed in sterile DMEM in a 90mm Nunc™ tissue culture plate and the skin along the ventral surface of the trunk was cut along the midline, blunt dissected and pealed back to the limbs using forceps. A single vertical cut through the abdominal muscles and ribcage was made in a caudal-rostral direction, and then the pectoralis major muscles were excised using forceps and transferred to a fresh tissue culture plate. Large pieces of muscle were diced using forceps to achieve relatively uniform small chunks, which were then transferred to an empty tissue culture dish and dissociated in 3ml of 0.25% trypsin at 37°C for 30 minutes. The trypsin was inactivated with 5ml MEF media and the suspension was centrifuged and passed through a 40µm filter. The cells were then cultured on a fresh 90mm Nunc™ tissue culture plate 37°C for 30 minutes to allow fibroblasts to adhere to the plastic. Cells remaining in suspension were collected, centrifuged and resuspended in 1ml Chick Primary Muscle Media (CPMM) for counting via haemocytometer prior to further culture. Roughly $1x10^6$ cells were obtained per chick embryo.

2.2.2.11 Production of Chick Embryo Extract

Fertilised chick eggs were incubated at 37°C for 10 days before the surface of the eggs was sprayed with 70% ethanol, a window was opened using surgical scissors, the embryos were decapitated using forceps and the torsos were placed in a 50ml falcon tube containing 20ml DMEM. Once all embryos were collected, they were transferred to a 10ml syringe and forcefully pushed through using the plunger into a fresh 50ml falcon tube. The macerated mass was left on a roller table at room temperature for 1 hour to allow natural degradation of the tissue, and then centrifuged for 30 minutes (at 3000 RCF). The liquid fraction was collected, passed through a 40μm filter, and stored at -80°C until required.

2.2.2.12 Motor Neuron/Astrocyte Co-Cultures

To form aggregated cellular clusters of sorted ESC-derived MNs and astrocytes (Astroneural aggregates, AsNAs), purified motor neurons were mixed with astrocytes overnight in a hanging drop culture, in a 1:1 ratio of MNs to astrocytes, with 20,000 cells per 20μl drop. MN-astrocyte aggregates were then collected and plated on matrigel-coated 18mm coverslips in 12-well plates (BD Falcon) in ADFNK medium supplemented with 10ng/ml GDNF (R&D Systems) for *in vitro* electrophysiological characterisation, or directly on top of pre-plated muscle cultures for the NMJ model.

Alternatively, 100,000 purified astrocytes were plated on 18mm coverslips in 12-well plates in ADFNK to create a uniform monolayer. The following day, ESC-derived MNs were purified by MACS, and plated on top of the astrocyte monolayer at 10,000 cells per 18mm coverslip. All cultures were fed every 2 days, with supplementary 10ng/ml GDNF added if required, and treated with 1μM 5-Fluoro-2'-deoxyuridine (FDU) from day 2-5 to kill contaminating proliferative cells.

2.2.2.13 Muscle/Motor Neuron Co-Cultures

In all muscle/MN co-cultures, the muscle cells were plated 1 day prior to the addition of MNs, with various culture conditions and cell densities tested. For the ESC-derived myoblasts, unsorted "Day 2+3" MN-EBs were added directly on top of the pre-plated muscle in a 1:1 mix of Myoblast media and ADFNK supplemented with 10ng/ml GDNF.

Both MN-EBs and AsNAs were co-cultured with chick primary muscle, again added the day after preparation and plating of the muscle. For these experiments, a 1:1 mix of CPMM and ADFNK was used. All cultures were fed every 2 days and treated with 1µM 5-Fluoro-2'-deoxyuridine (FDU) from day 2-5 to kill contaminating proliferative cells.

For chronic photostimulation experiments using AsNAs, 6-well culture plates were placed on top of a custom-built heat sink and LED assembly after 1 day in vitro. Cultures were then alternated between stimulation and rest cycles every 48 hours. The blue LEDs (Royal-Blue, 447.5 nm Rebel LED) were topped with collimators, powered by a DC/DC LED driver (Recom) and controlled by a digital I/O device (USB-6501, National Instruments) and custom-written software (Andrew Lowe). The culture medium was supplemented with a cocktail of antioxidants (110 µM vitamin C, 100 µM Trolox, 77 nM superoxide dismutase; all from Sigma and 3.2 µM glutathione from Fisher). Flashes were delivered at 40% LED intensity for 20 ms in bursts of 5 at 20 Hz, every 5 s. The light intensity of the LEDs was adjusted so as to cause reliable activation of ChR2 whilst limiting any potential damage caused by long-term exposure to high-energy light.

2.2.2.14 Hybridoma Cell Culture

Hybridoma cell lines for antibodies of interest (MF20 and F5D) were ordered from the Developmental Studies Hybridoma Bank (DSHB). Frozen vials were thawed upon arrival in hybridoma media (IMDM) and centrifuged for 4 minutes at 3200 RCF to obtain a cell pellet. They were then resuspended in 1ml IMDM, counted using a haemocytometer and transferred to a

sterile T-75 tissue culture flask in 20ml IMDM for culture at an initial concentration of 1 million cells per ml. These cultures were monitored by visual observation and split 1:4 into new T-75 flasks every 2 days with fresh IMDM. For the production of antibody supernatant, the cultures were allowed to overgrow for 4 days, at which point the cells were centrifuged and discarded and the supernatant was frozen at -80°C for testing via immunocytochemistry. To maintain viable stocks of the hybridomas, cultures were centrifuged before becoming confluent, counted and resuspended in Recovery™ Cell Culture Freezing Medium and quickly aliquoted into freezing vials at $4x10^6$ cells per ml.

2.2.3 Magnetic Activated Cell Sorting

ES cell-derived embryoid bodies (EBs) were collected by sedimentation, washed twice with L-15 media (Life Technologies), and then dissociated in 2ml AccuMax dissociation buffer (Millipore). Adherent cultures were washed twice with PBS before dissociation with 5ml Accumax. Dissociated cells were then washed three times in ADFN media (Advanced DMEM/F12 [Life Technologies] in a 1:1 ratio with Neurobasal medium [Life Technologies]) and taken up in 2ml MACS buffer, passed through a 40µm nylon cell strainer (BD Falcon), and taken up in 200µl MACS buffer with 1:100 α-hCD14 antibody (26ic) and incubated for 15 minutes at 4°C. Following this, the cells were centrifuged and taken up in 400µl MACS buffer with 1:10 α-mIgG MACS beads (Milteny) and incubated for 15 minutes at 4°C. A MS-column (Milteny) was inserted into a MiniMACS magnet (Milteny) and pre-washed with 500µl MACS buffer. After centrifugation, cells were taken up in 1ml MACS buffer and applied to the column, which was then washed three times with 500µl MACS buffer. The column was then removed from the magnet, and cells were eluted with 1ml MACS buffer, and eluted cells were counted with a haemocytometer.

2.2.4 Flow Cytometry

Flow cytometry analysis was carried out on a BD Accuri™ C6 flow cytometer (BD Biosciences) according to the manufacturer's instructions. Samples of 100,000 cells were collected from

dissociated pre—sorted cells, flow-through and eluate throughout the MACS procedure, and labelled with directly Phycoerythrin (PE)-conjugated anti-CD14 (26ic) primary antibody for 15 minutes on ice. A sample of unlabelled cells was run first at high flow rate for 10,000 events to establish the size and granulosity of the cell samples and define the "P1" thresholds. The labelled samples were then run at medium flow rate for 10,000 events within P1.

2.2.5 Preparation of Sterile Glass Coverslips

Glass coverslips were first placed in a glass beaker containing 1M HCl acid and heated at 50°C overnight. This was replaced with fresh 1M HCl the following day and left at room temperature overnight. The coverslips were then washed 3x with ddH_20 followed by 100% ethanol at room temperature for 2 hours. Again, the coverslips were washed 1x with ddH_20 followed by 70% ethanol at room temperature overnight. Finally, the coverslips were washed 3x with ddH_20, dried on filter paper in a sterile fume hood and autoclaved prior to use.

2.2.6 Immunocytochemistry

Cells were fixed with 4% paraformaldehyde in 15% sucrose for 30 minutes at room temperature, and then washed with PBS three times and left in PBS overnight at 4°C. Samples were then blocked with PBS + 0.1% Triton X-100 (PBST) + 3% BSA for 1 hour at room temperature, followed by overnight incubation at 4°C with primary antibodies at 1:500 dilution (see table 2.1). Samples were then washed three times with PBS, and secondary antibodies applied at 1:1000 dilution at room temperature for 1 hour (see table 2.2). If used, TOPRO-3 was applied at a 1:5000 dilution alongside secondary antibodies. Samples on slides were then washed three times with PBST, VectorShield (Vector Laboratories) was applied and a coverslip placed over the cells for imaging. For coverslips, a drop of Vectorshield was applied to imaging slides and the coverslips were inverted onto the drop, while preventing bubble formation.

Primary Antibodies	Catalogue Reference, Supplier
Rabbit anti-GFP	A11122, Life technologies
Chick anti-GFP	Ab13970, Abcam
Mouse anti-CD14	Hybridoma 26ic, ATCC
Rabbit anti-CD14	Ab133503, Abcam
Rabbit anti-GFAP	Z0334, DAKO
Mouse anti-myosin heavy chain (Mf20)	Hybridoma MF20, DSHB
Mouse anti-myosin heavy chain (My32)	18-0105, Life technologies
Mouse anti-myogenin (F5d)	Hybridoma F5D, DSHB
Mouse anti-*Myod1*	16148, Abcam
Mouse anti-MCadherin	611100, BD Biosciences
Mouse anti-Synaptophysin	Ab8049, Abcam
Goat anti-Choline acetyltransferase	Ab144, Millipore
Mouse anti-ankyrin-G 2b	N106/65, 75-147, NeuroMab
Rabbit anti-pikbα	14D4, Cell signalling technology

Figure 2.3 Table of primary antibodies used. All primary antibodies were used at 1/500 concentration from stock. Small aliquots were made from stock solution to reduce freeze-thaw cycles.

Secondary Antibodies/Fluorescent labels	Catalogue Reference, Supplier
α-Bungarotoxin Alexa Fluor 555 conjugate	B35451, Life technologies
Phalloidin Alexa Fluor 555 conjugate	A34055, Life technologies
Donkey anti-mouse Alexa Fluor 488	A21202, Life technologies
Donkey anti-mouse Alexa Fluor 568	A10037, Life technologies
Donkey anti-rabbit Alexa Fluor 488	A21206, Life technologies
Donkey anti-rabbit Alexa Fluor 568	A10042, Life technologies
Goat anti-Chicken Alexa Fluor 488	A11039, Life technologies
Donkey anti-Goat Alexa Fluor 568488	A11057, Life technologies
Topro-3	T3605, Life technologies

Figure 2.4 Table of secondary antibodies and fluorescently conjugated labels used. All secondary antibodies were used at 1/1000 concentration from stock, while Bungarotoxin-555 and Phalloidin-555 were used at 1/50, and topro-3 was used at 1/5000. Small aliquots were made to reduce freeze-thaw cycles, and both stock and aliquoted samples were kept in darkness to prevent photobleaching.

2.2.7 *In Vitro* Electrophysiology

All electrophysiology data was obtained from visually targeted whole-cell patch-clamp recordings of ES cells, ES cell-derived motor neurons or COS-7 cells. The cultures were maintained for the duration of the patching protocol in an HBS extracellular solution (pH 7.4, ~280 mOsm) at room temperature that also contained (in mM): 136 NaCl, 2.5 KCl, 10 HEPES, 10 D-glucose, 2 $CaCl_2$ and 1.3 $MgCl_2$. Pipettes were pulled from borosilicate glass (out diameter 1.5 mm, inner diameter 1.17 mm, Harvard Apparatus), with a resistance of 3-6 MΩ, and were filled with an internal solution containing (in mM): 130 K-gluconate, 10 NaCl, 1 EGTA, 0.133 $CaCl_2$, 2 $MgCl_2$, 10 HEPES, 3.5 MgATP, 1 NaGTP. Recordings were acquired with the Pulse software linked to a HEKA EPC10/2 amplifier. Signals were Bessel filtered at 10 kHz (filter 1), and 2.9 kHz (filter 2), digitized and sampled at 25-50 kHz (20-40 μs sample interval). Fast capacitance was compensated for in the on-cell configuration.

Electrophysiological parameters were analysed using custom functions written in Matlab. The resting membrane potential was estimated immediately following membrane patch rupture in current clamp mode with zero holding current and was adjusted for an estimated liquid junction potential of +10mV. With slow capacitance compensation inactive in voltage-clamp mode, I used responses to a 10mV hyperpolarisation step to estimate the cell's membrane resistance (Rm; from the steady holding current at the new voltage) and membrane capacitance (Cm; from the area under the exponentially-decaying current from peak to holding).

Analysis of action potential characteristics was carried out in current clamp mode. A baseline current was injected to hold the cell at -60 mV, simulating a normal resting potential (V_{hold}). In this condition, 10ms duration current steps of increasing amplitude (increments of 2, 5 or 10pA) were injected into the neuronal soma until it reliably fired an action potential (V_m > 0mV).

For evaluation of firing behaviour and maturation, cells were held at -60mV in current clamp mode and subjected to either 500ms duration current steps of increasing amplitude (increments

of 10 or 20pA) or a 500ms duration blue (~488nm at 170mW/mm^2) light exposure provided by a shutter-controlled Xenon-arc lamp (Lambda-LS, Sutter Instruments, UK) with appropriate excitation filters (Chroma Tech. Corp., USA) but no neutral density filtering.

Analysis of electrophysiological data was performed using custom-written functions in Matlab (Mathworks), as in Grubb and Burrone, 2010.

2.2.8 Image analysis

Imaging was performed using a Carl Zeiss LSM 710 confocal microscope or an Inverted Microscope with a 20x/0.8 or 10x/0.25 numerical aperture air objective. Zen 2008 acquisition software (Carl Zeiss) or Metamorph was used to obtain and export most images as .lsm files or TIFF files respectively. Images of patch clamp experiments were obtained using an Olympus 100X oil immersion objective and a CCD camera (CoolSnap HQ, Photometrics). The Slidebook software was used to acquire these images (1,392 X 1,040 pixels with 2X2 pixel binning; 0.5 µm z-axis steps). Image stacks were converted into single maximum intensity z-axis projections, and exported as raw 16-bit TIFF files.

2.2.9 Statistical Analysis

All statistical analysis was carried out in Prism (GraphPad). Where data was found to have a normal distribution (using the D'Agostino & Pearson omnibus normality test), parametric tests were used including students T-Test and one-way ANOVA followed by Tukeys multiple comparisons test to determine individual differences between treatments. Where data did not have a normal distribution, or normality testing was not possible due to low *n* numbers, the non-parametric Mann-Whitney U or Kruskal-Wallis test with Dunn's multiple comparisons test were used. All tests were two-tailed, with the confidence level set at 0.05.

Chapter III

Establishing and Characterising Optogenetic Motor Neurons

3.1 Introduction and Aims

Motor neurons (MNs) are responsible for eliciting motor behaviour, by controlling muscle contraction. As with other neuronal subtypes, the functional output of MNs is determined by their electrophysiology. When a mature MN is sufficiently depolarised, for example by excitatory post-synaptic potentials (EPSPs) driven by neurotransmitters binding membrane receptors on its dendritic arbour, it will typically fire an action potential (AP) along its axon. APs are the primary means of information transfer in neuronal networks, and generally result in neurotransmitter release at the axon terminal(s). In the case of a vertebrate spinal motor neuron, an AP will result in the release of acetylcholine at the axon terminal, which is a specialised synapse with skeletal muscle called a neuromuscular junction (NMJ).

An AP can be measured as a rapid change in the membrane potential (voltage) of the neuron, and indeed MNs have served as an extensively studied model system in electrophysiology (Wen and Brehm, 2010; Zhang et al., 2010, 2009). Recent advances in molecular biology and genetics have given rise to the field of optogenetics, allowing researchers to not only record from neurons, but to dictate their activity non-invasively using light stimulation (Boyden et al., 2005; Fenno et al., 2011; Nagel et al., 2003). While transient transfection of primary MNs does allow expression of optogenetic components *in vitro*, transfection efficiencies are low and often temporary. To better utilise the tools offered by optogenetics to both study and manipulate MNs, we took the approach of creating stable transgenic murine embryonic stem cell (ESC) lines.

Using ESCs allows the production of large quantities of cellular material to work with, and clonal selection of cell lines ensures a homogenous genotype among studied cells. The differentiation

of ESCs into MNs has been well established (Li et al., 2005; Wichterle et al., 2002), and a reliable yield of 30% is achievable. Combining stem cell technology with optogenetics should allow the characterisation and optimisation of optogenetic motor neurons, which can then studied and manipulated *in vitro* or *in vivo* as a source of graft material. These developments could greatly enhance our understanding of basic developmental and cellular biology, electrophysiology, disease modelling and even potentially contribute to regenerative medicine strategies for motor neuron diseases.

3.2 Establishing Optogenetic Motor Neurons

3.2.1 Hb9::CD14-IRES-GFP Embryonic Stem Cells

A previously generated ESC line used in our lab was taken as a starting point for the generation of all following cell lines due to its utility in identifying and purifying motor neurons during *in vitro* differentiation. This cell line contains a stably integrated transgene consisting of the motor neuron specific Hb9 promoter driving a CD14-IRES-GFP construct (see figure 3.1, (Machado et al., 2014)). The internal ribosome entry site (IRES) is a nucleotide sequence that enables independent translation of a second protein from a single mRNA molecule ((Filbin and Kieft, 2009)(Komar et al., 2012)). This construct therefore results expression of a human *Cd14* transgene in cells committed to a MN fate which is driven by the MN-specific Hb9 promoter, and this cell surface marker can be used to selectively purify the desired cell type (in this case, MNs) by magnetic activated cell sorting (MACS). In addition, translation initiated by the IRES element results in GFP expression, allowing visual confirmation of successful differentiation.

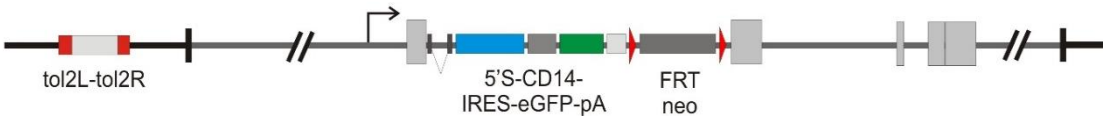

Figure 3.1 Transgene integrated into the parental cell line, Hb9::CD14-IRES-GFP. The motor neuron specific promoter Hb9 drives the expression of CD14 and enhanced GFP in differentiating motor neurons. This transgene was inserted into the genome by tol2-mediated transposition using tol2 transposase. (Adapted from Machado et al., 2014)

Using well established protocols to drive differentiation of spinal MNs using this cell line results in embryoid bodies (EBs) containing immature GFP-positive MNs, as shown in figure 3.2 below. Dissociating these EBs and purifying the MNs results in relatively pure cultures of ESC-derived MNs that extend multiple neurites within a few days of plating, and readily cluster together into aggregates as seen in figure 3.2c.

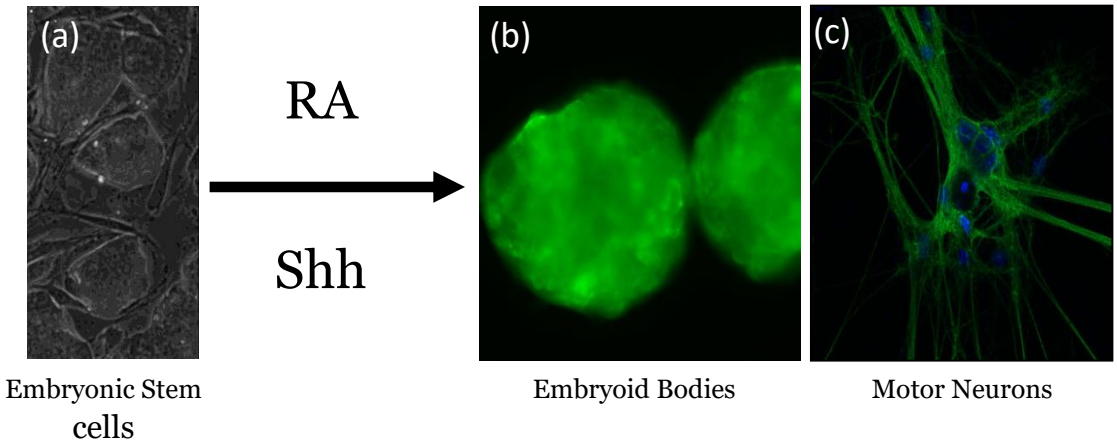

Figure 3.2 Differentiation of ESCs containing the Hb9::GFP-IRES-CD14 transgene. (a) ES cell colonies are dissociated and cultured in suspension to form EBs for 2 days, followed by 3 days of differentiation in the presence of retinoic acid (RA) and a sonic hedgehog agonist (Shh). **(b)** Resulting EBs contain GFP-positive MNs which can be dissociated and sorted to give relatively pure cultures of ESC-derived MNs as shown in **(c).**

3.2.2 Channelrhodopsin-2 Expression

Channelrhodopsin-2 (ChR2) is probably the best characterised and most widely used optogenetic tool, and although it is a microbial type 1 opsin, it is ideally suited to manipulating animal neurons due to its unitary nature (light-gating and ion conductance in one protein) and good kinetic properties allowing millisecond control of neuronal activity (Boyden et al., 2005; Fenno et al., 2011; Nagel et al., 2003).

The first strategy our lab adopted was to introduce ChR2 into the previously published A2.lox murine ES cell line, which contains a tetracycline response element (TRE) at the *Rosa26* gene

locus followed by a floxed *Cre* gene, allowing a similarly loxP flanked DNA sequence to be inserted downstream of the TRE by cre-mediated recombination (Iacovino et al., 2011). This results in a single-copy doxycycline inducible ChR2 transgene expressed from a known genomic locus (Fig. 3.3a). While this strategy did result in motor neurons that were sensitive to blue light stimulation following overnight doxycycline induction of the ChR2 as shown in figure 3.4b, this phenotype was relatively short-lived, with expression of the ChR2 transgene rapidly diminishing over 3-4 days in culture and light-responses similarly diminished and eventually lost entirely (data not shown).

The next approach we adopted was to drive the expression of a myc-tagged ChR2 using the endogenous microtubule-associated protein tau (*Mapt*) promoter via gene targeting (Fig. 3.3b). *Mapt* is a well characterised gene expressed predominantly in neural lineages associated with the specialised cytoskeleton of the axon (Binder et al., 1985; Weingarten et al., 1975). Using this promoter should therefore result in long-term stable expression of the transgene in neurons (Tucker et al., 2001).

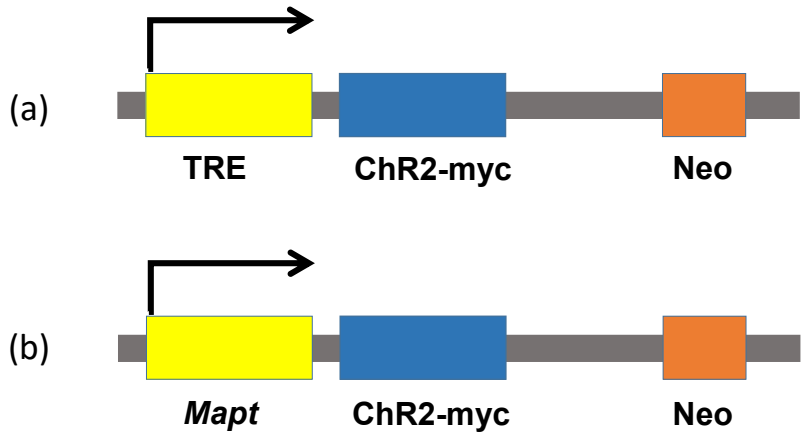

Figure 3.3 Strategies for expression of ChR2 in murine embryonic stem cells. (a) Using A2.lox embryonic stem cells and taking advantage of the inducible cassette exchange method, ChR2 was introduced into the *Rosa26* locus under the control of a tetracycline response element (TRE). **(b)** A myc-tagged ChR2 was put downstream of the endogenous *Mapt* promoter to drive pan-neuronal expression. The construct was introduced into Hb9::GFP-IRES-CD14 ES cells via electroporation.

(a) Parental ESC-Derived MNs (ChR2-)

(b) iDox ESC-Derived MNs (ChR2+)

(c) COS7 Cells: CMV::ChR2-myc

(d) ESC-Derived MNs: Mapt::ChR2-myc

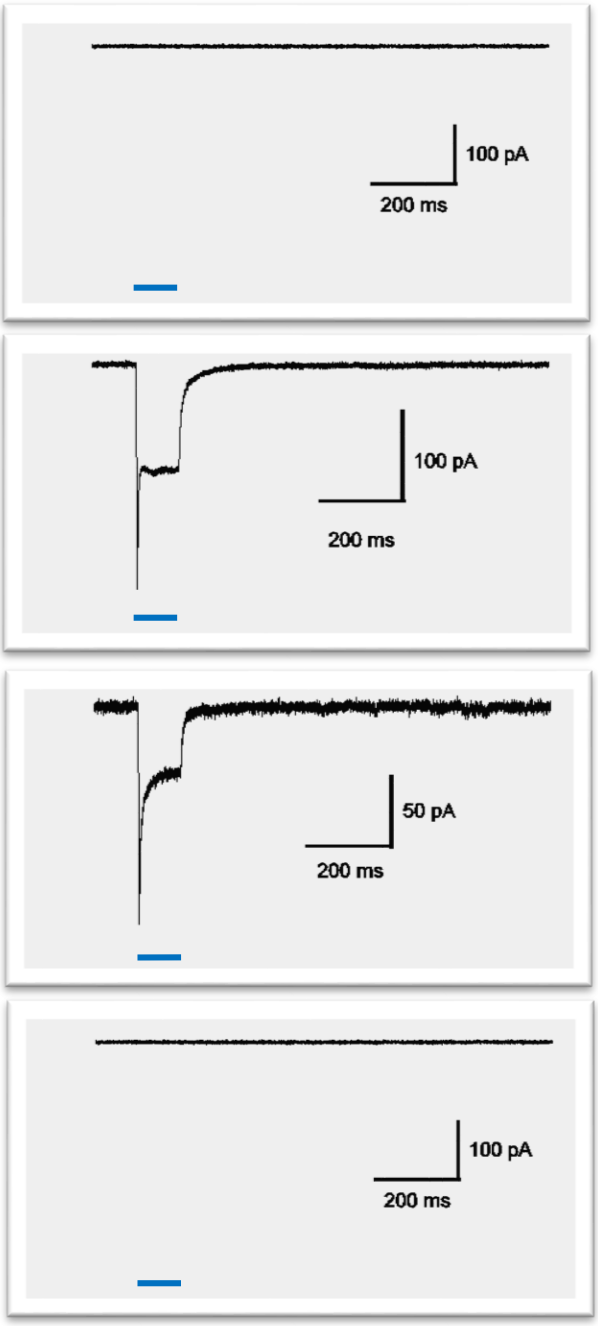

Figure 3.4 Representative Voltage-clamp responses during blue light photostimulation of ESC-derived MNs using two different ChR2 expression strategies (a) Motor neurons derived from the parental Hb9::GFP-IRES-CD14 cell line display no current response to a 100ms blue light stimulus. **(b)** A blue light stimulus elicits a clear depolarising current in MNs differentiated from TRE::ChR2 ES cells 1 day after doxycycline induction. **(c)** Transient expression of the Mapt::ChR2-myc construct in COS-7 cells confers sensitivity to blue light stimulation and results in inward currents of over 100pA. **(d)** ES cells stably transfected with the ChR2-myc construct under the control of the *Mapt* promoter show no current respsonse to blue light stimulation.

The myc-tag is a commonly used amino acid motif allowing detection of a tagged protein by immunocytochemistry with antibodies against the myc peptide sequence. A CMV::ChR2-myc construct was first tested by transient transfection into COS-7 cells, a transformed cell line derived from simian kidney tissue (Gluzman, 1981). These cells serve as a fast and simple mammalian cell line to test expression of transfected DNA. Patch clamp experiments carried out one day after transfection via lipofectamine-2000 revealed clear inward currents in transfected COS-7 cells in response to blue light stimulation (Fig. 3.4c). Following this result, a ChR2-myc construct was introduced into Hb9::GFP-IRES-CD14 ES cells by electroporation, and stably integrated into the genome downstream of the *Mapt* promoter by gene targeting. Patch clamp recording of MNs derived from this ES cell line however showed no response to a 100ms blue light stimulus. As no commercial antibody currently exists for ChR2, immunostaining for the myc-tag would be carried out to confirm expression of the ChR2 transgene, however we determined from previous experiments that the myc-tag used in this construct was mutated prior to transfection (unpublished observations). Instead, semi-quantitative PCR was used to analyse and confirm expression of ChR2 mRNA in MNs derived from this ES cell line (Fig. 3.5).

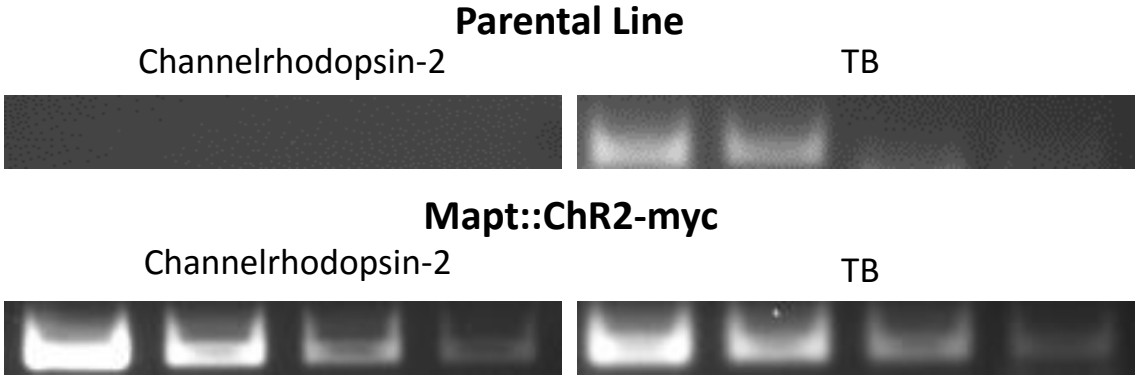

Figure 3.5 Mapt::ChR2-myc motor neurons express channelrhodopsin-2 mRNA. Motor neurons derived from the parental line show expression of the TATA box binding protein (TBP) positive control, but no channelrhodopsin-2 expression. Mapt::ChR2-myc motor neurons show relatively high levels of channelrhodopsin-2 expression. The 4 lanes shown in each condition represent serial dilutions of the RT-PCR product corresponding to 1:25, 1:125, 1:625 and 1:3125 respectively.

While the Hb9::GFP-IRES-CD14 parental line MNs show no expression of ChR2 mRNA, somewhat surprisingly the Mapt::ChR2-myc motor neurons do express ChR2 mRNA as shown in figure 3.5. This suggests the lack of sensitivity to blue light stimulation seen in the Mapt::ChR2-myc MNs is not due to lack of expression of the transgene, and may instead represent a problem in post-translational modification or trafficking of the protein.

3.2.3 Channelrhodopsin-2-YFP Transgene

The next strategy adopted to generate optogenetic ESC-derived MNs was to stably integrate a ChR2-YFP transgene under the control of the ubiquitous CAG promoter into the genome of the Hb9::GFP-IRES-CD14 parental ES cell line using tol2-mediated transposition (Kawakami et al., 2000). The DNA construct shown in figure 3.6 was made and transiently transfected into COS-7 cells (as described previously) to validate it.

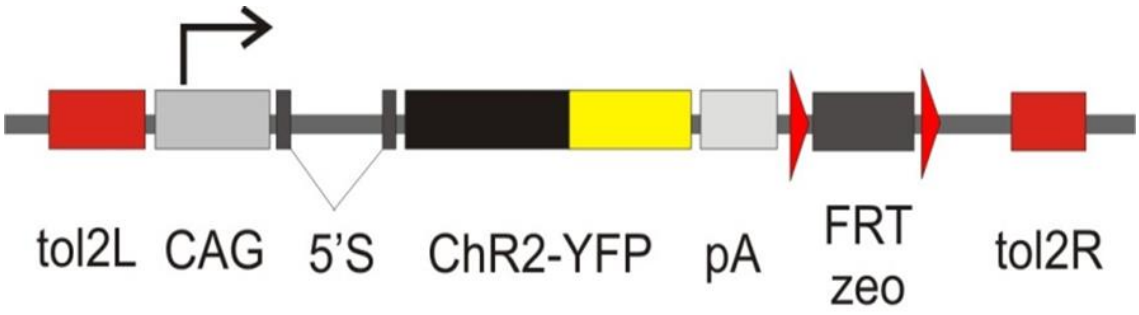

Figure 3.6 Ubiquitous ChR2-YFP expression transgene. The ubiquitous CAG promoter drives the expression of a ChR2-YFP fusion protein in all cells containing the construct. Tol2-mediated transposition is utilised to enable stable integration into the genome of the parental Hb9::CD14-IRES-GFP ES cell line.

Expression of this construct in COS-7 cells confers sensitivity to blue-light as demonstrated by the large inward current in response to optical stimulation (Fig. 3.7a). Following this result, the construct was electroporated into Hb9::GFP-IRES-CD14 ES cells along with the a plasmid containing the tol2 transposase to drive tol2-mediated transposition events and stable integration of the transgene into the genome. Electroporated ES cells were plated on a mouse embryonic feeder cell layer, allowed to recover for 2 days, and then subjected to zeocin

selection. Resistant colonies with clear fluorescence in the YFP emission frequency were selected for expansion and then further screened by patch clamp electrophysiology. A representative trace from an ES cell line expressing the ChR2-YFP transgene is shown in figure 3.7b. A clear inward current is seen in response to blue-light stimulation, similar to expression in COS-7 cells. Importantly, motor neurons derived from this ES cell line and patched one day after MACS retain this optogenetic phenotype, also displaying clear depolarising currents in response to blue light, as shown in figure 3.7c.

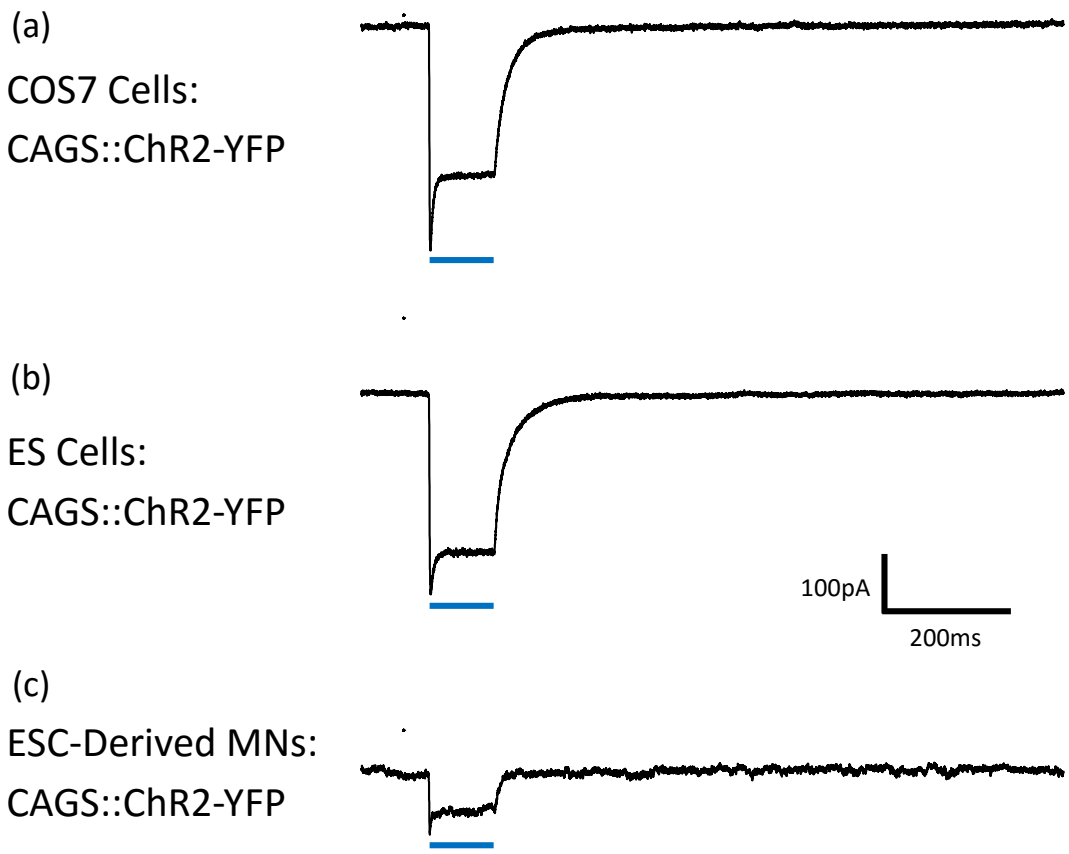

Figure 3.7 Blue light photostimulation of cells expressing ChR2-YFP (a) Transient expression of the CAG::ChR2-YFP construct in COS-7 cells confers sensitivity to blue light stimulation and results in inward currents of over 100pA. **(b)** ES cells stably transfected with the ChR2-YFP construct also display a clear current response to a 100ms blue light stimulation. **(c)** A 100ms blue light stimulus elicits a clear depolarising current in MNs differentiated from ES cells expressing the CAG::ChR2-YFP construct 1 day after magnetic activated cell sorting.

3.3 Optimising *In Vitro* Culture of ES Cell-Derived Motor Neurons

3.3.1 MACS Sorted Motor Neurons

After successfully screening and selecting an ES cell line that stably expresses the ChR2-YFP transgene in differentiated MNs, the next priority was to achieve reliable long-term *in vitro* culture of MACS-sorted MNs to allow functional analysis and characterisation. MACS-sorted ChR2-YFP MNs were plated at a density of 100k cells per 18mm matrigel-coated glass coverslip, and cultured in standard tissue culture conditions, with full media replacements every 2 days. Patch clamp experiments in both voltage and current clamp modalities revealed the gradual developmental maturation of the MNs, and confirmed stable expression and function of the ChR2-YFP transgene (Fig. 3.8). Live imaging of these cultures in phase contrast at 100x magnification reveals that ES cell-derived MNs rapidly extend neurites (clearly visible after 1 day in culture; Fig.3.8 a), and initially dispersed and separate neurons quickly aggregate together into large clusters (Fig.3.8 b + c). Current clamp recordings shown in figure 3.8 g-i show the development of electrophysiological properties resembling adult motor neurons, however by 7 days *in vitro* (DIV) ESC-derived MNs still do not display a fully mature functional phenotype, with successive action potentials displaying reduced amplitude and frequency during a 500ms current injection, and eventually failing to generate spikes, rather than sustaining AP amplitude and frequency (Carlin et al., 2000). While *in vitro* culture beyond 1 week should allow the complete maturation of these MNs, this was not possible to test in this format, as cultures of purified ESC-derived MNs rapidly deteriorated after only a few days in culture, and almost all MNs were dead after 1 week.

One explanation for the premature death of purified MNs *in vitro* could be the lack of supporting cell types, most notably glia. Astrocytes have been shown to be particularly important for MN survival, contributing to metabolic and trophic support, supplying survival signalling factors and regulating the extracellular environment (Blackburn et al., 2009; Ransom and Ransom, 2012).

To achieve long-term *in vitro* survival of ESC-derived MNs it may therefore be necessary to co-culture them with astrocytes.

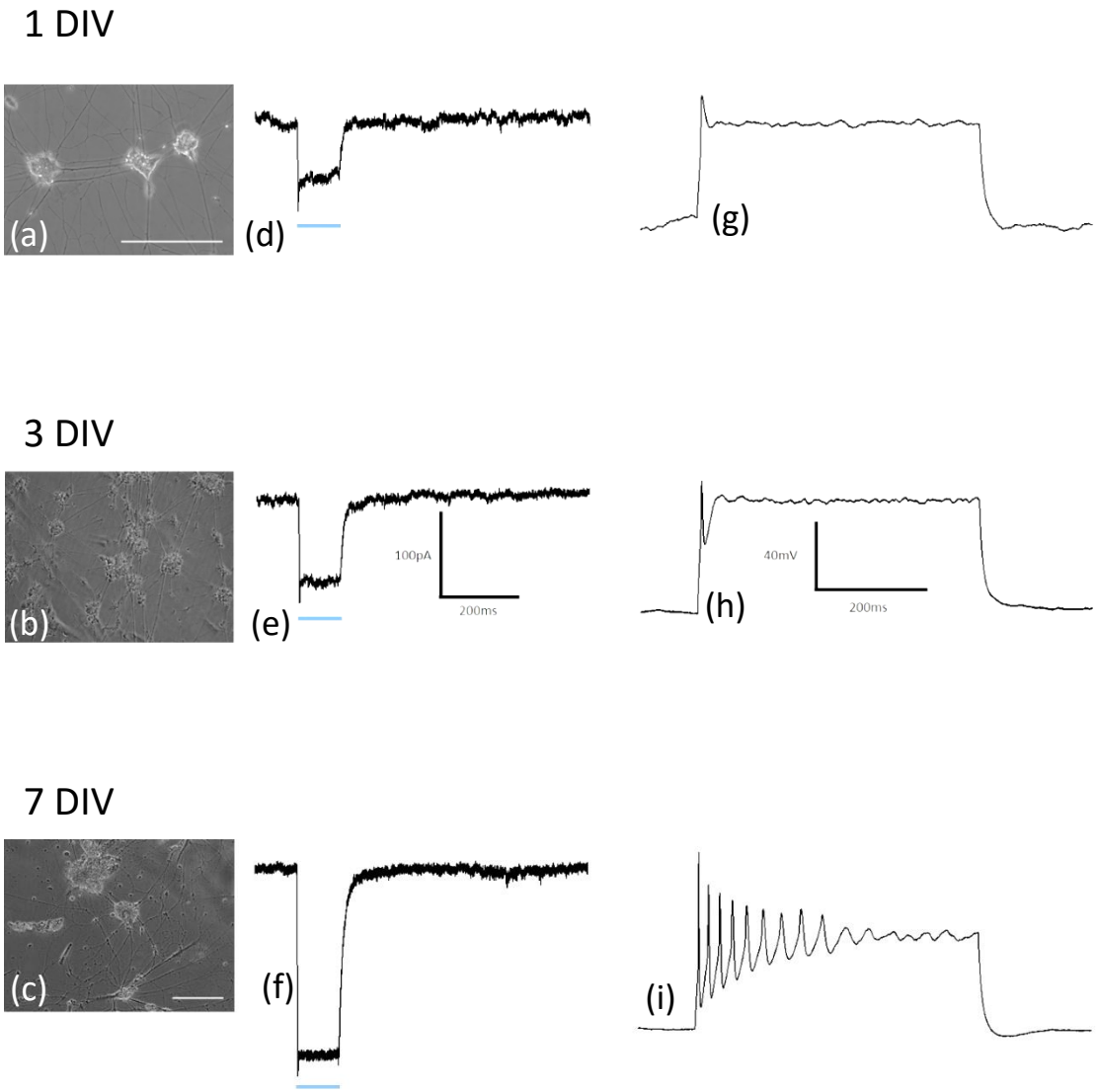

Figure 3.8 Representative images and patch clamp responses from *in vitro* culture of MACS sorted ChR2-YFP positive ESC-derived MNs (a-c) Phase contrast images of ESC-derived MNS cultured on glass coverslips in standard conditions; day 1, 3 and 7 respectively. **(d-f)** Representative current responses to a 100ms blue light stimulus; day 1, 3 and 7 respectively. **(g-i)** Representative maximum voltage responses to a 500ms stepped current pulse; day 1, 3 and 7 respectively. Scale bar = 100μm.

3.3.2 Dissociated EB Cultures

To address the issue of poor long-term survival of pure MN cultures, ESC-derived MNs were cultured from dissociated EBs, without MACS sorting. Previous studies have shown that the same conditions used to differentiate spinal MNs from ES cells also generate astrocytes, which typically arise later during the differentiation (Kessaris et al., 2001). Un-sorted, dissociated EBs should therefore contain MNs and supporting glia, in addition to other uncharacterised cell types. While the presence of other contaminating cell types in these cultures complicates interpretation of the data, it may improve the long-term survival of MNs cultured *in vitro*.

Figure 3.9 shows the results of *in vitro* culture of dissociated ChR2-YFP positive EBs. MN clustering is not as obvious in this condition, and neurite development is also obscured by the presence of many contaminating cell types (Fig. 3.9 a-c). Visually guided patch clamp of MNs determined by GFP expression and morphology reveal maintenance of sensitivity to blue-light stimulation (fig. 3.9 d-f), as well reliable voltage responses to a 500ms stepped current pulse (Fig. 3.9 g-h). While MN survival does appear to be improved in this condition, analysis and characterisation of MNs beyond 7 days *in vitro* remained impossible, due to overgrowth of contaminating proliferative cells.

One interesting observation from patch clamp experiments of MNs in the dissociated EB cultures was that they displayed increased spontaneous activity, never observed in cultures of MACS sorted MNs (Fig. 3.10). This activity may be due to the presence of other neuronal subtypes present in the dissociated cultures, such as spinal interneurons, which share a similar developmental origin to spinal MNs, and have been observed in ES cell-derived cultures previously (Miles et al., 2004).

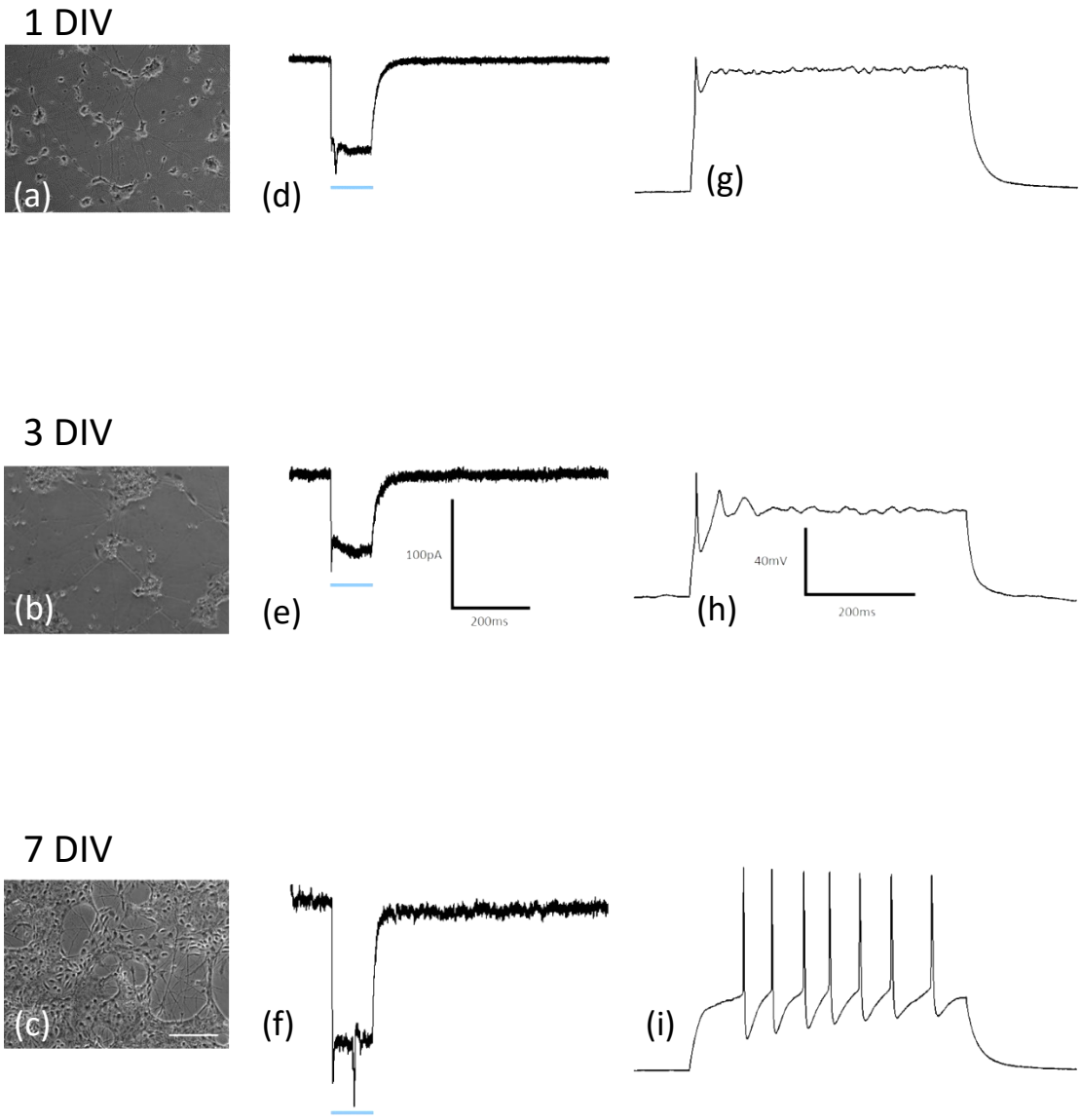

Figure 3.9 Representative images and patch clamp responses from *in vitro* culture of dissociated ChR2-YFP positive EBs (a-c) Phase contrast images of dissociated EBs cultured on glass coverslips in standard conditions; day 1, 3 and 7 respectively. **(d-f)** Representative current responses to a 100ms blue light stimulus; day 1, 3 and 7 respectively. **(g-i)** Representative maximum voltage responses to a 500ms stepped current pulse; day 1, 3 and 7 respectively.

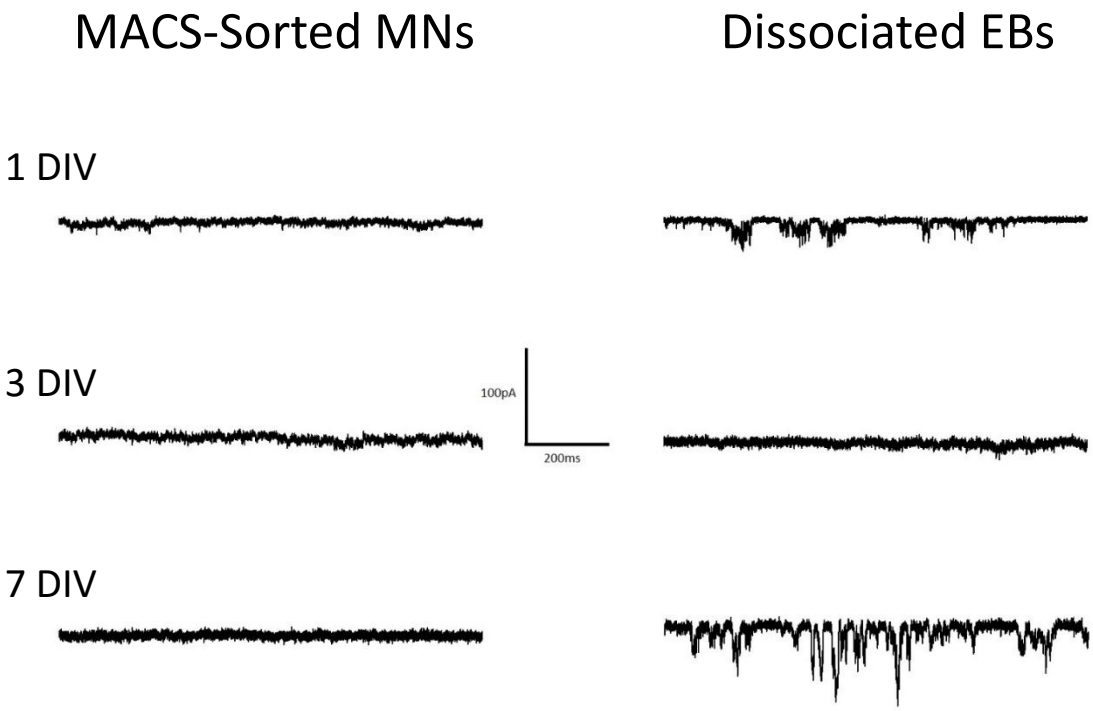

Figure 3.10 Spontaneous activity observed in MNs from dissociated EBs is not seen in pure (MACS sorted) MN cultures Voltage clamp recordings from MACS sorted MNs (left) and from MNs in dissociated EB cultures (right).

3.3.3 Astrocyte/Motor Neuron Co-culture (Astro-Neural Aggregates)

In order to achieve stable, long-term *in vitro* culture of ESC-derived MNs, it appears to be necessary to combine the advantages of MACS-sorting the desired cell population(s) to remove contaminating proliferative cells, and co-culture of MNs with astrocytes to provide trophic support and survival signals. This requires the independent differentiation and MACS-sorting of ESC-derived astrocytes to produce two separate cellular populations that can be combined in *in vitro* culture.

As mentioned previously, the differentiation of ESC-derived astrocytes is initially identical to that of ESC-derived MNs. However, similar to *in vivo* development, astrocytes are formed later in the differentiation (Kessaris et al., 2001). To produce high numbers of terminally differentiated astrocytes it is therefore necessary to dissociate EBs and culture the cells for a further 7 days in an adherent culture system (see Chapter 2.2.2).

To enable MACS purification of terminally differentiated astrocytes, a new tol2-based construct was designed and made using the same cell surface sortable marker CD14, but this time under the control of a short 2.2Kb Glial Fibrillary Acidic Protein (Gfap) promoter (see figure 3.11; (Brenner et al., 1994)). *Gfap* encodes a type III intermediate filament, and while its expression has been found in multiple cell types, it is most commonly associated with astrocytes in the CNS, and is not expressed by neurons (Baba et al., 1997). Using a short promoter of this gene therefore drives expression of the CD14 MACS-sortable surface marker in cells committed to an astrocyte fate, allowing purification of ESC-derived astrocytes.

Following differentiation, ESC-derived astrocytes were mixed with ESC-derived MNs in a 1:1 ratio and cultured for one night in hanging drop culture (see Chapter 2.2.2.12). This resulted in relatively small clusters of mixed astrocytes and MNs (Astro-neural aggregates; AsNAs) that were then plated on matrigel-coated glass coverslips. Culture of AsNAs in standard tissue culture

conditions enabled long-term survival of ESC-derived MNs *in vitro*, not seen in cultures of pure ESC-derived MNs.

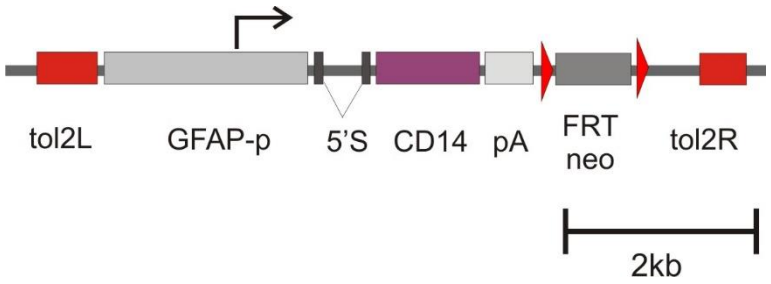

Figure 3.11 A short Glial Fibrillary Acidic Protein (Gfap) promoter allows specific expression of CD14 in ESC-derived astrocytes. Tol2-mediated transposition was used to enable stable integration into the genome of the parental Hb9 embryonic stem cell line. Astrocyte differentiation (see Chapter 2.2.2) results in specific expression of the CD14 transgene in presumptive astrocytes.

Patch clamp recordings of these cultures in current clamp mode revealed a clear electrophysiological maturation of the MNs, which progressed from an immature, non-spiking phenotype at 3 days *in vitro* (DIV) to MNs capable of firing long trains of high frequency action potentials (APs) at 21 DIV (Fig 3.12). Current clamp recordings in response to stepped 10ms current injections also revealed the changing properties of the APs generated by the MNs, which became faster over time and gradually increased in voltage (Fig. 3.12).

Voltage clamp recordings of these cultures revealed the stable long-term expression and function of the ChR2-YFP transgene in the MNs, with blue-light stimulation eliciting strong depolarising currents in all MNs tested (Fig. 3.13). In addition, a 500ms blue light stimulus presented during current clamp of the ESC-derived MNs resulted in a similar activity and maturation profile as seen with current injection (Fig. 3.13). Blue-light stimulation of MNs in 6 DIV AsNAs cultures resulted in a clear voltage response with a low-frequency train of APs, while the same stimulation applied to 21 DIV MNs elicited a long train of relatively high frequency APs (Fig. 3.13).

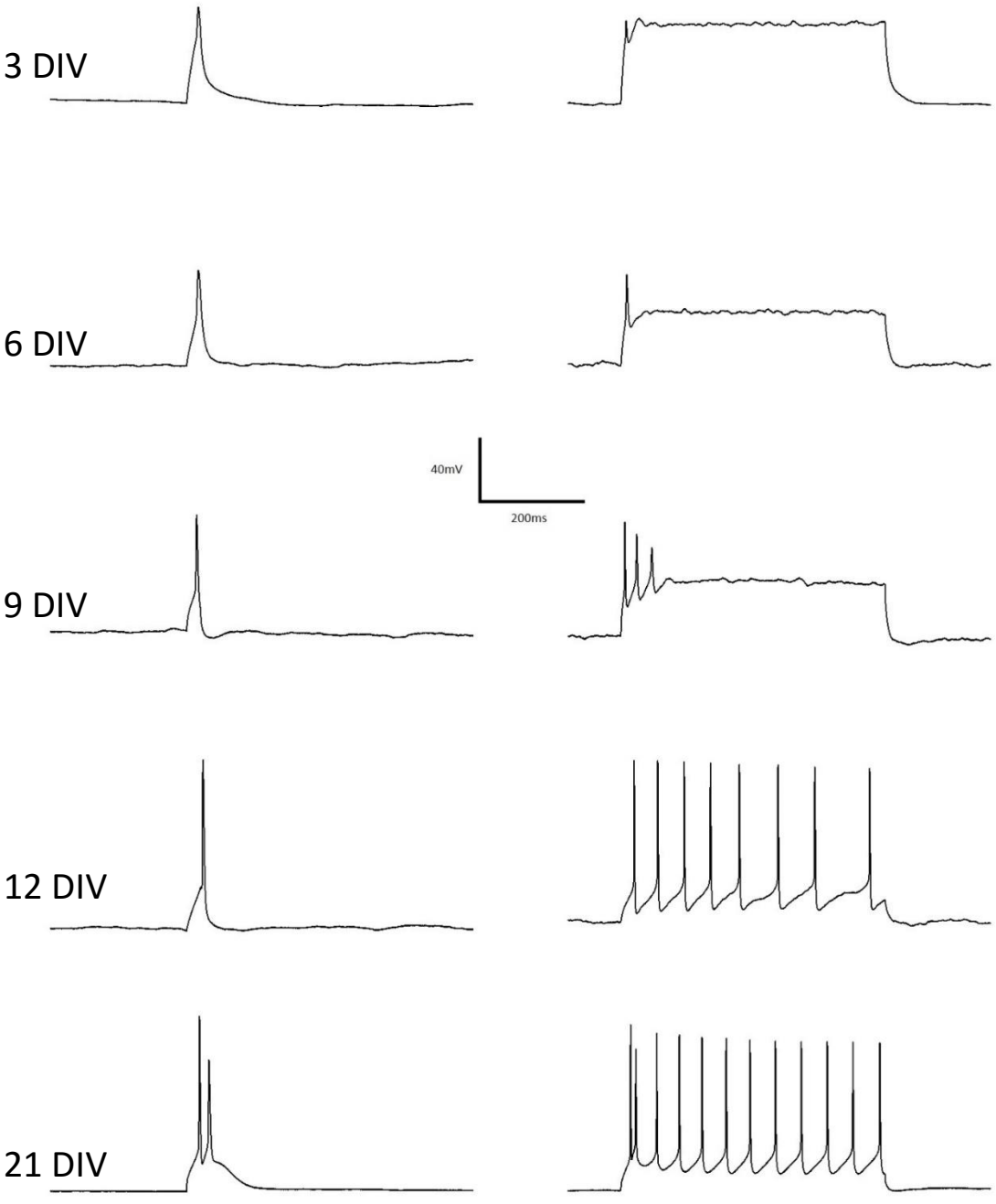

Figure 3.12 Current clamp recordings of ESC-derived MNs in astro-neural aggregate culture reveal electrophysiological maturation of firing properties Representative peak voltage responses of MNs from multiple time points *in vitro* to injection of 10ms stepped current pulse are shown in the left column, while peak responses to a 500ms stepped current pulse are shown in the right column.

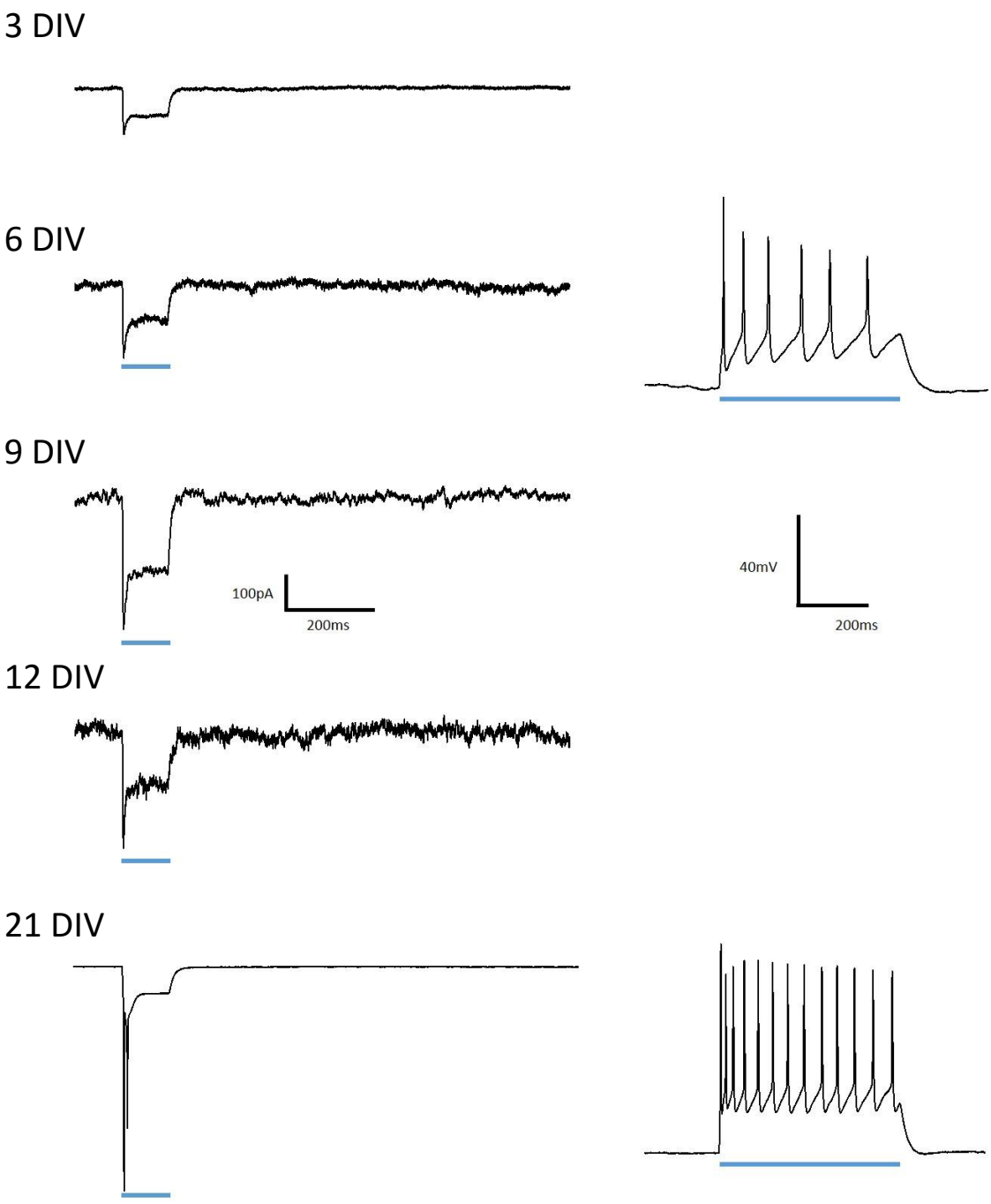

Figure 3.13 Blue-light stimulation of ESC-derived MNs in astro-neural aggregate culture reveals long term functional expression of a ChR2-YFP transgene and robust control of ESC-derived MN activity *in vitro* Representative current responses of MNs from multiple time points *in vitro* to a 10ms blue-light stimulation are shown in the left column, while voltage respsonses to a 500ms blue-light pulse are shown in the right column.

Epifluorescence imaging of the AsNAs cultures also provided insights into the maturation of MNs in these cultures (Fig. 3.14). At early time points, MNs remain tightly clustered in the AsNAs aggregates, and while clear neurites are visible, individual cell bodies are hard to distinguish (Fig. 3.14 a + a'). After 1 week of culture, the MNs have begun to migrate out of the AsNAs', and MN somas are more easily visible. Throughout the *in vitro* culture of ESC-derived MNs, the cell somas appear to grow in size, and the complexity of the neurite network continues to increase (Fig. 3.14). Both these observations indicate the continued growth and maturation of the MNs *in vitro.*

3.3.4 ESC-derived motor neurons have an axon initial segment

One possible explanation for the observed electrophysiological maturation of ESC-derived MNs seen in Chapter 3.3.3 is the concurrent assembly and development of the axon initial segment (AIS) in the immature MNs. The AIS is a specialised region of the proximal axon found in most neurons that serves a number of functions. The initial recruitment of scaffolding proteins associated with the AIS in one neurite shortly after symmetry-breaking helps define that process as the axon, and consequently all other processes as dendrites (Barnes and Polleux, 2009). Additionally, the AIS maintains this functional distinction by acting as a selective diffusion barrier for cytoskeletal transport of proteins in developing and mature neurons, essentially restricting axonal proteins to the axon and dendritic proteins to the dendrites or soma (Song et al., 2009). Perhaps the most important role of the AIS however is the fact that it functions as the initiation point for action potential firing (Grubb and Burrone, 2010a). The AIS contains a very high density of both voltage-gated potassium (Kv) and sodium channels (Nav), with up to 50 times more sodium channels found in this region compared to the dendrites or soma (Duflocq et al., 2011; Kole et al., 2008). This density of voltage gated channels gives the AIS the lowest threshold for AP firing of any subcellular area of the neuron, and so it is here that incoming currents from the dendrites and soma are summed to give the classic "all-or-nothing" output of an AP.

As the AIS is so key to AP initiation, modulation and duration, the observed electrophysiological development of ESC-derived MNs *in vitro* may be directly related to the assembly and function of the AIS (Ogawa and Rasband, 2008). To investigate this possibility, I analysed the ESC-derived MNs for the presence of a key component of the AIS, Ankyrin G, by immunocytochemistry. Ankyrin G is a cytoskeletal scaffolding protein that is thought to be the principle organiser of the AIS. Many other AIS-related proteins, including the cell adhesion molecules NF-186 and NrCAM, βIV spectrin, and even Nav and Kv channels have Ankyrin G binding motifs present, that when mutated prevent the recruitment of the respective protein to the AIS (Garrido et al., 2003; Garver et al., 1997; Lemaillet et al., 2003; Pan et al., 2006; Yang et al., 2007). Further, knockdown of Ankyrin G expression by shRNA prevented the clustering of most other AIS components, confirming its importance to AIS assembly and structure (Hedstrom et al., 2007).

Immunocytochemistry using an anti-Ankyrin G monoclonal antibody did not reveal the presence of an AIS in ESC-derived MNs at any time point investigated, as shown in figure 3.15. Parallel control experiments using primary rat hippocampal neuronal cultures however did label the AIS successfully with this antibody, suggesting either that the antibody did not work in the ESC-derived MNs possibly due to species differences in the epitope structure, or that ESC-derived MNs do not possess an AIS. This finding is in contrast to recent literature reporting the presence and characterisation of an AIS in somatic mouse MNs *in vivo* (Duflocq et al., 2011; Le Bras et al., 2014; Molofsky et al., 2014). To further investigate the development of an AIS *in vitro* in ESC-derived MNs I therefore tested an alternative marker of the AIS, phosphorylated I kappaB alpha (pIκBα).

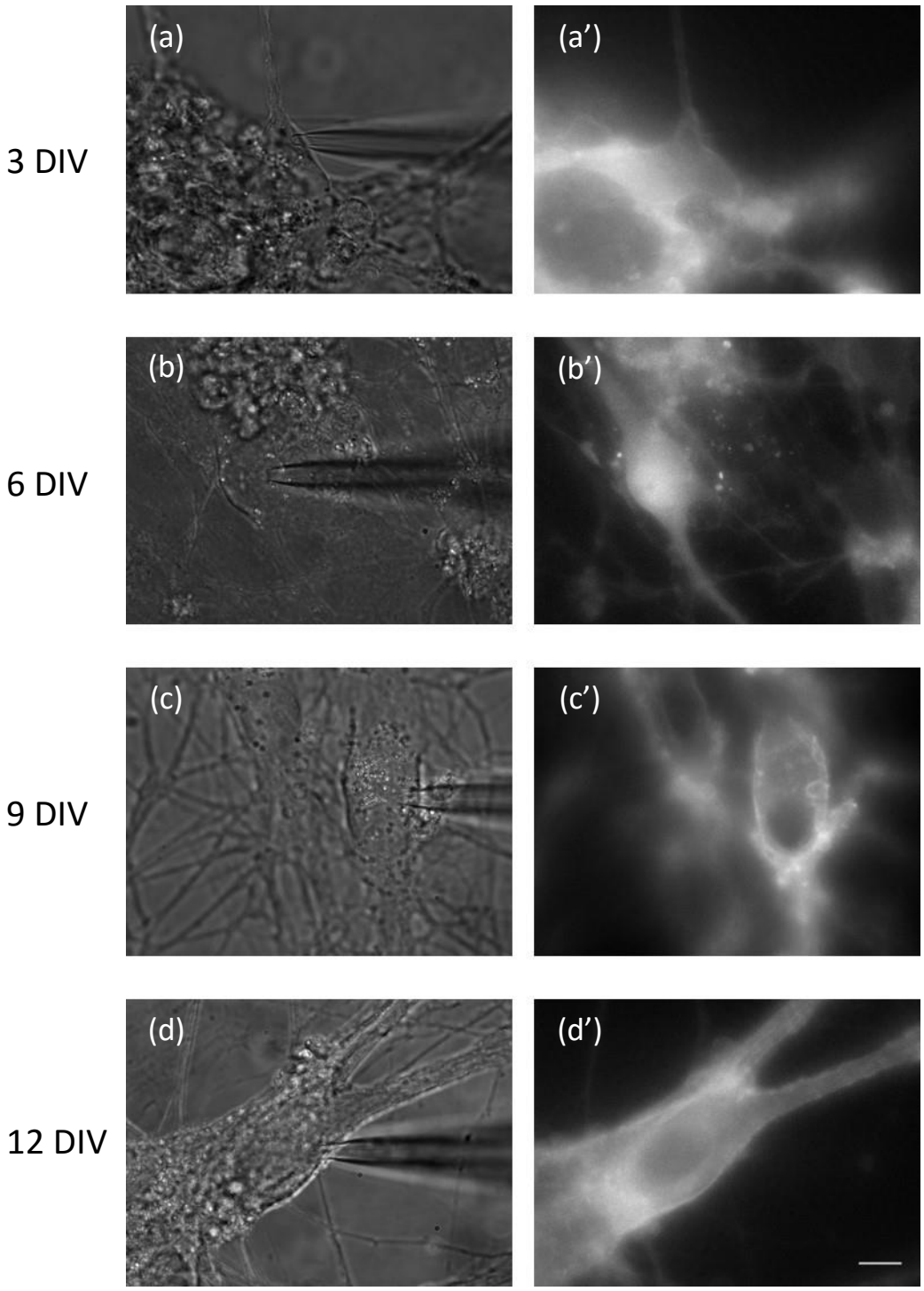

Figure 3.14 Epifluorescence imaging of ESC-derived MNs in astro-neural aggregate culture reveals morphological changes and continued growth *in vitro* Representative images of MNs cultured in astro-neural aggregates and patched at multiple time points *in vitro*. All images captured at 100x magnification, with phase contrast on the left column, and 488nm-epifluorescence on the right. Scale bar = 10μm.

Based on reports from the literature showing specific enrichment of pIκBα at the AIS, I investigated an antibody against pIκBα as an alternative marker of the AIS in primary hippocampal cells (Sanchez-Ponce et al., 2008). Comparing the labelling of pIκBα to ankyrin G revealed strong co-localisation of the two antibodies. This finding supports pIκBα as a good marker of the AIS, despite being unnecessary for AIS assembly, and the labelling likely being due to cross-reactivity with a phosphorylated epitope of a protein associated with the AIS cytoskeleton (Fig. 3.16; (Buffington et al., 2012)). While The pIκBα antibody also displayed relatively strong labelling of the cell soma, which may be explained due to the role of IκBα in regulating the nuclear localisation of NK-kappaB, and the ubiquitin-mediated degradation of pIκBα in the cytosol (Kanarek and Ben-Neriah, 2012).

Immunostaining ESC-derived MNs with the pIκBα antibody did label a small region of a single neurite proximal to the soma in all cells imaged, indicating that ESC-derived MNs do possess an AIS (Fig. 3.17). This result is in contrast to immunostaining with the Ankyrin G antibody performed on the same sample, which again did not label the AIS in ESC-derived MNs (Fig. 3.17). pIκBα labelling at multiple time points *in vitro* revealed the presence of an AIS-like structure in the proximal axon of all MNs as early as 3 DIV, although the intensity of staining did increase with time in culture (Fig. 3.18 and Fig. 3.19).

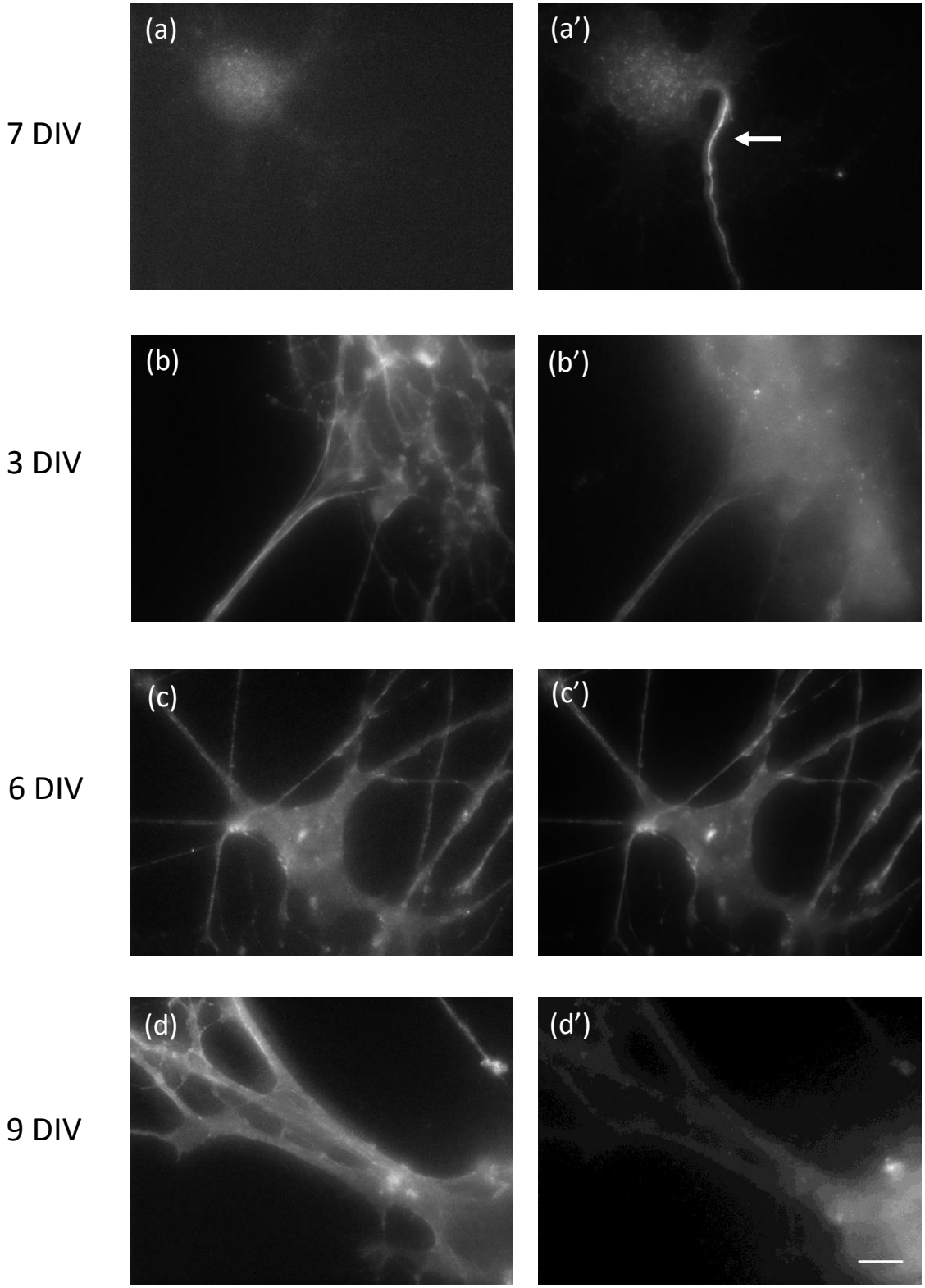

Figure 3.15 Immunostaining does not reveal an ankyrin G positive AIS in ESC-derived MNs (a') Immunolabelling using an antibody against ankyrin G reveals a clearly defined AIS (white arrow) in 7 DIV dissociated rat hippocampal neurons, and only a faint non-specific signal to a GFP antibody seen in the cell soma **(a)**. **(b-d)** While GFP signal is seen thoughout the MN soma and neurites, no specific labelling of an AIS is seen with the ankyrin G antibody **(b'-d')**. Scale bar = 10μm.

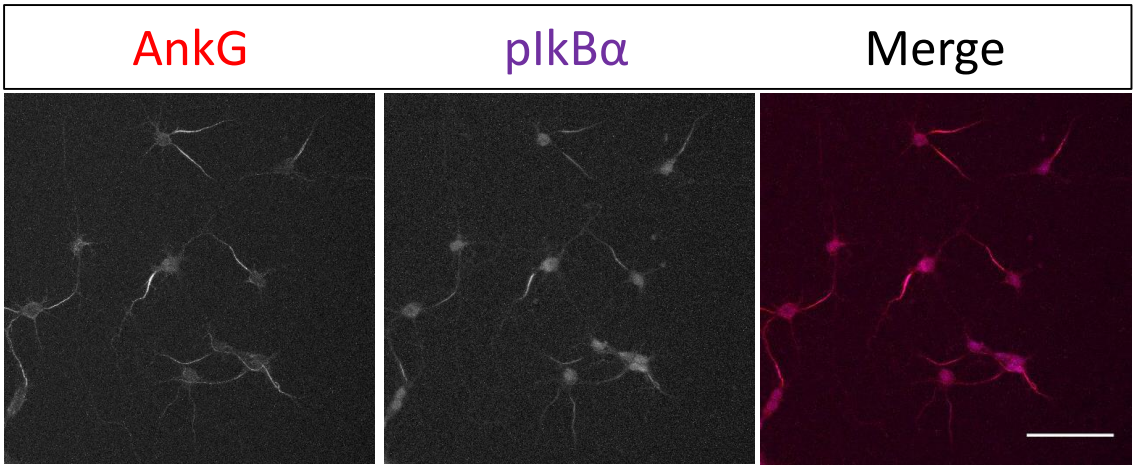

Figure 3.16 An antibody against phosphorylated IκB α (pIκBα) specifically labels the AIS in dissociated rat hippocampal neurons. Immunolabelling with pIkBα co-localises directly with ankyrin G labelling in 7 DIV rat hippocampal neurons. Scale bar = 100μm.

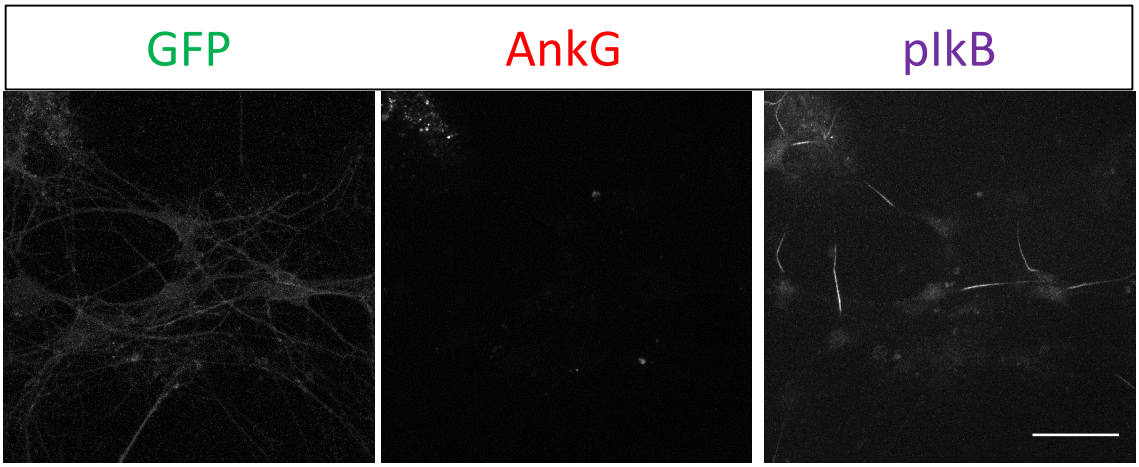

Figure 3.17 Immunostaining 6 DIV ESC-derived MNs in astro-neural aggregate culture with the pIκBα antibody reveals clear AIS' localised adjacent to the soma in the axon. While no ankyrin G signal is observed in ESC-derived MNs, the pIκBα antibody specifically labels the AIS of these neurons in the proximal axon. Scale Bar = 100μm.

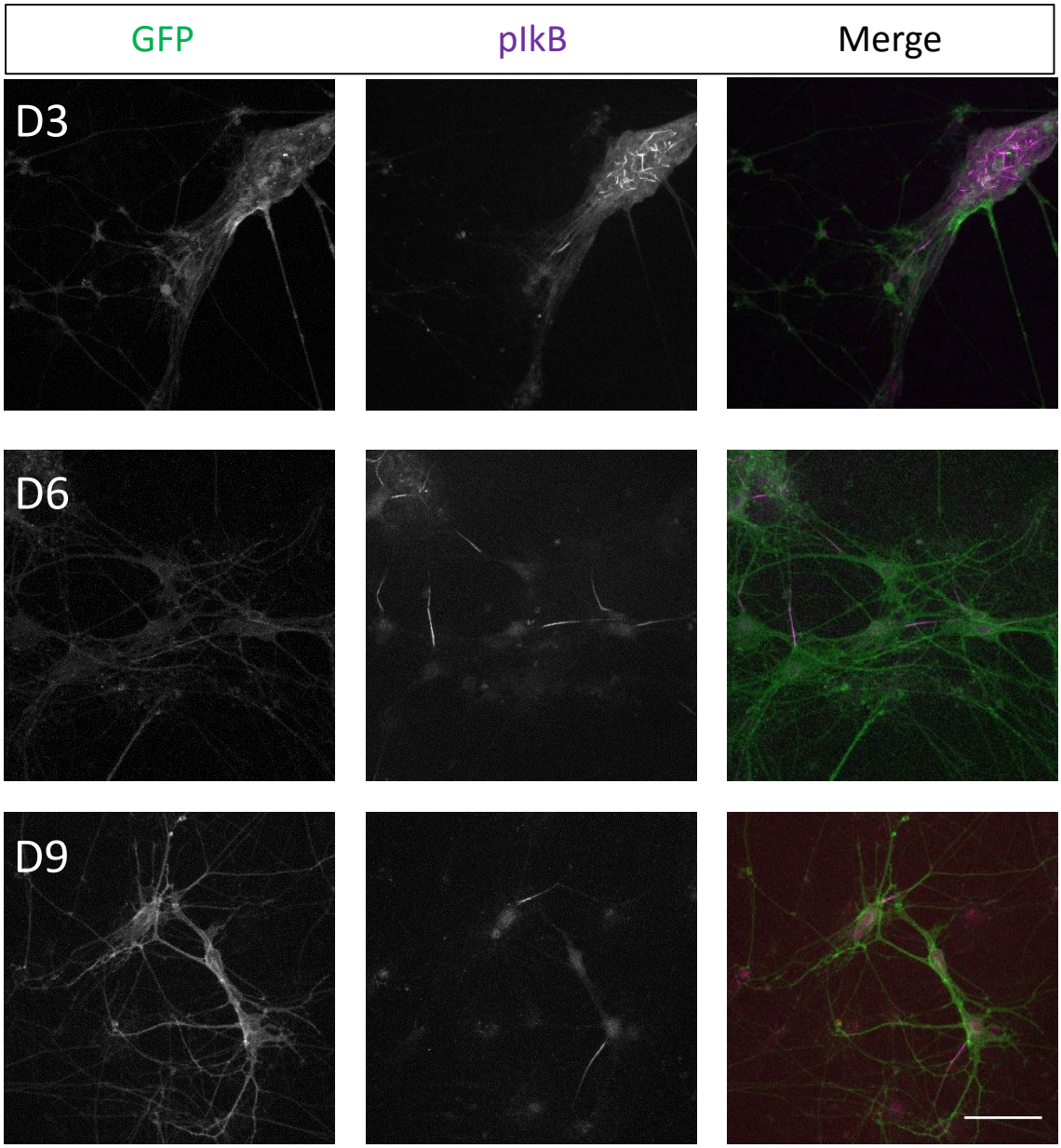

Figure 3.18 ESC-derived MNs possess an AIS in the proximal axon from as early as 3 DIV. pIκBα antibody labelling reveals the AIS of ESC-derived MNs throughout a 3-week *in vitro* culture period. Note the development from aggregated clusters of neurons to a more dispersed format with elaboration of complex dendritic arbours. Scale Bar = 100μm.

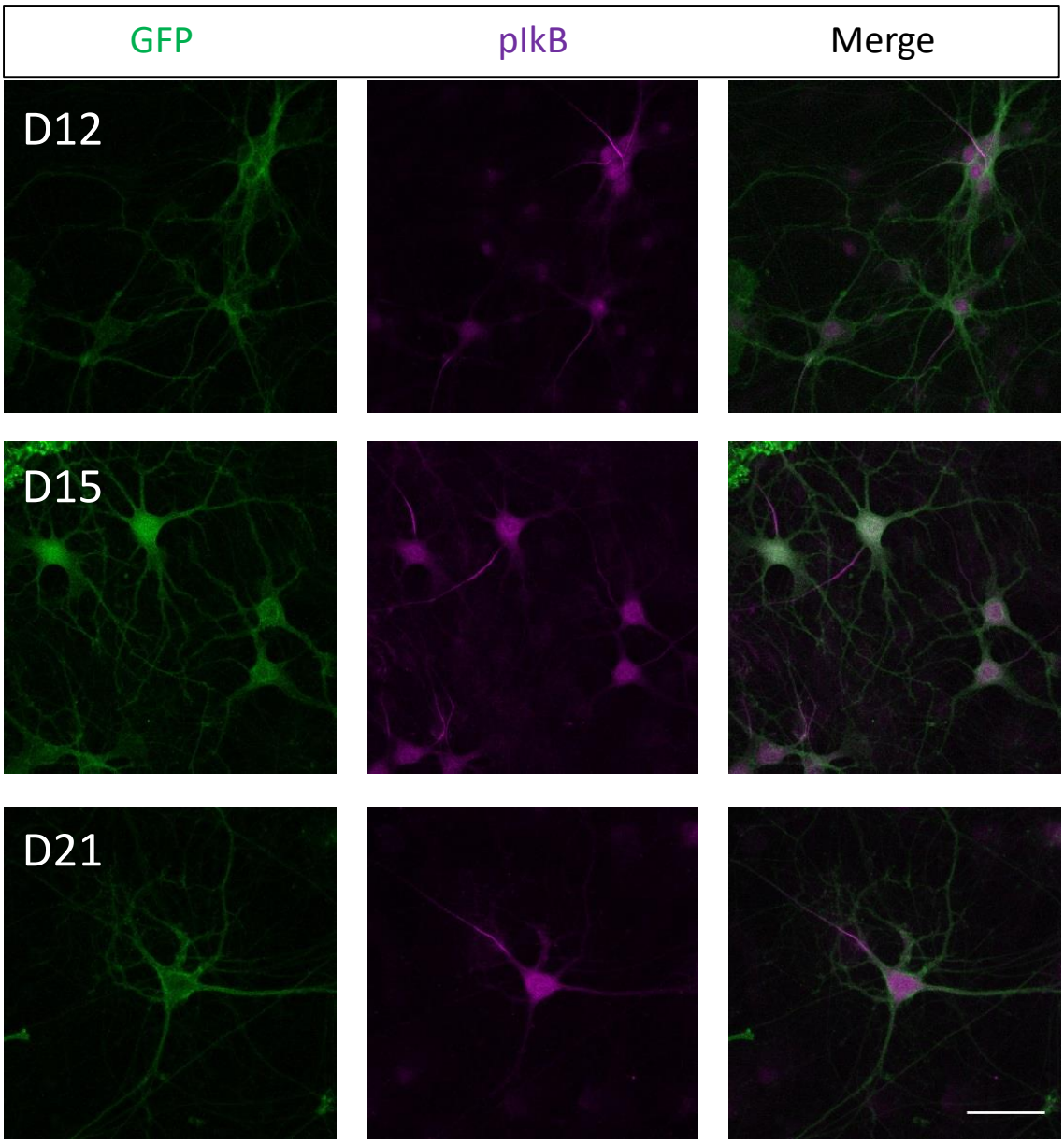

Figure 3.19 ESC-derived MNs possess an AIS in the proximal axon up to three weeks in culture. pIκBα antibody labelling reveals the AIS of ESC-derived MNs throughout a 3-week *in vitro* culture period. Note the presence of a single axon/AIS in each neuron, and the complex branched dendrites. Scale Bar = 100μm.

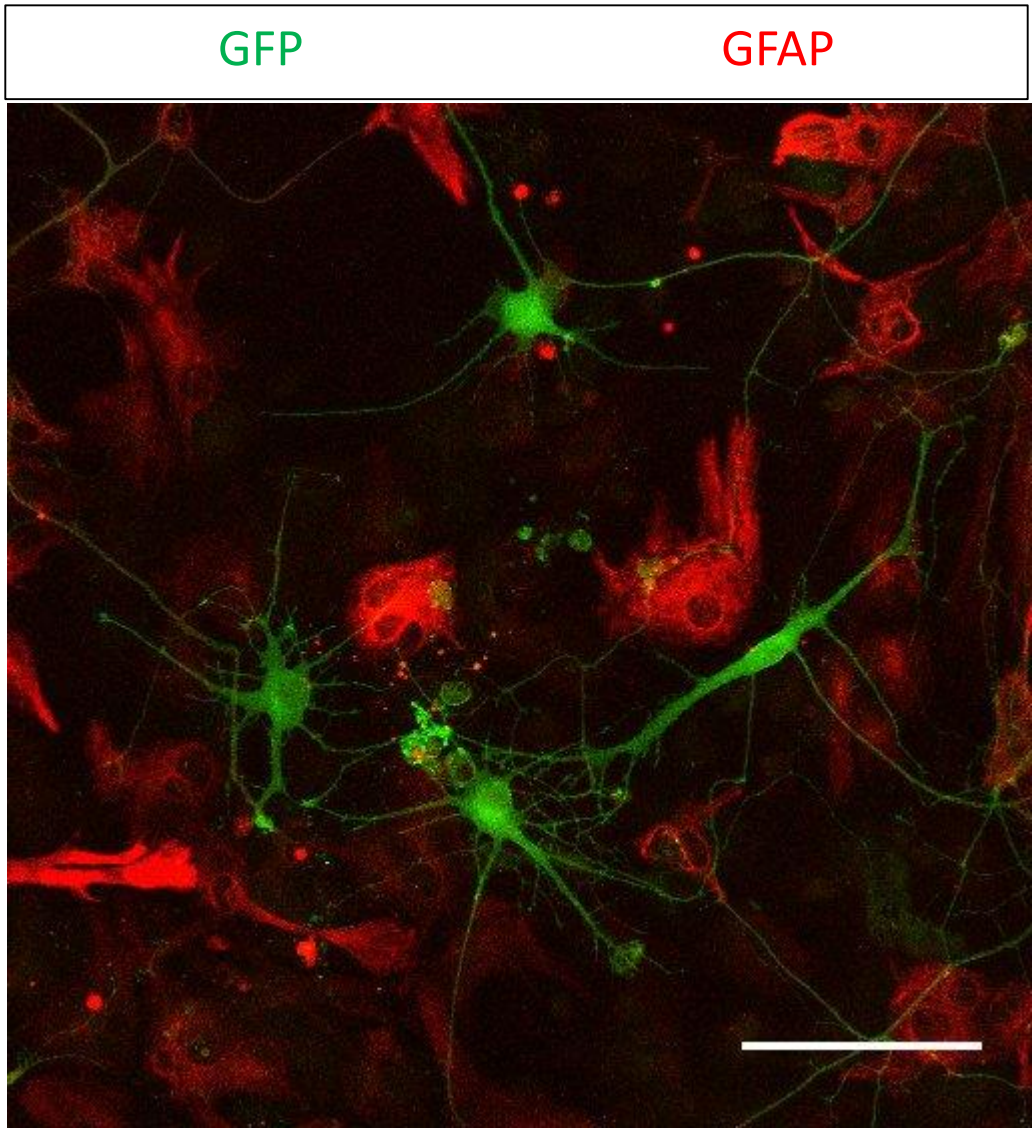

Figure 3.20 ESC-derived MNs plated on a monolayer of ESC-derived astrocytes develop a mature morphology more rapidly than MNs cultured in aggregates. ESC-derived MNs (green) after 3 DIV of culture on an ESC-derived astrocyte monolayer (red). Extensive MN neurite extension and elaboration is revealed by the GFP labelling, not previously seen in aggregated cultures by this time point. Scale bar = 100μm.

3.3.5 Astrocyte/Motor Neuron Co-culture (Astrocyte Monolayers)

While the hanging-drop based AsNAs culture described previously allows long-term survival of ESC-derived MNs *in vitro*, it has some drawbacks that limit the reproducibility and reliability of the system. The distribution of both astrocytes and MNs from AsNAs on a 2D-surface such as a glass coverslip hard to control, especially at the beginning of a culture. In addition, MNs in AsNAs first migrate out of the aggregate before extending neurites (see Fig. 3.18), leading to discrepancies in the developmental morphology and potentially electrophysiological maturity of individual MNs within the same culture, due to initial positions within an astro-neural aggregate.

In order to develop an *in vitro* culture protocol more reliable than the AsNAs method described previously, I first plated a monolayer of MACS-sorted ESC-derived astrocytes on glass coverslips, and allowed them to attach and stabilise overnight. The following day, MACS-sorted ESC-derived MNs were plated on top of the astrocytes, in known densities (10,000 per 18mm coverslip, see Chapter 2.2.2.12). These conditions resulted in more reproducible cultures, and the morphology of ESC-derived MNs developed more quickly in this format, as shown in figure 3.20, where day 3 MNs have extensive neurite extension more closely resembling day 6 MNs from the AsNAs cultures.

In vitro patch clamp analysis of the electrophysiological properties of ESC-derived MNs in these cultures revealed a similar maturation phenotype as seen with AsNAs culture (Fig. 3.21). However, when cultured on astrocyte monolayers, the functional maturation of ESC-derived MNs appears to be accelerated, with day 7 MNs able to fire trains of APs in response to direct current stimulation, similar to day 12 MNs in AsNAs culture (Fig. 3.21). This advanced maturation was also seen in response to blue-light stimulation, progressing from a single AP at 3DIV to train of APs at 35DIV, with a frequency of 50-60 Hz (Fig. 3.21).

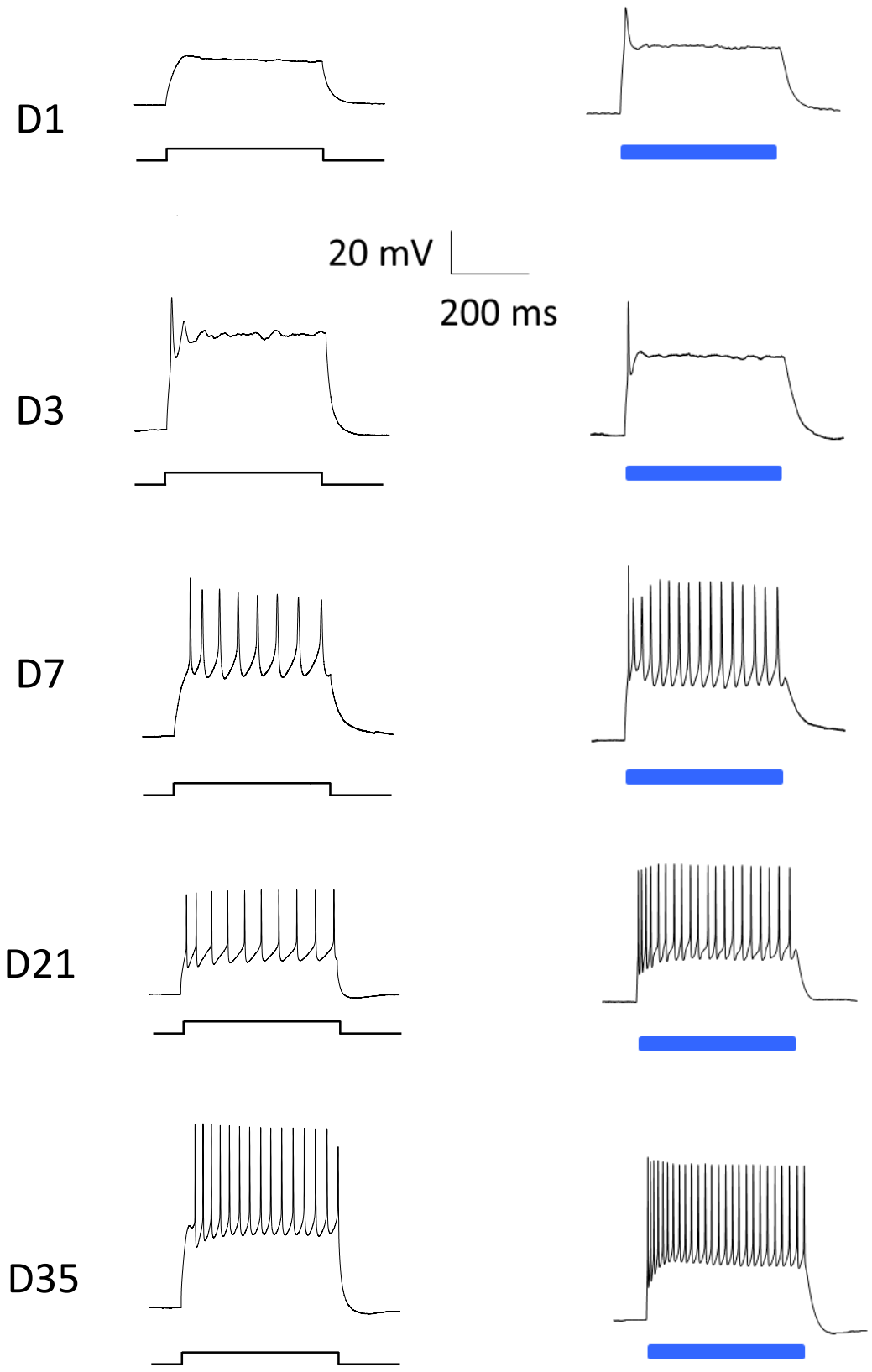

Figure 3.21 ESC-derived MNs cultured on astrocyte monolayers show an accelerated functional maturation compared to aggregate cultures, and photostimulation closely mimics responses to direct current injection. Representative peak voltage responses to a 500ms stepped current pulse over a 4 week time course are shown in the left column, while voltage responses to a 500ms blue-light pulse are shown in the right column.

Detailed analysis of the properties of single APs elicited by a 10ms current pulse from multiple experiments similarly reveals the electrophysiological maturation of the ESC-derived MNs over time in culture (Fig. 3.22). Both the AP voltage threshold (Fig. 3.22 a) and the width at half height (Fig. 3.22 c) decreased over time in culture, indicating the depolarisation required to elicit an AP reduced, and the speed of resulting APs increased. The membrane capacitance (Fig. 3.22 e) and current threshold (Fig. 3.22 d) of the MNs both increased over time in culture. An increase in membrane capacitance is associated with an increase in the surface area of the plasma membrane, revealing the continued growth of MNs and particularly extension and elaboration of axonal and dendritic processes. The maximum voltage (Fig. 3.22 b) of recorded APs showed a tendency to increase over time, although this increase was not significant (beyond day 3). The resting membrane potential (Fig. 3.22 g) of ESC-derived MNs was fairly consistent throughout the culture, although a small (but significant) drop was seen at both 3 DIV and 35 DIV.

Analysis of the input current density against AP firing frequency is shown in figure 3.23. This reveals the classic sigmoidal curve associated with electrophysiological maturation of neurons, with more mature neurons initially requiring more current to elicit a response (due to their increased membrane resistance/size), but then able to achieve higher firing rates at higher current densities (Fig. 3.23). Less mature neurons require a smaller current density to fire APs, but then are unable to sustain firing activity beyond a certain current density, at which point they revert to a non-spiking response.

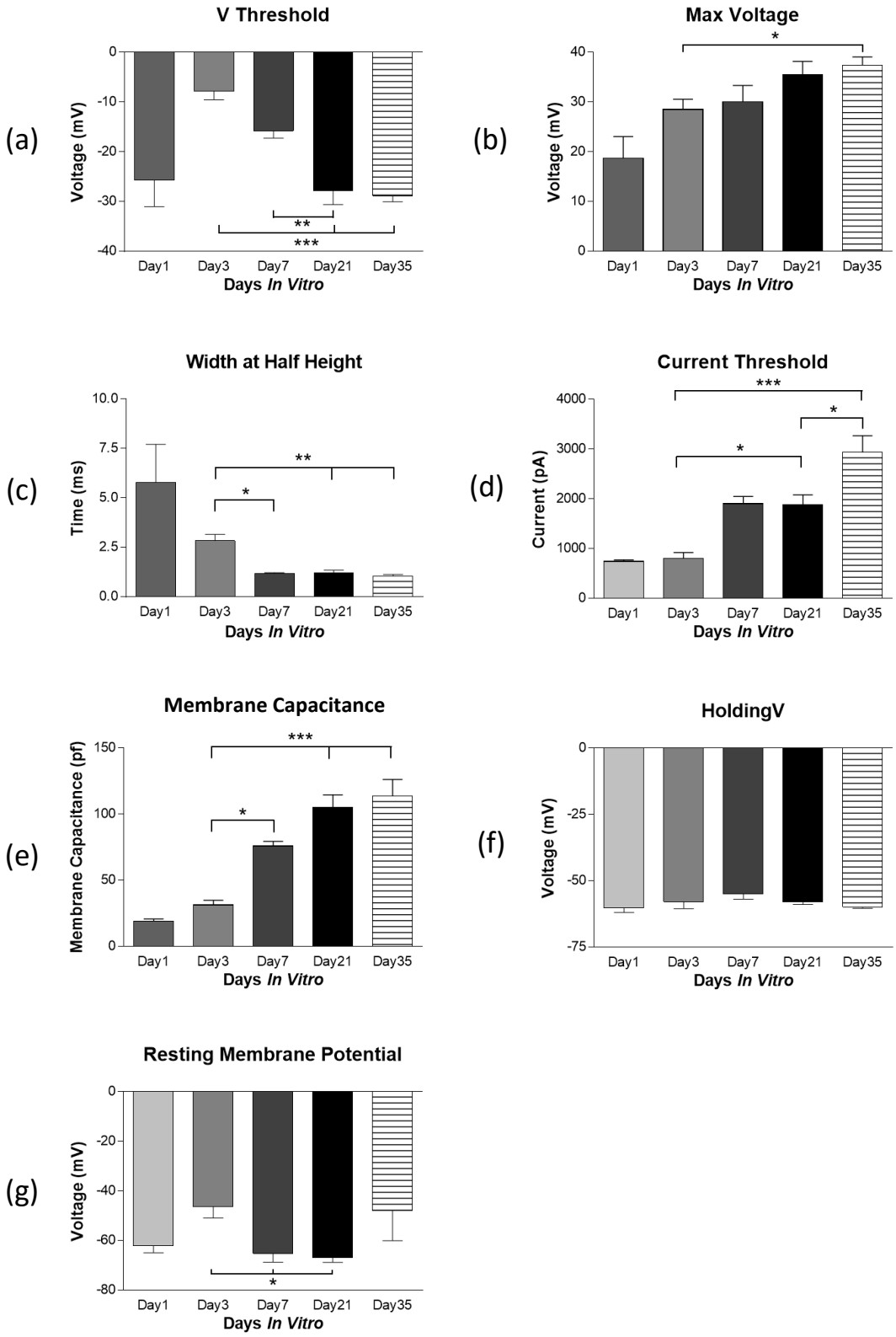

Figure 3.22 Analysis of single action potentials elicited in ESC-derived MNs by a 10ms current pulse across the time series investigated. The average voltage threshold **(a)**, maximum voltage reached **(b),** speed of AP **(c)**, current threshold **(d)**, membrane capacitance **(e)**, holding voltage **(f)**, and resting membrane potential of ESC-derived MNs at various time points in astrocyte monolayer culture. Results of one-way ANOVA; * = p <0.05, ** = p <0.01, *** = p <0.001. N number for each time point is: Day 1 = 6, Day 3 = 6, Day 7 = 4, Day 21 = 8, Day 35 = 10.

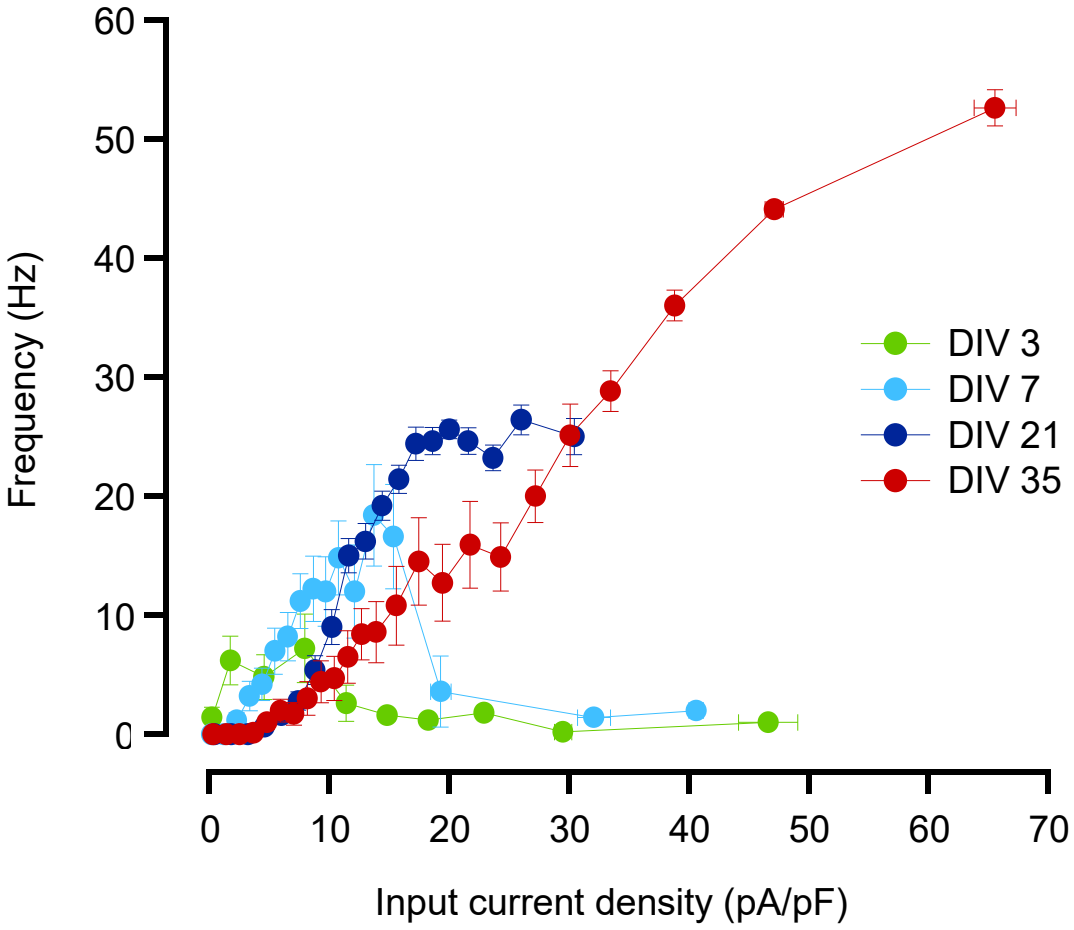

Figure 3.23 Input/output curve of ESC-derived MNs cultured on astrocyte monolayers. Analysis of ESC-derived MNs stimulated with a steadily increasing 500ms current injection in current clamp mode. Note the progression over time from low-firing low-threshold responses to high-threshold high-frequency activity at later time points.

Chapter IV

Establishing and Characterising *In Vitro* Muscle Culture

4.1 Introduction and Aims

While successful differentiation, optogenetic control and long-term survival and maturation of ESC-derived MNs both *in vitro* and *in vivo* are important steps towards using these cells for motor neuron disease modelling, they are not sufficient for a reliable and thorough model in themselves. For a more complete model it is necessary to include the relevant post-synaptic target of the MNs, skeletal muscle. Having both MNs and muscle gives a more complete neuromuscular "circuit", and should allow for a better analysis of the functional viability of the MNs, enabling muscle contraction to be analysed in addition to AP firing within the MNs. Perhaps more importantly, many recent studies have highlighted the degeneration of the distal axon and the specialised synapse between MNs and muscle, the neuromuscular junction (NMJ), as one of the earliest markers of motor neuron disease (Dupuis and Loeffler, 2009; Fischer et al., 2004; Frey et al., 2000). Indeed, in mouse models of ALS even complete rescue of MN cell soma death has only marginal effects on disease progression and does not affect survival rates, implicating NMJ breakdown and dysfunction as the key pathological events in the disease (Dewil et al., 2007; Gould et al., 2006b; Rouaux et al., 2007).

For these reasons, I aimed to produce, characterise and optimise *in vitro* skeletal muscle cultures, to facilitate the generation of a better *in vitro* neuromuscular disease model.

4.2 Establishing ESC-Derived Muscle

4.2.1 Creation of doxycycline-inducible *Myod1* ES cells

A great strength of stem cell based technologies is the ability to generate transgenic cell lines relatively quickly and efficiently, while maintaining clonal populations that can be expanded to generate as much experimental material as necessary. Having taken advantage of these attributes for the MN component in introducing cell-sorting markers and channelrhodopsin-2, my first strategy to develop an *in vitro* muscle culture was also based on differentiating embryonic stem cells. In addition to high reproducibility and scalability, this approach has the added advantage of enabling fast and efficient generation of transgenic cell lines, without resorting to the generation of transgenic animals or transient methods to overexpress or knockdown or knockout candidate genes. Both the neuromuscular channelopathies including non-dystrophic myotonia (NDM), periodic paralysis (PP), and congenital myasthenic syndrome (CMS) and the muscular dystrophies including Duchenne muscular dystrophy and Becker muscular dystrophy among others are caused by gene mutations effective in the muscle, and might be best studied and subjected to high-throughput screening efforts in stem cell derived muscle containing the relevant mutations (Sharp and Trivedi, 2014; Shieh, 2013; Suetterlin et al., 2014). Indeed, even in ALS and spinal muscular atrophy (SMA), typically thought of as defects of the motor neurons, recent evidence suggests that muscle plays an important role in contributing to the disease progression, and the muscle genotype may be an important factor to dissect and analyse to fully understand the disease mechanisms (Anderson et al., 2003; Dobrowolny et al., 2008; Jokic et al., 2005).

While the *in vitro* differentiation of embryonic stem cells into MNs by small molecules has been well characterised, the generation of skeletal myoblasts from ESCs by exogenous factors has remained elusive. The *in vivo* development of skeletal muscle has been intensely studied, progressing from the generation of the paraxial mesoderm, through somitogenesis to migration

of myoblasts out of the myotome to their final destinations in the body, (Buckingham, 2006; Gros et al., 2005). The genetic program that directs myogenesis has also been determined, with Pax3 and Pax7 being expressed in myogenic progenitors as well as satellite cells, and Myod1 and Myf5 being important in commitment to myoblast fate and terminal differentiation. However, the molecular signals involved in directing this process are less well understood, hindering *in vitro* myogenesis from stem cells (Bajard et al., 2006; Kassar-Duchossoy et al., 2004; Lagha et al., 2008; Relaix et al., 2005; Tapscott, 2005).

To achieve reliable differentiation of murine ESCs into skeletal myoblasts, I therefore decided to take an inducible transgenic approach, rather than induction via exogenous signalling. Expression of myogenic transgenes in ESCs has been reported previously to lead to enrichment of myogenic progenitor populations of Pax3/Pax7 positive cells, as well as committed myoblasts that express markers of terminal muscle differentiation (Albini et al., 2013; Darabi et al., 2008b, 2011b; Tanaka et al., 2013). Indeed, one of these, Myod1, has been shown to cause fate conversion to skeletal myoblasts in many different primary cell types including dermal fibroblasts, chondroblasts, smooth muscle, and retinal pigmented epithelial cells, as well as ES cells (Choi et al., 1990; Tanaka et al., 2013). For these reasons, Myod1 was an ideal candidate to drive muscle differentiation in murine ES cells.

To introduce an inducible *Myod1* transgene stably into a ES cell line, I took advantage of a technique reported previously called inducible cassette exchange (Iacovino et al., 2011). This technique involves replacing a floxed *cre* transgene in a previously generated ES cell line (A2Lox.cre) with a transgene of interest that must be floxed itself. The floxed *cre* allele is located in the *Hprt* locus, downstream of a tetracycline response element (TRE), enabling directed integration of the transgene at this genomic site, and chemically inducible expression of the transgene. To take advantage of this relatively fast and efficient method for generating transgenic cell lines, I generated a floxed *Myod1* construct on a p2Lox vector, and co-transfected it into A2Lox.cre ES cells with CAG::*Cre*, to ensure recombination. The *Myod1* vector also

contained a neomycin resistance gene, to allow screening of positive transfectants by neomycin. A successful transfection and recombination event would produce ES cells with the transgenes shown in figure 4.1 in the genome at the *Hprt* locus.

ES colonies that survived the antibiotic selection were picked, expanded and split for further analysis. To test functional expression of the inducible *Myod1* transgene, selected clones were exposed to doxycycline in the culture media. To facilitate myogenic differentiation, ESCs were first subjected to embryoid body culture, which initiates ESC differentiation and can promote mesodermal progenitor differentiation (Darabi et al., 2012; Hosoyama et al., 2014; Hwang et al., 2013; Iacovino et al., 2011). Upon addition of doxycycline, positive clones were observed to change morphology over the course of 3-4 days, with individual cells elongating to acquire a spindle shape morphology, reminiscent of *in vivo* myoblasts (Fig. 4.2) (Chen and Quinn, 1992). Immunocytochemistry revealed expression of myosin heavy chain (MHC) in the spindle shaped cells, a terminal marker of myogenic differentiation. Comparison of these cultures to controls without doxycycline induction revealed no change in morphology or expression of MHC, indicating specific induction of the *Myod1* transgene in response to doxycycline signalling. These results confirm the successful generation of an inducible-*Myod1* ES cell line ("iMyoD"), and reliable differentiation to a myogenic lineage in response to doxycycline induction.

Figure 4.1 Transgenes integrated into the *Hprt* locus of A2Lox.cre ES cells to produce doxycycline-inducible *Myod1* ES cells. The muscle differentiation factor *Myod1* is driven by a tetracycline response element (TRE) to allow inducible expression of Myod1. A neomycin resistance gene allows selection of positive clones.

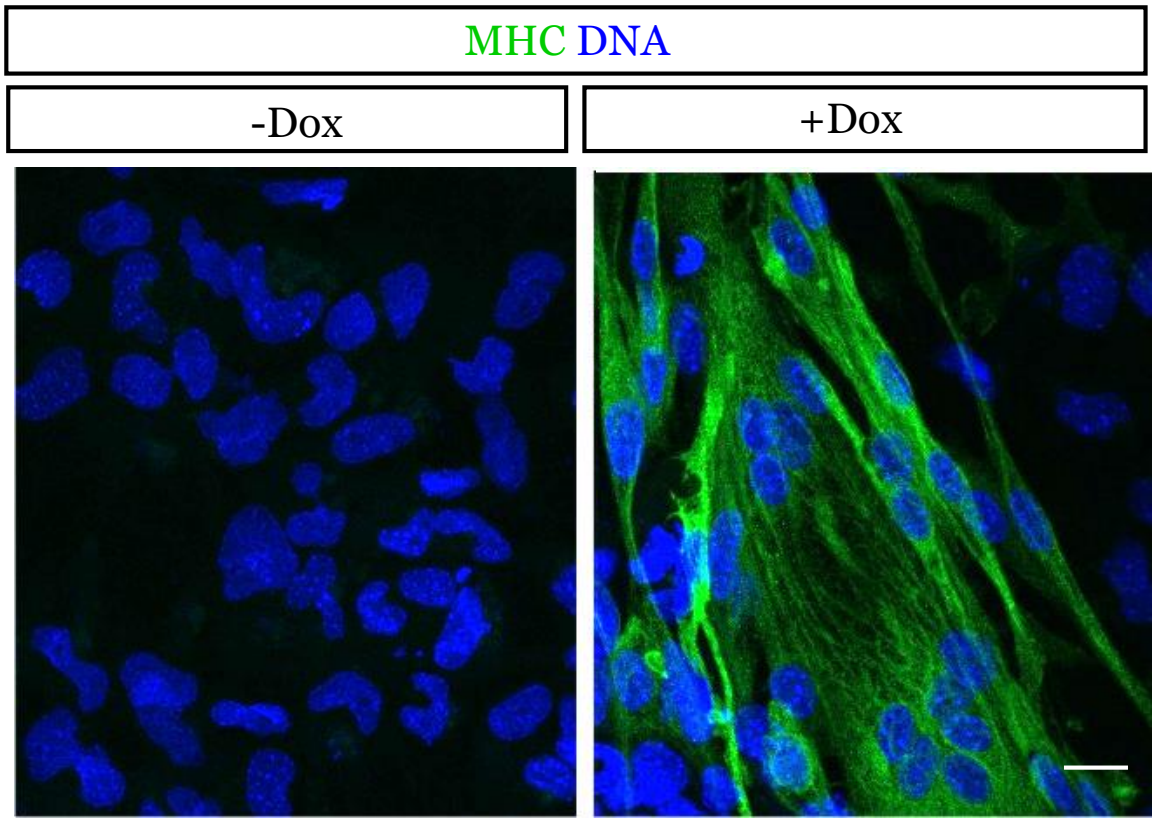

Figure 4.2 Doxycycline-induced *Myod1* transgene expression results in a spindle-shaped morphology and myosin heavy chain expression in murine ES cells. ES cells containing a doxycycline inducible *Myod1* transgene express myosin heavy chain (MHC; green) and assume an elongated, spindle shape after exposure to doxycycline *in vitro.* Control cells retain a round morphology and do no express MHC.

4.2.2 Producing MACS-sortable ESC-derived muscle

Although the induction of the *Myod1* transgene does drive a subset of ES cells to a myogenic fate, not all cells respond similarly to doxycycline induction, and in fact many do not express MHC, do not change morphology and do not exit the cell cycle, as is typical for differentiating myoblasts. These proliferative contaminating cells are not committed to a myogenic lineage, and rapidly overgrow *in vitro* cultures of induced myoblasts, preventing stable long-term culture.

Purification of the myoblast population following differentiation should remove the contaminating cells, and allow pure, long-term cultures of ES cell-derived myoblasts. To allow sorting of the myogenic population from contaminating cells, I generated a tol2 transposon based construct to enable MACS-sorting, similar to the strategy used for ES cell-derived MNs. Expression of a mouse CD14 transgene was again used as a cell surface marker, this time under the control of a small promoter region from the *Myogenin* gene, a muscle specific nuclear transcription factor downstream of *Myod1* in the muscle differentiation program (Fig. 4.3) (Brennan and Olson, 1990; Yee and Rigby, 1993). A hygromycin resistance gene was inserted downstream of the CD14 poly-A sequence to enable selection of positive colonies by antibiotic resistance.

iMyoD ES cells were co-transfected with the Myogenin::CD14 construct and tol2-transposase to drive tol2-mediated transposition events enabling stable insertion into the genome. Following colony picking after Hygromycin selection, candidate clones were subjected to doxycycline-induced myogenic differentiation and screened for CD14 expression by immunocytochemistry. Multiple clones were clearly positive for CD14 expression, as shown in figure 4.4, however significant differences were observed in expression levels and specificity. Clone C4 ("iMyoD C4") was selected for expansion and further analysis due to its relatively high expression of CD14 specifically in spindle-shaped cells, with no expression observed in rounded, undifferentiated cells (Fig. 4.4).

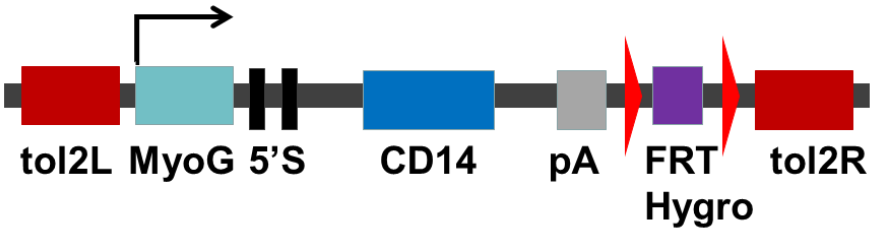

Figure 4.3 Tol2-based construct used to drive specific expression of the MACS-sortable marker CD14 in myogenic cells using a promoter from the *Myogenin* gene. The muscle specific nuclear transcription factor Myogenin drives specific expression of CD14 in committed myoblasts. This construct was stably integrated in the genome of iMyoD ES cells via tol2-mediated transposition. A hygromycin resistance gene allowed selection of positive clones using antibiotic resistance.

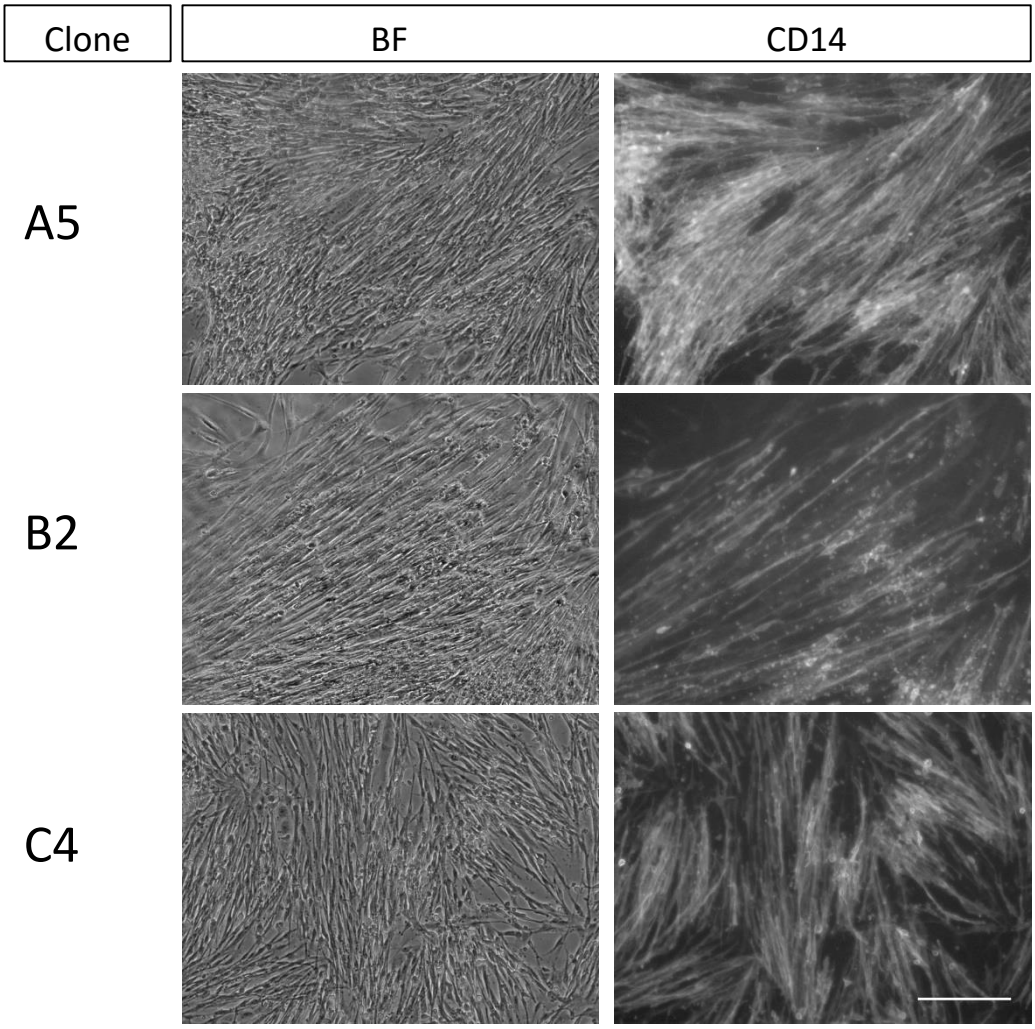

Figure 4.4 Screening for CD14 expression during myogenic differentiation of iMyoD ES cells. Representative images from the immunostaining for CD14 in clones selected after transfection with the tol2-based Myogenin::CD14 construct. Varying levels of CD14 expression were observed between clones, with clone "C4" showing the most specific, high-level expression in spindle-shaped myoblasts. Scale bar = 100µm.

4.2.3 Genomic integration site mapping of iMyoD "C4"

Variation in the expression levels and profile of the *Myogenin*::CD14 transgene in different clones may be a result of integration into different regions of the genome. The epigenetic landscape of the surrounding DNA, including methylation status and histone modification, can influence the expression level of transgenes, and could result in poor or absent expression (Baum et al., 2006; Fontes and Lakshmipathy, 2013). Additionally, if the transgene were to insert into the sequence of an endogenous gene, it may lead to altered expression or function of that gene, ultimately leading to unpredictable and undesirable effects in the cell line, potentially invalidating the use of the cells in experiments. For these reasons, and to better characterise the candidate MACS-sortable clone C4, I carried out inverse PCR mapping of the integration site of the sortable transgene. This technique relies on cutting out a small stretch of the tol2 transposable element sequences at either end of the transgene along with a short section of the surrounding genomic DNA using restriction endonucleases. These excised DNA fragments are then self-ligated and amplified by sequential PCR reactions using nested inverted primers designed to amplify part of the tol2 sequence and the genomic DNA. The products of the second PCR reaction are then inserted into a pGEM plasmid and sequenced. This procedure is depicted schematically in figure 4.5 below. The genomic sequence can then be compared to genomic sequence databases to identify where the transgene has inserted into the genome.

While multiple samples were obtained from the inverse PCR reactions against both the left and right Tol2 insertion sequences, only one sample from the Tol2 R group (MA2ii) gave reliable results, having both primer sites intact along with the Tol2 sequence and a stretch of genomic DNA (Fig. 4.6 a). The genomic sequence recovered in this sample was analysed using the nucleotide BLAST application on the NCBI webpage (http://blast.ncbi.nlm.nih.gov/Blast.cgi). This search revealed sequence homology to chromosome 2, in the middle of a gene called *Tanc1* (Fig. 4.6b). One sample against the Tol2 L side also contained genomic DNA that matched to a sequence 5' of the *Cacna1a* gene on chromosome 8, however no primer binding sites were

found, making this result unreliable (data not shown).

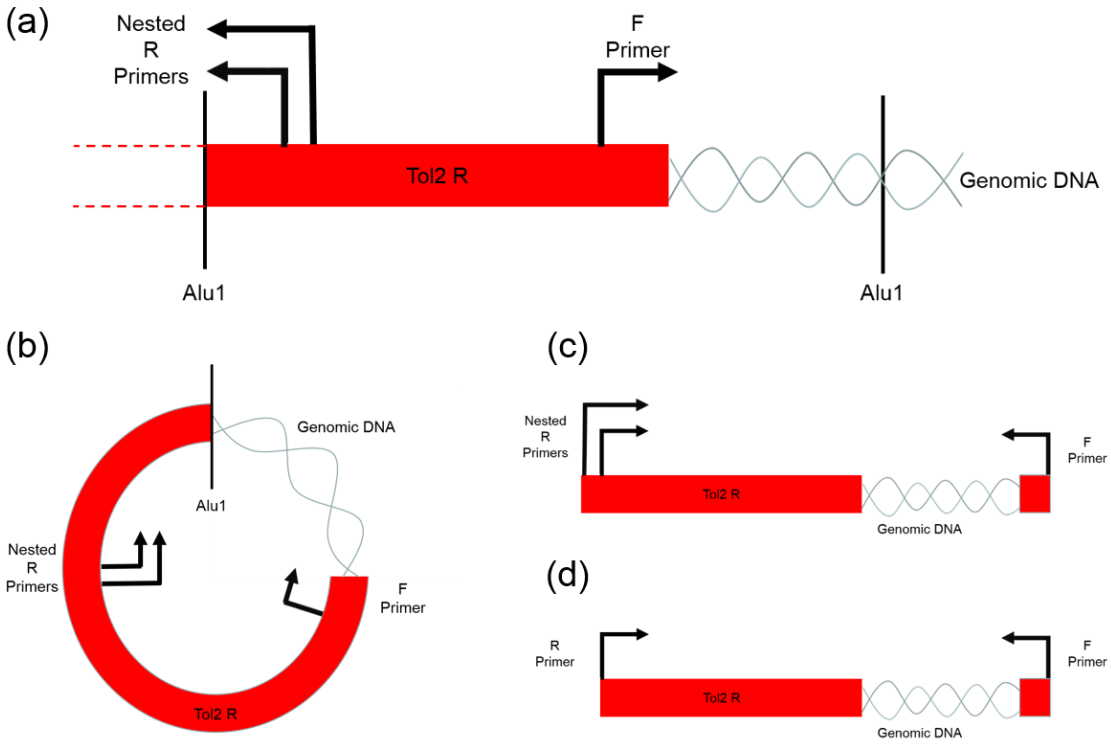

Figure 4.5 Schematic outlining the steps involved in inverse PCR mapping. (a) Nested, inverted PCR primers are designed against the ends of the flanking Tol2 insertion sequences. A restriction endonuclease that recognises a 4-base pair sequence upstream of the reverse primers (e.g. Alu1) is used to digest the genomic DNA, cutting at unknown point in the genomic DNA downstream of the Tol2 site, releasing a fragment with the primers and some genomic DNA. **(b)** The digest products are self-ligated, and subjected to two PCR reactions using the nested primers. The predicted product of the first reaction is shown in **(c)**, and the second reaction is shown in **(d)**. This product can then be inserted into a p-GEM vector for sequencing (see Fig. 4.6).

(a)

CGGCCGCCATGGCGGCCGCGGGAATTCGATTTGGAAGAA
AATGGAGGAAGTATGTGATTCATCAGCAGCTAGGACGCC
AGGGATGAGGACAGGAAGGGCCTTCCTCACATCTGAATC
CCCAGAGGTATAAAGTACTTGAGTAATTTTACTTGATTACT
GTACTTAAGTATTATTTTTGGGGATTTTTACTTTACTTGAG
TACAATTAAAAATCAATACTTTTACTTTTACTTAATTACATT
TTTTTAGAAAAAAAAAGTACTTTTTACTCCTCACAATTTTATT
TACAGTCAAAAAGTACTTATTTTTTGGAGATCACTTCATTC
TATTTTCCCTTGCTATTACCAAAATCACTAGTGAATTCGCG
GCCGCCTGCAGGTCG

(b)

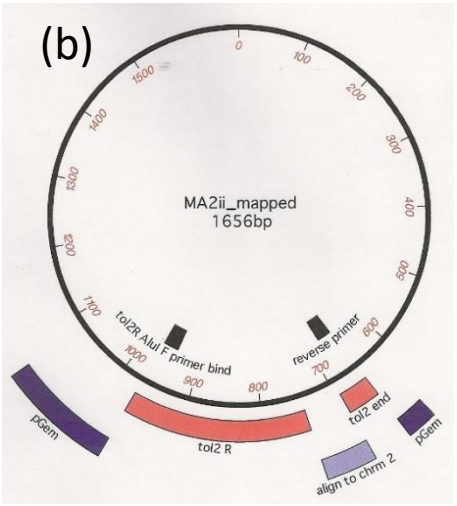

(c)

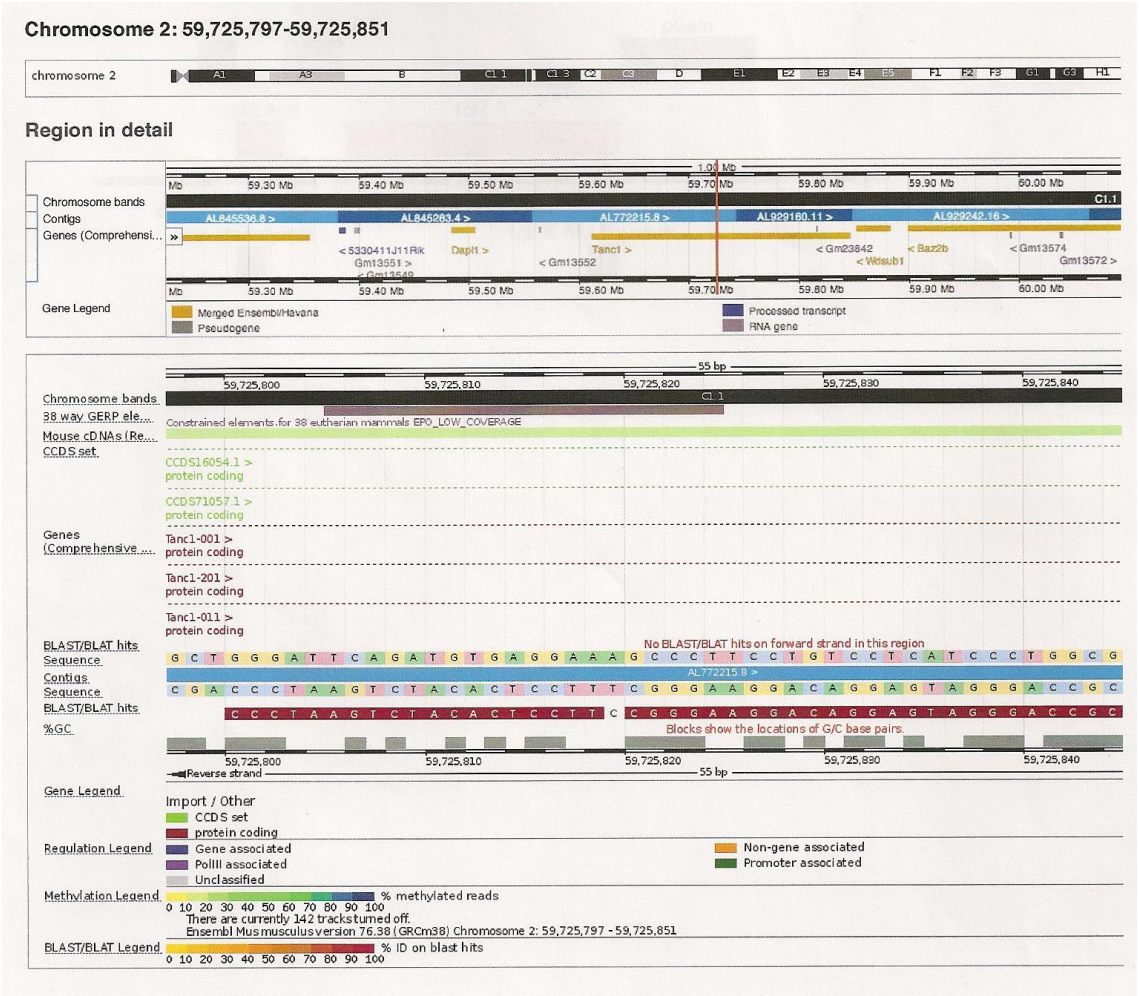

Figure 4.6 Inverse PCR mapping of the genomic integration site of *Myogenin*::CD14 tol2 transgene into the iMyoD cell line. (a) Sequence alignment results from a successful inverse PCR (iPCR) reaction using primers and restriction endonucleases against the tol2R element. Un-highlighted text is pGem sequence, red highlights indicate Tol2R sequence, and grey highlights indicate genomic DNA. White text shows primer binding sites. **(b)** The amplified sequence matched the tol2R sequence and included the primer binding sites. A small sequence of genomic DNA was amplified, which was found to match a region inside the Tanc1 gene on chromosome 2 **(c)**.

4.2.4 Analysis of MACS efficiency

While immunocytochemistry revealed strong, specific expression of the CD14 transgene in presumptive myoblasts (Fig. 4.4), it was still unknown whether this would allow reliable MACS-sorting of the muscle fraction following differentiation. To analyse the efficiency of MACS utilising the CD14 surface tag, I carried out multiple repeats of the differentiation and MACS sort and analysed the pre-sort, flow-through and eluate by immunocytochemistry. As shown in figure 4.7, there was a significant enrichment for myoblast-like cells in the eluted fraction compared to both the pre-sort and the flow-through. There was a clear depletion of cells expressing MHC in the flow-through, as would be predicted for a successful purification. Analysis of multiple (n=3) MACS-sorts performed on different days revealed an average enrichment to 90.7% ± 4.6% MHC positive cells in the eluate, from 23% ± 3.6% MHC positive cells in the pre-sort (Fig. 4.7e). The flow-through was depleted to 11% ± 4.2% MHC positive cells. These results confirm the reliable and reproducible purification of the myogenic cell fraction from the initially mixed population of differentiating cells *in vitro*, and validate the use of the *Myogenin*::CD14 transgene to allow sorting of ESC-derived myoblasts.

To strengthen the evidence showing functional purification of the myogenic cell fraction, I analysed multiple MACS samples by flow cytometry immediately after sorting. Using a directly conjugated phycoerythrin (PE) antibody against CD14 revealed an enrichment of labelled cells in the eluate fraction compared to both the pre-sort and the flow-through (Fig. 4.9). Unlabelled cells from the pre-sort sample were used to set the gate “P1”, based on size and granularity using the forward and side scatter values respectively. P1 was set to capture all single cells, while cell debris and aggregates were not counted. The percentage of cells counted in the primary gate “P1” was equivalent in all three samples, with 60.8% in the pre-sort, 60% in the flow-through and 63.6% in the eluate (Fig. 4.9). The percentage of cells that had relatively high levels of PE-staining in each sample was higher than the observed MHC expression in immunocytochemistry analysis, however this could be due to non-specific or background

staining due to the fast labelling protocol used for flow cytometry. Alternatively, it is possible that many more non-MHC expressing cells do express CD14 on their surface than first thought, leading to the higher PE-staining observed in flow cytometry, although these cells do not appear in the eluate fraction as shown in figure 4.6, and therefore should not contaminate the purified myoblast-like population.

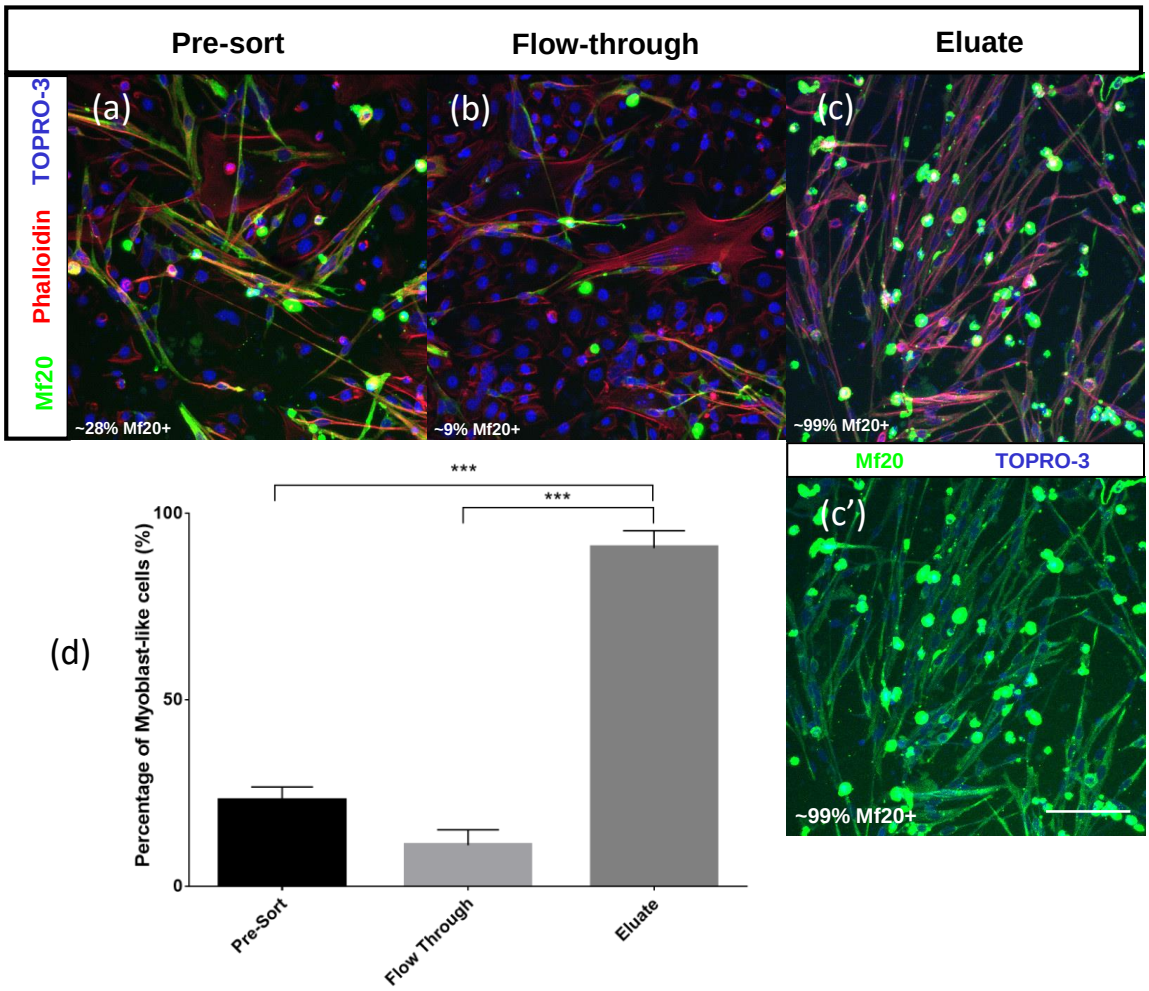

Figure 4.7 MACS sorting iMyoD C4 results in a reproducible, purified myoblast population. Representative immunostains from the pre-sort **(a)**, flow-through **(b)** and eluate **(c)** fractions from MACS-sorting iMyoD C4. **(c')** The eluate fraction showing only myosin heavy chain (green) and DNA (blue) labelling, revealing the high purity of mononuclear myogenic cells. **(d)** Bar graph showing average sorting efficiency over 3 MACS sorts. Scale bar = 100μm; One way ANOVA * = p <0.05, ** = p <0.01, *** = p <0.001.

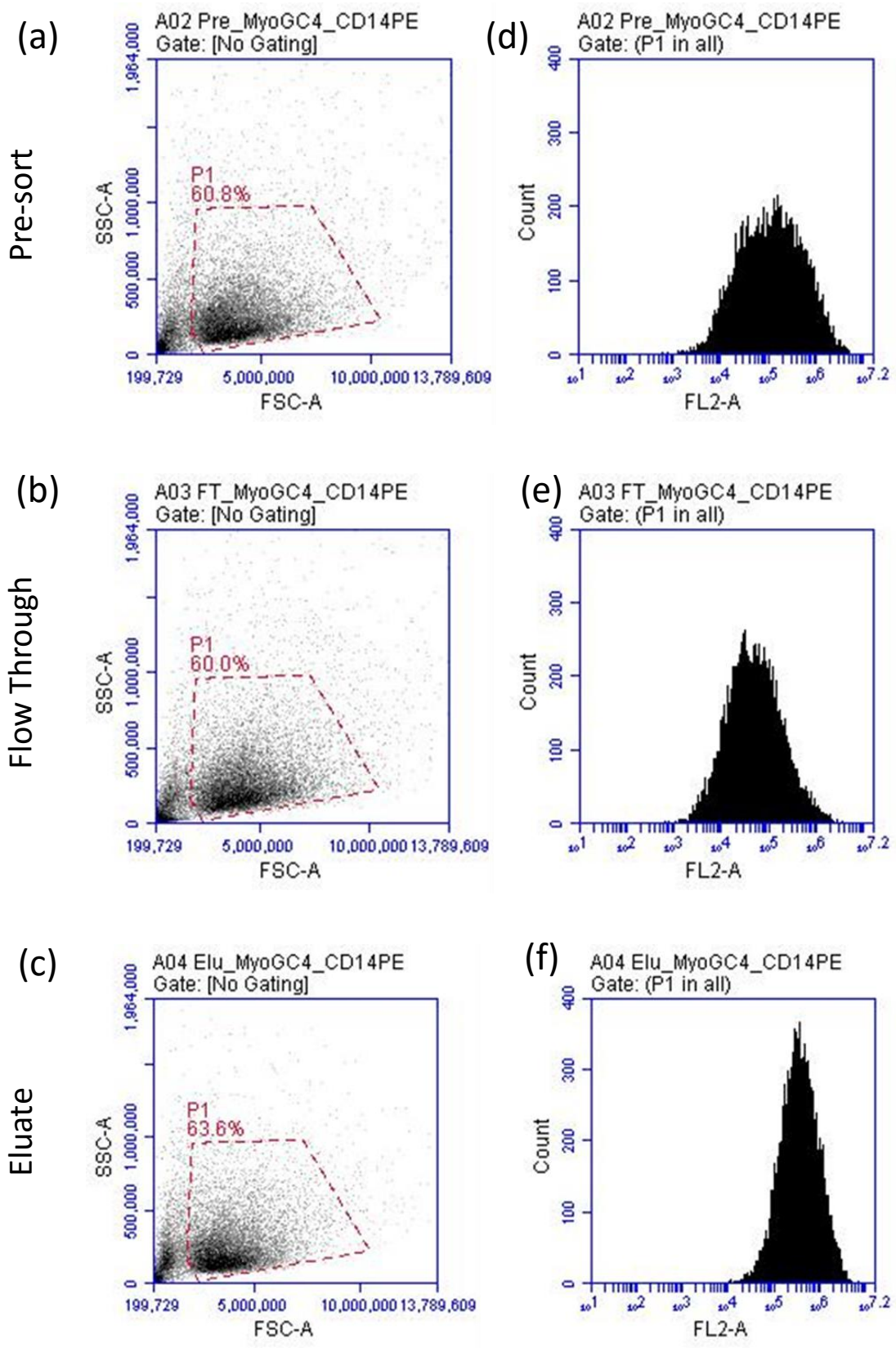

Figure 4.8 Gating and sample distribution for flow cytometry. Scatter plots from a representative MACS sort of iMyoD C4 showing the size and granulosity of cells in the pre-sort **(a)**, flow-through **(b)** and eluate **(c)** respectively [arbitrary units]. **(d-f)** Histograms showing the distribution of PE fluorescence in the sample populations from (a-c) [arbitrary units].

(a)

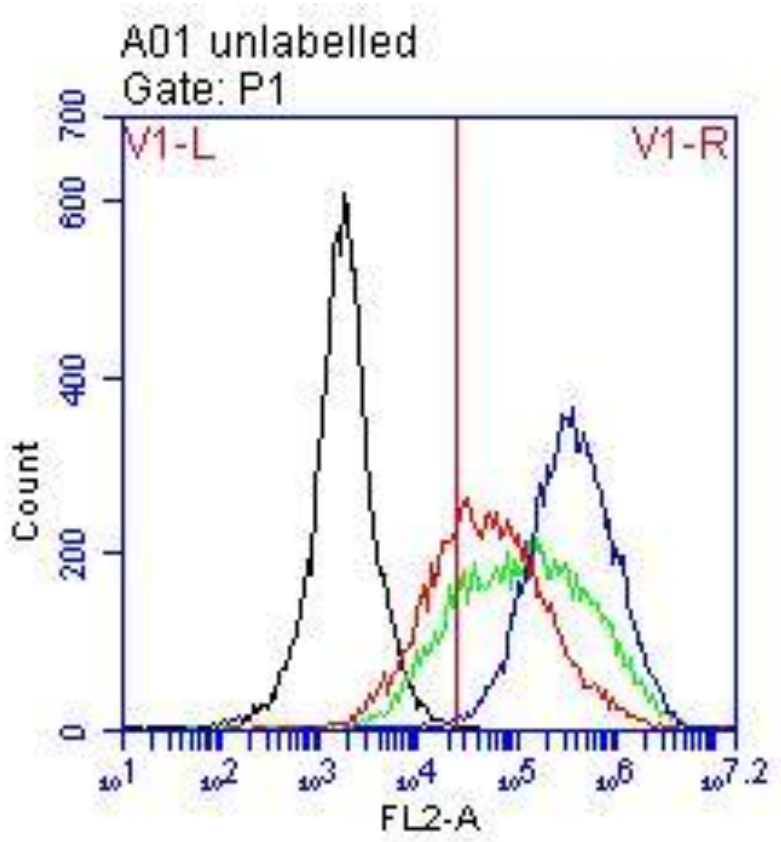

(b)

	Plot 4 (FL2-A)		
	This Plot	V1-L	V1-R
	% of All	% of This Plot	% of This Plot
A01 unlabelled	47.70%	99.92%	0.08%
A02 Pre_MyoGC4_C...	60.83%	17.82%	82.18%
A03 FT_MyoGC4_CD...	60.02%	31.41%	68.59%
A04 Elu_MyoGC4_CD...	63.65%	0.73%	99.27%

Figure 4.9 Flow cytometric analysis of MACS-sorted iMyoD C4. (a) Combined histogram plot showing the PE fluorescence distribution in the pre-sort (green), flow-through (red) and eluate (blue) respectively. Control unlabelled cells from the pre-sort sample are shown in black [arbitrary units]. **(b)** Table indicating percentages of cells in each sample found above or below an arbitrary fluorescence threshold set at the upper limit of unlabelled cell autofluorescence [purple line in (a)].

4.2.5 Characterisation and optimisation of ESC-derived muscle

Comparison of doxycycline-induced iMyoD C4 cultures to non-induced cultures immediately after differentiation *in vitro* revealed the expression of multiple myogenic markers in the doxycycline-induced cells (Fig. 4.10). Myosin heavy chain was observed in the cytoplasm of induced myoblasts, but was completely absent in uninduced cells (Fig. 4.10 a + a'). Myogenin, a nuclear transcription factor downstream of Myf5 and Myod1, was also observed in in the nuclei of induced cells, but again was not detected in uninduced cells (Fig. 4.10 b + b'). MCadherin, a muscle specific cell adhesion molecule, was also observed in doxycycline-induced conditions, found predominantly along the plasma membrane of spindle shaped myoblasts (Fig. 4.10 c). Not only was MCadherin expression not found in uninduced cells, but the morphology of the cells was also noticeably different, with a more rounded appearance (Fig. 4.10 c'). An antibody against a fast skeletal muscle specific epitope, My32, revealed clear expression in induced cells in a cytoskeletal arrangement, with no staining present in the uninduced population (Fig. 4.10 d + d'). Finally, Myod1 is clearly visible in the nuclei of cells exposed to doxycycline, but again absent from the control population (Fig. 4.10 e + e'). Myod1 expression would be predicted in the induced condition regardless of myogenic differentiation however, as the expression of the protein is being directly driven via the *Myod1* transgene under the control of the tetracycline response element.

Analysis of muscle marker expression in doxycycline-induced cultures after one week *in vitro* shows continued expression of muscle-specific proteins, and the initiation of cell fusion to form immature myotubes (Fig. 4.11). Myogenin expression remains clear in the nuclei, while MCadherin expression is also found surrounding the presumptive myotubes (Fig. 4.11 a + a', b + b'). These results confirm the myogenic commitment of doxycycline-induced iMyoD C4 cells *in vitro,* with multiple muscle specific proteins expressed and correctly localised.

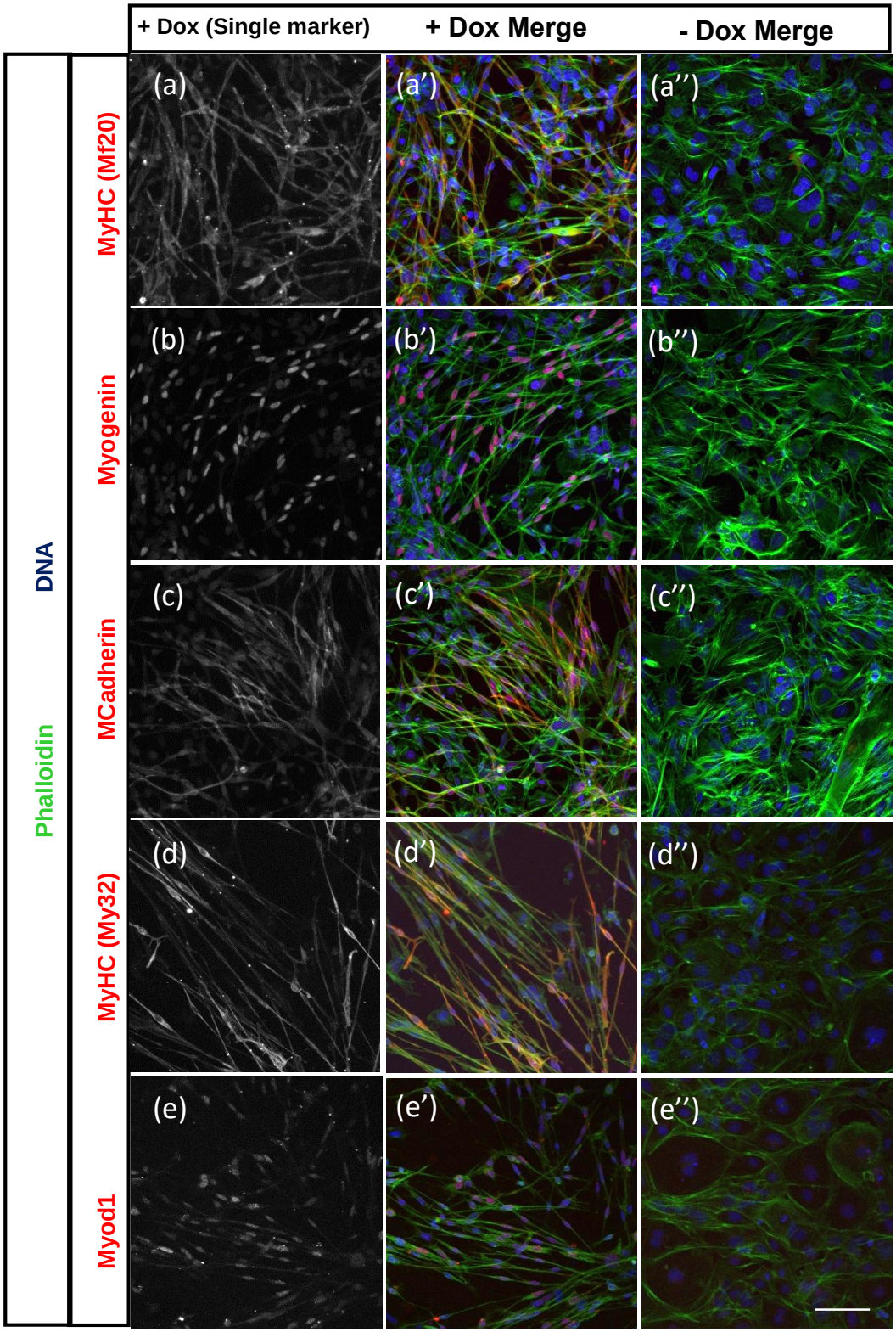

Figure 4.10 Doxycycline induced iMyoD C4-derived myoblasts express multiple muscle-specific proteins. (a-e) Antibody labelling against muscle-specific proteins expressed by day 1 doxycycline induced iMyoD C4 myoblasts. Mf20 labels an embryonic isoform of myosin heavy chain (myHC), while My32 labels a fast skeletal muscle specific isoform of MHC. **(a'-e')** Merged images of muscle markers shown in (a-e) with a nuclear DNA marker and phalloidin, which stains f-actin. **(a''-e'')** Uninduced control cells show no expression of any of the muscle markers, and have a different morphology as shown by phalloidin labelling (green). DNA labelled with topro-3 is shown in blue. Scale bar = 100 μm.

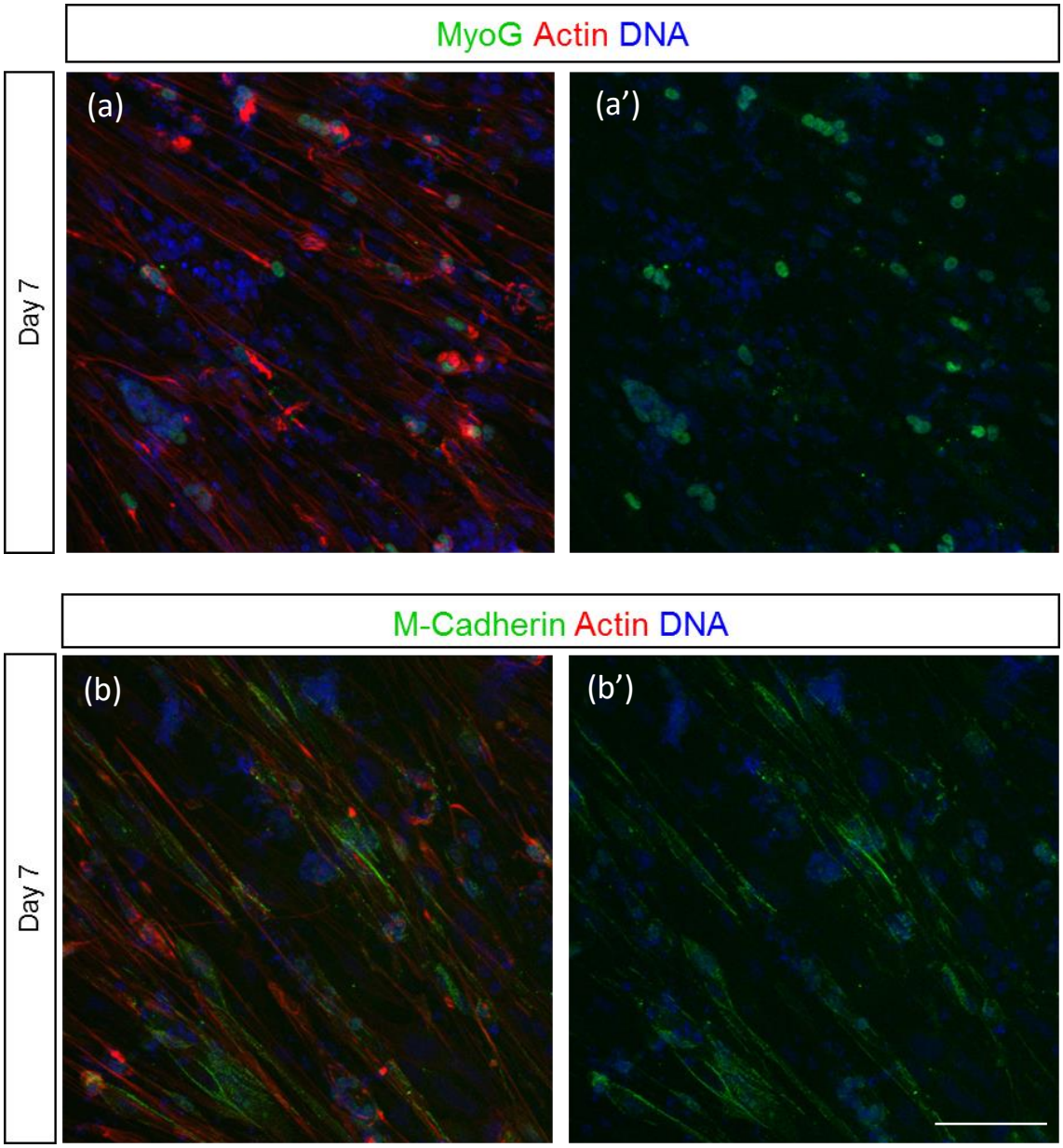

Figure 4.11 iMyoD C4-derived myoblasts maintain expression of muscle-specific proteins after 1 week in culture. (a+a') Nuclear Myogenin labelling remains visible in day 7 cultures of ESC-derived muscle. Not all nuclei are Myogenin positive, indicating substantial proliferation of contaminating cell types and possible termination of Myogenin expression in maturing myotubes. Fusion of myoblasts to form multinucleated myotubes is evident from the close proximity of many Myogenin labelled nuclei. **(b+b')** M-Cadherin expression is seen in day 7 ESC-muscle cultures, localised to the plasma membrane. DNA counterstaining with Topro-3 reveals aggregations of DNA, possibly indicative of cell death, especially when not associated within an F-actin/M-Cadherin labelled cell. Scale bar = 100 μm.

To establish the optimal conditions for *in vitro* culture of MACS-sorted iMyoD C4 muscle, purified myoblasts were plated at multiple densities on different matrigel-coated cell culture substrates with various culture conditions changed. The viability of ESC-derived muscle culture was assessed on 8 well permanox slides (Fig. 4.12), 24 well plastic Nunc™ tissue culture plates (Fig. 4.13) and in 24 well tissue culture plates in co-culture with mouse embryonic fibroblasts (Fig. 4.14).

ESC-derived myoblasts were plated on permanox slides at either 100,000 or 200,000 cells per well, based on previous experience using these slides. One day after plating, the wells with 100k cells were roughly 50% confluent, mono-nuclear, and had the characteristic spindle-shaped morphology of myoblasts (Fig. 4.12). Wells with 200k cells were almost confluent, and had the same single-celled myoblast morphology. Detached, rounded cells were observed at both densities, indicating a failure of some cells to attach to the substrate. There were no obvious differences between the cells plated in the standard myoblast media versus cells cultured in myoblast media plus chick embryo extract (CEE), used to culture primary skeletal myoblasts *in vitro*.

Five days after initial plating, much cell death was apparent in all the permanox conditions, although survival appeared slightly better in the more confluent wells (Fig. 4.12). Cells in the 100k wells were extremely sparse, with multiple detached and rounded clusters of cells indicative of death and detachment. More cells remained attached in the 200k wells, however the confluency had also decreased from initial plating. Many more clusters of round, dead cells were observed in the higher density conditions, perhaps as a result of detachment from the substrate and subsequent cell death, as spontaneous contractile activity was observed as early as 3 days *in vitro*. Cells that remained attached at day 5 maintained the elongated spindle shape, and some evidence of alignment and fusion was observed in the 200k wells, although myotubes were short and thin. In both conditions, more cells remained attached around the edges of the well, close to the wall, although by day 12 all cells plated on permanox slides had died.

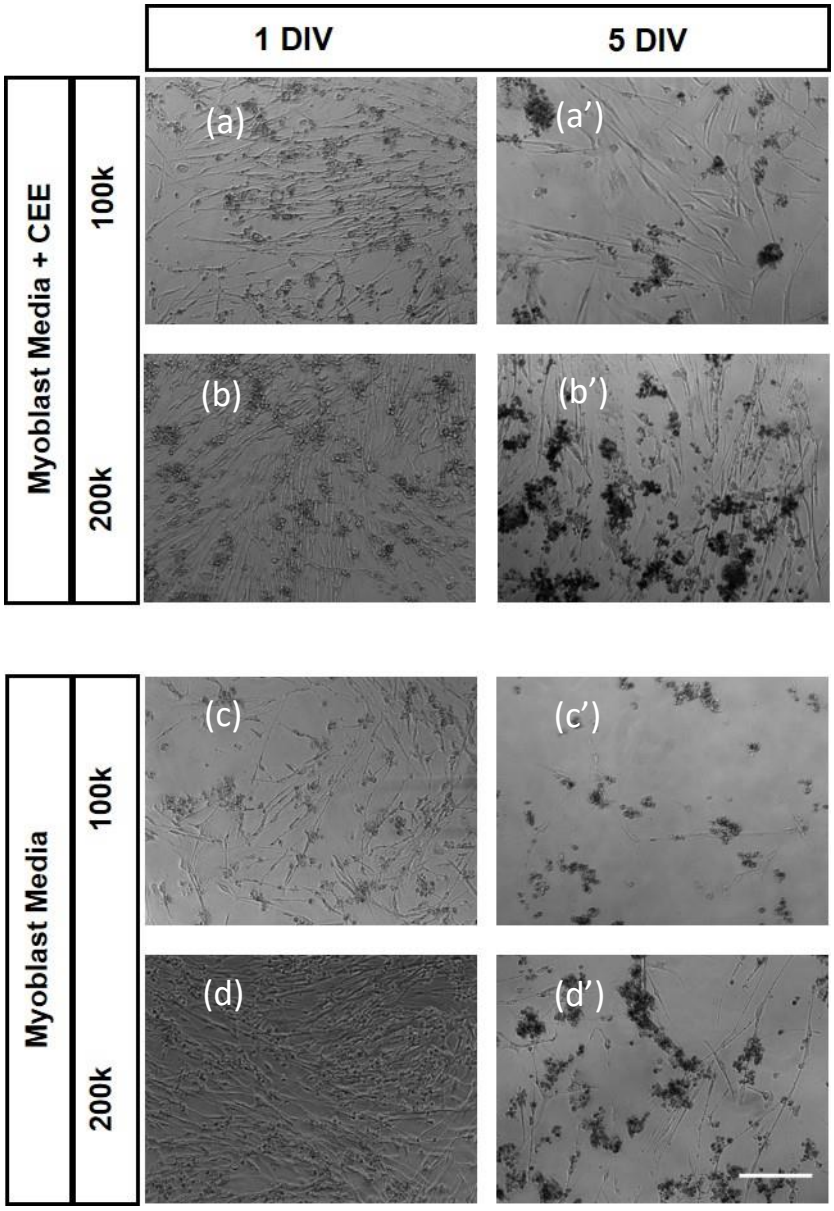

Figure 4.12 *In vitro* culture of iMyoD C4 myoblasts on 8 well Permanox slides. (a-d) MyoG C4 cultures imaged after 1 day *in vitro*, in media supplemented with chick embryo extract **(a + b)** or without **(c + d)**. After 5 days of *in vitro* on permanox slides much cell death was observed in all conditions **(a'-d')**. Scale bar = 100µm.

Due to the larger surface area of 24 well Nunc™ tissue culture plates, MACS-purified myoblasts were plated on matrigel at 200k or 400k per well. Again, cells were generally sparser in the 200k condition compared to the 400k wells, and all attached cells had an elongated spindle shape morphology (Fig. 4.13). Some myoblasts displayed slight branching morphology in cultures plated on the tissue culture plates, particularly in the lower density conditions. In contrast to the 8 well permanox slides, there were very few rounded or dead cells observed on the Nunc™ plates after 1 day *in vitro*, suggesting better initial attachment and survival. There were no clear differences between cells cultured in standard myoblast media or myoblast media with CEE on tissue culture plates at day 1 (Fig. 4.13).

Significant cell death was observed in cultures on Nunc™ tissue culture plates in all conditions after 5 days *in vitro* (Fig. 4.13). The wells plated with 200k cells were noticeable sparser by day 5, with many round dead cells and cell debris visible. Remaining myoblasts in the 200k conditions displayed blebbing of the plasma membrane, and were often slightly branched, extending multiple short membrane processes, not typical of healthy myoblasts. While wells plated with 400k cell remained fairly confluent, multiple dead or rounded cells were visible in both myoblast media and myoblast media supplemented with CEE, indicating detachment from the substrate possibly as a result of spontaneous contractile activity. Cells that remained attached in the 400k wells retained the bipolar spindle shaped morphology, and some evidence of fusion was observed. Multiple large, flat cells were seen in wells cultured with CEE by 5 DIV on tissue culture plates, possibly due to contamination with proliferative fibroblast-like cells, however these cells also displayed membrane blebbing, disrupted nuclei and a granular cytoplasm, possibly due to cell death by apoptosis (Wyllie, 1997). Compared to permanox slides, myoblast survival was in general better after 5 DIV on Nunc™ tissue culture plastic.

Analysis of cultures on Nunc™ tissue culture plates at 12 DIV revealed almost complete cell death in all conditions (Fig. 4.13). Very few myoblasts remained attached in the 200k wells, with only detached dead cells and debris evident in most areas. The same was true for wells plated with 400k cells, however a few more spindle-shaped myoblasts remained attached in the wells supplemented with CEE.

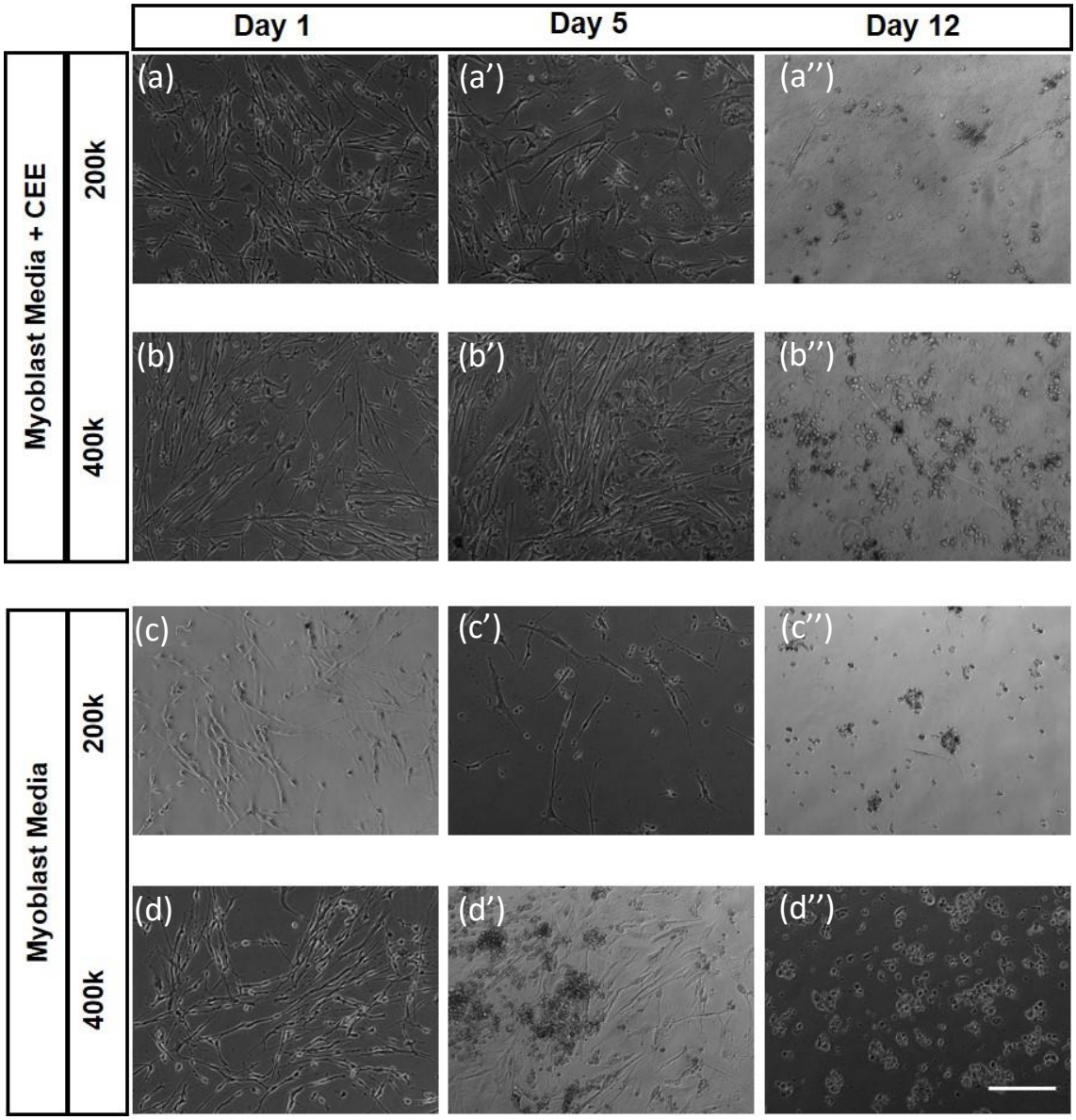

Figure 4.13 *In vitro* culture of iMyoD C4 myoblasts on 24 well Nunc™ tissue culture plates. MyoG C4 cultures imaged after 1 day *in vitro*, in media supplemented with chick embryo extract **(a + b)** or without **(c + d)**. After 5 days on tissue culture plates, cell death was observed in all conditions, but most prominently in lower density wells **(a'-d')**. After 12 DIV very few cells remained attached and alive in any condition **(a''-d'').** Scale bar = 100µm.

As a method to improve the survival of ESC-derived myoblasts *in vitro*, I co-cultured MACS-sorted iMyoD C4 derived myoblasts with mitotically inactivated mouse embryonic fibroblasts (MEFs), to act as a mechanical and trophic support, in order to reduce detachment from the culture substrate and promote long-term culture. A monolayer of MEFs was plated on matrigel-coated 24 well Nunc™ tissue culture plates one day prior to MACS-sorting and plating of iMyoD C4 derived myoblasts. One day after plating the myoblasts, long, thin, spindle-shaped myoblasts were clearly visible above a confluent layer of fibroblasts (Fig. 4.14). Some round cells and cell debris was visible in all conditions, indicating a failure of some cells to attach, as seen in cultures without MEFs. By day 5, a clear decrease in the number of myoblasts was observed in all conditions. This decrease was most notable in wells plated with 200k myoblasts, and slight branching of remaining myoblasts was evident, similar to 5 DIV myoblasts plated on Nunc™ tissue culture plates without MEFs (Fig. 4.13). Wells seeded with 400k myoblasts showed some evidence of fusion, and occasionally spontaneous contractile activity was seen, however the majority of cells remained mononuclear and unaligned. Significant granulation in the nucleus and cytoplasm of the MEFs was also observed on day 5, suggesting decreasing viability in the MEF population. Both MEFs and myoblasts appeared slightly more confluent in wells supplemented with CEE.

By 12 days *in vitro,* massive cell death was evident in all conditions. Multiple round cells were observed in suspension in most wells, and very few elongated myoblast-like cells remained attached, particularly in wells not supplemented with CEE (Fig. 4.14). A few fused, multinucleated, myotubes remained in the 400k wells supplemented with CEE, however they had fragmented nuclei and a granular cytoplasm, and very little spontaneous contractile activity was observed. While a majority of fibroblasts were still present, many had died, disrupting the initially confluent monolayer.

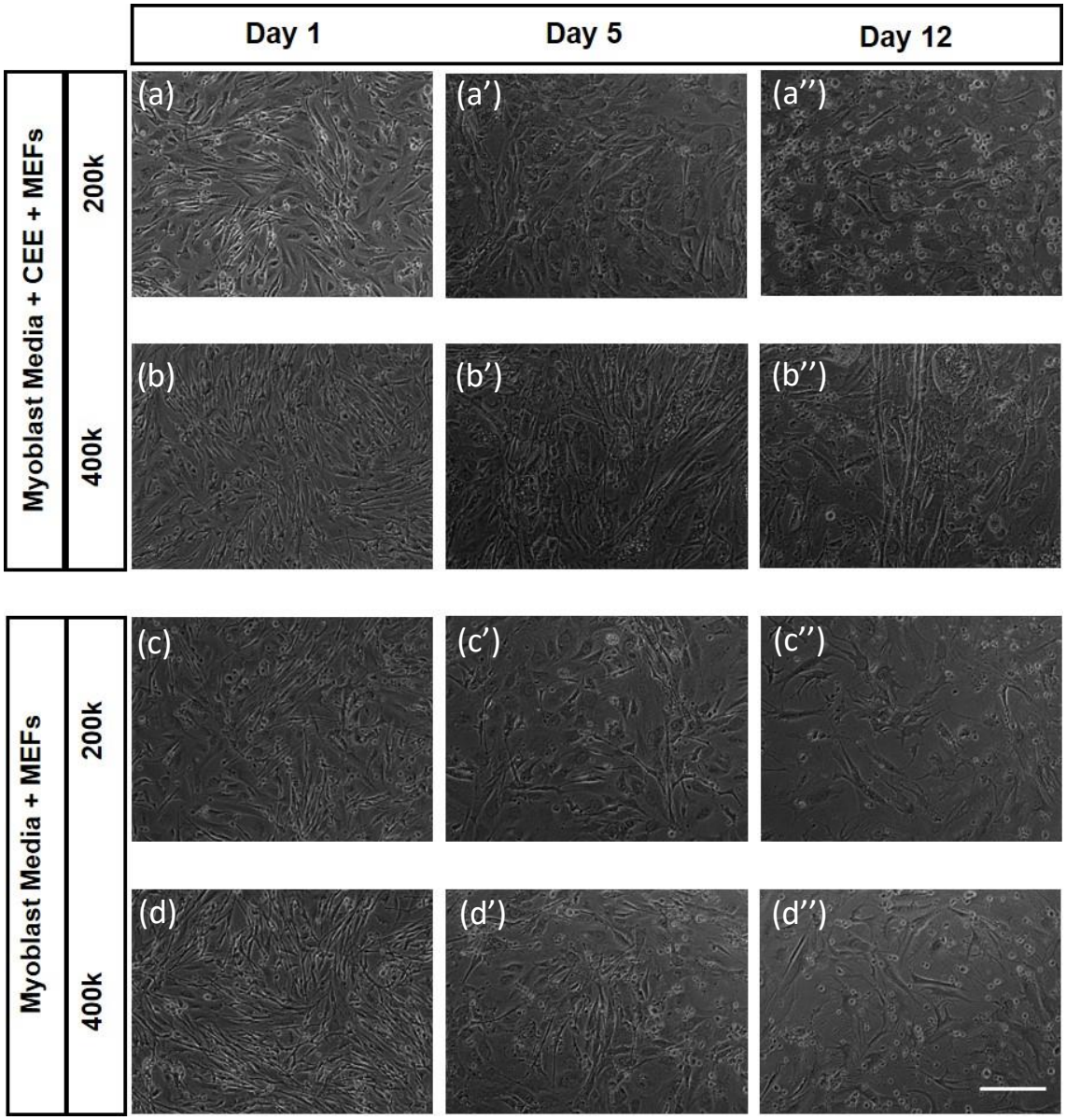

Figure 4.14 *In vitro* co-culture of iMyoD C4 myoblasts with mouse embryonic feeder cells on 24 well Nunc™ tissue culture plates. (a) MyoG C4 derived myoblasts co-cultured with mouse embryonic fibroblasts (MEFs) imaged after 1 day *in vitro*, in media supplemented with chick embryo (CEE) extract **(a + b)** or without **(c + d)**. After 5 days on tissue culture plates, myoblast cell death was observed in all conditions, and granulation was seen in the cytoplasm of many MEFs **(a'-d')**. After 12 DIV long, fused myotubes were observed in wells plated with CEE and MEFs, however much cell death was also apparent **(b'').** Very few myoblasts remained in the other conditions, and significant loss of MEFs was also observed **(a'', c'' and d'').** Scale bar = 100µm.

In general, iMyoD C4 ESC-derived muscle cultures did not survive beyond 2 weeks *in vitro* in any of the conditions tested, and while fusion to form contractile myotubes was observed, only a minority of myoblasts were able to develop to this maturity. One notable exception to this trend is shown in figure 4.15 below. In this experiment, large clusters of myoblasts did not adhere to the cell culture substrate, and instead formed free-floating aggregates reminiscent of embryoid bodies formed during ES cell differentiation into motor neurons (Wichterle et al., 2002). These aggregates survived long-term *in vitro*, and clear spontaneous contractile activity was observed after 1 week in culture. Analysis of aggregates by immunohistochemistry on cryosections cut through an aggregate after 6 weeks of culture revealed long, multinucleated myofibrils with clear F-actin striations characteristic of mature striated skeletal muscle sarcomeres (Berendse et al., 2003; Goulding et al., 1997). While promising, unfortunately attempts to repeat this suspension aggregate culture were unsuccessful, resulting in cell death within the first week, as seen in adherent cultures. Further testing and optimisation is therefore required to repeat the mature differentiation shown in figure 4.15, and better understand *in vitro* ESC-derived skeletal muscle culture.

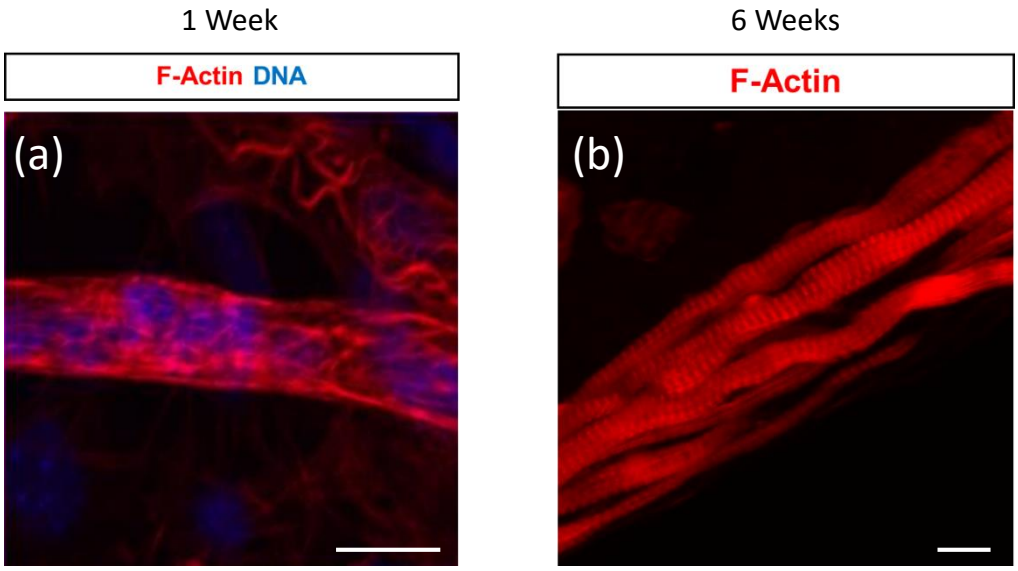

Figure 4.15 Long-term *in vitro* culture of iMyoD C4 myoblasts as aggregates enabled maturation to contractile, multinucleated myotubes with visible sarcomeric structure. (a) After 7 DIV, ESC-derived myoblasts formed multinucleated myotubes, however labelling of F-actin with phalloidin reveals no clear cytoskeletal structure. **(b)** After 6 weeks *in vitro*, iMyoD C4 derived cells formed long, multinucleated myotubes with characteristic sarcomeric structure revealed by F-actin staining. Scale bar = 100µm.

4.2.6 Analysis of ESC-derived muscle contractile activity

Spontaneous contraction of myotubes was frequently observed in iMyoD C4 derived muscle cultures, with activity noted as early as 3 days *in vitro*. This activity was present in the absence of neuronal innervation or external stimulation, and was fairly sporadic in nature, with no obvious pattern or consistency. Movies of live iMyoD C4 derived muscle cultures taken using an optical microscope allowed recording of this phenotype, enabling frame-by-frame analysis of muscle contraction using imaging software (ImageJ). The methodology used to analyse the movies is summarised in figure 4.16 below.

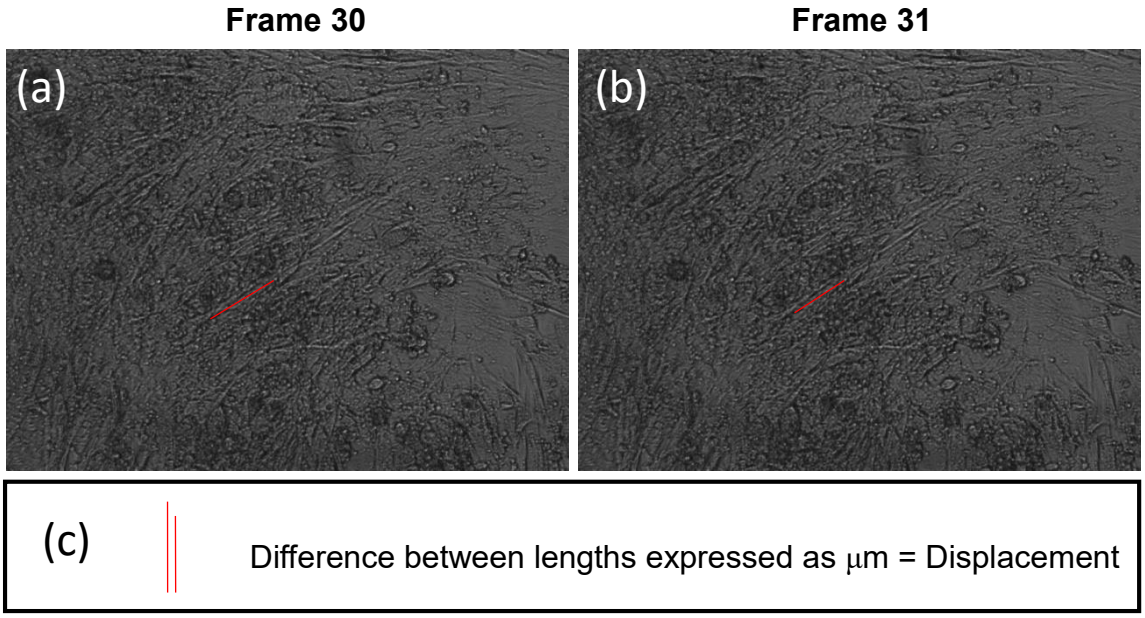

Figure 4.16 Frame-by-frame analysis of iMyoD C4 spontaneous contractile activity. Sequential frames from a time-lapse movie of an iMyoD C4 culture are shown. Persistent visual landmarks are chosen on an active myocyte, and a line is drawn between them [shown in red] **(a).** These landmarks are identified in all frames of the movie, and a line is generated for each frame **(b)**. **(c)** The length of the red line in all frames is then measured, and the difference between the length of the line in each frame from the baseline (longest length measured) is calculated to give the displacement of the visual landmarks (muscle contraction), expressed as μm.

Analysis of day 4 monolayer cultures of iMyoD C4 derived muscle revealed relatively strong, synchronised contractions occurring across the culture, with a fairly low frequency (Fig. 4.17). In

two of the movies (Fig. 4.17 a+b), contractions causing a displacement of around 15μm were recorded, occurring in bursts. The maximum displacement measured during a contraction in this format was 17.5μm (Fig. 4.17 a). When contractions occurred in quick succession, a full recovery to baseline was not seen, indicating residual tension between contractions. In the third movie analysed only one small contraction was recorded, happening in isolation, with the end of a previous contraction captured at the start of the movie (Fig. 4.17 c). Of the 6 time-lapse movies recorded of these cultures, contraction events were only observed in 3, highlighting the sporadic nature of this phenotype at 4 DIV. While observing these cultures, particularly powerful contractions were seen to cause tearing of the monolayer, and detachment from the culture substrate. This effect likely contributes to the difficulty of maintaining these cultures long-term *in vitro*.

Small contractions were also noted in some mononuclear myoblasts that had not fused at 4 DIV (Fig. 4.18). Contractile activity in individual myoblasts was much weaker, causing a displacement of less than 5μm in all measured examples. While not all mononuclear myoblasts showed contractile activity, the frequency of these contractions in active myoblasts was much higher than that seen in fused cultures. The difference in contraction strength between fused cultures and individual myoblasts is shown in figure 4.19 below, which also indicates the variation between samples recorded in each condition. The average displacement measured in fused monolayer cultures was 14.1μm ± 0.5 while in single myoblasts it was 1.17μm ± 0.04 (± S.E.M). The standard deviation within each sample group as shown on figure 4.19 was relatively large, indicating the high variability between contraction events, even within the same culture. While more work needs to be done to better characterise the spontaneous activity of iMyoD C4 derived muscle and allow more detailed analysis, this preliminary study reveals the development of a functional muscle phenotype, and shows the maturation of this phenotype in conjunction with the progressive maturation of myocyte morphology.

(a)

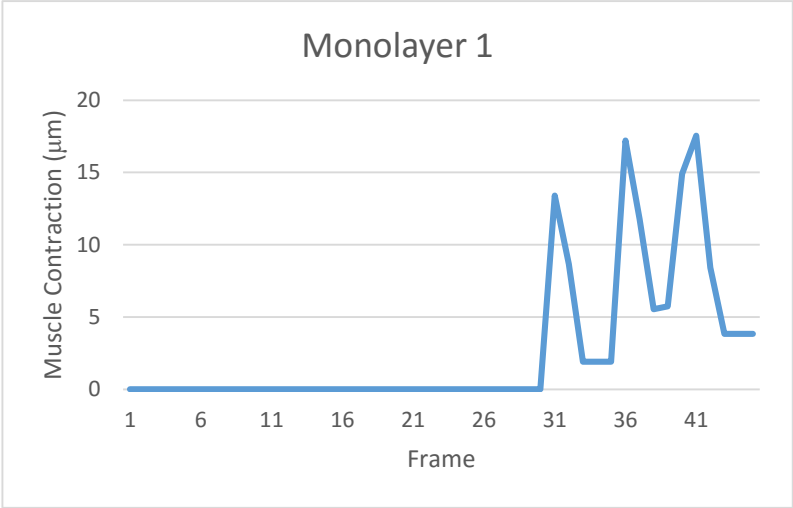

(b)

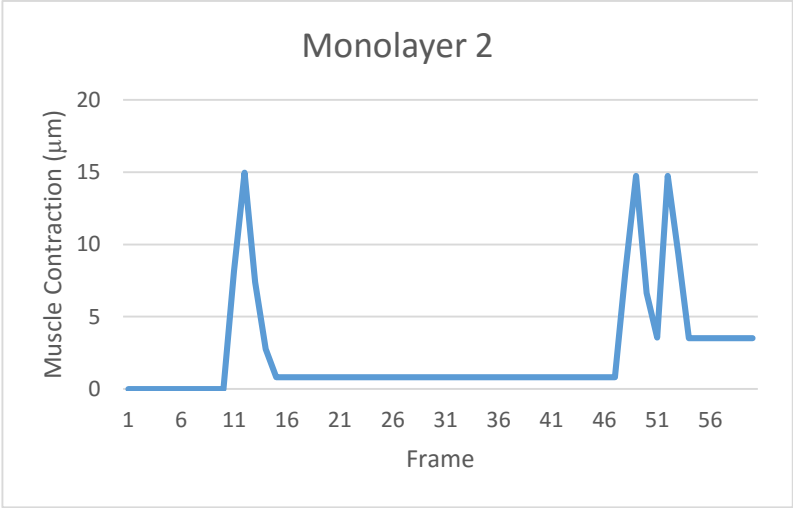

(c)

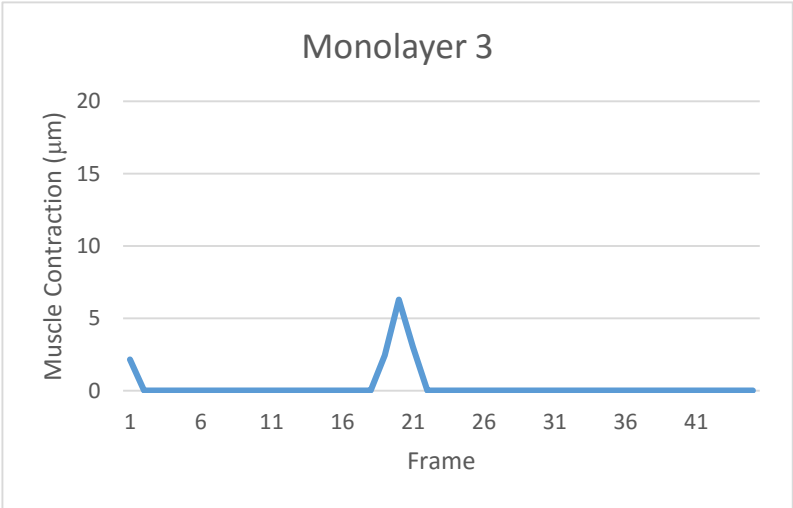

Figure 4.17 Analysis of fused iMyoD C4 monolayers after 4 DIV reveals sporadic, spontaneous contractile activity. Six time-lapse movies recorded on an optical microscope were analysed frame-by-frame as summarised in figure 4.16. In three movies, clear contractile events were observed **(a, b + c)**. Although displacement was observed across most of the imaged area in all movies, one representative region was selected for analysis in each sample.

(a)

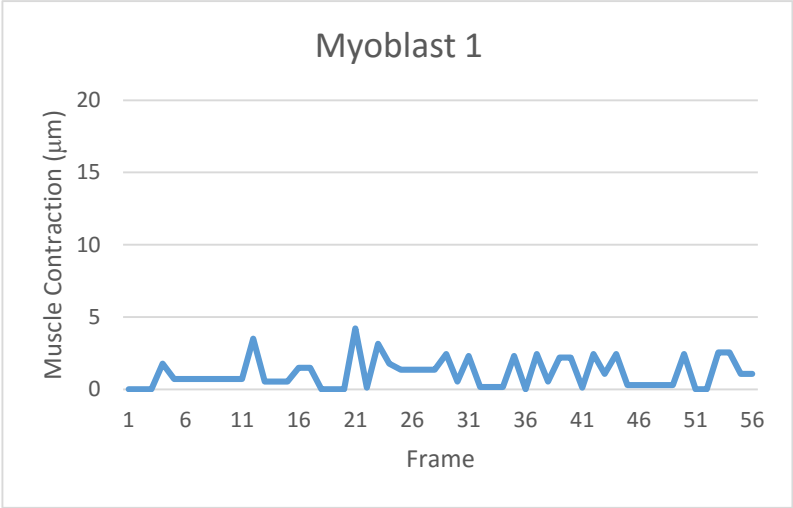

(b)

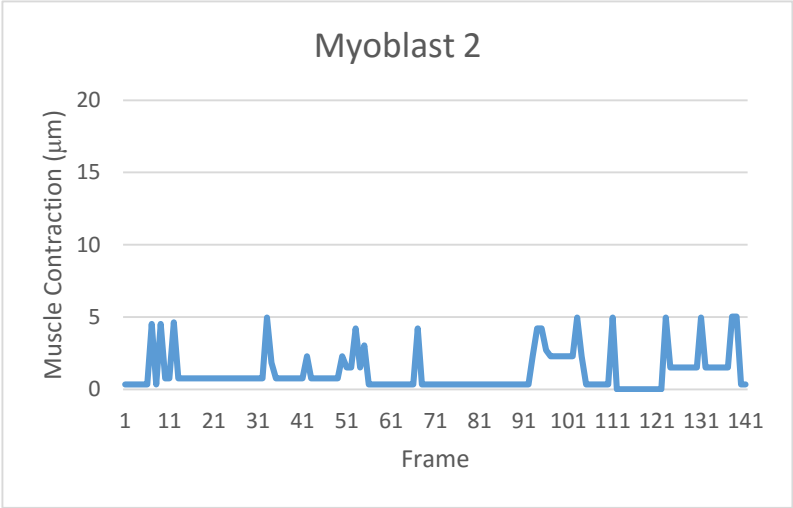

Figure 4.18 Analysis of individual iMyoD C4 myoblasts after 4 DIV reveals weak but frequent spontaneous contractile activity. Time-lapse movies recorded on an optical microscope were analysed frame-by-frame as summarised in figure 4.16. Weak contractile events were observed in some myoblasts in the absence of fusion **(a + b)**.

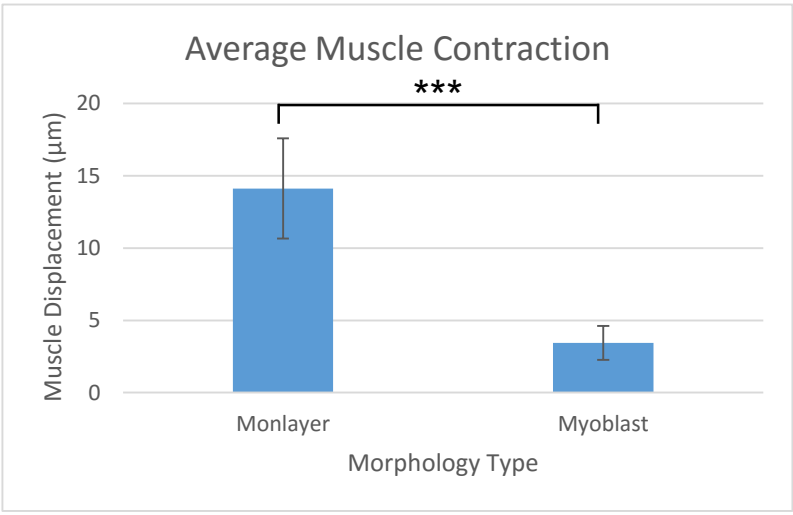

Figure 4.19 Analysis of iMyoD C4 spontaneous contractile activity after 4 DIV. Average displacement caused by contractile events in fused monolayer cultures (n=3) against mononuclear myoblasts (n=3). Average displacement was 14.1 ± 0.5 and 1.17 ± 0.04 (± S.E.M) in monolayers and myoblasts respectively. Error bars show the standard deviation. Two-tailed T-test * = p <0.05, ** = p <0.01, *** = p <0.001.

4.3 Establishing Chick Primary Skeletal Muscle Culture

4.3.1 Optimisation of primary skeletal muscle culture

Due to the difficulties experienced in maintaining long-term *in vitro* cultures of ESC-derived, MACS-sorted muscle, an alternative functional target tissue for ESC-derived MNs was sought. Primary chick skeletal muscle was identified as an ideal substitute, primarily due to the existence of well-established protocols for its culture, as well as its relative ease of accessibility and availability (Caplan, 1976; Gerstenfeld et al., 1984). Embryonic chick skeletal muscle was obtained by dissection of E10 chick pectoral muscles (as described in Chapter 2.2.2), providing a large quantity of muscle tissue. Mechanical and chemical dissociation of this tissue results in a single-celled suspension containing skeletal myoblasts as well as contaminating cells including fibroblasts and endothelial cells. Short incubation of this cell suspension in a 90cm Nunc™ tissue culture plate allowed adhesion of the majority of contaminating cells to the plate, while myoblasts remained in suspension, enabling a reduction in contaminating cell contribution to the final experimental material. Treatment of cultures with 5-fluoro-2'-deoxyuridine (FDU), an antimetabolite that prevents DNA replication via inhibiting thymidine synthesis, for 2 days at 2 DIV further reduced the contaminating cell population, allowing more stable long-term culture (Longley et al., 2003). This adapted and optimised method for chick skeletal muscle culture is outlined in figure 4.20 below.

To determine the ideal culture parameters for primary chick skeletal muscle, optimisation experiments on multiple cell culture substrates in various conditions were tested, similar to experiments conducted with ESC-derived myoblasts previously. Hemin, a porphyrin iron chelating agent similar to heme, was tested as an alternative to chick embryo extract (CEE) in promoting myogenic differentiation and survival, as it has been reported to improve myotube maturation, growth and function *in vitro* (Funanage et al., 1989; Schroedl et al., 1988). Different concentrations of matrigel coating and cell density were also assessed.

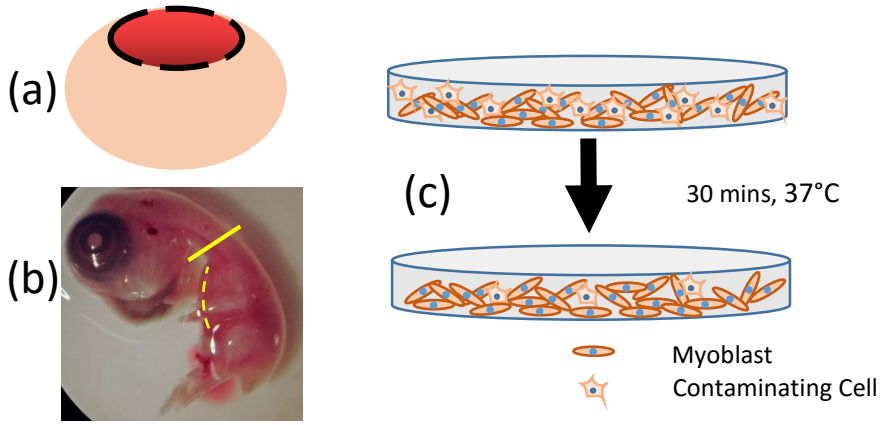

Figure 4.20 Schematic of the preparation of chick primary skeletal muscle for *in vitro* culture. (a) Day 10 eggs are sprayed with 70% ethanol prior to opening a "window" using surgical scissors. **(b)** The embryo is removed and placed in a dish of sterile DMEM, and decapitated using forceps (solid line). The skin along the ventral surface (dashed line) is cut and pealed back to the limbs. A single vertical cut through the abdominal muscles and ribcage is made, and the pectoralis major muscles are excised and enzymatically dissociated in 3ml of 0.25% trypsin at 37°C for 30 minutes. **(c)** Following inactivation of trypsin, cells are passed through a 40µm filter to a 90mm tissue culture plate, where incubation at 37°C for 30 minutes allows contaminating cells such as fibroblasts to adhere to the plastic. Myoblasts remaining in suspension are collected for culture plating. (D10 Chick image adapted from flikr.)

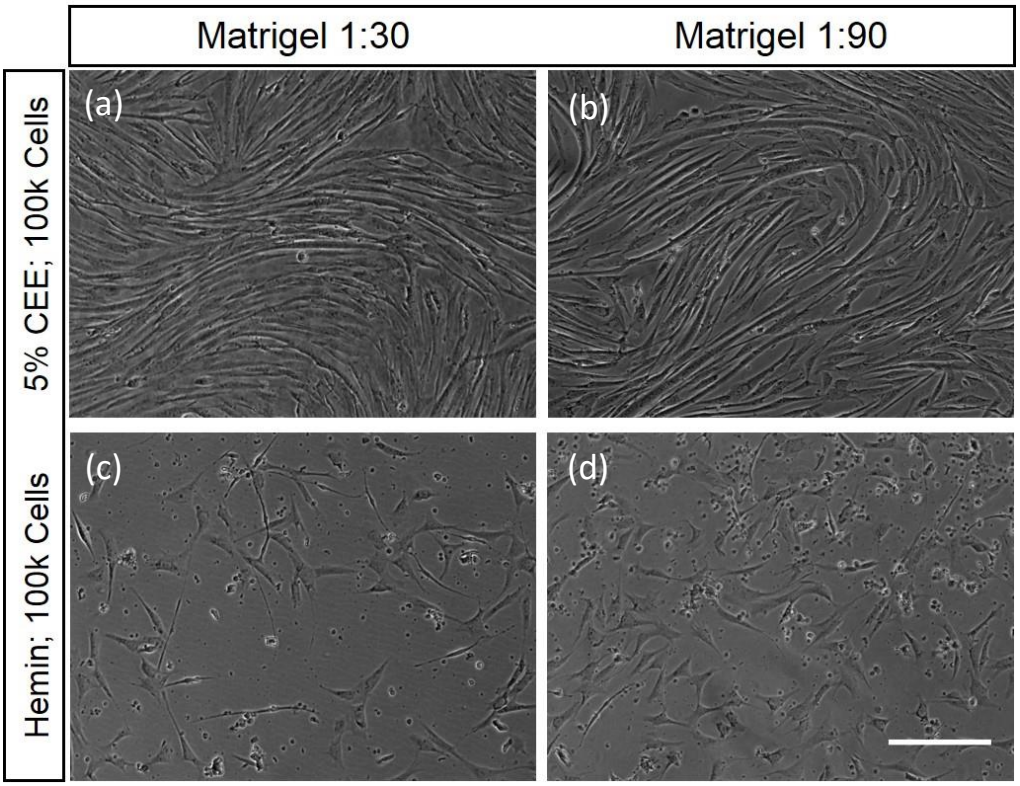

Figure 4.21 Media supplemented with chick embryo extract promotes primary chick skeletal myoblast attachment and survival on 24 well Nunc™ tissue culture plates. (a-d) Chick Primary Myoblasts imaged after 3 DIV on a 24w tissue culture plate. Cells cultured in media supplemented with chick embryo extract (CEE) formed confluent monolayers of spindle shaped myoblasts **(a+b)**, while cells cultured in media with hemin generally detached and died **(c+d)**. Matrigel concentration did not appear to have a major influence in either condition. Scale bar = 100µm.

Primary chick skeletal myoblasts plated on 24 well Nunc™ tissue culture plates in standard muscle media supplemented with CEE at 100k cells per well formed confluent monolayers of elongated cells at 3 DIV (Fig. 4.21 a+b). Cultures in these conditions did not appear to be affected by matrigel concentration, with cells on 1:30 matrigel closely resembling cells plated on 1:90 matrigel. Some cell fusion was already apparent after 3 DIV, with small myotubes observed throughout the cultures. Clear alignment between adjacent myoblasts was seen, however alignment was not consistent across the cells within each well, with different areas of the cultures aligned in different polarities. Very few dead cells or cell debris was observed in these conditions at day 3. Conversely, cultures of 100k cells on 24 well tissue culture plates fed with media containing hemin showed significant cell death, and failed to form a confluent monolayer (Fig. 4.21 c+d). Many rounded detached cells were observed suspended in the media, and debris from dead cells was apparent across the cultures. Cells that remained attached in these conditions rarely had the characteristic elongated spindle-shaped morphology of myoblasts, and instead extended multiple short membrane processes resembling fibroblasts. There was no evidence of fusion or alignment in cultures fed with hemin. Similar to cultures fed with CEE, matrigel concentration did not seem to influence these results.

Tissue culture plates seeded with 200k cells displayed similar results to those seen with 100k cells (Fig. 4.22). Myoblasts cultured in medium containing 5% CEE formed a confluent, ordered monolayer of spindle-shaped cells at both matrigel concentrations tested (Fig. 4.22 a+b). Wells fed with media containing hemin did appear more confluent than equivalent conditions using 100k cells, however the morphology of the myoblasts remained poor, and multiple dead cells and cell debris was observed (Fig. 4.22 c+d). Again, matrigel concentration appeared to have little influence over the condition of cultures plated on 24 well Nunc™ tissue culture plates.

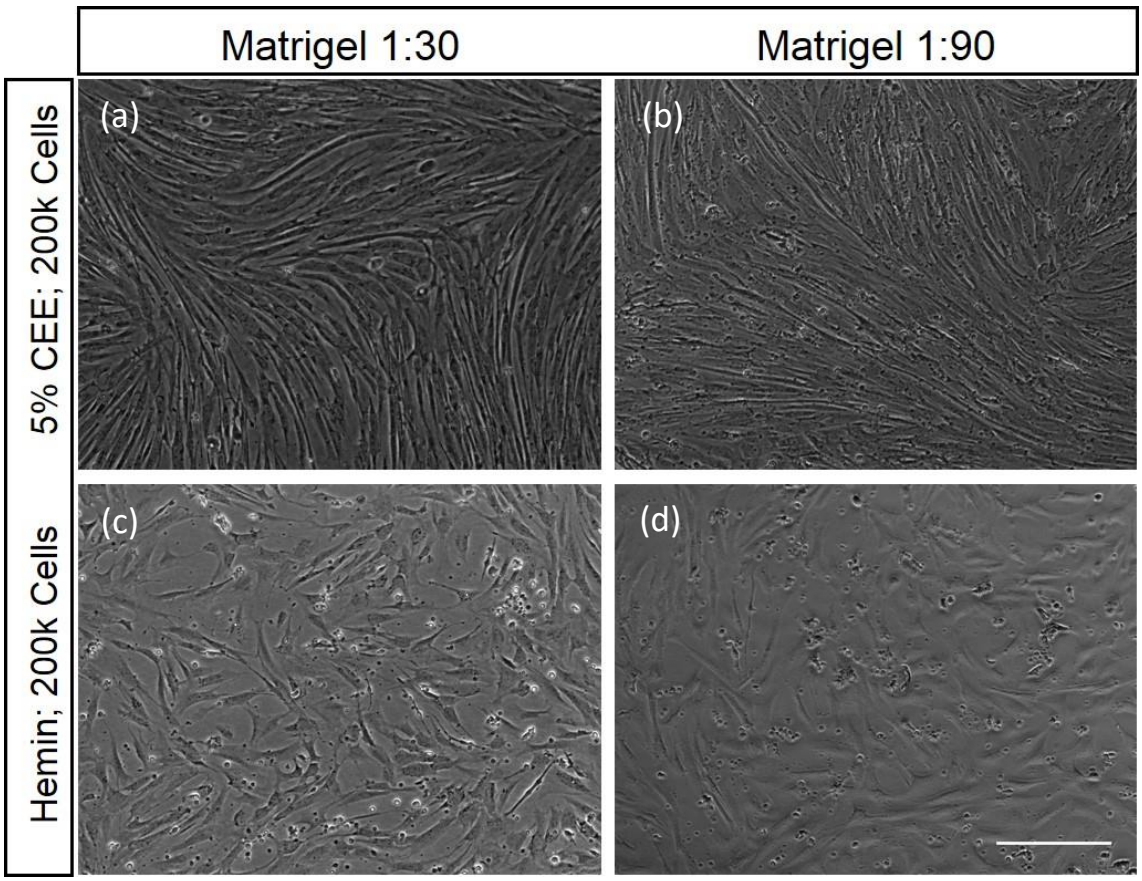

Figure 4.22 Matrigel concentration does not appear to influence primary chick skeletal myoblasts culture on 24 well Nunc™ tissue culture plates. (a-d) Chick Primary Myoblasts imaged after 3DIV on a 24w tissue culture plate at 200k per well. The higher seeding density did not appear to influence cells culture with CEE **(a+b)**, and did not improve cultures with hemin **(c+d)**. Matrigel concentration did not appear to have a major influence in either condition. Scale bar = 100µm.

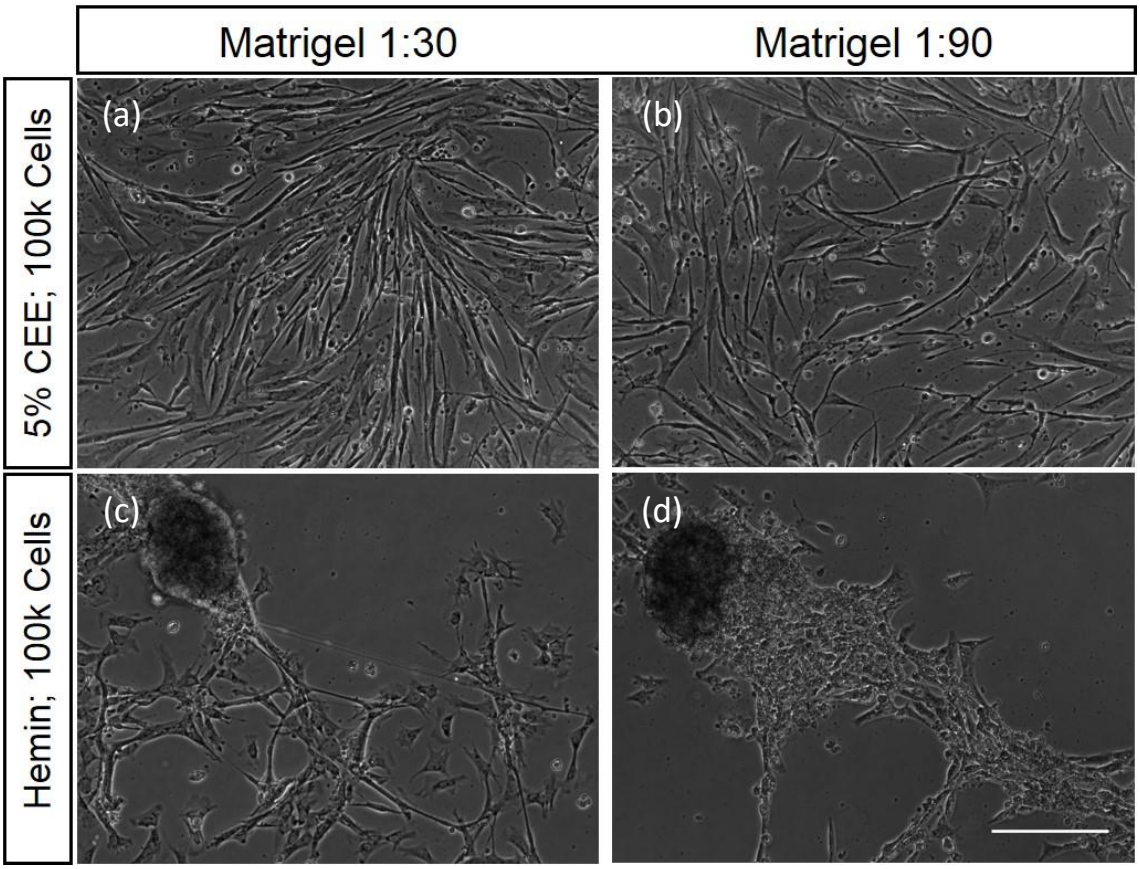

Figure 4.23 Culture of primary chick skeletal myoblasts on 8 well permanox slides with CEE- or hemin-supplemented media. (a-d) Chick Primary Myoblasts imaged after 3DIV on an 8w permanox slide at 100k per well. Myoblasts cultured in media supplemented with chick embryo extract (CEE) formed monolayers of spindle shaped myoblasts **(a+b)**, while cells cultured in media with hemin detached over most of the slide, and formed large aggregates **(c+d)**. Matrigel concentration did not appear to have a major influence in either condition, with perhaps fewer myoblasts attaching to wells with 1:90 matrigel **(b)**. Scale bar = 100µm.

8 well permanox slides were tested due to their ease of use in multiple imaging paradigms, as well as their small sample size allowing multiple conditions to be tested in parallel. Primary chick skeletal myoblasts plated on 8 well permanox slides with media supplemented with CEE had a relatively good morphology, and evidence of cell fusion and partial alignment was observed (Fig. 4.23 a+b). Cultures plated on 1:30 matrigel appeared slightly more confluent than cultures on 1:90 matrigel, indicating possible failure of or loss of attachment to the substrate in the lower concentration matrigel condition. Cell debris was observed at both concentrations of matrigel, indicative of cell death, with slightly more seen in the 1:90 matrigel wells. This difference may be due to the aforementioned failure to attach to the substrate of the lower concentration matrigel, also leading to the increased debris and less confluent culture.

Similar to results with hemin on 24 well tissue culture plates, primary myoblasts fed with hemin media on 8 well permanox slides had a fibroblast-like morphology, and significant cell death and debris was evident (Fig. 4.23 c+d). Aggregates of dead cells were observed in both matrigel concentrations. There was no evidence of alignment or fusion of myotubes, and matrigel concentration again appeared to have no significant effect on cell survival, attachment or morphology.

The final substrate tested for chick skeletal myoblast culture was 18mm glass coverslips, which, while requiring larger numbers of cells due to their larger surface area, allow epifluorescent and confocal microscopy as well as electrophysiological manipulation of the samples. Coverslips plated with 300k cells showed characteristic spindle shaped morphology and partial alignment in media with CEE and 1:30 matrigel at 3 DIV (Fig. 4.25 a+b). Some gaps in the myoblast monolayer were present however, suggesting non-confluence at this cell density. Unlike the previous substrates, the matrigel concentration did appear to influence cultures plated on glass coverslips, as the 1:90 matrigel condition had a less clearly defined morphology and a less confluent monolayer, with large bare patches visible adjacent to aggregates of detached cells.

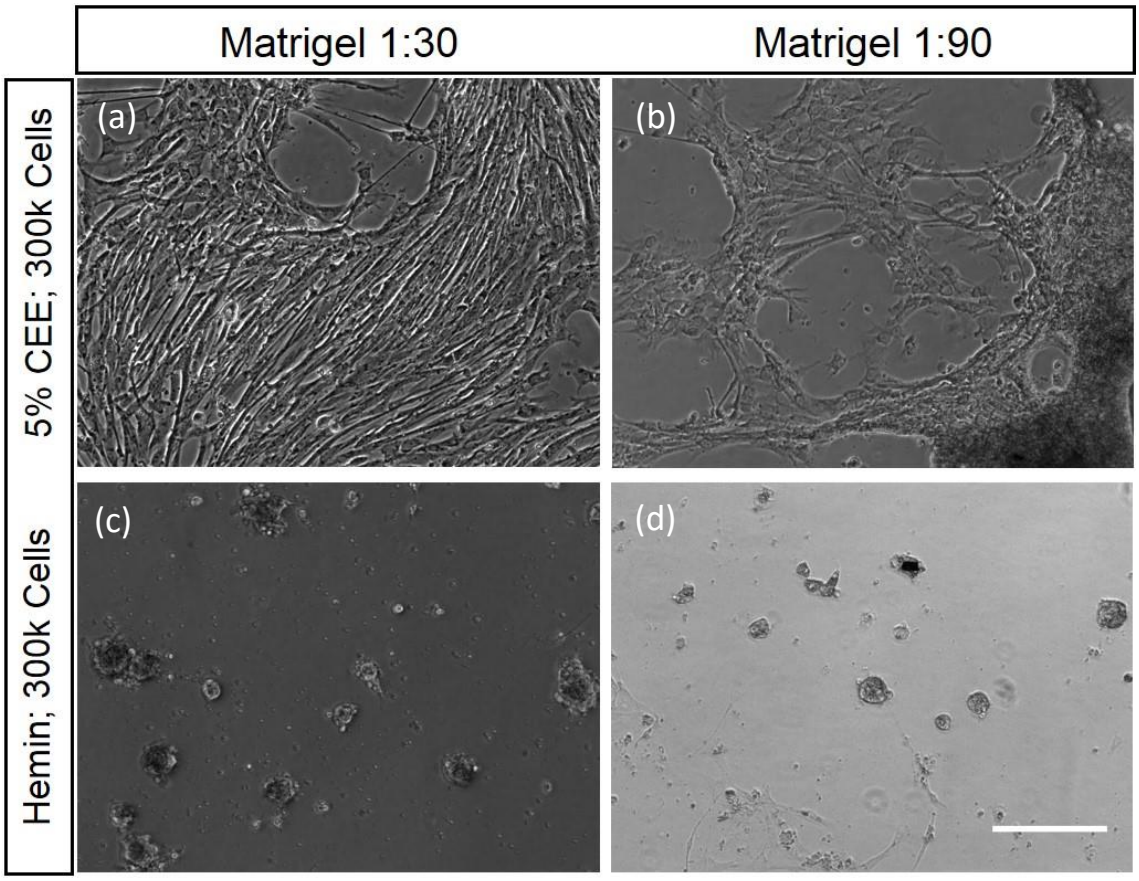

Figure 4.24 Culture of primary chick skeletal myoblasts on glass coverslips with CEE- or hemin-supplemented media. (a-d) Chick Primary Myoblasts imaged after 3 DIV on a glass coverslips. Myoblasts cultured in media supplemented with chick embryo extract (CEE) attached and had a spindle shaped morphology, with gaps in the monolayer visible **(a+b)**, while cells cultured in media with hemin generally detached and died **(c+d)**. Matrigel concentration had little effect in either condition. Scale bar = 100µm.

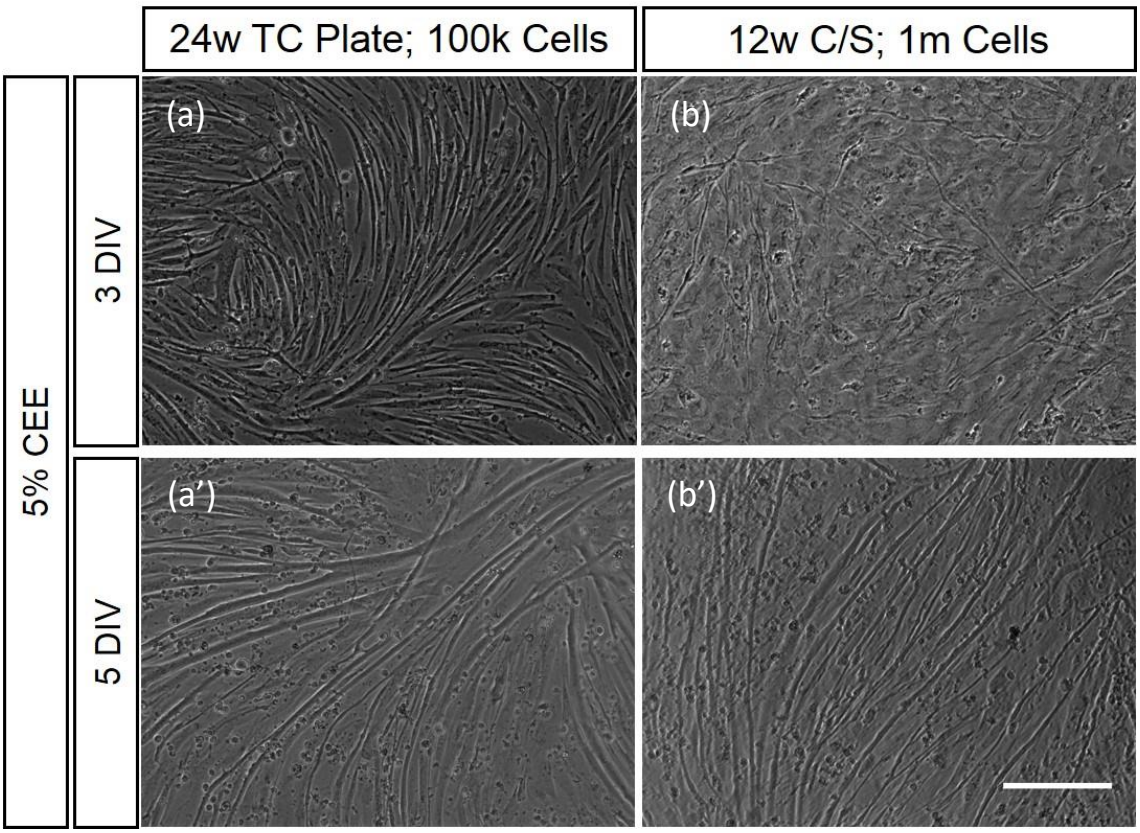

Figure 4.25 Culture of high density primary chick myoblasts on tissue culture plates or glass coverslips improves survival and enables fusion of multinucleated myotubes. (a) 100k chick primary myoblasts imaged after 3 DIV on a 24 well tissue culture plate, with the characteristic spindle-shaped morphology. **(b)** 1 million chick myoblasts cultured on a glass coverslip after 3 DIV. **(a'+b')**, After 5 DIV, chick myoblast cultures on tissue culture plates and glass coverslips look very similar, with partial alignment of long, contractile, multinucleated myotubes formed by fusion of myoblasts. Note the improvement in **(b+b')** from cultures of 300k chick myoblasts on glass coverslips shown in figure 4.20. Scale bar = 100µm.

Chick skeletal myoblasts plated on coverslips fed with media containing hemin did not survive to 3 DIV, with only aggregates of dead cells and cell debris remaining (Fig. 4.24 c+d). Unlike the previous substrates, no cells remained by 3 DIV, with even fibroblast-like cells not observed. Matrigel concentration did not influence survival or attachment in this condition, with total cell death observed in both matrigel concentrations.

From these results, the best substrates for *in vitro* culture of primary chick skeletal myoblasts were determined to be Nunc™ tissue culture plates and glass coverslips, coated with matrigel at a 1:30 dilution. Both of these materials allow attachment of large, confluent monolayers of myoblasts, which then adopt the characteristic spindle-shape morphology and partial alignment necessary for myotube fusion and further differentiation. Media supplemented with chick embryo extract allows robust survival and differentiation of myoblasts, while hemin appeared to be insufficient for both attachment and survival in the conditions tested here.

To further improve primary muscle culture on 18mm glass coverslips, a larger quantity of cells is required to ensure a confluent monolayer. To assess the impact of this optimisation and directly compare this condition to tissue culture plates in terms of survival and functional differentiation, 18mm glass coverslips were plated with 1 million primary cells, and imaged at 3 and 5 DIV (Fig. 4.25).

Coverslips plated with 1 million primary cells did form a complete monolayer, however individual cell morphologies were hard to distinguish, possibly due to over-confluence (Fig. 4.25 b). Thin, elongated cells resembling embryonic myoblasts were observed in these cultures, however the majority of cells were impossible to identify under phase contrast imaging. Cells plated on the tissue culture plate had the same pattern and morphology as shown in figure 4.21a, with a confluent monolayer of clearly resolved spindle-shaped myoblasts partially aligning in patches (Fig. 4.25 a). Very few dead or detached cells were seen in either condition. After 5 DIV, fused, multinucleated myotubes were observed in both cultures, generally running in parallel to nearby myotubes. Some cell death was observed on both glass coverslips and

plastic tissue culture plates, however this was fairly minimal, with little debris present. Cultures of 1 million cells on glass coverslips were generally very similar in appearance and development to cultures of 100k cells on Nunc™ tissue culture plates. As glass coverslips allow electrophysiological analysis and confocal imaging, and conferred no disadvantage in culture development or survival, this condition was chosen for future experiments using chick primary muscle.

4.3.2 Characterisation of primary chick skeletal muscle

Immunocytochemistry of chick primary muscle cultures on glass coverslips allowed investigation of skeletal muscle specific protein expression and clearly revealed the development of multinucleated myotubes (Fig. 4.26 + 4.27). Primary chick myoblasts after 1 day *in vitro* are mononuclear, with the characteristic spindle-shape morphology seen previously. Nuclear staining using topro-3, a DNA intercalating dye, revealed that the majority of cells in the culture were indeed myoblasts, as determined by nuclei contained within elongated cells, however significant numbers of nuclei were observed in cells with a more fibroblast-like appearance (Fig. 4.26). While some immunoreactivity was observed using the MCadherin antibody, this was very weak, and possibly only due to background staining (Fig. 4.26 a). Both antibodies against myosin heavy chain (MF20 + My32) labelled myoblasts, however again this labelling was very weak, particularly in the case of My32 (Fig. 4.26 b+c). The intensity of antibody labelling was variable between individual myoblasts within the same culture, which was particularly noticeable with MF20 (Fig. 4.26 b). Bright puncta were visible in samples labelled with MF20, however this is most likely an artefact cause by aggregation of antibody and non-specific binding.

After one week in culture, long, multinucleated myotubes were observed in all samples (Fig. 4.27). Very few mononuclear myoblasts remained by this time point, indicating that the termination of proliferation and concurrent fusion of myoblasts to form myotubes had occurred. Again the MCadherin antibody showed only very weak, non-specific labelling, which is likely due

to bleed-through or background labelling (Fig. 4.27 a). The MF20 antibody showed clear, specific labelling of myotubes, with some puncta artefacts (Fig. 4.27 b). While multiple nuclei were observed within each myotube, many nuclei were seen outside the F-actin and MHC labelled myotubes, indicating continued proliferation of contaminating cells (Fig. 4.27 b'). My32 also clearly labelled chick primary myotubes in a specific manner (Fig. 4.27 c). As My32 is selective for a fast skeletal myosin heavy chain isotype, this labelling confirms that the cultured muscle is of this type. Again, many nuclei were observed not contained in the myotubes, revealing the presence of many contaminating cells (Fig. 4.27 c'). Encouragingly, both MF20 and My32 labelling was absent from the nuclei within the myotubes, which is expected due to the cytosolic localisation of the epitope. Some fluorescent puncta were seen in day 7 My32 immunostains, but again these are likely artefacts caused by aggregation of antibody or debris. Myogenin expression was also investigated, however the antibody used did not bind chick myogenin, and the immunostains failed (data not shown).

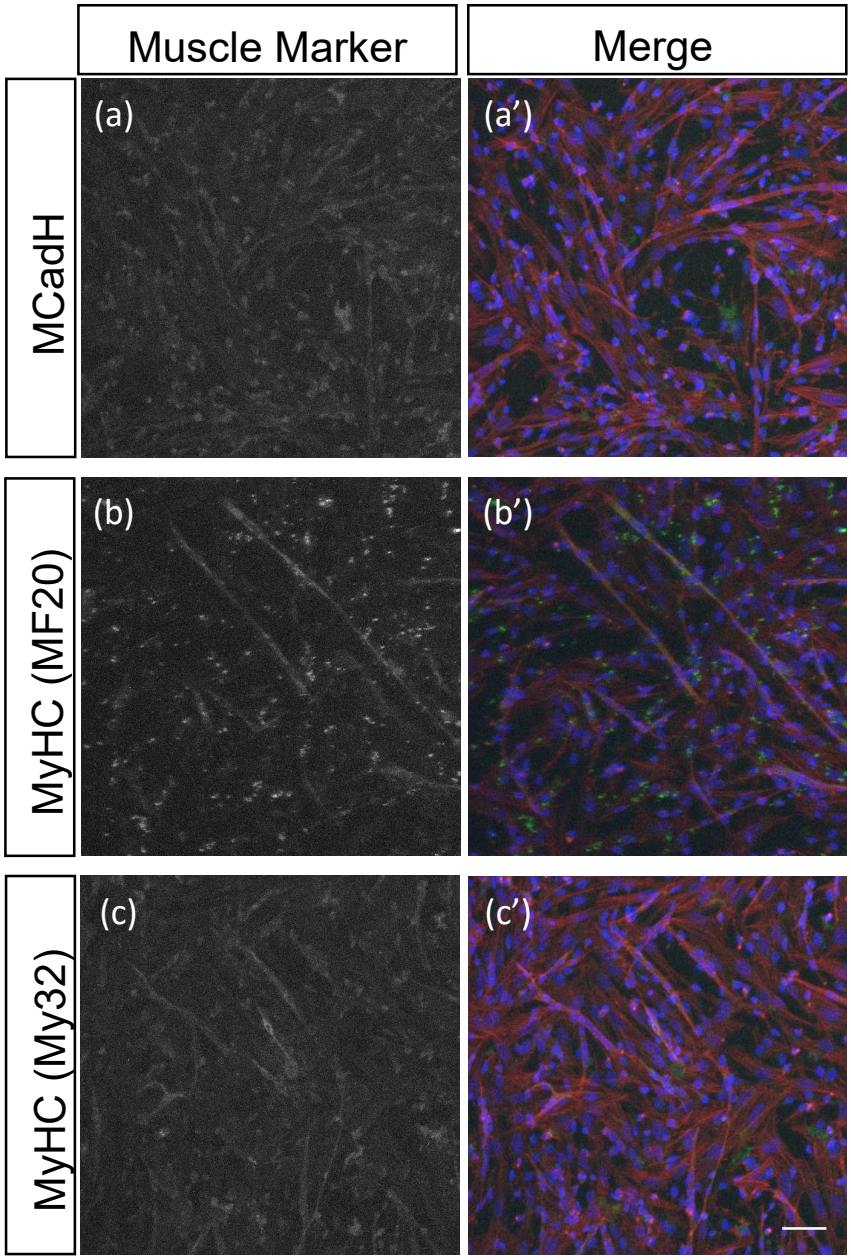

Figure 4.26 Chick primary myoblasts express muscle-specific proteins at 1 day *in vitro*. (a-c) Antibody labelling against muscle-specific proteins expressed by day 1 chick primary myoblasts. Mf20 and My32 labelling confirm the muscle phenotype, and indicate fast skeletal muscle due to My32 binding only a fast skeletal specific isoform of MyHC. MCadherin labelling **(a)** is less reliable, and may possibly be due to non-specific background staining. **(a'-c')** F-actin labelling (phalloidin; red) and DNA labelling (Topro-3; blue) reveal the spindle shaped morphology of the myoblasts, and the presence of many contaminating cells in these cultures. Scale bar = 100 μm.

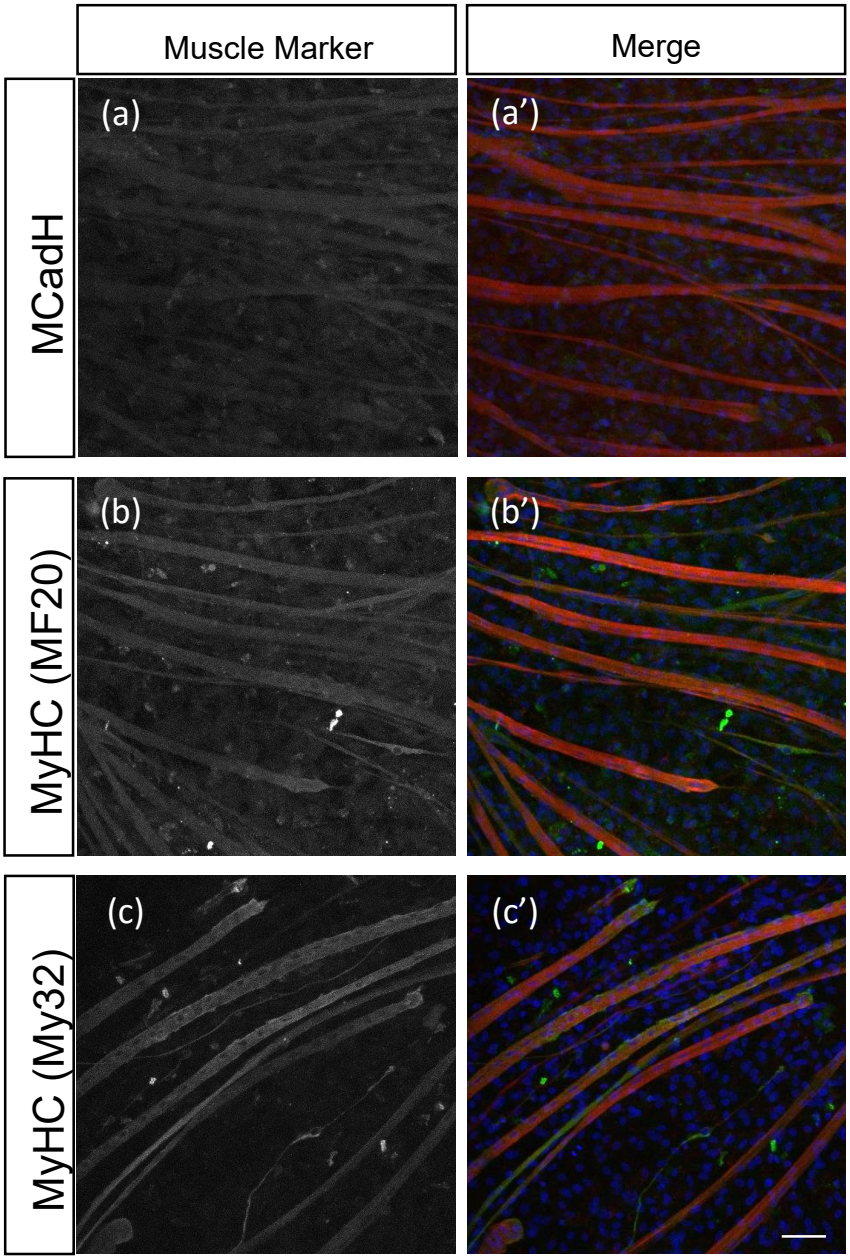

Figure 4.27 Multinucleated myotube formation and expression of fast-skeletal muscle specific proteins by chick primary myoblasts after 1 week of culture. (a-c) Antibody labelling against muscle-specific proteins expressed by day 7 chick primary myoblasts. My32 labelling is now stronger, while Mf20 labelling appears weaker, suggesting further differentiation to a fast skeletal phenotype. MCadherin labelling **(a)** is again very weak, and may possibly be due to non-specific background staining. **(a'-c')** F-actin labelling (phalloidin; red) and DNA labelling (Topro-3; blue) reveal long, multinucleated myotubes surrounded by many proliferative contaminating cells. No clear sarcomeric structure was visible in these images. Scale bar = 100 μm.

Chapter V

Modelling Neuromuscular Junctions *In Vitro*

5.1 Introduction and Aims

Having tested and established various conditions for the *in vitro* culture of both ESC-derived and chick primary skeletal muscle, the next aim was to combine these cultures with the ESC-derived motor neurons previously described in this thesis to create an *in vitro* neuromuscular model system. Co-culture of ESC-derived MNs with skeletal muscle should allow investigation of synapse formation and maturation, and may influence functional phenotypes such as muscle contraction. An additional advantage of using the ESC-derived MNs described here is the incorporation of optogenetics, enabling non-invasive manipulation of neuronal activity via Channelrhodopsin-2. By exposing co-cultures of skeletal muscle and ESC-derived MNs to blue light, activity can be induced in the neuronal population without directly influencing the muscle tissue. As populations of MACS-sorted ESC-MNs have little spontaneous acitivity, this light-evoked activity may be important for NMJ formation and stabilisation *in vitro*. Additionally, if functional synapses are present between optogenetic MNs and mature skeletal muscle, this activity should result in light-evoked contractile events.

As mentioned previously, a successful *in vitro* MN-muscle co-culture could serve as a useful model system for investigating neuromuscular disease, and a key requisite of such a model would be the development of neuromuscular junctions (NMJs). This is due to the central importance of the NMJ in neuromuscular circuit function and dysfunction, especially as recent studies have shown that NMJ destabilisation is one of the earliest detectable signs in ALS and other MN diseases, and is perhaps more relevant to disease progression than MN cell death (Fischer et al., 2004; Gould et al., 2006a; Murray et al., 2008). While *in vitro* MN-muscle co-cultures have been generated previously, the accuracy with which they model the *in vivo* system

is questionable, particularly with reference to the morphology of the NMJ (Guo et al., 2010; Kubo et al., 2009; Umbach et al., 2012).

The aims of this chapter therefore were to develop and optimise co-culture of ESC-derived MNs with both ESC-derived and chick primary skeletal muscle, and to assess these cultures for their utility in modelling neuromuscular circuits *in vitro,* with particular reference to NMJs.

5.2 ESC-Derived Muscle/Embryoid Body Co-Culture

5.2.1 Spontaneous contractions in EB/muscle co-culture

Neuromuscular junction (NMJ) formation *in vivo* is a dynamic process requiring input from both the presynaptic motor neuron terminal and the post-synaptic muscle end plate in order to develop and stabilise a mature synapse, as discussed previously (Chapter 1.2.3). While pure cultures of MACS sorted ESC-derived MNs appear to have little to no spontaneous activity (Fig. 3.10), unsorted EB cultures have higher levels of spontaneous activity (Fig 3.10), possibly driven by ventral-type spinal interneurons generated during the differentiation of MNs from ES cells using retinoic acid and sonic hedgehog. For this reason, initial co-culture experiments were performed with un-sorted embryoid bodies (EBs), as NMJ formation could be hindered in co-cultures with purified MNs due to a lack of presynaptic activity and acetylcholine release. EBs generated from ES cells containing the ChR2-YFP transgene on the Hb9::GFP-IRES-CD14 background were collected at the same developmental time point as the MNs would normally

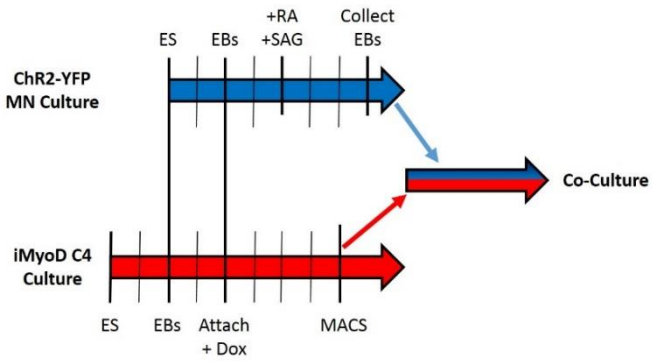

Figure 5.1 Time frame for EB/iMyoD C4 Co-Culture. Culture of iMyoD C4 ES cells is started first (red arrow), as they take longer to differentiate and are plated as a monolayer before addition of EBs. MN culture (blue arrow) is started 2 days after iMyoD C4, allowing harvesting of mature EBs and addition to the co-culture (blue and red arrow) 1 day after muscle monolayer plating. Black bars represent 1 day in culture.

be purified by MACS sorting, and plated on monolayers of 1 DIV MACS sorted ESC-derived myoblast monolayers. Once both the MN and muscle lineages were combined *in vitro*, the media was changed to a 50:50 mix of ADFNK and Myoblast media (see Chapter 2.1.3). A summary of the co-culture protocol used is presented in figure 5.1 below.

Spontaneous contractile activity was observed in these cultures as early as 3 DIV, similar to cultures of pure ESC-derived muscle (see Fig. 4.17 + 4.18). As with pure ESC-derived muscle cultures, this activity was sporadic in nature, and there was much variation in activity observed between cells within the same culture. Extensive myoblast fusion to form multinucleated myotubes was observed by 3 DIV, with fewer mononuclear myoblasts remaining than seen in myoblast only cultures. The EBs attached to the surface of the myoblast monolayer 24 hours after plating, and small round cells could be seen spreading away from each central cluster by 2 DIV (Fig. 5.2). Long, thin processes were observed extending out from each EB and growing through the surrounding cells, indicative of neurite growth into the muscle tissue, as can be seen in figure 5.2 below.

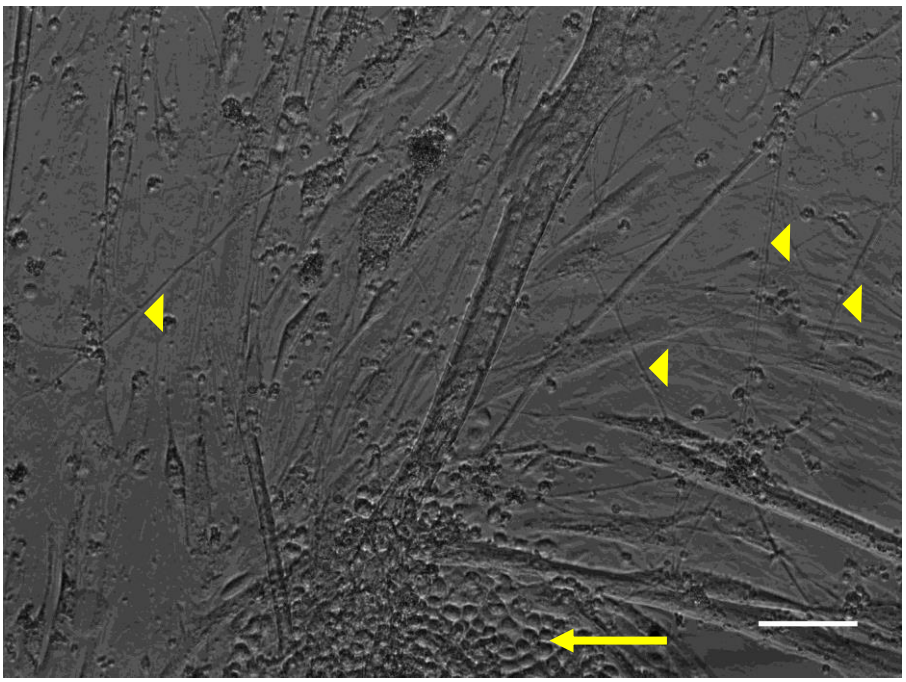

Figure 5.2 Embryoid bodies containing ESC-derived MNs extend neurites in co-culture with ESC-derived skeletal muscle. A representative bright-field image of an EB/ESC-muscle co-culture at 4 DIV. Notice the small, round cells spreading out from the EB at the bottom of the image (yellow arrow), and the multiple neurites visible extending out from the EB (yellow arrow heads). Scale bar = 100μm.

Frame-by-frame analysis of time-lapse movies of these spontaneous contractions after 4 DIV using the same method as detailed previously (Fig. 4.16) reveals a similar pattern of activity to that seen in cultures of pure ESC-derived muscle (Fig. 5.3). The maximum strength of the contractions was similar to that seen in pure cultures, with a maximum displacement in day 4 co-cultures measured at 16.4μm (Fig. 5.3 c), compared to 17.5μm in pure muscle cultures (Fig. 4.17 a). The average displacement measured was lower in the co-cultures, mainly due to more frequent but lower strength contractions seen in this culture condition (see Fig. 5.3 b), with an average displacement of 6.3μm ± 0.1 in co-cultures compared to 14.1μm ± 0.5 in pure iMyoD C4 monolayers. Extended periods of above-baseline displacement suggest a significant degree of tension on most myotubes imaged. All myotubes imaged that were situated near an EB showed some degree of activity, whereas less contraction was observed further away from the EBs within the same culture. Whereas most myotubes imaged displayed infrequent but relatively strong contractions, some myotubes displayed consistent, weak contractions, as shown in figure 5.3 b. These frequent, weak contractions more closely resemble those seen in individual myoblasts (Fig. 4.18), and produce only a marginally stronger ($p < 0.0001$; ***) displacement of 5μm ± 0.1 compared to 3.4μm ± 0.04 seen in myoblasts.

5.2.2 Light evoked contractions in EB/muscle co-culture

Due to the co-culture containing MNs positive for the ChR2-YFP transgene, it was possible to directly excite the ESC-derived MNs via blue light exposure while not directly stimulating the muscle populations. Figure 5.4 shows analysis of representative time-lapse movies where a blue-light stimulus was used to stimulate the MNs via ChR2. As can be seen from these movies, blue light stimulation resulted in an immediate strong contraction in myotubes near EBs (Fig. 5.4). In movies where 2 blue light stimuli were presented, 2 contractions are recorded in nearby muscle tissue (Fig. 5.4 b+c). Recovery to baseline after light-evoked contractions was not immediate upon removal of the stimulus, and in one case a high level of displacement was maintained for the duration of the movie (Fig. 5.4 b).

(a)

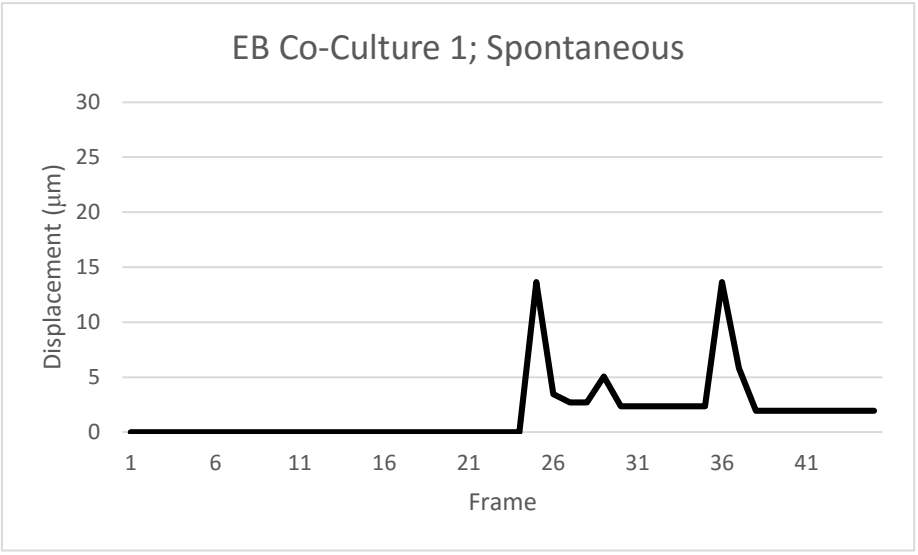

(b)

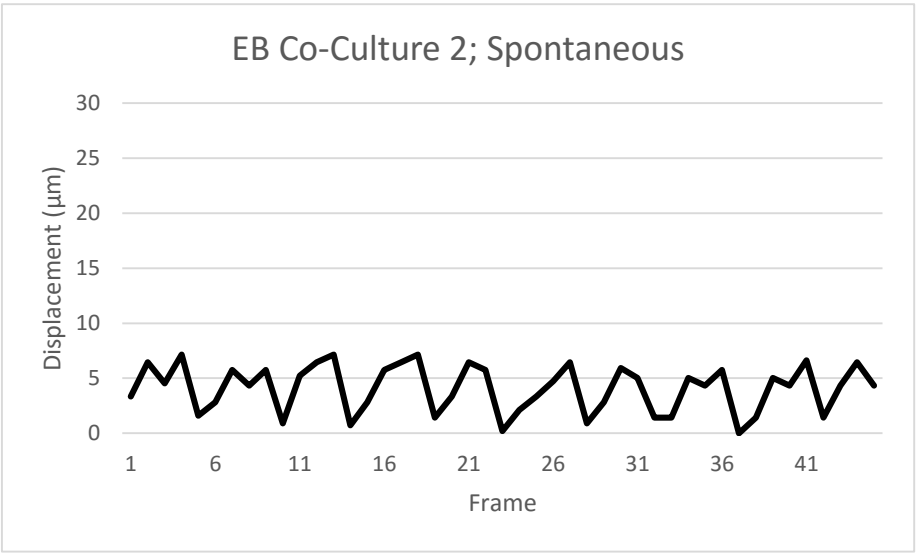

(c)

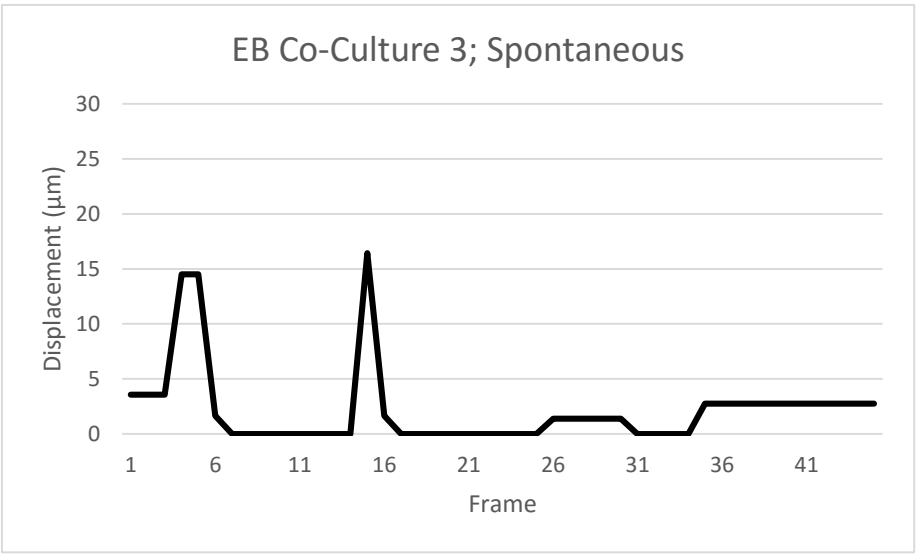

Figure 5.3 iMyoD C4 monolayers co-cultured with ESC-derived EBs show spontaneous contractions after 4 days *in vitro*. Five time-lapse movies recorded on an optical microscope were analysed frame-by-frame as summarised in figure 4.16. Shown here is analysis of three representative movies showing clear contractile events **(a, b + c)**. Note the consistent contractions seen in **(b)** compared to the stronger, but less frequent activity in **(a)** and **(c)**.

(a)

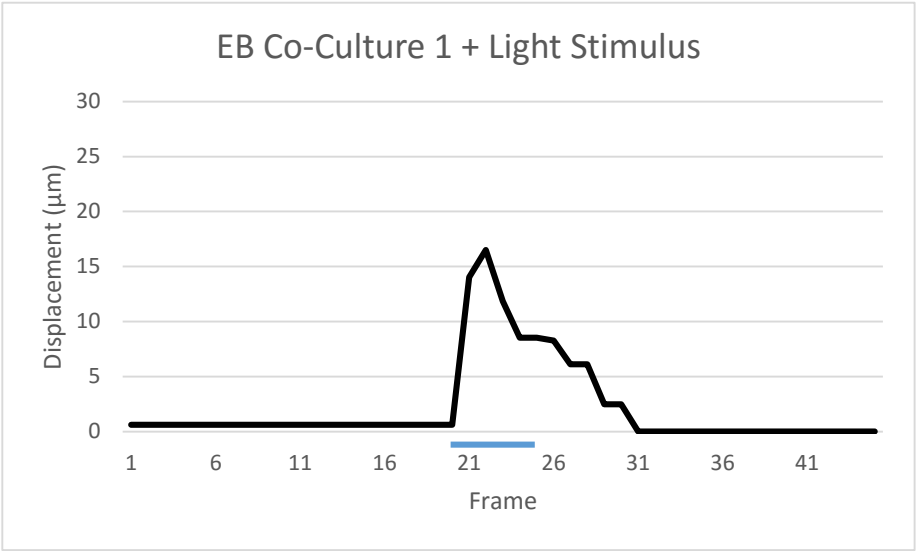

(b)

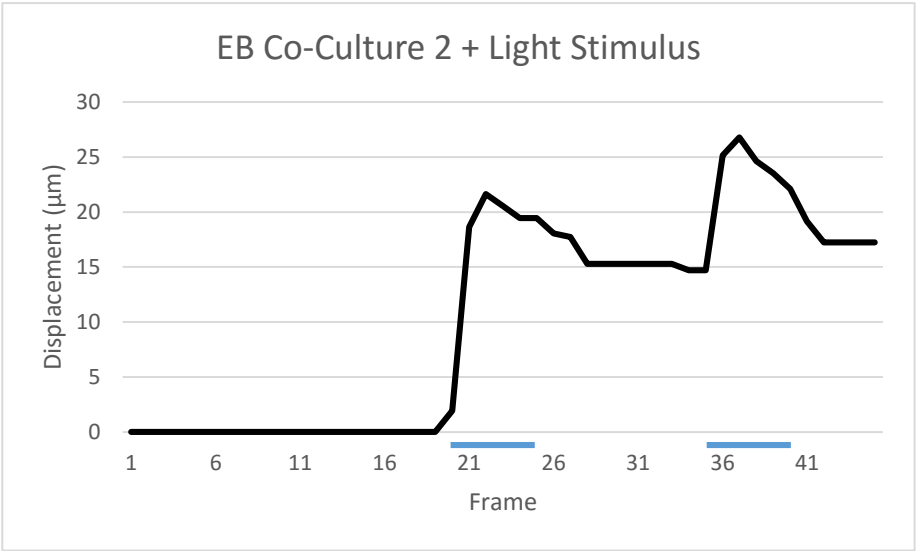

(c)

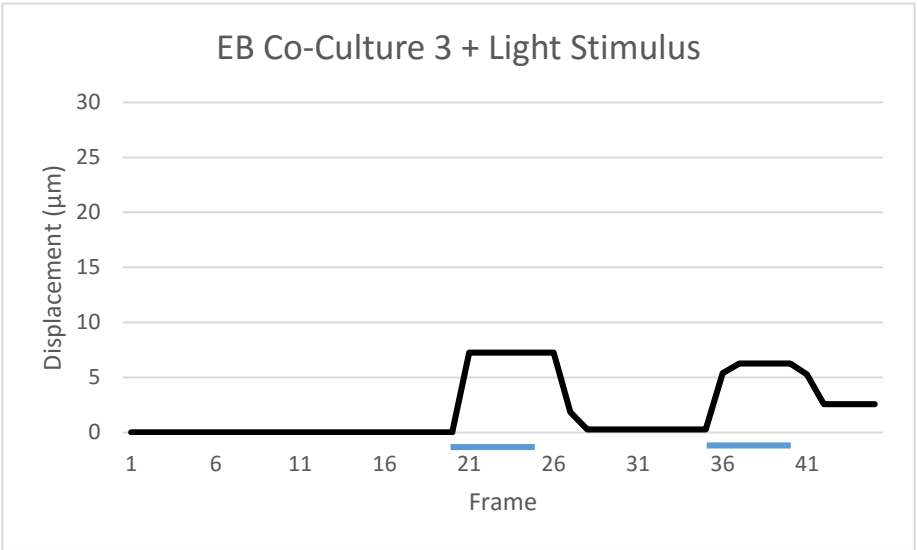

Figure 5.4 iMyoD C4 muscle co-cultured with EBs contract in response to blue-light stimulation. Frame-by-frame analysis of time-lapse movies of 4 DIV co-cultures showing clear contractile events in response to a blue-light stimulus **(a, b + c)**. One stimulus is applied in **(a)**, while two separate stimuli are presented in **(b)** and **(c)**. The blue light stimulus was presented manually at frame 20 and frame 35, indicated by blue bars under the graph.

Time lapse movies of day 12 ESC-muscle/EB co-cultures were also recorded with and without blue-light stimuli as shown in figures 5.5 and 5.6 below. While the overall viability of these cultures was severely reduced at this time-point, a clear contractile response was still observed upon presentation of the light stimuli in most cases (Fig. 5.5). The contractions produced in response to the light stimulus were weaker in day 12 cultures than contractions observed in day 4 cultures, with an average displacement of 7.75μm ± 0.39 at day 12 compared to 15.69μm ± 1.6 at day 4. In one example, no obvious stimulus-evoked response was observed, with a low-level constant contractile activity being present throughout the time-lapse (Fig. 5.5 c). This spontaneous activity had a similar amplitude as the one seen in single contractile myoblasts and spontaneous contractions of day 4 Myog::CD14 myoblast-derived monolayers, with an average displacement of 2.85μm ± 0.04. In one case multiple smaller contractile events were observed within one light-stimulus, with an additional contraction occurring after termination of the stimulus (Fig. 5.5 b).

Comparison of the activity of the same 12 DIV myotubes in co-culture with EBs during recordings where no light stimulus was presented show very little spontaneous activity, and no clear contractile episodes as seen upon light stimulation (Fig. 5.6). Some low amplitude spontaneous activity was seen in "Myotube 3", similar to the activity observed for this cell during light presentation (Fig. 5.6 c). The activity of MyoG C4 muscle cultured for 12 days without EBs was also analysed with and without light stimulation, to control for unexpected effects of the light stimulus. Examples of myotubes with both high and low level spontaneous activity were observed, however no response to a blue light stimulus was seen in any culture not containing EBs (Fig. 5.7). The average displacement produced by light-evoked and spontaneous contractions in co-cultures at both 4 DIV and 12 DIV are shown in figure 5.8. Contractions caused by blue-light stimulation of the cultures were significantly stronger than the spontaneous activity at both time points. The contractions recorded from day 12 co-cultures were weaker in both stimulated and non-stimulated recordings

(a)

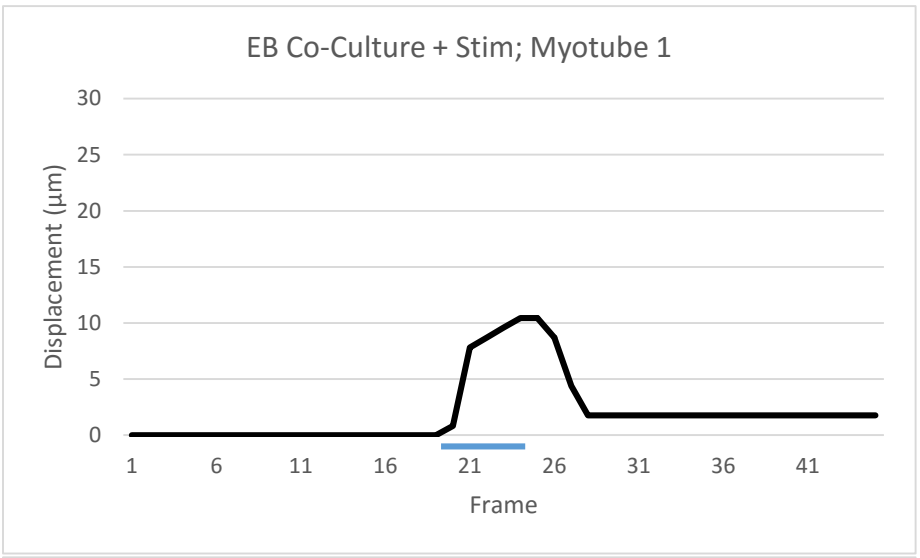

(b)

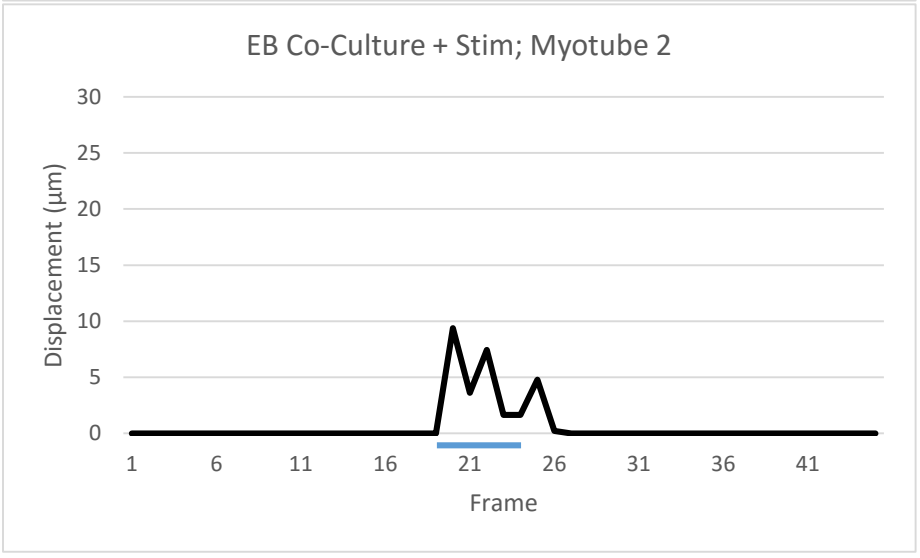

(c)

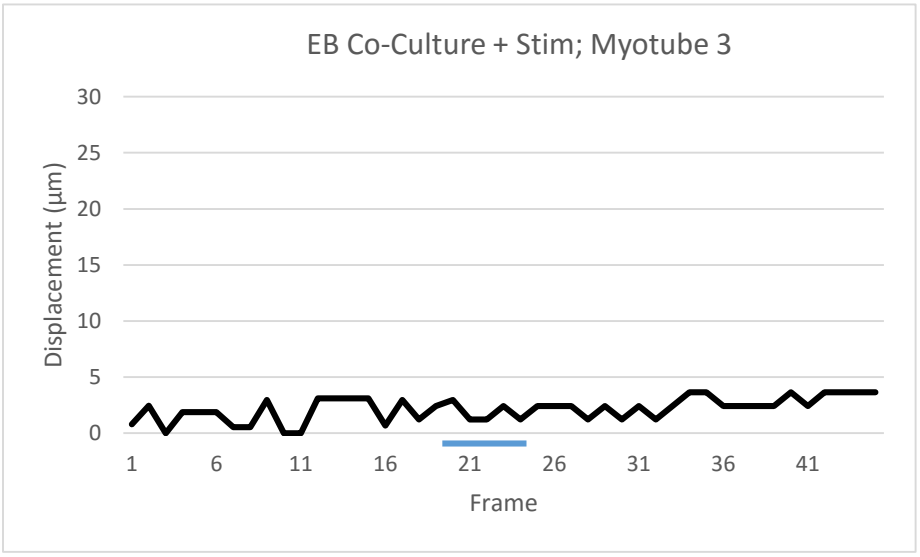

Figure 5.5 Day 12 iMyoD C4 muscle/EB co-cultures show light-evoked contractions. Frame-by-frame analysis of time-lapse movies of 12 DIV co-cultures showing clear contractile events in response to a blue-light stimulus **(a, b + c)**. While much spontaneous activity was observed in **(c),** no contractile response was observed in in response to light stimulation**.** The blue light stimulus was presented manually at frame 20, indicated by blue bars under the graph.

(a)

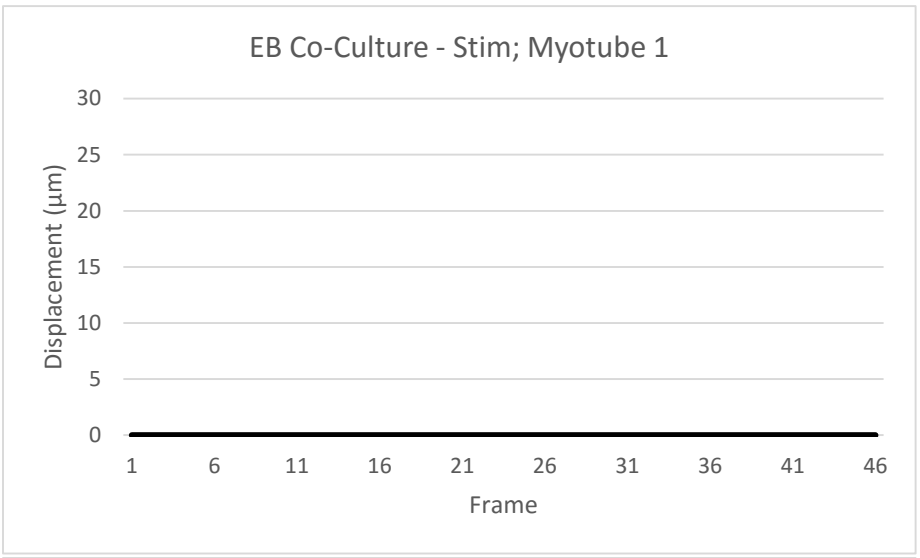

(b)

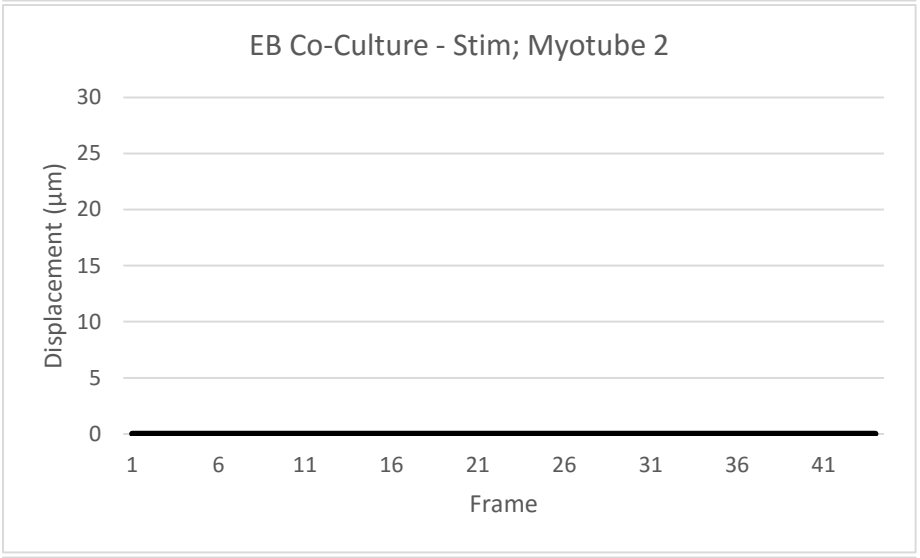

(c)

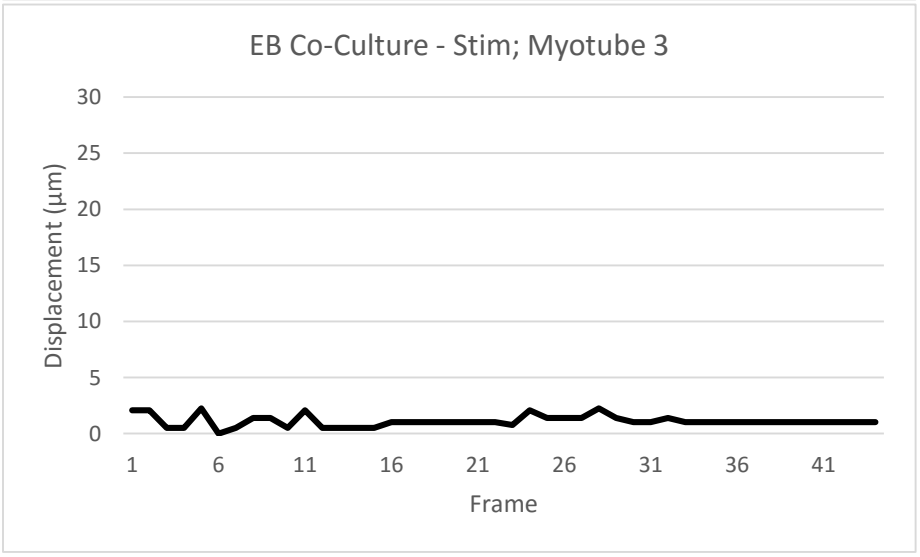

Figure 5.6 iMyoD C4 muscle co-cultured with EBs show little activity in the absence of a blue-light stimulus. Frame-by-frame analysis of time-lapse movies of 12 DIV co-cultures showing few if any contractile events when no blue-light stimulus is presented **(a, b + c)**. Some spontaneous activity is seen in **(c)**, similar to the level of activity seen in this culture in figure 5.4.

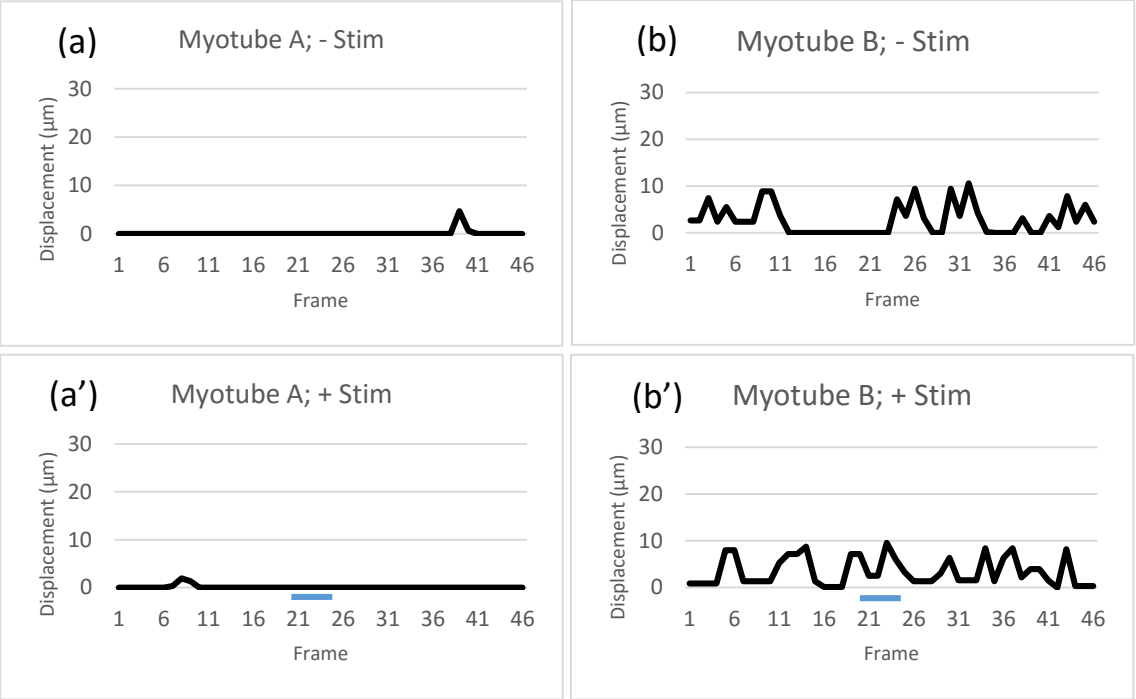

Figure 5.7 Pure iMyoD C4 muscle cultures show no response to blue-light stimulation. (a + b) Frame-by-frame analysis of time-lapse movies of 12 DIV cultures of iMyoD C4. While some spontaneous activity was observed, no contractile events were seen in response to a blue-light stimulus **(a' + b')**. The blue light stimulus was presented manually at frame 20, indicated by blue bars under the graphs (a' + b').

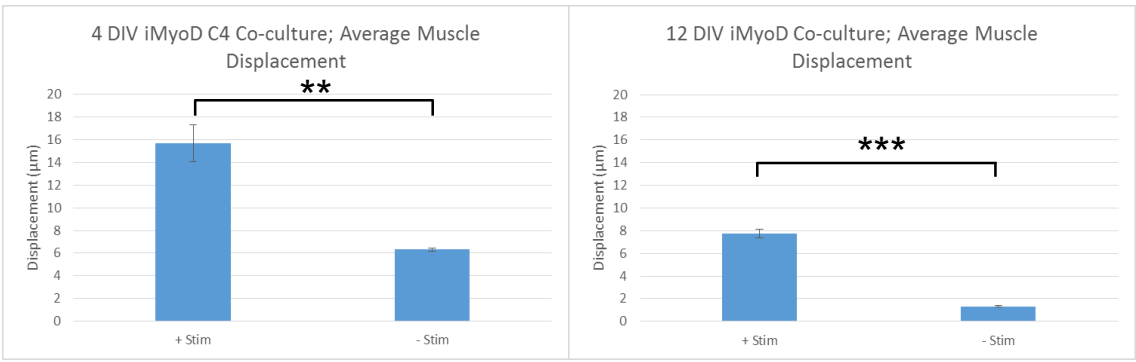

Figure 5.8 Average muscle displacement is much higher in iMyoD C4 muscle/EB co-cultures upon presentation with a blue-light stimulus. Average displacement calculated from frame-by-frame analysis of time-lapse movies of 4 (n= 3 and 5 for +/- stim respectively) and 12 DIV (n= 4 and 4 for +/- stim respectively) co-cultures. At both time points, light stimulation caused a greater muscle contraction than seen from spontaneous activity. Error bars show S.E.M. Mann Whitney U Test, * = p <0.05, ** = p <0.01, *** = p <0.001.

than day 4, however the increased strength of light-evoked activity was still clear (Fig. 5.8). Tables detailing muscle contraction values are presented in Appendix A.

5.2.3 Synapse formation in EB/muscle co-cultures

To check for the presence of neuromuscular junctions in these co-cultures, immunocytochemistry was performed on day 14 using an anti-GFP antibody to label the MN axons and a fluorescently tagged α-Bungarotoxin, a snake toxin which specifically blocks the skeletal muscle nicotinic acetylcholine receptor, to label post-synaptic nicotinic acetylcholine receptors (Samson and Levitt, 2008). As can be seen in figure 5.8, extensive growth of GFP positive neurites was seen throughout the cultures. GFP positive MN cell bodies tended to remain clustered with each other, while the neurites exited the MN clusters and invaded the surrounding muscle tissue (Fig. 5.9). Fusion of myoblasts was evident from the staining for DNA, revealing multiple nuclei within many α-Bungarotoxin positive cells (Fig. 5.9 b'). Many nuclei were observed that were not associated with either α-Bungarotoxin staining or GFP, identifying them as contaminating cells, possibly derived from the unsorted EBs.

While a background level of α-Bungarotoxin staining was present along the entire surface of most myocytes, bright patches of more specific staining were observed on some cells (Fig. 5.9 a', b' + c'). These concentrated patches were often closely opposed to GFP positive neurites (presumably axons), and indeed in some cases GFP positive processes were observed wrapping around α-Bungarotoxin positive myocytes. While the characteristic "pretzel" shaped neuromuscular junction morphology was not observed in these cultures, the close apposition of GFP positive MN axons with concentrated regions of α-Bungarotoxin positive membrane suggests the presence of simple, immature synapses between these ESC-derived populations.

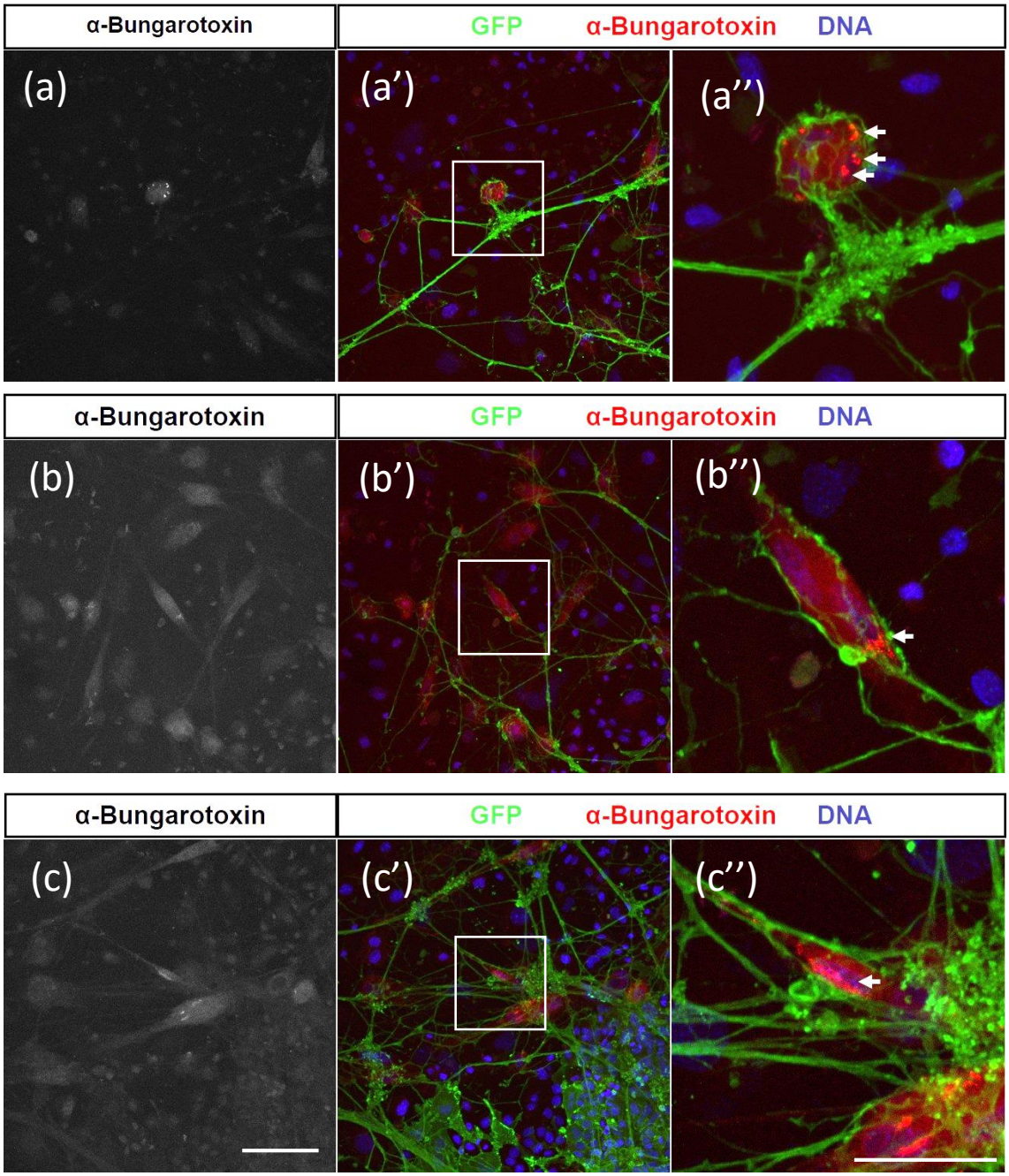

Figure 5.9 iMyoD C4 muscle/EB co-cultures have α-Bungarotoxin positive puncta closely opposed to GFP positive MN neurites, suggestive of neuromuscular synapses. Immunostaining of 14 DIV iMyoD C4 muscle/EB co-cultures labelled with α-Bungarotoxin (red), anti-GFP (green) and topro-3 (blue). **(a, b + c)** Bungarotoxin staining reveals labelled puncta on fused myoblasts. Evidence of myocyte fusion to form multinucleated fibres is clear **(b'')**, as well as development of NMJs, with close apposition of GFP positive neurites to α-Bungarotoxin positive puncta on myocutes **(a', b' + c')**. Images **(a'', b'' + c'')** show the white box in **(a', b' + c')** enlarged. White arrows indicate possible synapses on myocutes. Scale bars: a+a'-c+c'= 100 μm; a''-c''= 50 μm.

5.3 Primary Chick Skeletal Muscle/Embryoid Body Co-Culture

5.3.1 Early growth and morphology of CPM/EB co-cultures

As mentioned previously, long-term *in vitro* culture of iMyoD C4 derived myotubes proved problematic, despite testing multiple culture conditions, substrates and media (see Chapter 4). Although iMyoD C4 cultures showed contractile responses to light-stimulation after 12 days, and basic synapses between ESC-derived MNs and muscle were observed in 2 week old cultures, the viability of these preparations was clearly limited, with weaker contractile activity than that seen in 4 DIV cultures, and fewer living myotubes remaining attached than after 4 days *in vitro*.

Therefore, to provide a more stable post-synaptic target for ESC-derived MNs, allowing the development of more mature neuromuscular circuits, chick primary skeletal muscle (CPM) was used in co-culture with ESC-derived MNs. Initial experiments used unsorted embryoid bodies (EBs), as used in the previous experiments with ESC-derived muscle, due to the spontaneous activity of this mixed neuronal population, and positive results using these cells in the aforementioned cultures.

Primary muscle co-cultures were prepared in a similar way to the ESC-derived muscle co-cultures described in figure 5.1, with the muscle plated on matrigel-coated glass coverslips 1 day prior to seeding with EBs containing MNs carrying both the Hb9::GFP-IRES-CD14 and CAG::ChR2-YFP transgenes, as well as a ubiquitously expressed GDNF transgene to promote survival (Bryson et al., 2014). Observation of these cultures revealed spontaneous contractile activity as early as 3 DIV, as seen in pure muscle cultures previously (see figure 4.17). Using an epifluorescent light microscope allowed visualisation of the GFP and YFP positive MNs, and extensive neurite extension into the surrounding muscle tissue was seen by 7 DIV (Fig. 5.10). Also over this time frame, myoblast fusion to form multinucleated myofibres was observed, with long, partially aligned myofibres seen in all cultures by 7 DIV (Fig. 5.10).

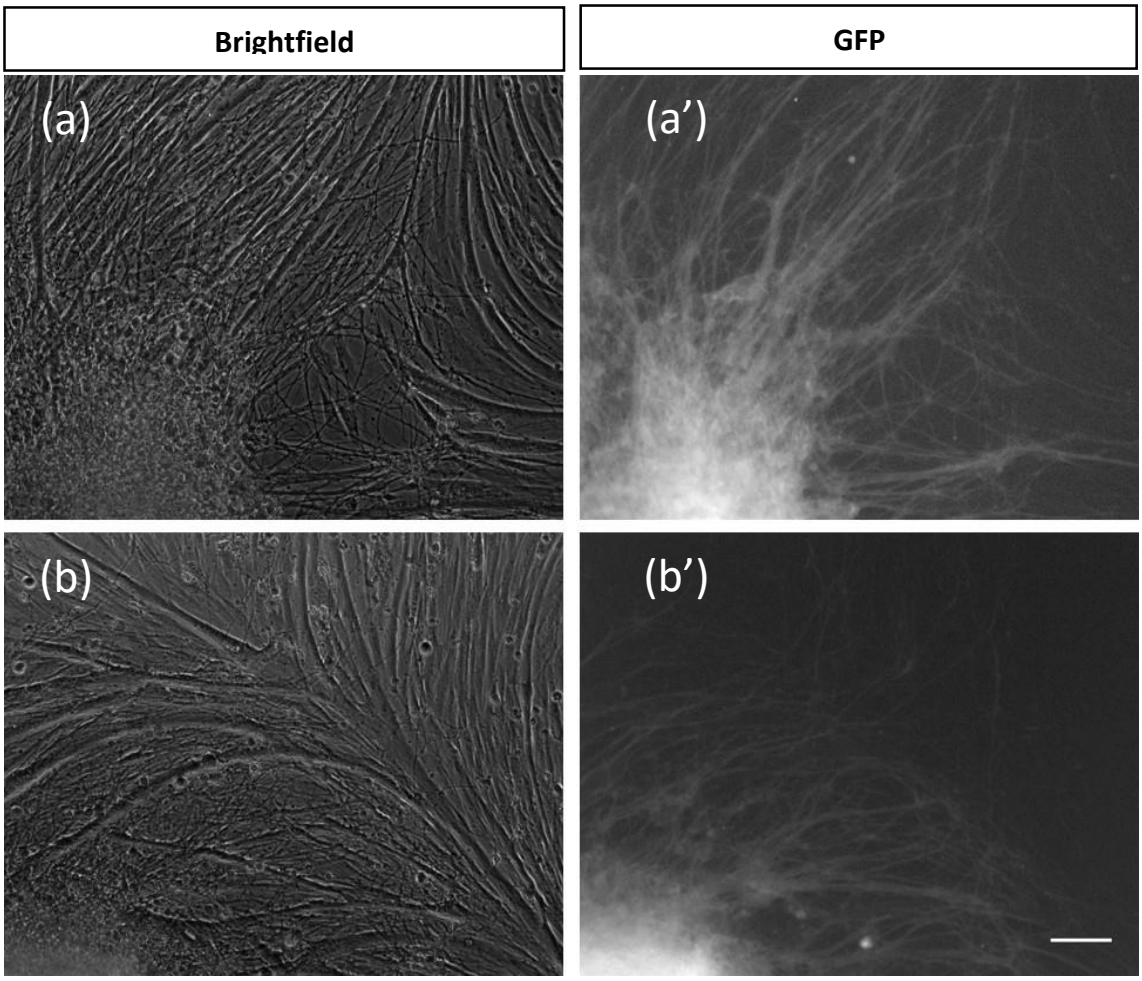

Figure 5.10 Motor neurons in embryoid bodies extend long neurites, innervating surrounding chick primary skeletal myofibres. Live brightfield (left) and epifluorescent (right) images of 7 DIV chick skeletal muscle/EB co-cultures. Note the fusion of chick myoblasts to form long, multinucleated myofibres (a + b), and the growth of GFP/YFP positive MN neurites, presumably axons, throughout the surrounding tissue (a' + b'). Scale bar = 100μm.

5.3.2 Contractile activity of CPM/EB co-cultures

Time lapse movies of CPM/EB co-cultures and controls were also recorded throughout long-term *in vitro* culture, with and without blue-light stimuli, as performed previously with ESC-derived muscle. Due to the improved survival of the primary muscle when compared to ESC-derived muscle, these cultures were viable *in vitro* for up to 4 weeks, allowing a longer time-course of investigation and more opportunity for circuit development and maturation.

Representative frame-by-frame analyses of co-cultures at 5 DIV are presented below in figure 5.11. As can be seen in Fig. 5.11 a, a blue-light stimulus presented at day 5 does produce a noticeable muscle contraction in the co-culture condition, with an average displacement of 23.87μm ± 1.37. The displacement caused by the stimulus was maintained for some time after the stimulus was removed, indicating prolonged tension in the muscle after direct stimulation of the MNs via ChR2 ceased. Very little spontaneous activity was observed at this time point, as indicated by the lack of displacement measured in co-cultures in the absence of light-stimulation (Fig. 5.11 a'). CPM cultures without EBs added were also recorded to provide a negative control for the EBs, and as shown in Fig. 5.11 b and b', little to no contractile activity was seen in this condition, regardless of light stimulation.

After 12 days *in vitro*, more spontaneous activity is seen in both co-cultures and pure muscle cultures, as shown in figure 5.12. A clear light-evoked contraction is evident in the co-culture condition, with a mean displacement of 32.32μm ± 1.2 (Fig. 5.12 a). Again, contractile activity continues after the removal of the light stimulus, and even reaches a larger displacement than during the stimulus period in this example. The spontaneous activity seen in the co-cultures was varied, but often achieved the same amplitude of displacement as seen during stimulation. Spontaneous contractions were seen in CPM control cultures without EBs, however this was very variable, with examples shown of low and high spontaneous activity (Fig. 5.12 b + c). No response to the blue-light stimulus was observed in any pure muscle control culture.

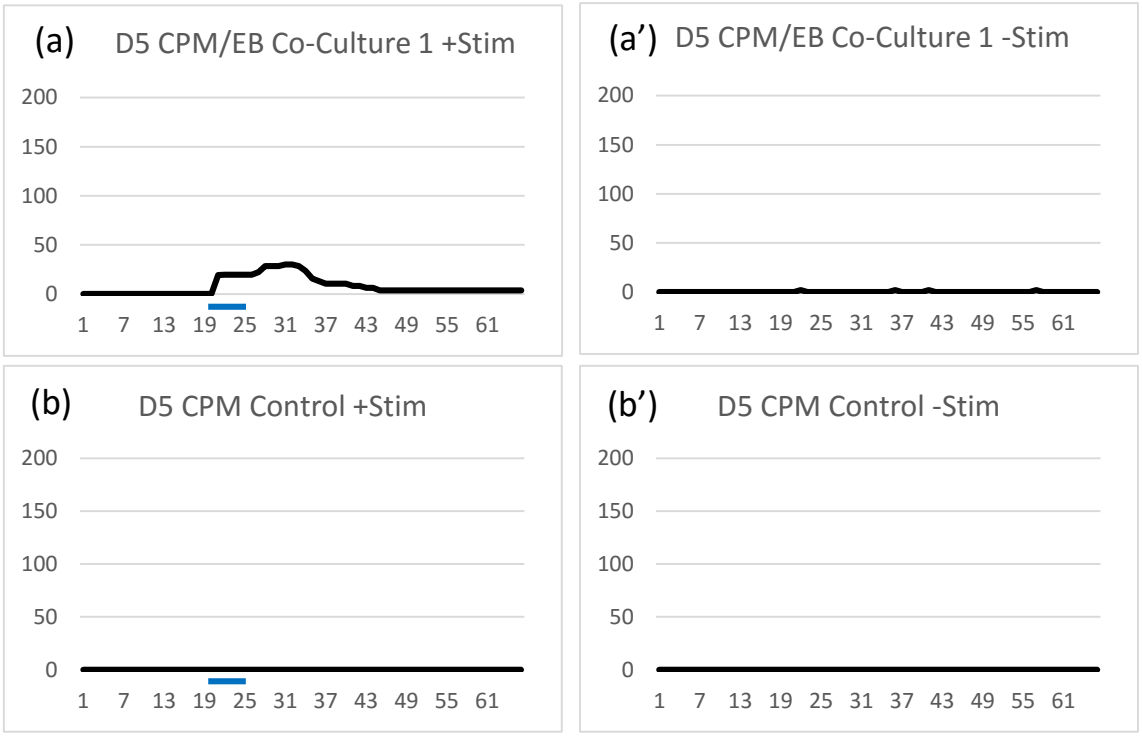

Figure 5.11 Light-evoked responses in CPM muscle co-cultured with EBs at 5 DIV. Frame-by-frame analysis of time-lapse movies of 5 DIV CPM/EB co-cultures and controls. **(a + b)** A clear contractile event in response to a blue light stimulus seen in the co-culture is not observed in the CPM only control. **(a' + b')** Very little contractile activity was observed in co-cultures or controls in the absence of a light stimulus.

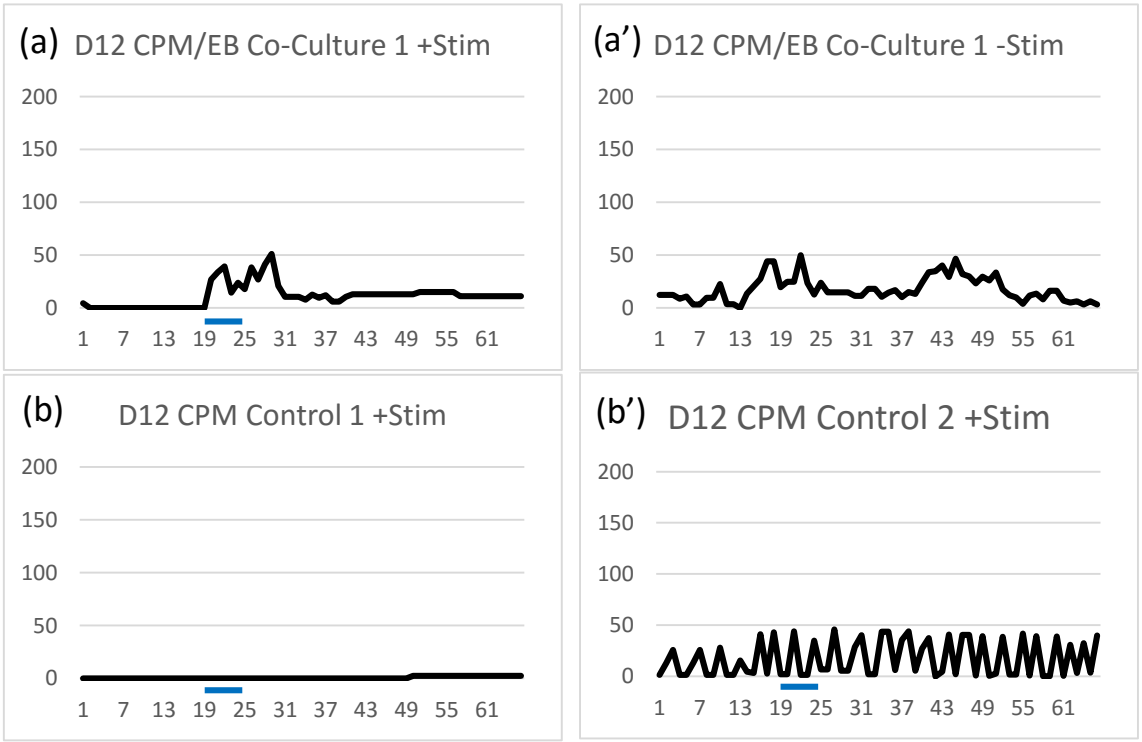

Figure 5.12 Light-evoked and spontaneous activity in co-cultures and controls at 12 DIV. Frame-by-frame analysis of time-lapse movies of 12 DIV CPM/EB co-cultures and controls. **(a + b)** A clear contractile event in response to a blue light stimulus seen in the co-culture is not observed in the CPM only control. **(a' + b')** Spontaneous activity was seen in co-cultures and controls at this time point.

Muscle contractions caused by light stimulation in co-cultures at day 20 were generally very strong, causing a clearly visible displacement as seen in figure 5.13 a and a'. In this example, a number of muscle fibres aligned between two close EBs, and light stimulation caused a strong contraction, bringing the EBs closer together, as indicated by the yellow and blue lines in the figure. The average displacement in stimulated cultures was 93.87μm ± 4.07. As before, no response to light stimulation was seen in pure muscle control cultures (Fig. 5.13 c). Spontaneous activity was seen in the absence of stimulation in both co-cultures and controls, however this was far weaker than light-evoked activity, and also noticeably weaker than spontaneous activity recorded in day 12 cultures (Fig. 5.13 b' and c').

Muscle activity was much lower in 26 DIV cultures, for both light-evoked responses and spontaneous activity (Fig. 5.14). Blue light stimulation did cause a muscle contraction; however this was weaker than contractions seen in 20 DIV cultures, with an average displacement of 32.92μm ± 1.36. Very little spontaneous activity was seen in the absence of a stimulus, either in co-cultures or muscle only controls.

The mean displacements caused by contractions in co-cultures are summarized in figure 5.15 below. At all time points studied, light-evoked contractions caused a greater displacement than spontaneous contractions. The greatest difference in evoked against spontaneous activity was seen at day 20, corresponding to the strongest evoked contractions. The strongest spontaneous activity was seen at day 12, with an average displacement of 28.48μm ± 0.84, not significantly lower than the average light-evoked contraction at this time point, of 32.32μm ± 1.72. A summary of the activity of these cultures is presented in figure 5.16, showing representative responses to blue-light stimulation and spontaneous activity in co-cultures and controls throughout the time course investigated. Tables detailing muscle contraction values are presented in Appendix A.

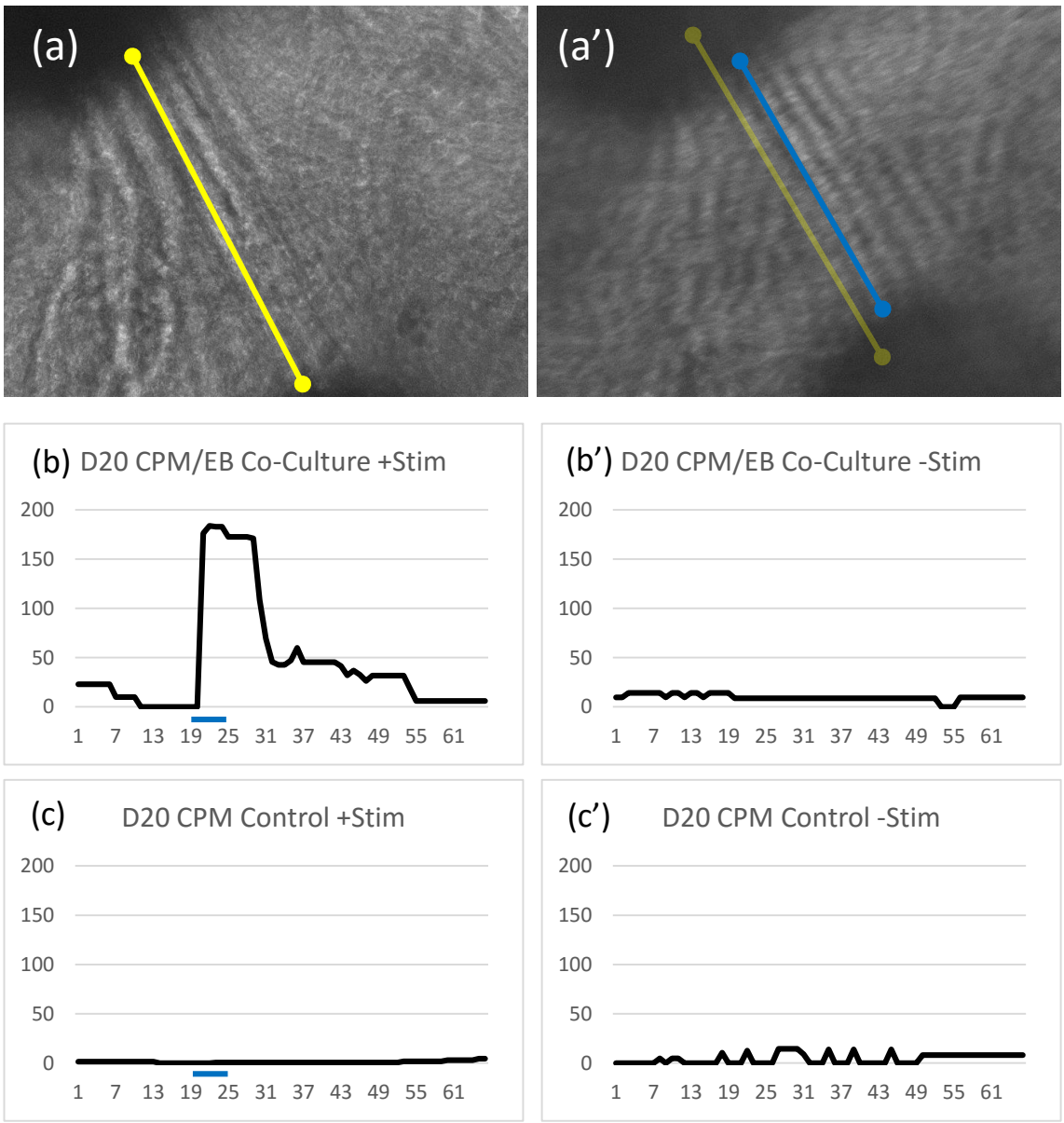

Figure 5.13 Light-evoked and spontaneous acitivity in co-cultures and controls at 20 DIV. Frame-by-frame analysis of time-lapse movies of 20 DIV CPM/EB co-cultures and controls. **(a + a')** Representative consecutive frames from a time-lapse movie of a 20 DIV co-culture, before and after a blue-light stimulus. Comparison of the distance markers from before the light stimulus (yellow line) and after (blue line) clearly show the displacement caused by the contraction. **(b + c)** A strong contractile event in response to a blue light stimulus seen in the co-culture is not observed in the CPM only control. **(b' + c')** Spontaneous activity was seen in both co-cultures and controls, however was much weaker than evoked activity, or spontaneous activity at 12 DIV.

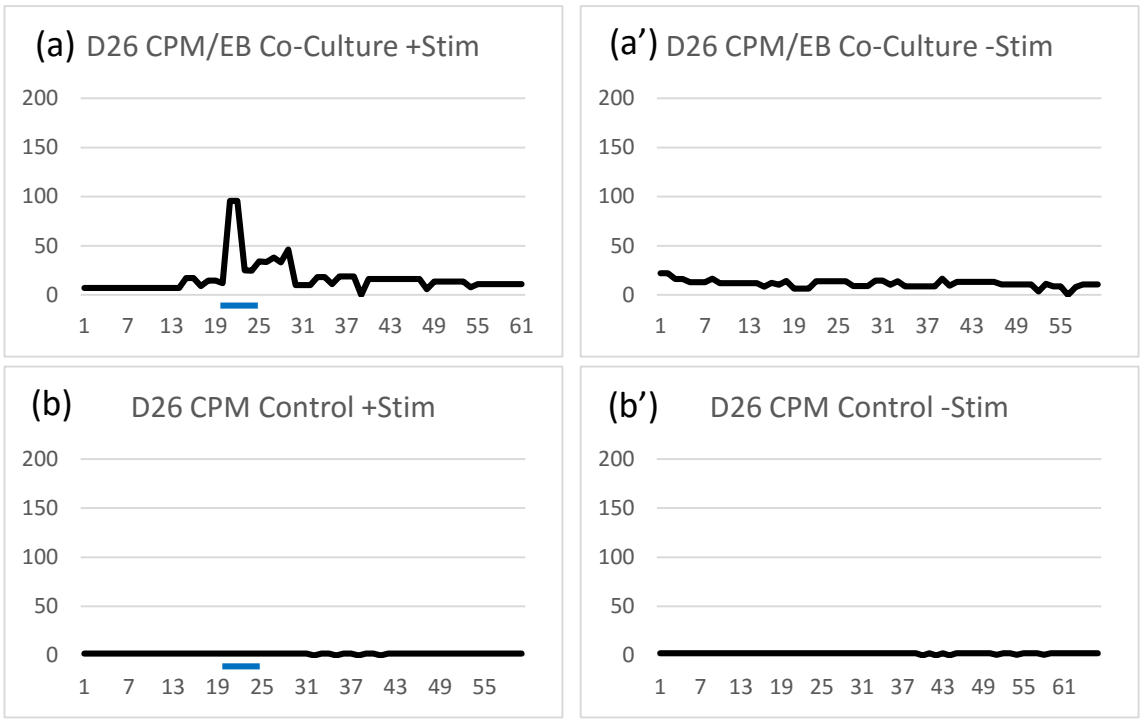

Figure 5.14 Light-evoked and spontaneous acitivity in co-cultures and controls at 26 DIV. Frame-by-frame analysis of time-lapse movies of 26 DIV CPM/EB co-cultures and controls. **(a + b)** Stimulus-evoked contractile acitivity seen in the co-culture is not observed in the CPM only control. **(a' + b')** Spontaneous activity was seen in both co-cultures and controls, however was much weaker than light-evoked activity, or spontaneous activity recorded at earlier time points.

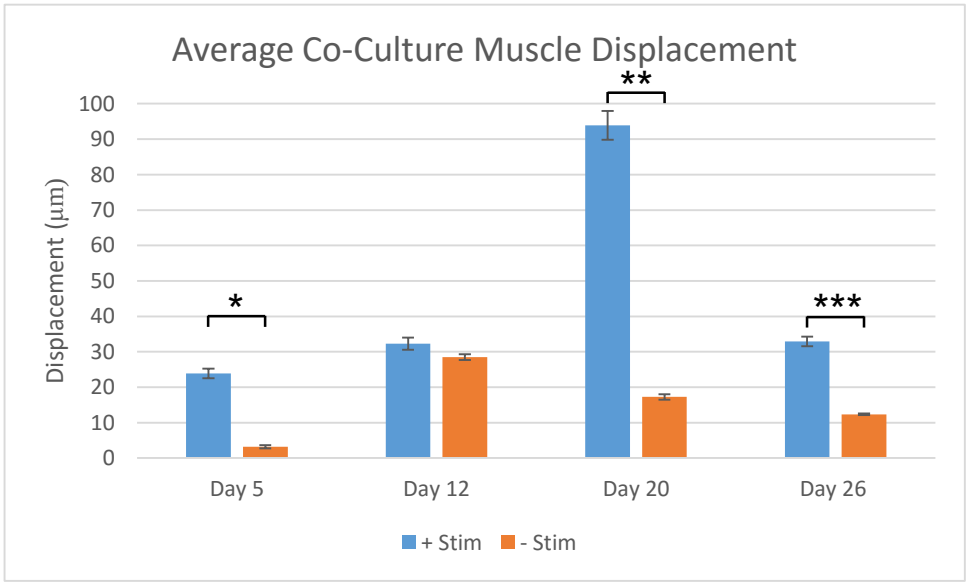

Figure 5.15 Average muscle displacement recorded in CPM/EB co-cultures, with or without blue-light stimulus. Averages include all contractile events, including spontaneous activity recorded in light-stimulated movies independent of the stimulus. n= 2 for Day 5 +/- stim, n= 2 for Day 12 +/- stim, n= 4 for Day 20 +/- stim and n= 2 and 3 for Day 20 -/+ stim respectively. Error bars show the S.E.M. Mann Whitney U Test, * = p <0.05, ** = p <0.01, *** = p <0.001.

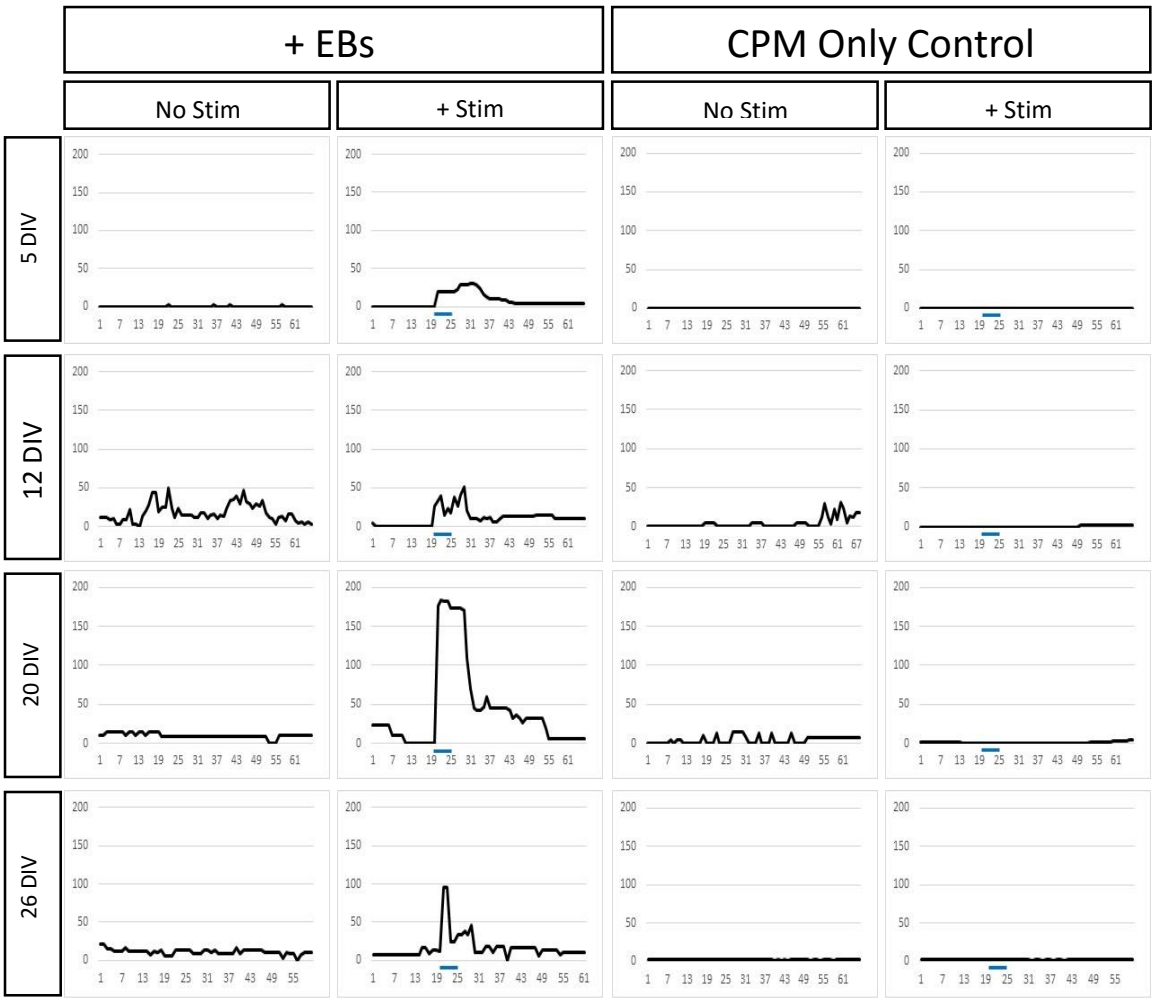

Figure 5.16 A representative summary of contractile acitivity in CPM/EB co-cultures and controls at all time points recorded, with and without blue-light stimulus. A blue-light stimulus induced contractile activity in co-cultures at all time points, while no response to light was seen in CPM only controls at any stage.

5.3.3 Neuromuscular junctions in CPM/EB co-cultures

Due to the clear light-evoked activity in the CPM, 14 DIV CPM/EB co-cultures was investigated for the presence of NMJs by immunocytochemistry, as done previously on iMyoD C4 muscle co-cultures (Fig. 5.8). Initial labelling was performed with α-Bungarotoxin to stain nicotinic acetylcholine receptors (nAChRs), highlighting the post-synaptic side of any NMJs, and a phalloidin toxin tagged with a fluorescent dye, to reveal the ultrastructure of the cytoskeleton. As can be seen in figure 5.17, clusters of bungarotoxin positive puncta were observed on some muscle fibres in the co-cultured samples. Some clusters resembled the characteristic "pretzel" shape of NMJs seen *in vivo*. No bungarotoxin puncta were observed in pure CPM cultures however, suggesting the requirement of MNs to induce and/or maintain these structures (Fig. 5.18).

Phalloidin labelling revealed clear striations in the muscle fibres, clearly visible in figure 5.17 a, typical of mature striated skeletal muscle. These striations were visible in pure CPM cultures and co-cultures with EBs, as seen in figures 5.17 and 5.18. Striations were even visible using standard brightfield microscopy as shown in figure 5.18 a''.

Immunostaining using an antibody against a fast skeletal muscle specific myosin heavy chain (My32) resulted in specific labelling of the CPM fibres, and again revealed clear striations showing the presence of mature sarcomeres (Fig. 5.19). Again, complex bungarotoxin positive clusters were seen on co-cultured muscle fibres, but were absent from pure muscle control cultures (Fig. 5.19). Individual nuclei are also visible in these images of both co-cultured and pure CPM as dim ovoids against the labelled myosin heavy chain sarcomeric structure, revealing the multinucleated state of these fibres, characteristic of mature skeletal muscle formed via myoblast fusion (Fig. 5.19).

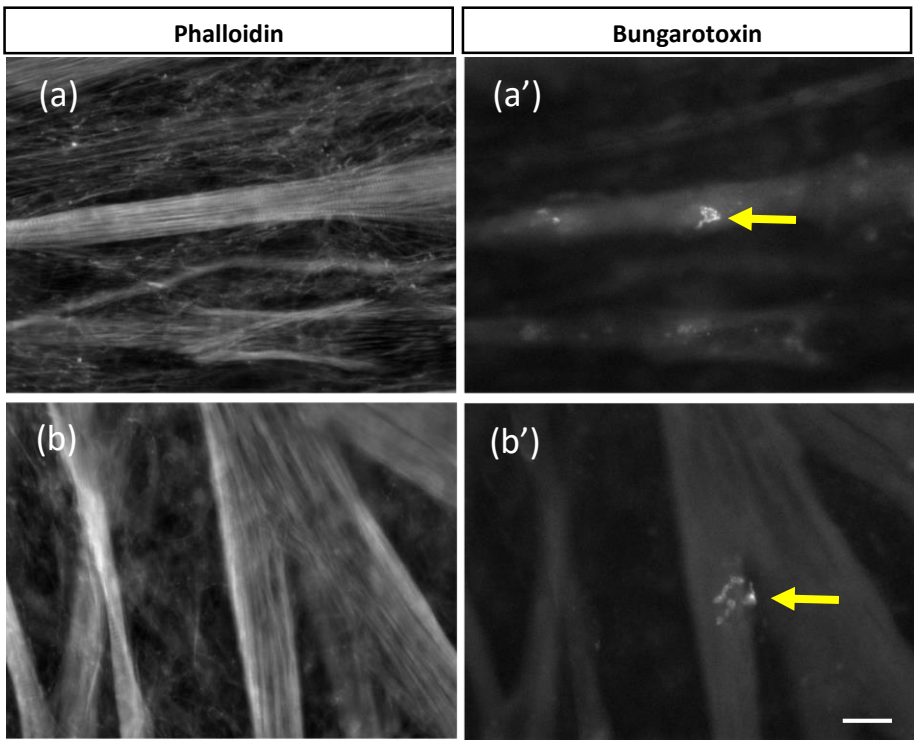

Figure 5.17 Chick muscle in 14 DIV CPM/EB co-cultures have clusters of bungarotoxin-labelled puncta resembling NMJ endplates. Immunocytochemistry using phalloidin **(a + b)** and α-bungarotoxin **(a' + b')** on 14 DIV CPM/EB co-cultures. Note the clustering of bungarotoxin puncta on muscle fibres resembling "pretzel" shaped NMJs (yellow arrows). Scale bar = 100μm.

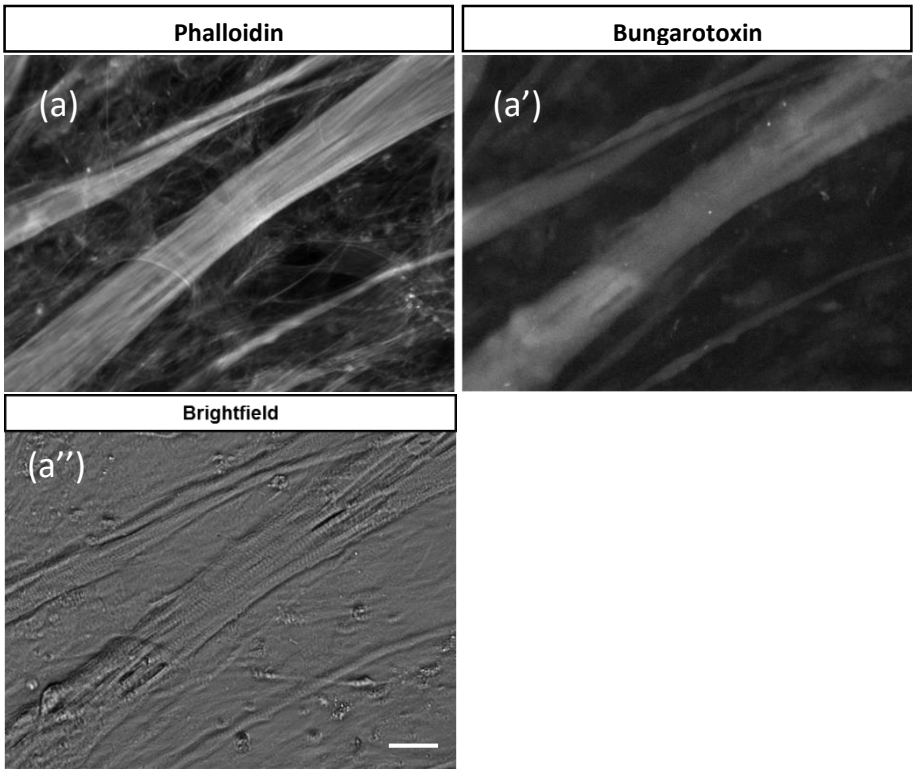

Figure 5.18 CPM control cultures have an absence of α-bungarotoxin puncta, however cytoskeletal striations are visible in muscle fibres. Immunocytochemistry using phalloidin **(a)** and α-bungarotoxin **(a')** on 14 DIV CPM control cultures. Note the lack of specific bungarotoxin positive puncta. **(a'')** A brightfield image of these fibres, showing visible striations. Scale bar = 100μm.

Immunostaining using antibodies against synaptophysin and choline actetyltransferase (ChAT), markers of pre-synaptic components of the NMJ, did reveal specific staining in co-cultured samples as shown in figures 5.20 and 5.21. While no large pretzel shaped bungarotoxin labelled clusters were seen in these examples, synaptophysin staining did appear clustered around the bungarotoxin puncta (Fig. 5.20). Immunostaining for ChAT was weaker than for synaptophysin, but MN axons are clearly labelled, and specific staining is seen near bungarotoxin puncta on the muscle fibres (Fig. 5.21). No specific staining for either synaptophysin or bungarotoxin was observed in pure CPM control cultures (Fig. 5.20 + 5.21).

Immunostaining was carried out at various time points throughout the long-term culture to investigate the developmental timeframe of NMJ development and maturation. At 7 DIV, extensive outgrowth of MN axons/dendrites was observed, as seen in figure 5.22. Multiple bungarotoxin positive puncta were visible after 1 week in culture, both on muscle fibres that were co-cultured with EBs and myofibres in pure muscle controls (Fig. 5.22). Regions of muscle fibres with less bungarotoxin staining were visible particularly in the pure muscle control samples and areas in co-cultures that were far away from EBs. While many puncta were closely associated with GFP positive processes from the MNs in the co-cultures, many puncta were also observed in isolation from GFP labelled neurites.

After 2 weeks *in vitro*, clear post-synaptic bungarotoxin positive motor end plates were visible on muscle fibres in co-cultures, as shown in figure 5.23. While some small puncta remained visible, a few large clusters had formed, some resembling the classic pretzel shape morphology seen *in vivo*. GFP positive MN processes could be seen specifically innervating these large end plates, often adopting a complex branched morphology within the region overlapping the bungarotoxin labelling (Fig. 5.23 + 5.24). GFP positive axons could be found at a greater distance from the EBs than at 7 DIV, suggesting continued growth and development of the MNs at this time point.

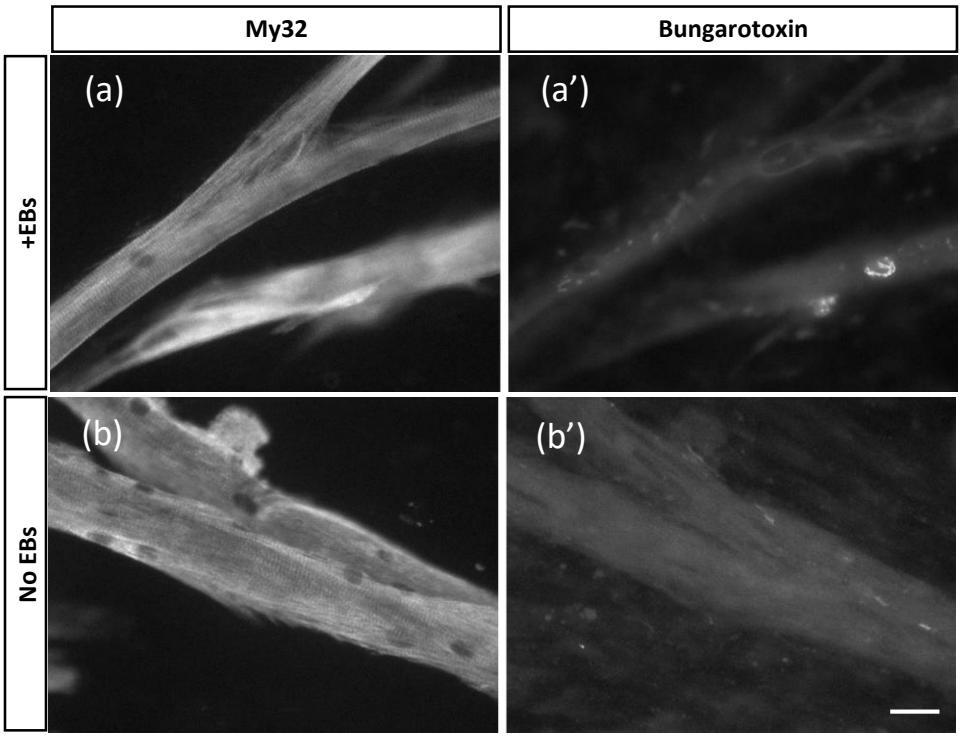

Figure 5.19 Chick primary muscle is labelled by My32, a marker of mature fast skeletal muscle. Immunocytochemistry using My32 and α-bungarotoxin on 14 DIV CPM/EB co-cultures **(a + a')** and controls **(b + b')**. Note the clear striations visible on the muscle fibres labelled with My32, revealing sarcomeric structure, and the multiple nuclei (dark ovoids) in each myotube. Also note the specific bungarotoxin labelling revealing a motor end plate in the co-culture **(a')**, not seen in the controls **(b')**. Scale bar = 100μm.

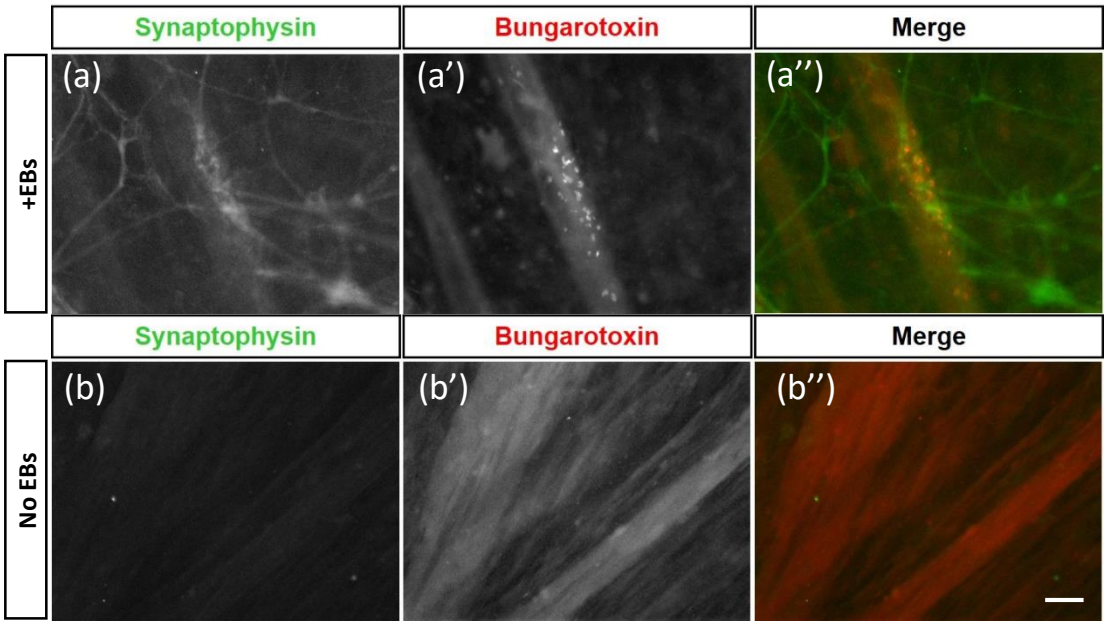

Figure 5.20 Diffuse synaptophysin labelling is seen in MN axons and co-localised with bungarotoxin puncta in 14 DIV CPM/EB co-cultures. 14 DIV CPM/EB co-cultures **(a, a' + a'')** and controls **(b, b' + b'')** labelled with synaptophysin and α-bungarotoxin. Note the co-localisation of snynaptophysin with bungarotoxin puncta in the co-cultures condition. Scale bar = 100μm.

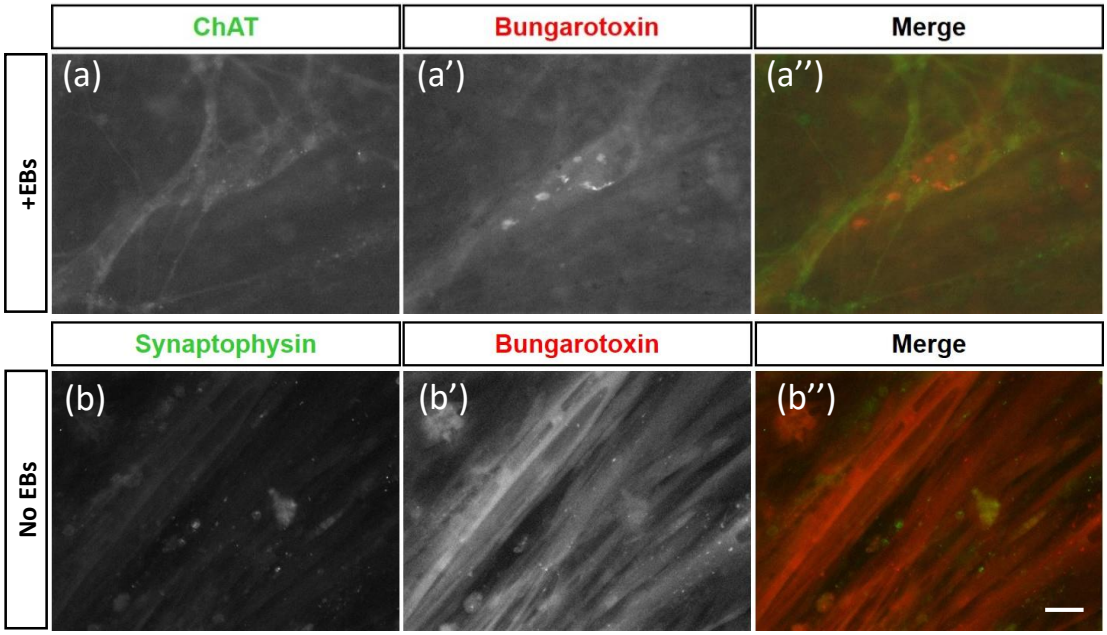

Figure 5.21 Specific choline acetyltransferase labelling seen in 14 DIV CPM/EB co-cultures is not seen in CPM only controls. 14 DIV CPM/EB co-cultures **(a, a' + a'')** and controls **(b, b' + b'')** labelled with ChAT and α-bungarotoxin. Note the lack of specific ChAT labelling in the control culture. Scale bar = 100μm.

In multiple cases single MN axons could be seen innervating multiple end plates (the post-synaptic structure where MN axons contact muscle fibres), and in a few cases multiple axons may be seen to overlap on the same NMJ (Fig 5.24). No large complex bungarotoxin end plates were seen in control cultures, but smaller puncta remained visible (data not shown).

At 21 DIV, large NMJs with complex morphology were still present in co-cultured samples, with clear innervation by GFP positive MN axons (Fig. 5.25). The majority of complex bungarotoxin positive end plates were found physically close to EBs, and were always contacted by GFP positive axons. Many smaller bungarotoxin puncta were still observed without innervation, or further away from EBs, in both pure muscle control and co-cultured conditions. While GFP labelled axons could still be seen extending out from EBs in the co-cultures, the labelling appeared weaker than at earlier time points, and as can be seen from figure 5.26 the majority of GFP positive neurites remained within the EB cluster, with only a minority exiting the EBs and invading the surrounding muscle fibres.

Immunostaining was performed on cultures at 28 DIV, however no large NMJs were found in co-cultures at this time point, with only small bungarotoxin puncta observed in co-cultures and controls (data not shown). While some GFP positive MN axons were still present near EBs, no specific innervation of motor end plates was seen, and surviving axons appeared faint, suggesting decline in the viability of the cultures at this stage. Additionally, contaminating proliferative cells were overgrowing most samples at this time point, despite treatment with FDU to inhibit proliferation, preventing clear image acquisition or antibody penetration.

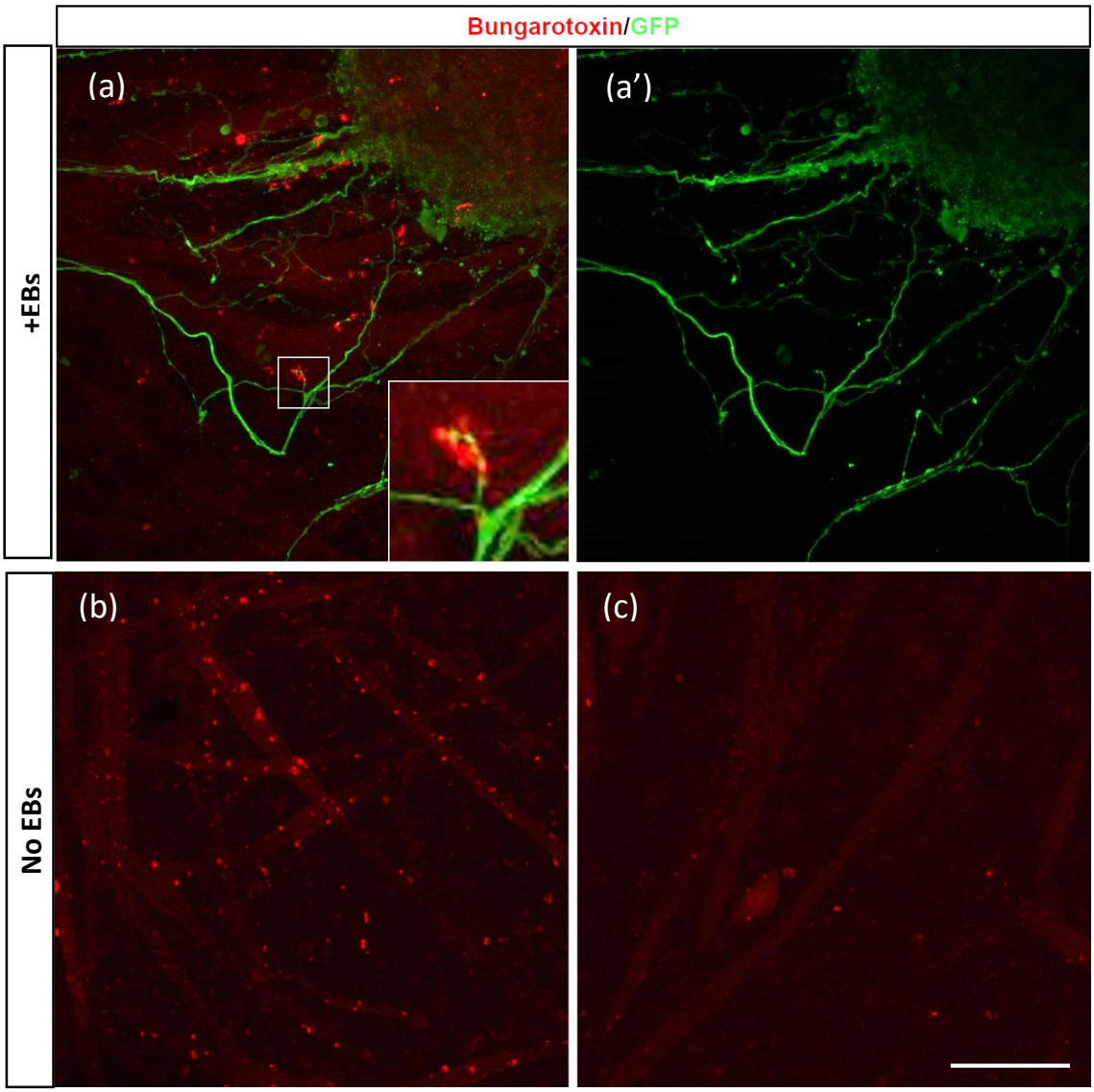

Figure 5.22 Extensive axon outgrowth and simple, small bungarotoxin puncta visible in 7 DIV CPM/AsNAs co-cultures. (a) CPM co-cultured with AsNAs after 7 DIV. Note the long GFP positive processes extending out of the aggregate at top right, and the multiple small clusters of nicotinic acetylcholine receptors (red) on the muscle fibres. The white box is shown enlarged in the bottom right to show detail of the colocalisation. The same image with only the GFP channel is shown in **(a')** to reveal details of the neurite morphology. **(b)** Day 7 CPM cultured alone showing multiple bungarotoxin puncta, while in another area far fewer puncta were observed on the muscle fibres **(c)**. Scale bar = 100μm.

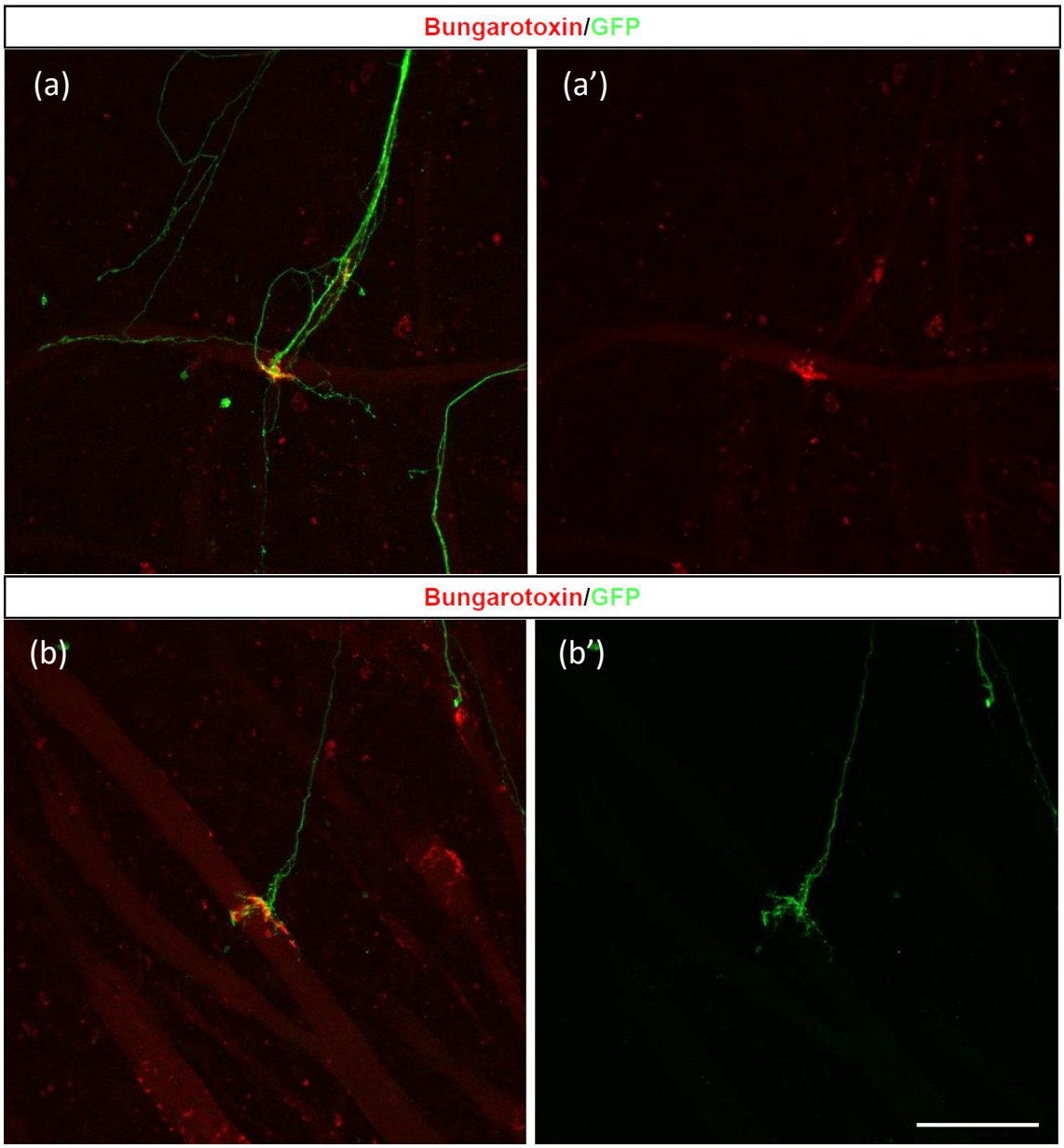

Figure 5.23 Specific innervation of large complex synapses by GFP positive axons in 14 DIV CPM/AsNAs co-cultures. (a + b) CPM co-cultured with AsNAs after 14 DIV. GFP positive processes contacting areas of specific bungarotoxin labelling (red) on muscle fibres. **(a' + b')** The same images with only one channel to reveal fine details of the synapses. Scale bar = 100μm.

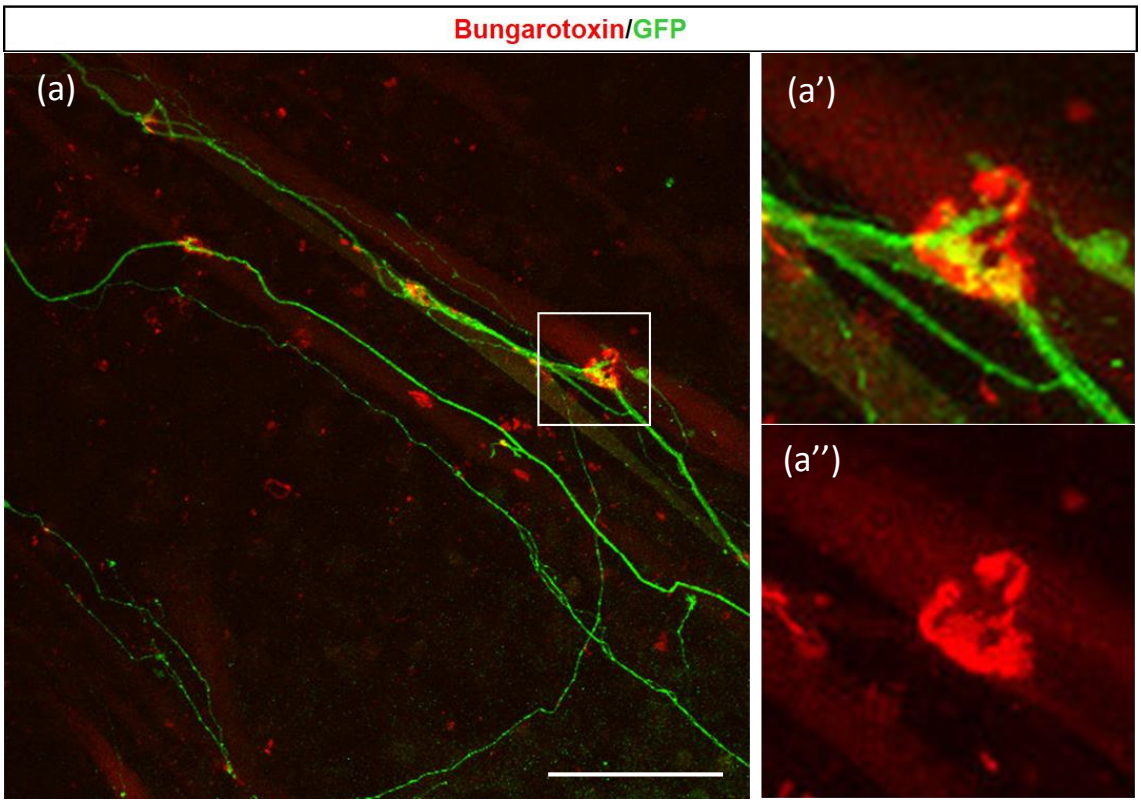

Figure 5.24 Neuromuscular junctions in 14 DIV CPM/AsNAs co-cultures develop the characteristic morphology of NMJs seen *in vivo*. (a) CPM co-cultured with AsNAs after 14 DIV. GFP positive processes innervating bungarotoxin labelled synapses (red) on muscle fibres. Note the classic "pretzel" shape morphology of the synapse. **(a' + a'')** Close up of the boxed region in **(a)** to show fine detail of the synapse. Scale bar = 100μm.

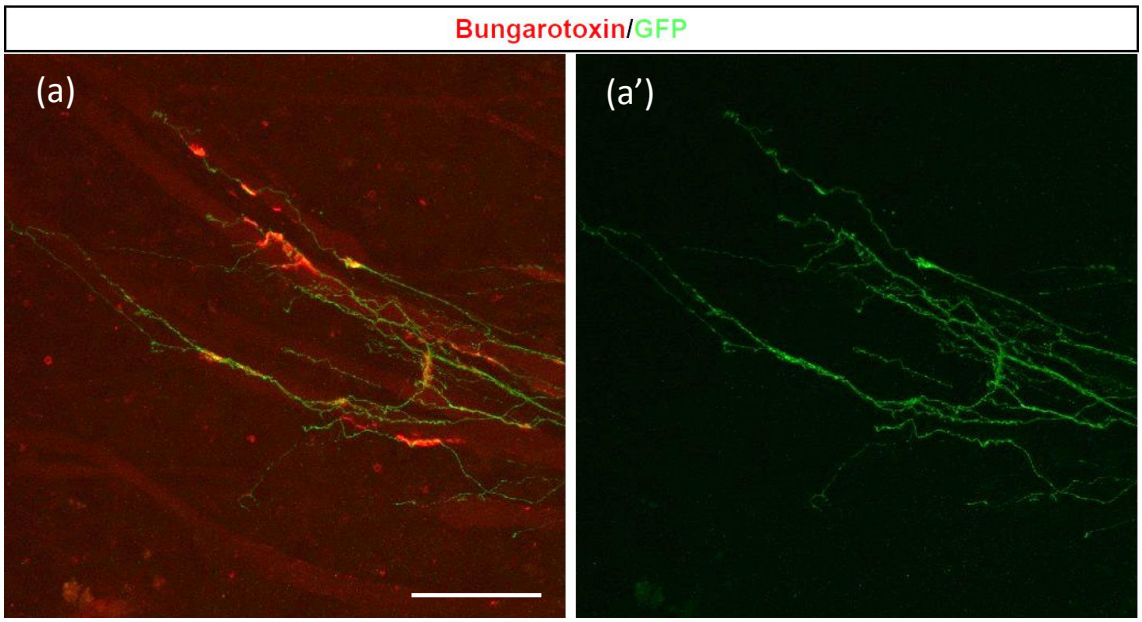

Figure 5.25 Complex synapses are maintained in 21 DIV CPM/AsNAs co-cultures, with innervation by GFP positive MN axons. (a) CPM co-cultured with AsNAs after 21 DIV. GFP positive neurites can be seen growing along muscle fibres and making extensive contacts with bungarotoxin positive synapses (red). **(a')** The same image with only one channel to reveal fine details of the axonal morphology. Scale bar = 100μm.

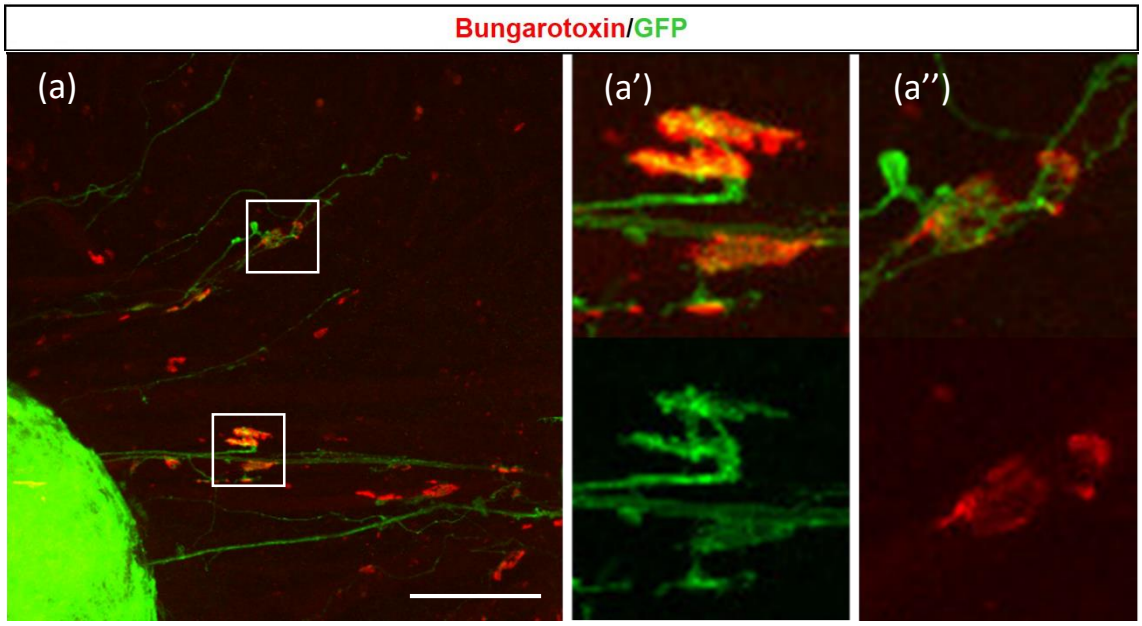

Figure 5.26 Multiple complex neuromuscular junctions innervated by GFP positive MN axons in 21 DIV CPM/AsNAs co-cultures. (a) CPM co-cultured with AsNAs after 21 DIV. GFP positive processes innervating bungarotoxin labelled synapses (red) on muscle fibres. Note the precise overlap of the axon terminals with the post-synaptic receptors. **(a' + a'')** Close-ups of the boxed regions in **(a),** showing fine details of the synapses. Scale bar = 100μm.

5.4 Chick Skeletal Muscle/Astro-neural Aggregate Co-Culture

5.4.1 Contractile activity of CPM/AsNAs co-cultures

Following the successful co-culture of MNs in EBs with CPM, ESC-derived MN co-culture with CPM was repeated using astro-neural aggregates (AsNAs), resulting in a better characterised and more reproducible neuronal population, with fewer unknown contaminating cell types. Due to the previously observed decrease in viability of co-cultures after 3 weeks *in vitro*, earlier time points were focused on for these experiments.

As no spontaneous activity was observed during previous patch clamp recordings of AsNA cultures, and multiple studies have shown MN activity is key to stabilisation and maturation of NMJs *in vivo* (Walsh and Lichtman, 2003; Wyatt and Balice-Gordon, 2003), a computer-controlled blue-LED array was incorporated into the tissue culture incubator to provide chronic photostimulation to the MN population. The stimulation protocol used was a two-day on/off cycle of 20ms bursts of 5 blue light flashes at 20 Hz, every 5 seconds (see Chapter 2.2.2.13). This protocol was based on previous work using the stimulation incubator showing detrimental effects on culture viability due to light toxicity if sustained for over 48 hours, or with more intense stimulation regimes (Grubb and Burrone, 2010; and unpublished observations). Control CPM/AsNAs co-cultures were not subjected to chronic photostimulation, but were stimulated to measure contractile responses to blue-light stimulation, while CPM only controls were grown in both conditions without co-culture with astro-neural aggregates.

Representative frame-by-frame analyses of chronically stimulated CPM/AsNAs co-cultures at 3 DIV are presented below in figure 5.27. As can be seen in Fig. 5.27 a, even at 3 DIV, a blue-light stimulus does produce a muscle contraction in these co-cultures, with an average displacement of 11.65μm ± 1.57. No contractile activity was noted in co-cultures in the absence of light stimulation, and no spontaneous activity was observed at this time point in either co-cultures or CPM only controls (Fig. 5.27).

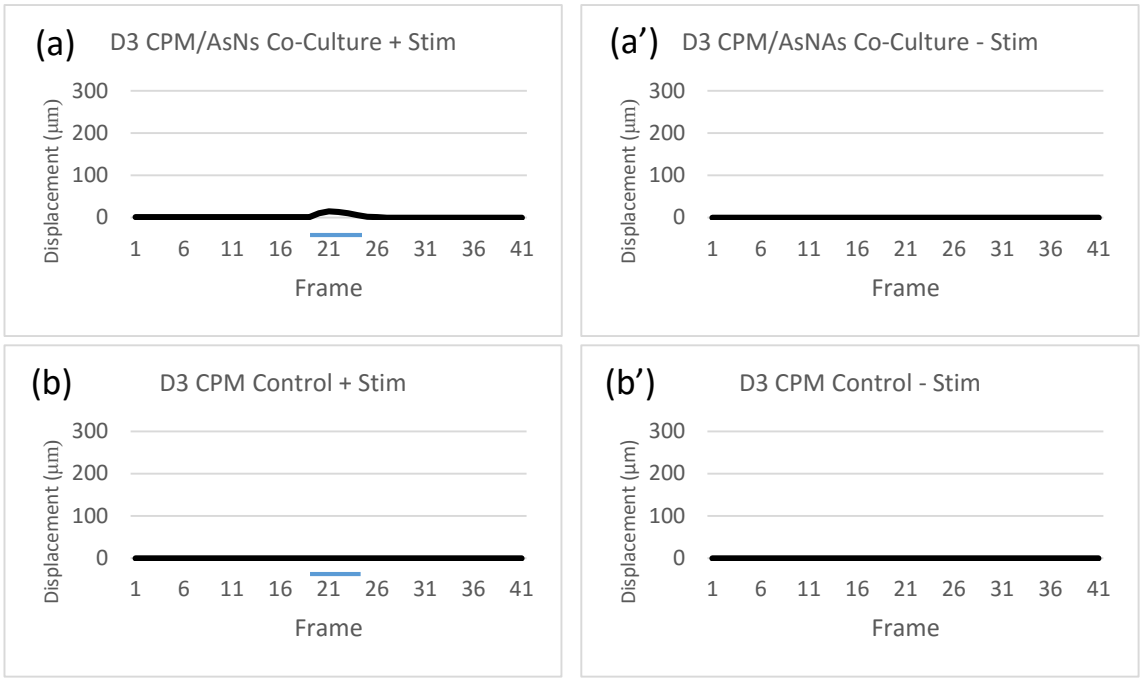

Figure 5.27 Light-evoked and spontaneous activity in chronically stimulated CPM/AsNAs co-cultures and controls at 3 DIV. Frame-by-frame analysis of time-lapse movies of 3 DIV CPM/AsNAs co-cultures and controls. **(a + b)** Contractile activity in response to a blue light stimulus seen in the co-culture is not observed in the CPM only control. **(a' + b')** No spontaneous activity was seen at this time point.

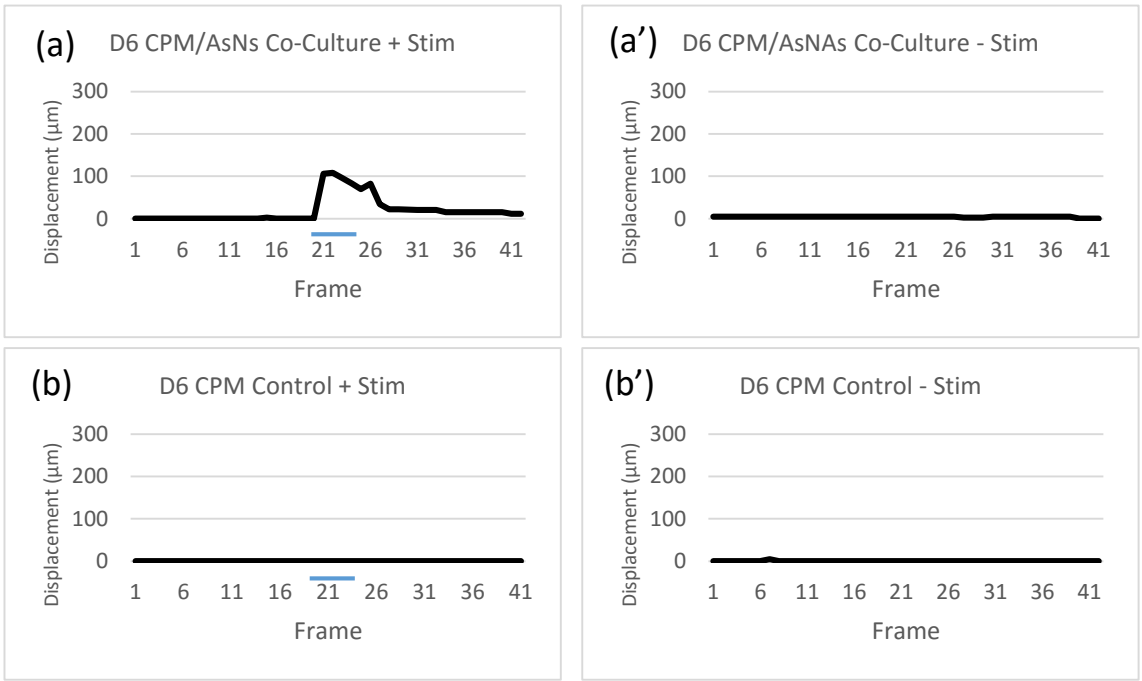

Figure 5.28 Light-evoked and spontaneous activity in chronically stimulated CPM/AsNAs co-cultures and controls at 6 DIV. Frame-by-frame analysis of time-lapse movies of 6 DIV CPM/AsNAs co-cultures and controls. **(a)** A strong light-evoked contraction seen in the co-culture is not observed in the CPM only control **(b)**. **(a' + b')** Some spontaneous activity was seen in both co-cultures and controls at this time point, however it was much weaker than light-evoked activity.

At 6 DIV, some spontaneous activity was observed in both co-cultures and controls, similar to levels seen in CPM/EB co-cultures previously (Fig. 5.28 a). Strong stimulus-evoked contractions were seen in chronically stimulated co-cultures at this time point, with an average displacement of 164.93μm ± 22.8, much higher than contractions seen in 5 DIV CPM/EB co-cultures (23.87μm ± 1.37). As before, no contractile activity was seen in CPM controls in response to blue-light stimulation (Fig. 5.28 b).

The strongest light-evoked contractions were observed in chronically stimulated 12 DIV CPM/AsNAs co-cultures, with a mean displacement of 252.97μm ± 5.4 (Fig. 5.29 a). A representative example is shown in figure 5.29. Light-evoked activity was also seen in non-chronically stimulated CPM/AsNAs co-cultures around this time-point (14 DIV), however this was much weaker than for equivalent chronically stimulated co-cultures, with an average displacement of 32.03μm ± 2.4 (Fig. 5.31 a). While significant spontaneous activity was seen in both co-cultures and controls, this was weaker on average than at 6 DIV [23.72μm ± 0.29 and 34.90μm ± 3.16 respectively] (Fig. 5.31 a). No response to the blue-light stimulus was observed in pure muscle control cultures.

Similar results were obtained for 20 DIV cultures, with a strong light-evoked contractile response seen in chronically stimulated CPM/AsNAs co-cultures, with an average displacement of 195.96μm ± 14.0 (Fig. 5.30 a), while non-chronically stimulated co-cultures showed an average displacement of 22.76μm ± 2.31 (Fig. 5.32 a). Spontaneous acitivity in the co-cultures remained relatively stable in both chronically stimulated and non-stimulated co-cultures (20.04μm ± 0.33 and 2.26μm ± 0.16 respectively), and no light-evoked activity was seen in CPM controls.

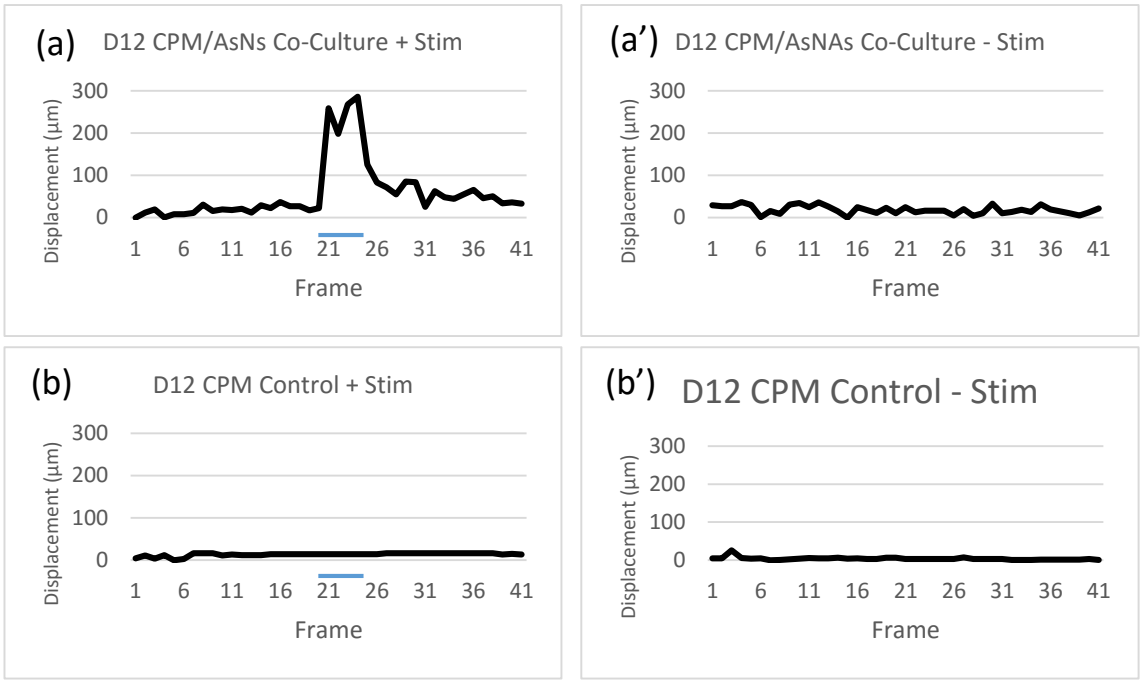

Figure 5.29 Light-evoked and spontaneous activity in chronically stimulated CPM/AsNAs co-cultures and controls at 12 DIV. Frame-by-frame analysis of time-lapse movies of 12 DIV CPM/AsNAs co-cultures and controls. **(a)** Again, a very strong light-evoked contraction seen in the co-culture was absent in the CPM only controls **(b)**. **(a' + b')** Low level spontaneous activity was seen in both co-cultures and controls at 12 DIV.

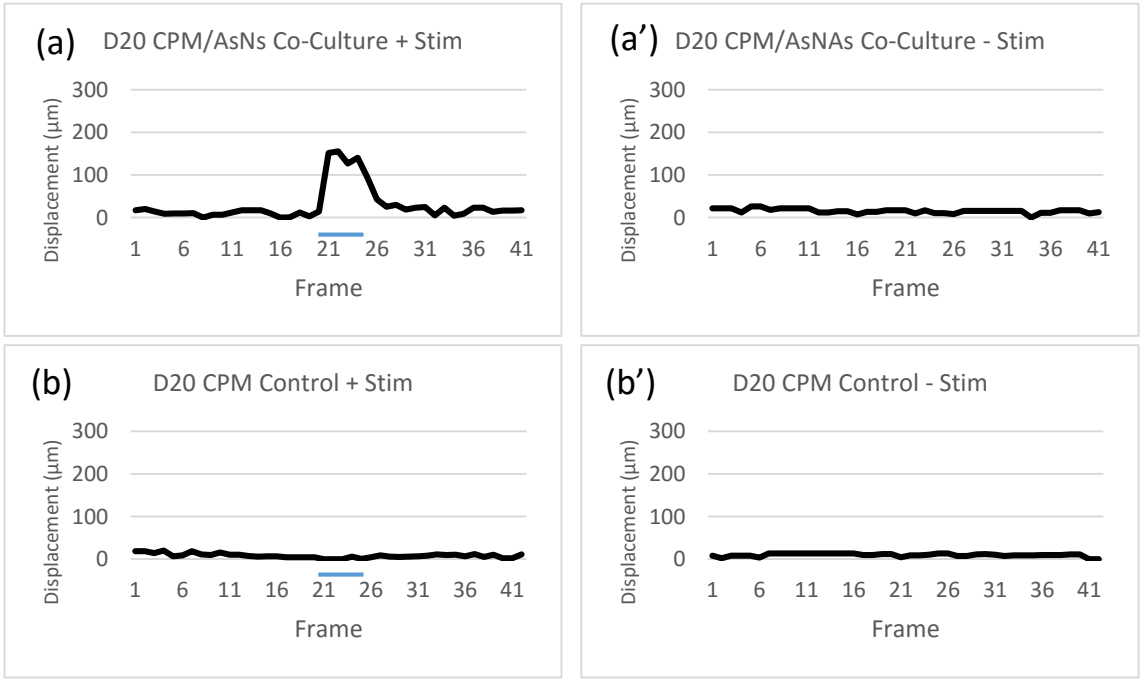

Figure 5.30 Light-evoked and spontaneous activity in chronically stimulated CPM/AsNAs co-cultures and controls at 20 DIV. Frame-by-frame analysis of time-lapse movies of 20 DIV CPM/AsNAs co-cultures and controls. **(a)** Clear light-evoked contractions were still apparent in the co-culture condition, and remained absent in CPM only controls **(b)**. **(a' + b')** Spontaneous activity was still observed in both co-cultures and controls at 20 DIV.

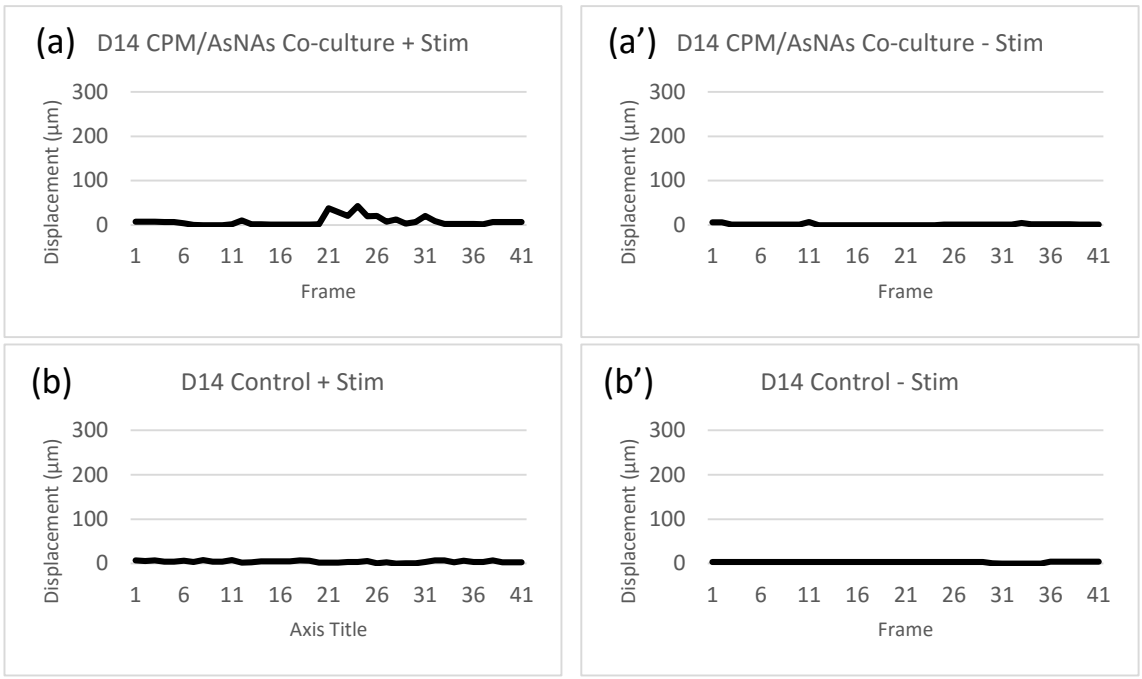

Figure 5.31 Light-evoked and spontaneous activity in non-chronically stimulated CPM/AsNAs co-cultures and controls at 14 DIV. Frame-by-frame analysis of time-lapse movies of 14 DIV CPM/AsNAs co-cultures and controls. **(a)** Weak light-evoked contractions seen in the co-culture were absent in the CPM only controls **(b)**. **(a' + b')** Very little spontaneous activity was seen in either co-cultures or controls at 14 DIV.

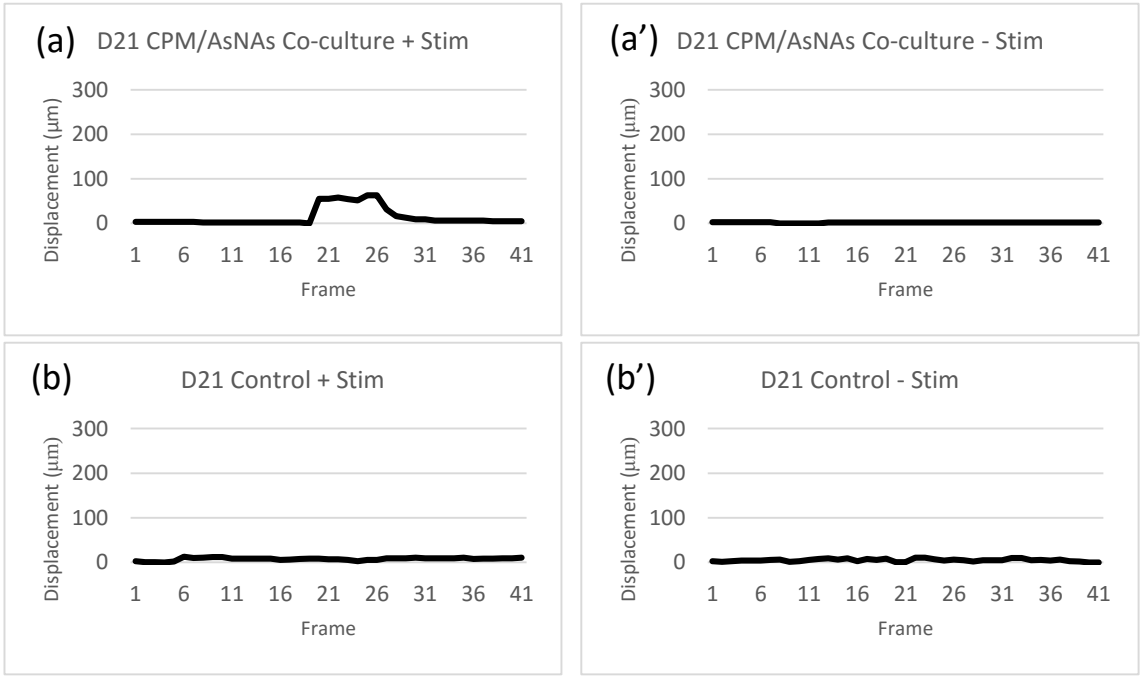

Figure 5.32 Light-evoked and spontaneous activity in non-chronically stimulated CPM/AsNAs co-cultures and controls at 21 DIV. Frame-by-frame analysis of time-lapse movies of 21 DIV CPM/AsNAs co-cultures and controls. **(a)** A clear light-evoked contraction seen in the co-culture condition was absent from CPM only controls **(b)**. **(a' + b')** Similar to 14 DIV, very little spontaneous activity was seen in either co-cultures or controls at 21 DIV.

Comparison of contractile activity in response to a blue-light stimulus across the time series of all conditions shows that measured displacement peaked at 12/14 DIV for chronically stimulated (252.97μm ± 5.44) and non-stimulated co-cultures respectively [32.03μm ± 2.4] (Fig. 5.33 a). This peak activity level for non-stimulated co-cultures was not significantly different to spontaneous activity seen in CPM only controls at 12 DIV, which achieved an average displacement of 23.60μm ± 0.35 during presentation of a blue-light stimulus, even in the absence of MNs (Fig. 5.33 a). When all spontaneous contractile events observed were analysed, in the absence of a blue-light photostimulation presentation, this trend was abolished (Fig. 5.33 b). The highest level of spontaneous activity was seen in 6 DIV chronically stimulated co-cultures, with an average displacement of 34.90μm ± 3.16. While significantly stronger than spontaneous contractions seen in CPM controls at this time point (1.67μm ± 0.32), this level of activity was not dissimilar to that seen in CPM controls at 12 DIV (25.28μm ± 0.90), and again the levels were similar at 20 DIV (Fig. 5.33 b). Spontaneous activity in non-chronically stimulated co-cultures appeared lower than the other conditions at 14 DIV and 21 DIV, but was not significantly different (6.73μm ± 0.77 and 2.26μm ± 0.16 respectively).

To further investigate the necessity of NMJs for the observed contractile activity in these cultures, chronically stimulated 20 DIV co-cultures were stimulated with blue light before and after treatment with α-bungarotoxin, a snake toxin which specifically blocks the skeletal muscle nicotinic acetylcholine receptor, found at the NMJ (Samson and Levitt, 2008). As shown in figure 5.34, before addition of α-bungarotoxin, a blue-light photostimulus resulted in a strong muscle contraction with a peak displacement of 210.19μm, while very little activity was seen in the absence of light stimulation. Following treatment with α-bungarotoxin, this light-evoked activity was completely ablated, with only very small spontaneous contractions observed (Fig. 5.34). This effect was reproducible, with no stimulus-evoked displacements seen in two independent co-cultures tested (data not shown). Interestingly, treatment with α-bungarotoxin also appeared to reduce spontaneous activity, with the average displacement for non-stimulated 20

DIV cultures being 2.27µm ± 0.25, compared to 20.04µm ± 0.33 for non-bungarotoxin treated cultures.

(a)

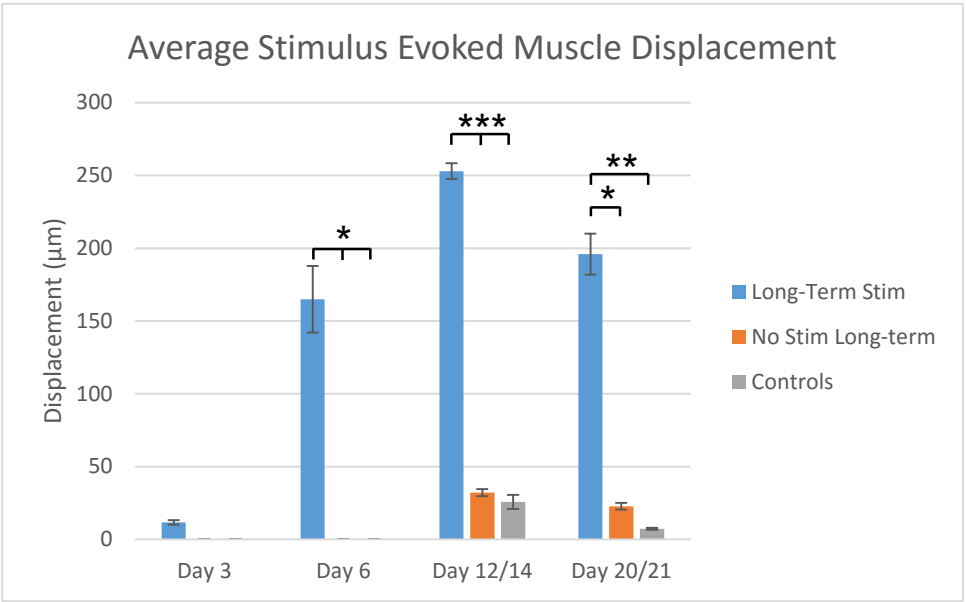

(b)

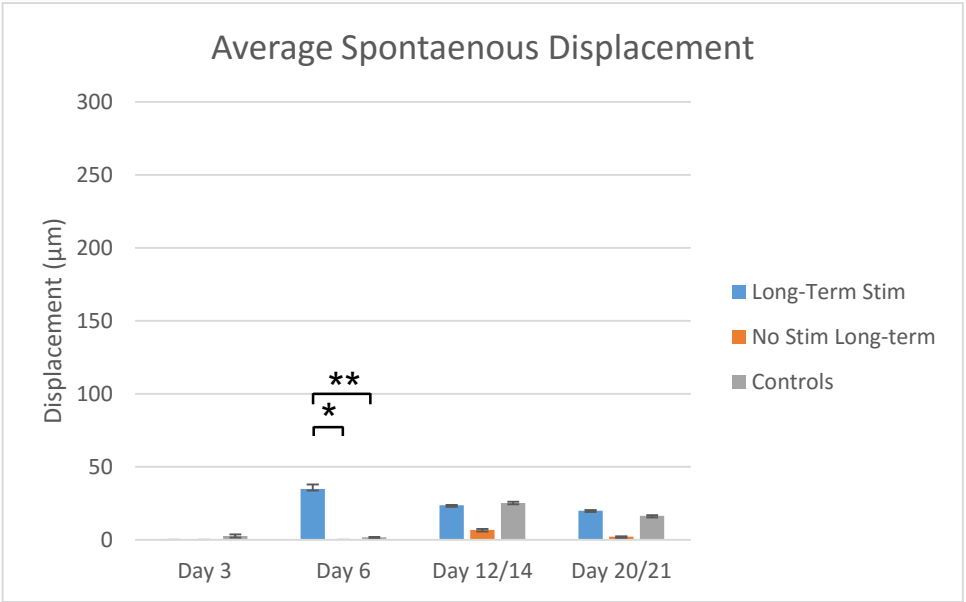

Figure 5.33 Average muscle displacement recorded in CPM/AsNAs co-cultures and controls, with and without chronic photostimulation. (a) Average displacement recorded in response to a blue-light stimulus in multiple movies across the time series in each condition. **(b)** Average displacement recordent in the absence of an acute blue-light stimulation. n= 2 for Day 3 +/- stim and controls, n= 3 for Day 6 +/- stim and controls, n= 2 for Day 12/14 +/- stim and n= 3 for D12/14 controls and n= 5 for Day 20/21 -/+ stim and n= 4 for controls. Error bars show the S.E.M. Kruskal-Wallis Test, * = p <0.05, ** = p <0.01, *** = p <0.001.

(a)

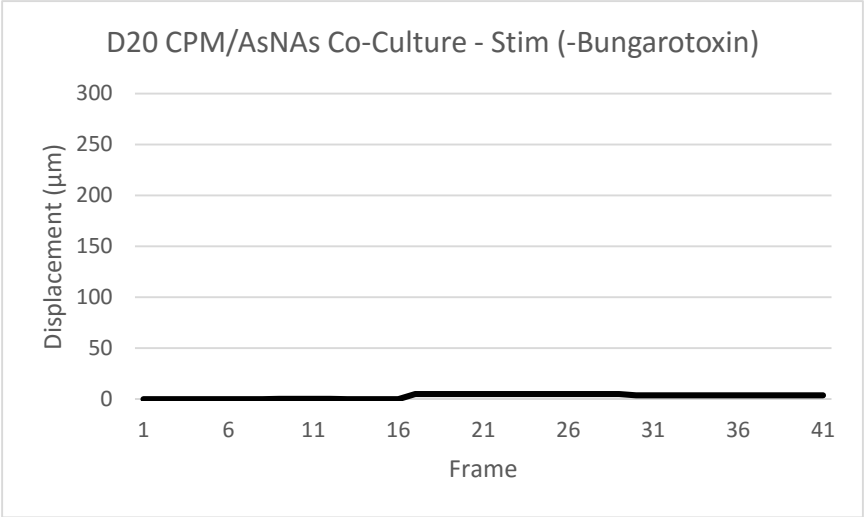

(b)

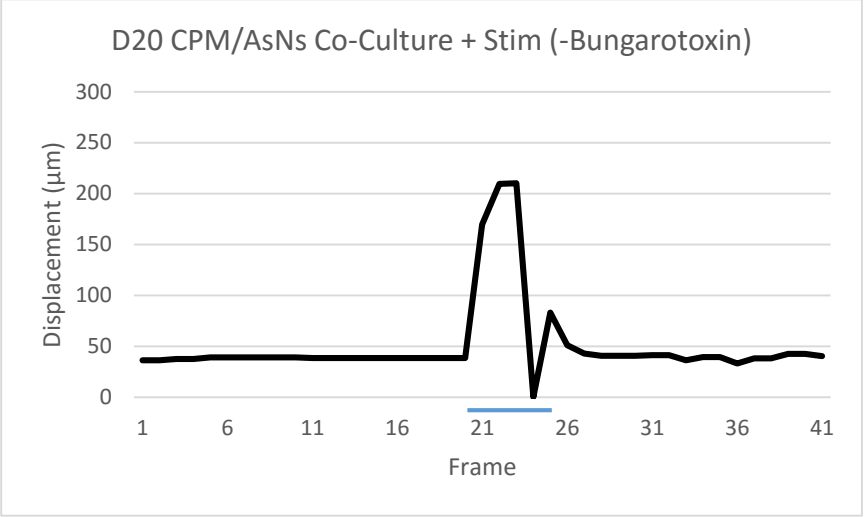

(c)

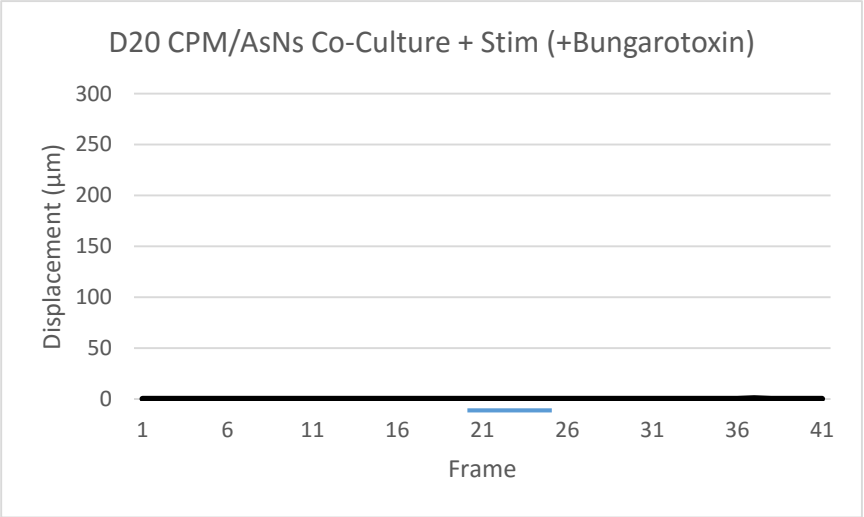

Figure 5.34 Treatment of CPM/AsNAs co-cultures with α-Bungarotoxin inhibits both spontaneous and light-evoked muscle activity at 20 DIV. Frame-by-frame analysis of time-lapse movies of 20 DIV CPM/AsNAs co-cultures before and after treatment with α-bungarotoxin. **(a)** Spontaneous activity was observed in 20 DIV co-cultures in the absence of a light stimulation and bungarotoxin. **(b)** A strong light-evoked contraction was seen in the absence of bungarotoxin. **(c)** After addition of bungarotoxin, the light-evoked contractile response is inhibited, and no spontaneous activity was observed for the duration of imaging.

5.4.2 Neuromuscular junctions in CPM/AsNAs co-cultures

Co-cultures of CPM with astro-neural aggregates were examined by immunocytochemistry at four time points throughout the experiment as done previously for CPM/EB co-cultures, to determine if NMJs had formed, and to investigate their morphological development. Both chronically stimulated and non-stimulated cultures were analysed. Co-cultures fixed at 7 DIV have clear bungarotoxin positive puncta closely opposed to GFP positive MN axons, as shown in figure 5.35 below. This matches the functional data obtained previously, showing that chronically stimulated 6 DIV co-cultures strongly respond to blue-light stimulation, indicating functional connectivity between the MN population and the muscle fibres (Fig. 5.28). While some functional synapses are clearly present at this stage, there is also evidence of continued growth and circuit development, as MN axon growth cones could be observed growing away from the AsNAs clusters into the muscle tissue (Fig. 5.35 b).

Day 14 CPM/AsNAs co-cultures were generally similar to 7 DIV samples, with multiple bungarotoxin puncta showing co-localisation with GFP from MN axons (Fig. 5.36). MN axons can be seen to associate with and grow along muscle fibres, with short branches extending to contact areas of high bungarotoxin staining to form synapses. In many cases, it appeared a single MN axon contacted multiple synapses on multiple muscle fibres, however confirmation of this would require single cell labelling to differentiate axons, as they often bundled together along muscle fibres, and became indistinguishable from each other. After 21 DIV, multiple large NMJ-like structures were visible in both chronically stimulated and not-stimulated CPM/AsNAs co-cultures, as can be seen in figure 5.37. Bungarotoxin puncta appeared larger, and in one example displayed the characteristic complex morphology of mature NMJs *in vivo* (Fig. 5.37 b). Most large bungarotoxin puncta were co-localised with GFP, while a few small puncta were not associated with MN axons. These results were similar for 28 DIV co-cultures, with GFP labelled axons closely matching the morphology of bungarotoxin labelled motor end plates (Fig. 5.38).

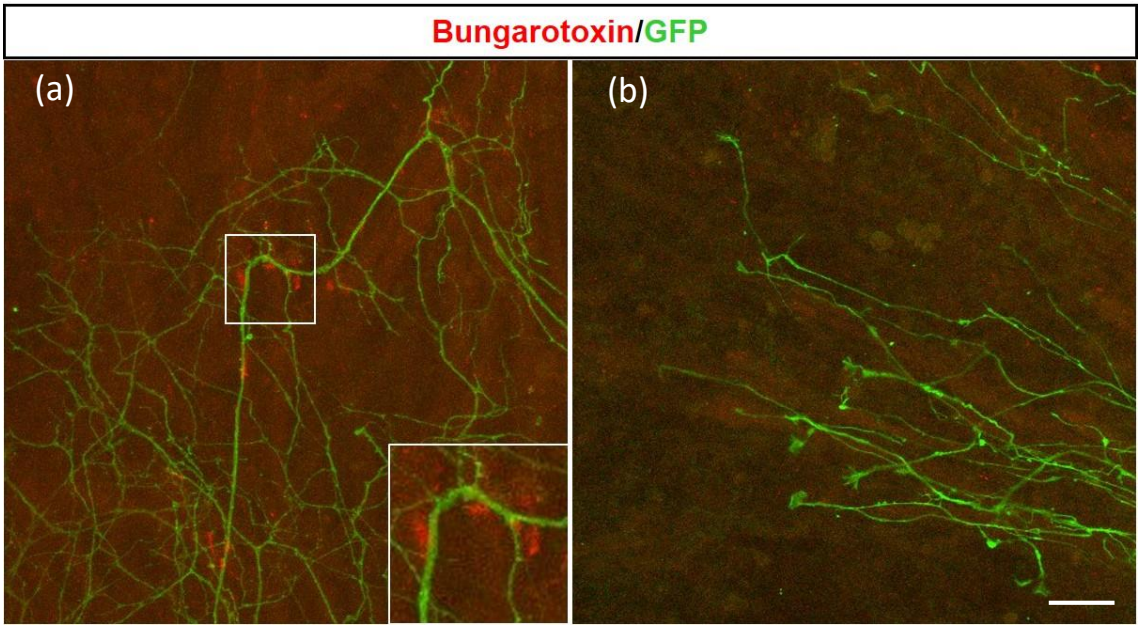

Figure 5.35 Extensive axon outgrowth with visible growth cones, and co-localisation with small bungarotoxin puncta visible in 7 DIV CPM/AsNAs co-cultures. (a) CPM co-cultured with AsNAs after 7 DIV (chronic stim). Note the long GFP positive processes extending across the muscle tissue, and the multiple small clusters of nicotinic acetylcholine receptors (red) on the muscle fibres contacted by GFP labelled axons. **(b)** Growth cones can be seen at the terminal of many GFP labelled processes at this time point (no chronic stim). Scale bar = 100μm.

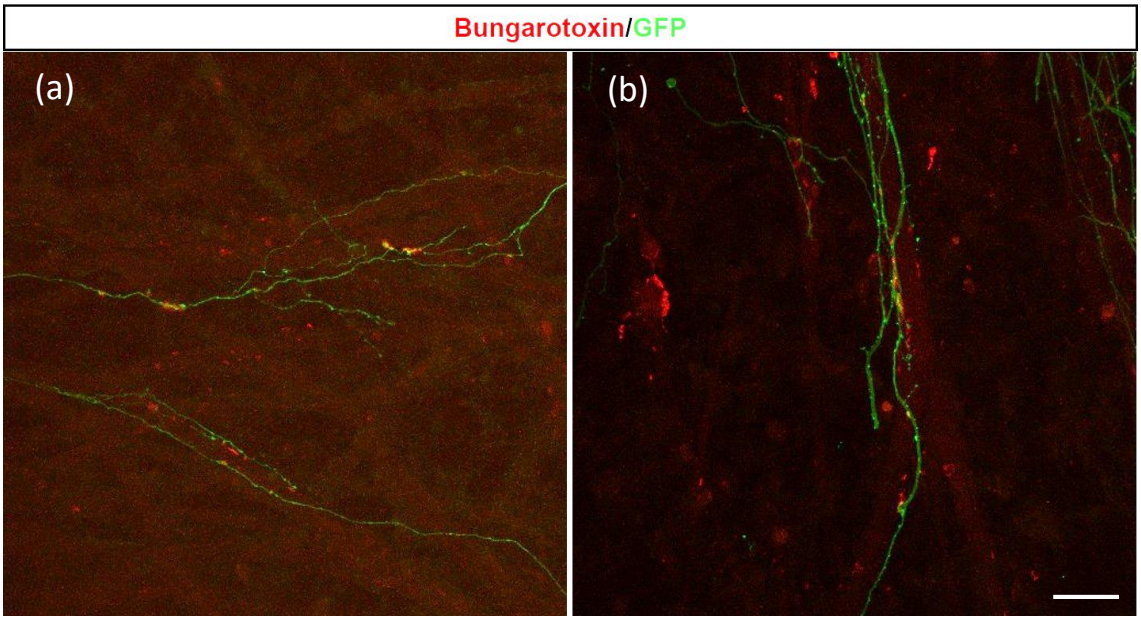

Figure 5.36 Specific innervation of complex bungarotoxin labelled synapses by GFP positive axons in 14 DIV CPM/AsNAs co-cultures. (a + b) CPM co-cultured with AsNAs after 14 DIV. GFP positive processes contacting areas of specific bungarotoxin labelling (red) on muscle fibres. (a = chronic stim; b = no chronic stim). Scale bar = 100μm.

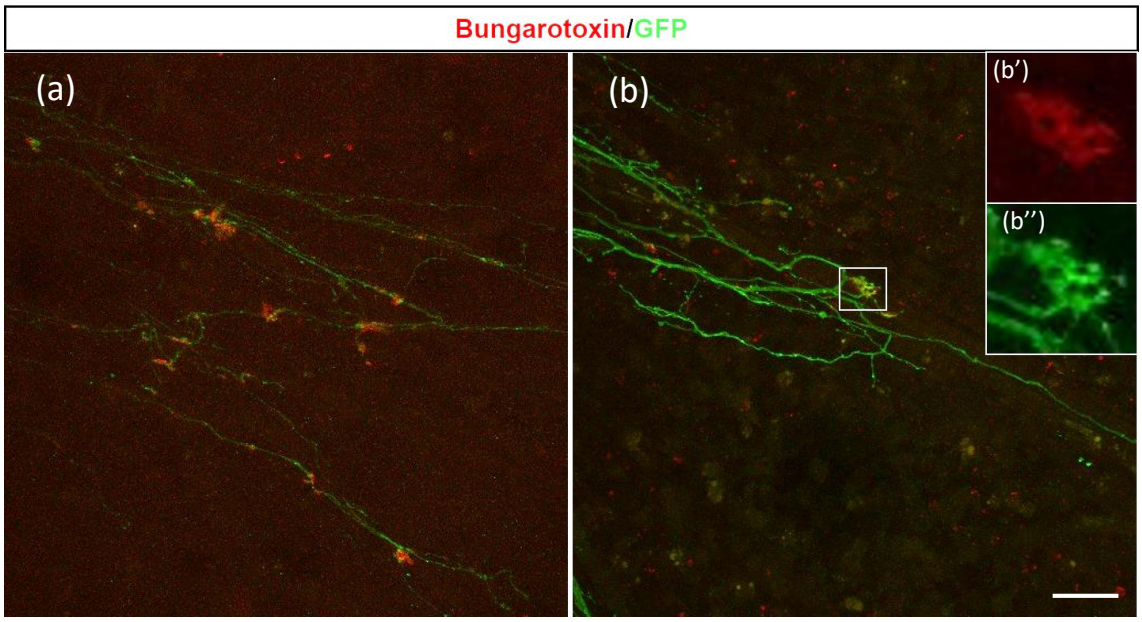

Figure 5.37 Co-localisation of GFP and bungarotoxin at complex neuromuscular junctions in 21 DIV CPM/AsNAs co-cultures. (a + b) CPM co-cultured with AsNAs after 21 DIV. GFP positive processes innervating bungarotoxin labelled synapses (red) on muscle fibres. Note the matching complex morphology of the synapse in **(b)**. **(b' + b'')** Close up of the boxed region in **(b)** to show fine detail of the synapse. (a = chronic stim; b = no chronic stim). Scale bar = 100μm.

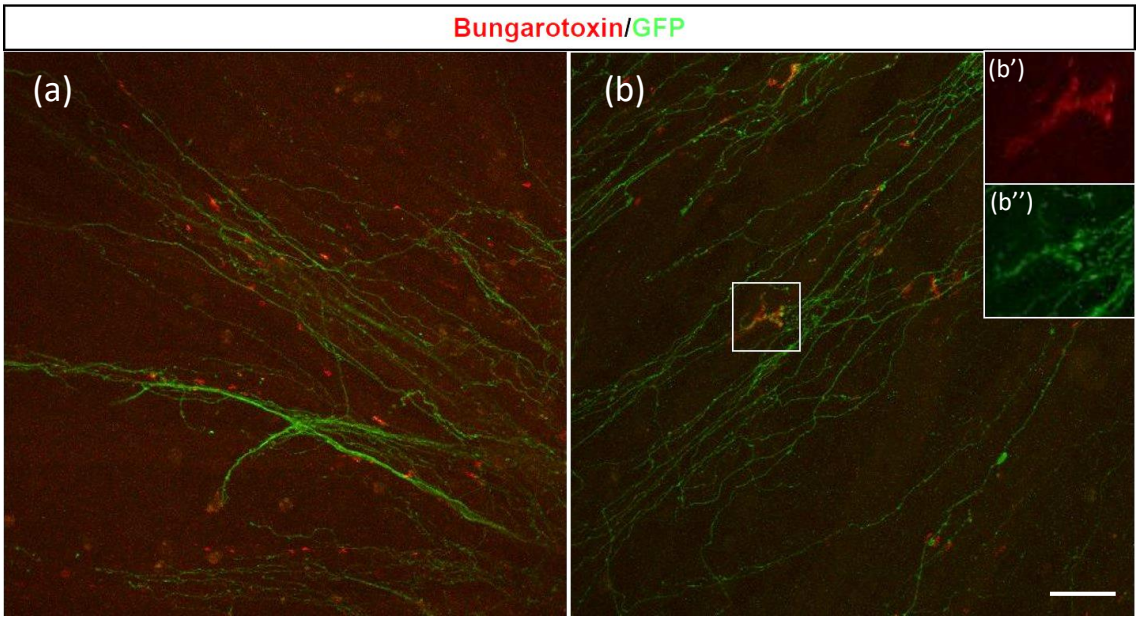

Figure 5.38 Innervation of multiple neuromuscular junction like structures in 28 DIV CPM/AsNAs co-cultures. (a + b) CPM co-cultured with AsNAs after 28 DIV, chronically stimulated. GFP positive processes innervating bungarotoxin labelled synapses (red) on muscle fibres. Note the precise co-localisation of GFP and bungarotoxin at the synapse in **(b)**. **(b' + b'')** Close up of the boxed region in **(b)** to show fine detail of the synapse. Scale bar = 100μm.

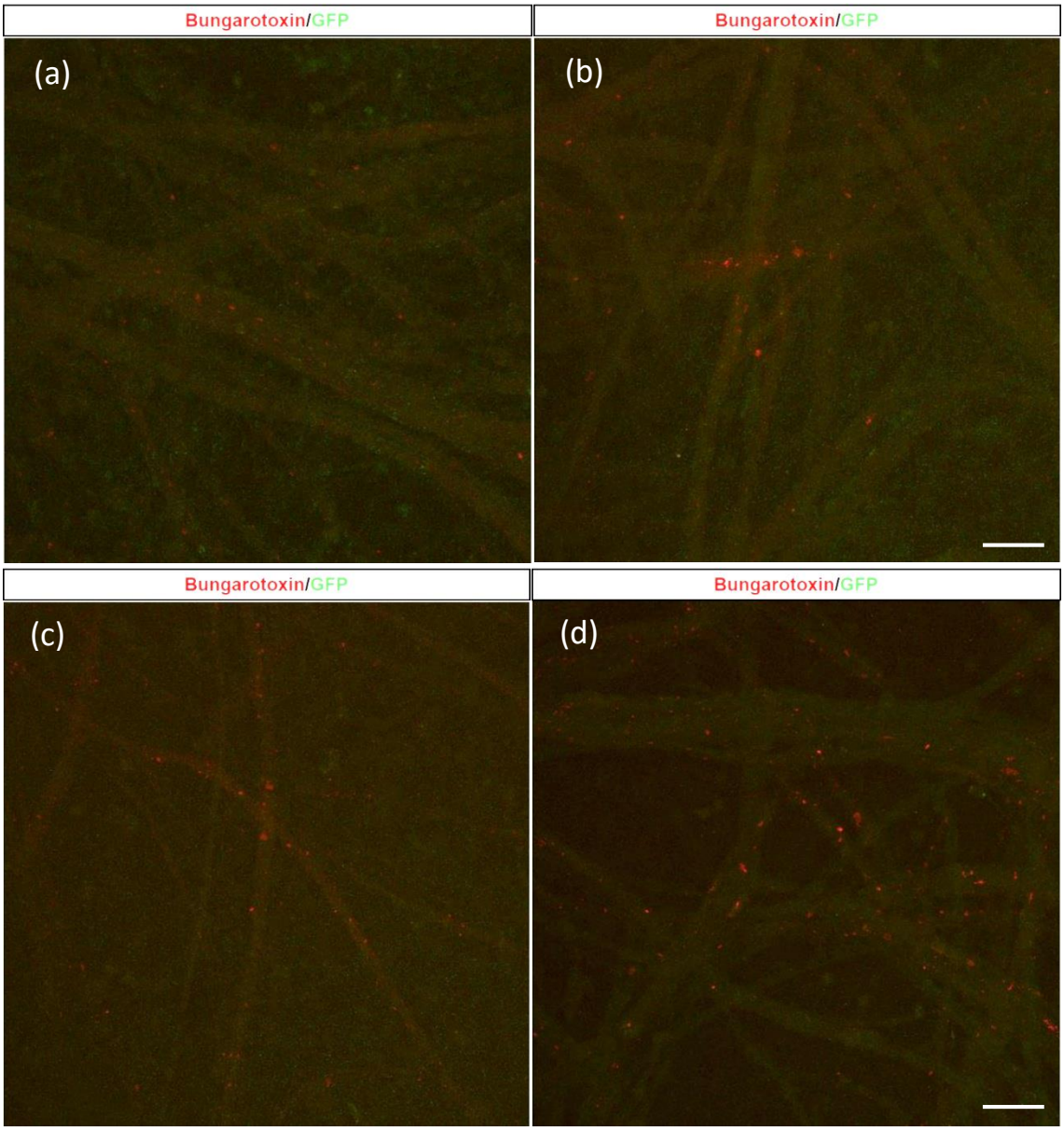

Figure 5.39 CPM cultured in the absence of motor neurons displays small, simple bungarotoxin puncta. CPM controls cultured in the absence of MNs for up to 28 DIV. Representative images of 7 DIV **(a),** 14 DIV **(b)**, 21 DIV **(c)**, and 28 DIV **(d)** are shown. Scale bare = 100μm.

No morphologically complex bungarotoxin puncta were observed in CPM only controls, with only small, simple puncta observed on the muscle fibres (Fig. 5.39). While there was some variation in the number of bungarotoxin puncta on individual muscle fibres, generally fewer puncta were observed in control samples compared to co-cultures.

While no clear differences could be observed between chronically stimulated and non-stimulated co-cultures by eye, analysis of NMJ number, size and innervation using ImageJ software enabled a more detailed investigation of synapse formation and development in these cultures over the time course investigated. For this analysis, an "NMJ" was defined as a bungarotoxin-labelled region with an area greater than 150 μm, while "innervation" was defined as direct overlap of GFP signal over the red bungarotoxin-labelled synapse. Innervation was further classified into partial or complete, depending on the degree of co-localisation between the green and red signals.

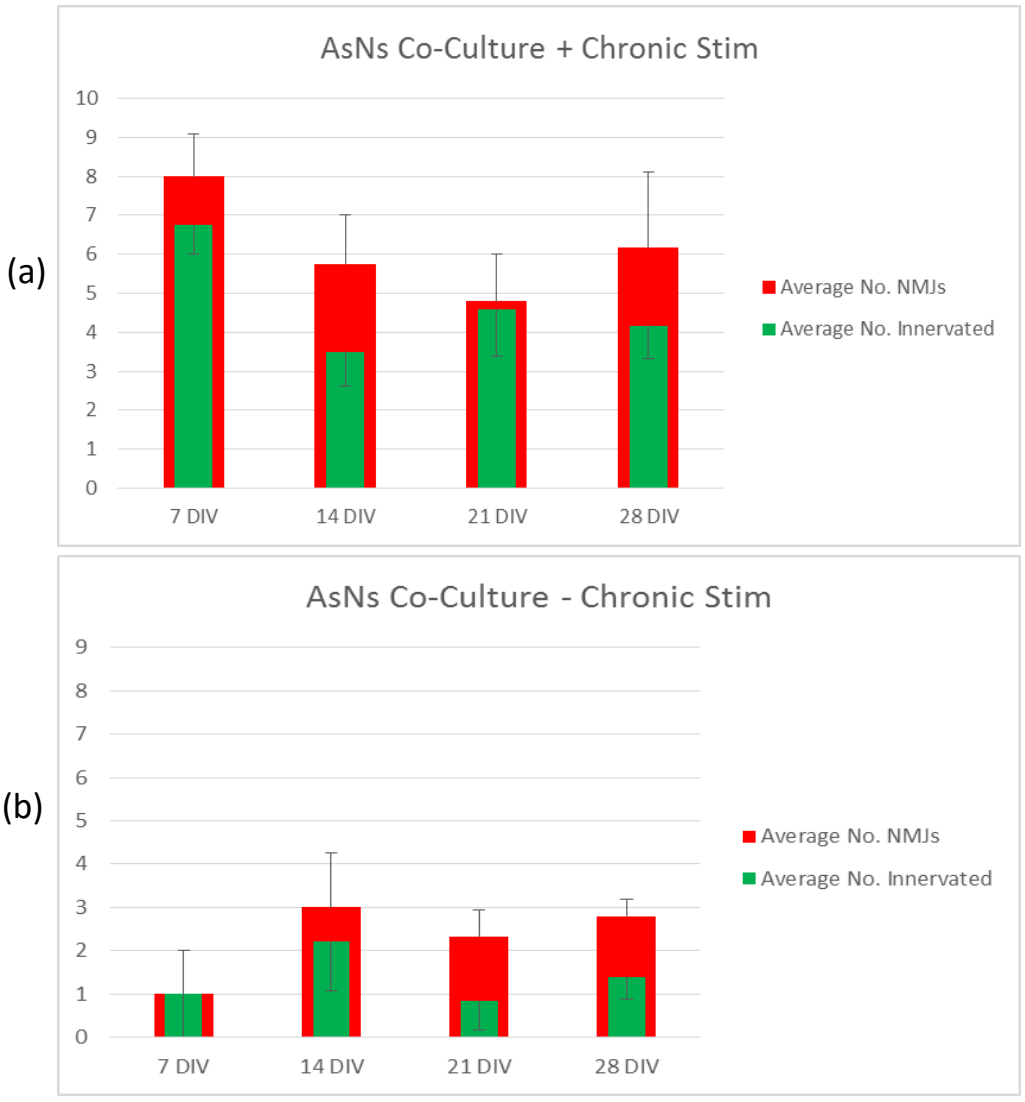

Figure 5.40 Average number of NMJs in CPM/AsNAs co-cultures, with and without chronic photostimulation. (a) Average number of NMJs (red bar) observed in a single image frame of co-cultures over the 4-week time course. The overlaid green bar indicates the average number of these NMJs that were innervated by ESC-derived MNs. n= 4 for Day 7, n= 4 for Day 14, n= 5 for Day 21 and n= 6 for D28. **(b)** Average number of NMJs and innervation status observed in non-chronically stimulated co-cultures. n= 3 for Day 7, n= 5 for Day 14, n= 6 for Day 21 and n= 5 for D28. Error bars show the S.E.M. ANOVA between timepoints revealed no significant differences, however a significant difference between chronic and non-chronic stim innervation (green bars) was seen at 7 and 21 DIV by two-tailed T-Test (P values 0.0059 and 0.0139 respectively).

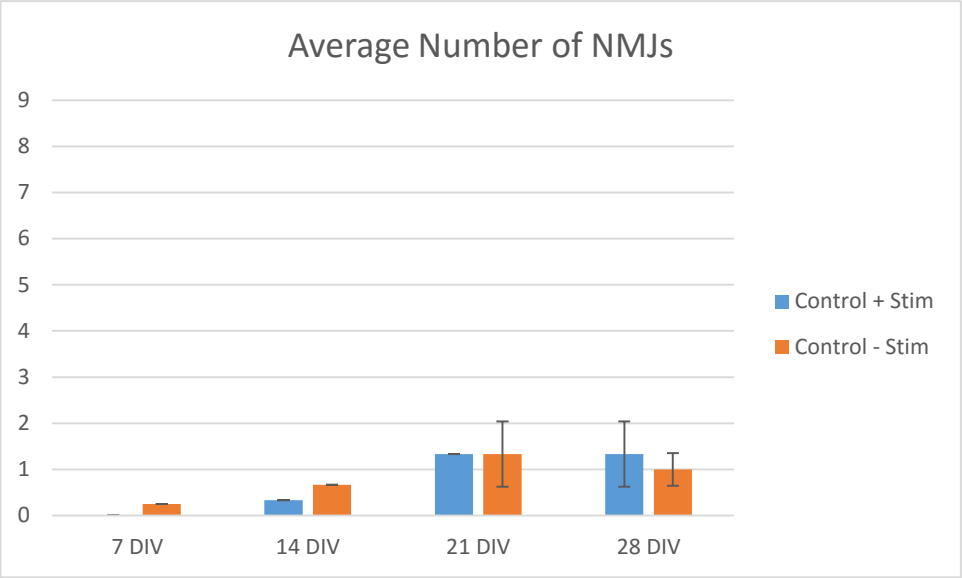

Figure 5.41 Average number of NMJs in CPM control cultures, with and without chronic photostimulation. Average number of NMJs observed in a single image frame of control cultures over the 4-week time course. n= 3 for both conditions at all time points. Error bars show the S.E.M. ANOVA between time points and T-Tests between +/- Stim at each time point, no significant difference found.

Chronically stimulated co-cultures had greater numbers of "NMJ-like" structures than non-stimulated co-cultures or CPM controls at all time-points investigated as shown in figure 5.40 and figure 5.41, however this difference was only significant at 7 DIV (**; p = 0.0059). The greatest number of NMJs was seen in chronically photostimulated co-cultures at 7 DIV, which possessed an average of 8 NMJ-like structures per image field. This is in contrast to non-stimulated co-cultures, which showed the highest number of NMJ-like structures at 14 DIV, with 3 per image field.

The highest degree of innervation of these structures by GFP positive MN axons in chronically stimulated cultures was seen at 21 DIV, with 95.8% of NMJs innervated, of which 21.7% were partially innervated (Fig. 3.40 a). Innervation was always above 50% in chronically stimulated cultures, with the lowest value being 60.9% at 14 DIV, of which 50% were partially innervated. In non-stimulated cultures, 100% innervation was seen at 7 DIV with 0% partial innervation, however this may be a result of the low number of NMJs seen at this time-point in this condition. Total innervation was lower in this condition at both 21 and 28 DIV, with 35.7% and 50% respectively (Fig. 5.40 b). Of these innervation values, partial innervation accounted for 40% and 57.1% respectively.

The average number of NMJ-like structures in CPM controls over the time-course is shown in figure 5.41. As can be seen in figure 5.41, the average number of NMJ-like structures was lower in CPM controls when compared to both chronically stimulated and un-stimulated co-cultures at every time point studied. The highest average number of NMJs seen in controls was at 21 DIV, with 1.3 NMJs per image field (Fig. 5.41). As no MNs were present in these cultures, there was 0% innervation by default. Tables detailing total counts of NMJs and innervation status are presented in Appendix A.

NMJ area was determined by tracing the outline of the bungarotoxin positive region freehand in ImageJ. Analysis of average NMJ area in all conditions over the time course is shown in figure 5.42. NMJs were generally larger in co-cultures than in CPM controls (Fig. 5.42). While NMJ area was slightly higher in chronically stimulated co-cultures at 14, 21 and 28 DIV than non-stimulated co-cultures, these differences were not significant (Fig. 5.42 a). The largest NMJs were seen at 21 DIV for chronically photostimulated co-cultures, with an average of 378.01 μm ± 10.82, while in non-stimulated co-cultures 28 DIV cultures possessed the largest NMJs, with an average of 291.49μm ± 9.55. In control cultures, the average NMJ size was typically just over the minimum threshold (150μm) used in this analysis (Fig. 5.42 b). Non-stimulated control cultures at 21 DIV had a larger average area of 285.39μm ± 41.27 compared to 162.68μm ± 2.12 in stimulated co-cultures, however this result for non-stimulated cultures has a very large standard deviation of 165.09 due to the presence of one large NMJ in a small sample size (n=4), and was not statistically significant. Further repeats would likely diminish this outlier.

A simple assessment of NMJ morphology was conducted on all NMJs included in this analysis, to investigate differences in NMJ maturation between the conditions. For this assessment, NMJs were defined as having either a “simple” or “complex” morphology. A simple morphology was defined as either a circular or non-branched linear shape, while “complex” was any branched or “pretzel-like” appearance.

(a)

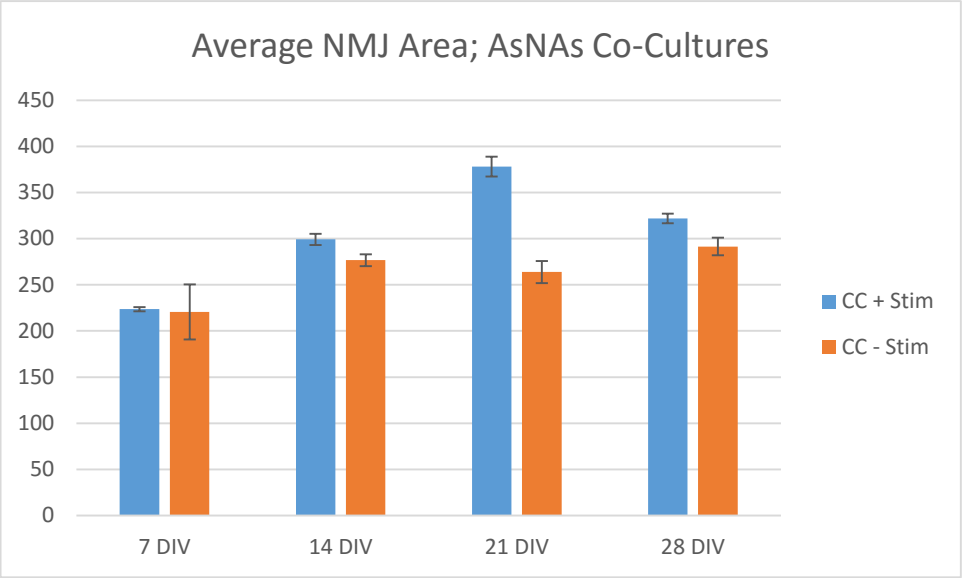

(b)

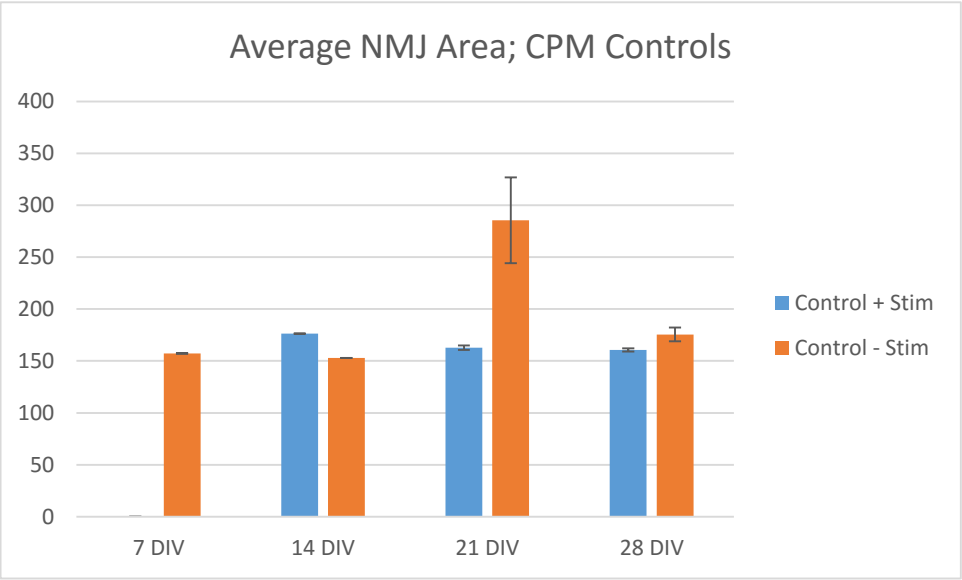

Figure 5.42 Average area of NMJs in CPM/AsNAs co-cultures and controls, with and without chronic photostimulation. (a) Average size of NMJs in chronically stimulated (blue bars) and unstimulated (orange bars) co-cultures. n= 4 for Day 7, n= 4 for Day 14, n= 5 for Day 21 and n= 6 for D28. **(b)** Average size of NMJs in chronically stimulated (blue bars) and unstimulated (orange bars) CPM control cultures. n= 3 for both conditions at all time points. Error bars show the S.E.M. ANOVA analysis was carried out between time points and T-Tests between +/- Stim at each time point, no significant differences found.

The results of this analysis are presented in figure 5.43 below. Complex NMJ morphologies were only observed on muscle fibres co-cultured with AsNAs; no complex NMJs were seen in CPM control cultures at any time point. The majority of NMJs in both chronically photostimulated and unstimulated co-cultures had a simple morphology. Synapses with a complex morphology first emerged after 14 DIV, with more complex NMJs seen in unstimulated cultures (Fig. 5.43). In chronically stimulated co-cultures, complex morphology was most frequently observed at 21 DIV (20.8%), with lower levels seen at 14 DIV and 28 DIV (8.7% and 10.8% respectively). For unstimulated co-cultures both 21 DIV and 28 DIV cultures showed the same proportion of complex NMJs (28.6%), while fewer were seen in 14 DIV cultures (13.3%).

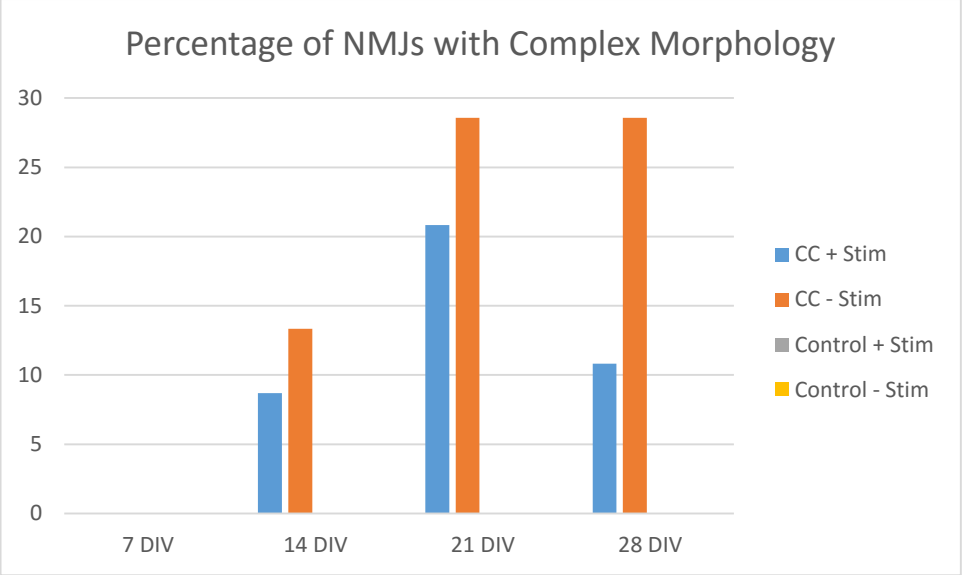

Figure 5.43 Percentage of NMJs across all time points with a complex morphology in CPM/AsNAs co-cultures and controls, with and without chronic photostimulation. No NMJs in CPM-only controls possessed a complex morphology, and so the bars for these conditions are not visible. Chronically stimulated (blue bars) and unstimulated (orange bars) co-culture did not develop complex morphology until at least 14 DIV. For co-cultures +/- Stim, n= 4 for Day 7, n= 4 for Day 14, n= 5 for Day 21 and n= 6 for D28. For controls +/- Stim n= 3 at all time points.

5.4.3 Incorporation of CPM/AsNAs co-cultures into a microfluidic device

As one of the primary aims of developing this *in vitro* neuromuscular co-culture is to provide a reliable, reproducible model for investigating neuromuscular circuit formation and function, I attempted to incorporate these cellular components into a simple microfluidic device. An Ibidi 3D chemotaxis slide was used, as it allows introduction of different cellular populations into two independent chambers, with a permeable channel connecting them, as shown in figure 5.44 below. This slide was coated with matrigel, and then astrocytes were loaded into one culture chamber, while chick primary muscle was loaded into the second chamber. The middle channel was filled with a higher concentration of matrigel to form a semi-permeable barrier, to inhibit cell invasion, but enabling axon outgrowth and innervation of the muscle chamber. Representative images of the microfluidic slide after 1 DIV, showing the two cellular chambers and the matrigel channel are presented in figure 5.44.

As can be seen from these images, this basic microfluidic device allows good separation of the different cell types, with a mostly empty permeable channel in between (Fig. 5.44 b). Both the astrocytes and the primary chick myoblasts attached to matrigel coated surface of the slide, and little invasion of the channel was seen. While the chick myoblasts formed a confluent monolayer, the astrocytes initially clumped up before spreading along the surface of the slide. Some evidence of myoblast fusion was already evident at this timepoint, however the majority of myoblasts remained unfused.

ESC-derived MACS sorted MNs were added to the astrocyte compartment on day 1, after the astrocytes had attached to the surface. Representative images of the microfluidic co-culture after 2 DIV are shown in figure 5.45. MNs can be seen associated with the astrocyte clusters, and attached to the surface of the chamber (Fig. 5.45). While some cells have invaded the middle channel on both sides of the device, the majority of cells remained in the separate compartments, segregating the different cellular populations.

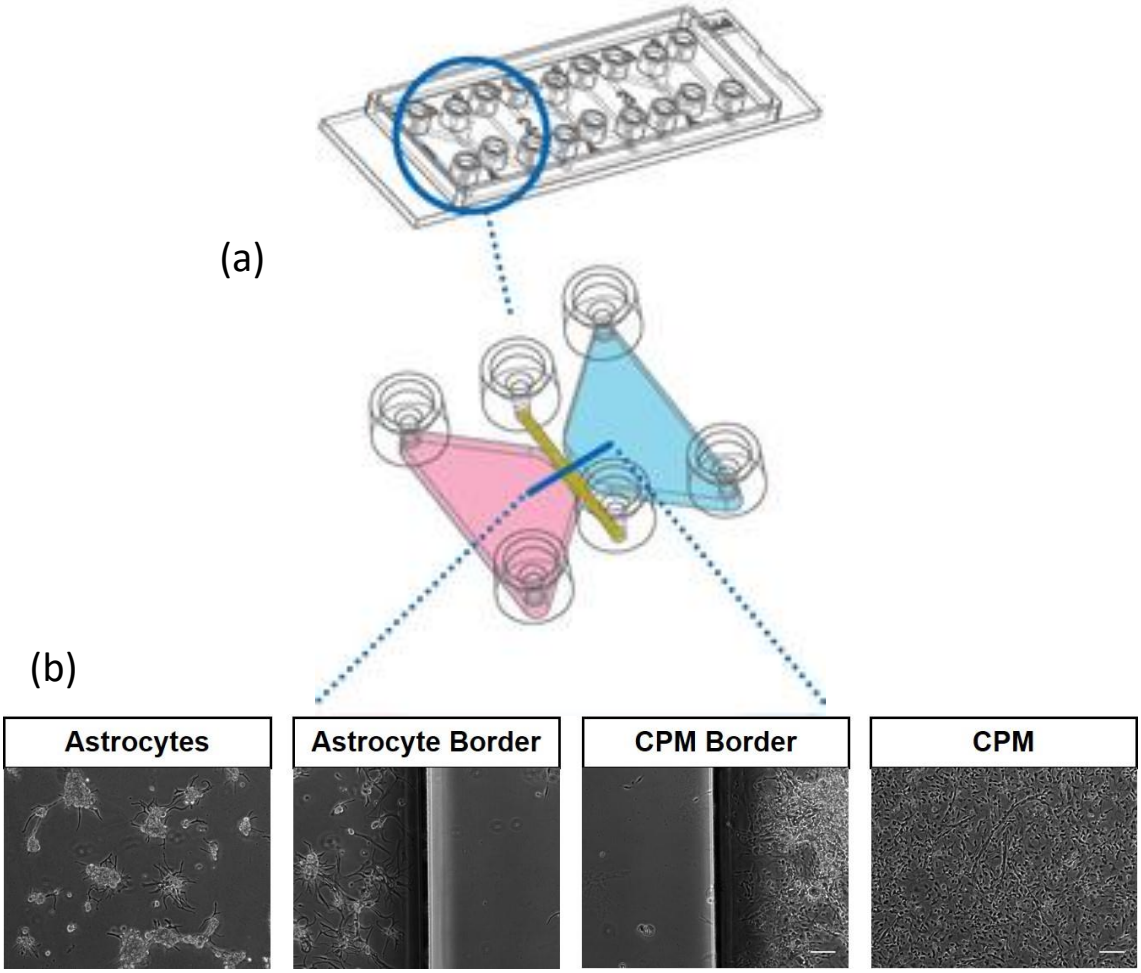

Figure 5.44 Incorporation of ESC-derived astrocytes and MNs with CPM in a simple microfluidic device. (a) An Ibidi 3d chemotaxis slide was used as a simple microfluidic device to separate the neural (pink) and muscular (blue) cellular components of a neuromuscular circuit, while allowing axonal innervation and connectivity. **(b)** Representative images from a microfluidic slide after 1 DIV, plated with astrocytes in the left chamber and CPM in the right chamber. The central channel was filled with concentrated matrigel, to inhibit cell mixing while allowing axon outgrowth. Scale bar = 100μm. (**a** adapted from image on http://ibidi.com/applications/ chemotaxis/u-slide-chemotaxis-3d/)

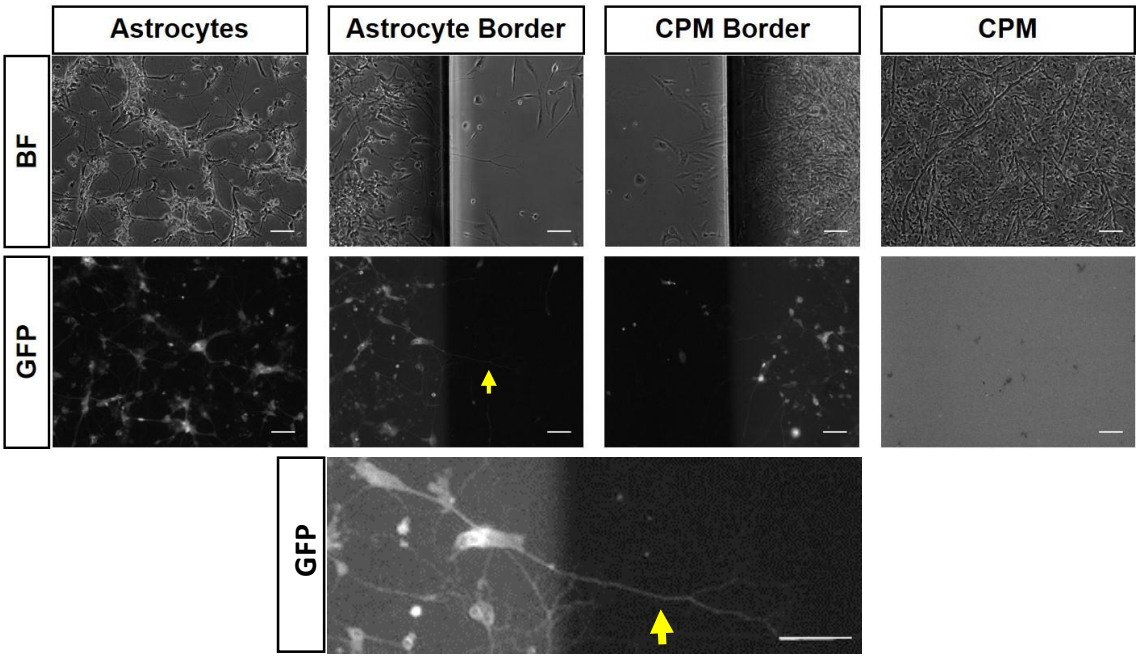

Figure 5.45 ESC-derived MNs cultured with ESC-derived astrocytes can extend axons through a matrigel channel towards a muscle target in a simple microfluidic device. Representative brightfield (top) and epifluorescent (middle) images from a microfluidic slide after 2 DIV, following addition of ESC-derived MNs in the left chamber. Note the GFP positive axon (yellow arrow) extending into the central channel towards the muscle chamber (enlarged at bottom). Scale bar = 100μm.

Using fluorescence microscopy, the GFP positive MNs can be identified. A network of GFP positive neurites can be seen extending throughout the neuronal chamber, with no apparent organisation or directionality (Fig. 5.45). Some GFP positive MNs can be seen in the central channel, and even in the CPM chamber at the border with the channel, indicating imperfect separation of the chambers. However, no GFP positive cells were seen in the central region of the CPM chamber, suggesting that contamination with motor neurons only occurred near the border with the middle channel. A long neurite can be seen invading the central channel from the neuronal chamber, and fluorescent imaging confirms this is a MN process, as it is GFP positive (Fig. 5.45). While this does prove the permeability of the matrigel barrier to MN axons, no axons were seen extending across the entire channel at this early time point.

Spontaneous contractile activity was observed in the CPM compartment, as shown in figure 5.46 below. This activity indicates that muscle contraction is possible in such a microfluidic device,

and can be easily recorded for analysis. While a longer time course of culture was intended, to determine if MN axons could invade the muscle compartment and form NMJs, the microfluidic devices were contaminated, and the experiment had to be stopped prematurely. Unfortunately this experiment could not be repeated due to time constraints, but on-going work in the lab aims to further develop this idea with custom-made microfluidic devices. This preliminary study shows the feasibility of culturing these cellular components in a microfluidic device, indicates the types of data obtainable, and enables future work to build upon this simple assay to develop reproducible, reliable *in vitro* models of neuromuscular circuit formation and development.

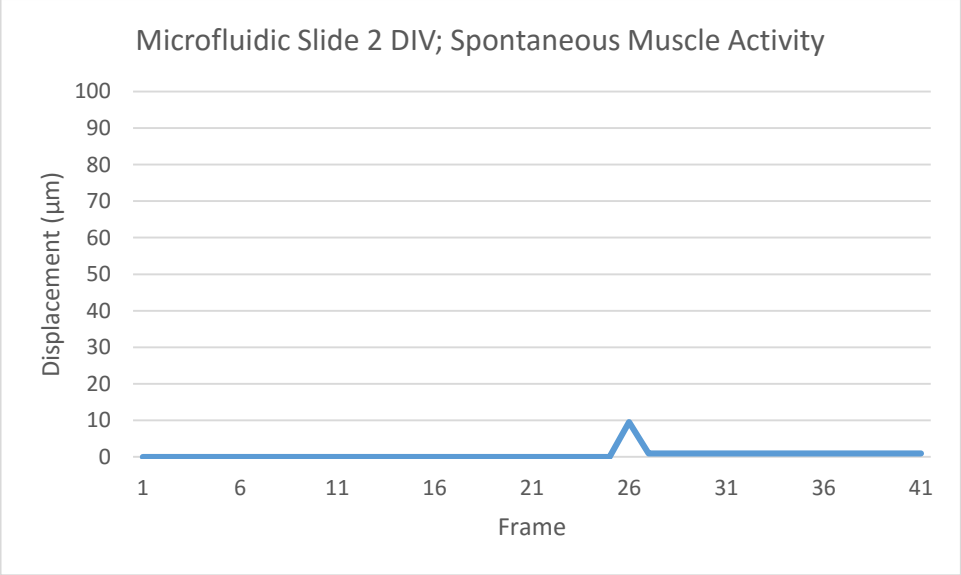

Figure 5.46 Spontaneous muscle activity recorded after 2 DIV in a microfluidic culture slide. Frame-by-frame analysis of a time-lapse movie of CPM after 2 DIV in a simple microfluidic device. Spontaneous activity was seen in some myocytes, even before undergoing significant fusion to form multinucleated myotubes.

Chapter VI

Discussion

The aim of this thesis was to develop a neuromuscular culture system containing both motor neurons and skeletal muscle derived from murine ESCs to enable characterisation and visualisation of function and development *in vitro*. A key objective was the development and maturation of neuromuscular junctions, as this structure is vital for normal neuromuscular function and appears key to the pathology of various neuromuscular diseases, including amyotrophic lateral sclerosis. Other important objectives included introducing MACS-sortable transgenes into stable ESC lines to allow purification of ESC-derived motor neurons and myoblasts from mixed populations, and incorporation of optogenetic components to enable non-invasive control of neuronal activity.

Both MNs and skeletal myoblasts were successfully produced from ESCs via exogenous factors and an inducible *Myod1* transgene respectively. Human CD14-based constructs were produced to enable MACS-purification of MNs and myoblasts using the Hb9 and myogenin promoters respectively. Co-culture of ESC-derived MNs with ESC-derived astrocytes enabled long-term survival of the MNs, allowing morphological and electrophysiological maturation as revealed by patch clamp recordings and confocal imaging. Introduction of a channelrhodopsin-2 transgene into the MN ESC-line provided external control of MN activity via blue-light stimulation, which closely replicated firing patterns seen with direct current injection.

While co-culture of ESC-derived MNs with ESC-derived myoblasts did result in immature synapse formation and contractile activity in ESC-derived myotubes, poor survival of the muscle tissue prevented long-term culture and maturation. Co-culture of ESC-derived MNs with primary chick skeletal muscle however did enable long-term *in vitro* culture, and NMJs with relatively mature morphologies were observed in these co-cultures after 2 weeks. Blue-light stimulation of ESC-

derived MNs via the channelrhodopsin-2 transgene resulted in strong contractions in surrounding muscle fibres, indicating the presence of functional NMJs between these populations.

These results demonstrate the use of ESC-derived cells for modelling clinically relevant cellular populations and tissues *in vitro*, recapitulating aspects of normal development including morphological and functional maturation. This work also demonstrates the value of transgenic stem cell lines in aspects ranging from directed differentiation to functional manipulation. Pluripotent SC-derived neuromuscular cultures such as this represent a reproducible and accessible model system to study various aspects of neuromuscular function and dysfunction in disease, and provide an ideal assay for pharmacological screens or other experimental therapies.

6.1 Embryonic Stem Cell-Derived Motor Neurons

6.1.1 Establishing optogenetic motor neurons

Multiple strategies for the expression of a channelrhodopsin-2 (ChR2) transgene in murine ES cells were undertaken for this work, described in chapter 3.2. While use of the A2.lox murine ES cell line described previously did enable successful integration of ChR2 downstream of an inducible tetracycline response element (TRE), this strategy did not result in stable, long-term expression of the transgene. This effect has been noted before in this cell line, whereby induction of transgene expression with doxycycline results in expression for a period of 3-4 days, after which the transgene becomes silenced (unpublished observations). This is thought to be due to epigenetic changes such as DNA methylation at the transgene locus, inhibiting transcription of the transgene.

The second strategy adopted was to use gene targeting to insert the transgene into the endogenous *MAPT* gene locus, thereby promoting expression of ChR2 specifically in neuronal cells. Confirmation that the DNA construct was functional and viable was obtained by transient transfection into COS-7 cells, which showed an inward current in response to blue-light stimulation during patch clamp experiments. However, motor neurons differentiated from

stably transfected, screened and selected ES cells did not show an electrophysiological response to photostimulation. While direct visualisation of the transgene via immunostaining was not possible due to mutation of the myc-tag, semi-quantitative PCR revealed significant levels of ChR2 mRNA in these motor neurons (MNs). This observation points to a problem in protein translation or trafficking to the membrane. Recent studies have shown that while ChR2 carries out its function at the plasma membrane, its trafficking to the membrane in mammalian neurons is dependent on fusion with a small soluble fluor moiety, such as GFP (Hochbaum et al., 2014). As the *MAPT* construct we designed was fused to a short myc tag as opposed to GFP, this may explain the lack of response to photostimulation seen in this cell line, due to failure to transport the protein to the plasma membrane, despite successful transcription of ChR2 mRNA.

The third strategy adopted here was to put ChR2 downstream of a constitutively active CAGs promoter, and insert the construct into the parental murine ES cell line via tol-2 mediated transposition. As done previously, the construct was first tested in COS-7 cells, where patch clamp studies revealed clear inward currents in transfected cells. Following antibiotic resistance selection and screening to identify stably transfected ES colonies, photostimulation was applied during voltage clamp to both undifferentiated ES cells and terminally differentiated MNs, both of which produced strong depolarising currents. This data confirmed that the transgene was expressed in the MN lineage and was functional, allowing direct control over electrophysiological properties of the stem cell-derived MNs via light.

6.1.2 Optimising *in vitro* culture of ES cell-derived motor neurons

Pure cultures of MACS-sorted ChR2-YFP positive stem cell-derived MNs showed sustained responses to photostimulation over a week of culture, confirming stable integration and expression of the transgene. Interestingly, the inward current elicited by a light pulse of the same length and intensity increased in amplitude over time in culture, indicating increased levels of ChR2 protein in the membrane at later time points. This could be due to increased transcription or translation leading to higher levels of the protein, and/or be due to low turnover

or degradation of the mature protein, allowing it to accumulate at the plasma membrane. This effect appears to more than compensate for the growth of the neurons and surface area of the membrane, enabling sufficient current to elicit APs in electrically mature neurons with elaborate dendritic and axonal arbours.

However, the viability of pure MN cultures rapidly declined within a few days of plating on coverslips, preventing long-term *in vitro* culture and functional maturation in this condition. One major reason for this may be the lack of supporting glia, such as astrocytes. Astrocytes have been shown to be particularly important for MN survival, contributing to metabolic and trophic support, supplying survival signalling factors and regulating the extracellular environment (Blackburn et al., 2009; Ransom and Ransom, 2012; Ullian et al., 2004). One key neurotrophic factor produced by astrocytes that has been identified is glial derived neurotrophic factor (GDNF), a distant member of the transforming growth factor-beta (TGF-beta) superfamily (Lin et al., 1993; Saarma, 2000). Initially shown to promote survival and morphological differentiation of midbrain dopaminergic neurons, it has since been demonstrated to influence MN survival, as well as having further roles in differentiation, migration and axon guidance (Gould et al., 2008; Henderson et al., 1994). Pure MACS-sorted MN cultures without glia will have little or no GDNF, limiting the viability of the cells. While recombinant GDNF added to the media did promote MN survival, widespread cell death was still observed, indicating the requirement of astrocyte-derived GDNF and/or astrocytes themselves (Stevenson, D., unpublished thesis, 2015).

Cultures of dissociated embryoid bodies (EBs) containing MNs resulted in improved long-term viability and MN survival, with similar results obtained showing functional expression of the ChR2-YFP transgene, an increasing light-response and electrical maturation over 1 week *in vitro*. This improved survival may be due to the presence of ES cell-derived astrocytes in the cultures, as the key signalling factors involved in spinal astrocyte differentiation are very similar to those for MNs; indeed the protocol developed in our lab to generate astrocytes from murine ES cells

is identical to the MN protocol for the first week. It would be interesting to confirm the presence of astrocytes in dissociated EB cultures using a marker such as glial fibrillary acidic protein (GFAP), and to determine the time course of emergence of this population.

While dissociated EB cultures promoted MN survival, many highly proliferative contaminating cells were also present in this condition, again limiting the long-term viability of the preparation. After the first week *in vitro*, most dissociated EB cultures were overgrown with proliferative cells of unknown identity, and died shortly after, preventing long-term investigation of MN development. While anti-proliferative compounds such as 5'-fluoro-2'-deoxyuridine [5-FdU, (Heidelberger et al., 1957)] were used to target this contaminating population, only temporary stalling of the overgrowth was possible in this format.

One interesting observation from dissociated EB cultures was the presence of significant spontaneous activity in the MNs, not seen in pure MN cultures. This activity may be due to the presence of other neuronal populations in the mixed culture, such as spinal interneurons. Spinal interneurons share a similar developmental pattern and origin with spinal MNs, and synapse with MNs *in vivo* and *in vitro* (Brown et al., 2014; Zhang et al., 2011). Unlike MN synapses with muscle, synapses between interneurons and MNs are thought to be largely glutamatergic, and may drive spontaneous activity (Zhang et al., 2011). It would be interesting to investigate the presence of spinal interneurons in these cultures using antibodies against markers such as Bhlhb5 for V1 and V2 interneurons and Lhx1 or Pitx2 for V3 interneurons, and to determine if synapses between interneurons and MNs are present (Francius et al., 2013; Wichterle et al., 2002). It would also be worth investigating if blocking glutamatergic signalling with NBQX or AP5 silences this spontaneous activity, to determine the influence of both AMPA and NMDA receptors respectively on MNs in mixed cultures.

To promote long-term survival of MNs *in vitro* without contaminating proliferative cells, we developed MACS-sortable ES cell-derived astrocytes, to allow co-culture of purified MNs with purified astrocytes. We combined the separate populations into aggregates via a hanging drop

protocol, which were then plated on glass coverslips for long-term culture. This format enabled long-term survival of MNs without overgrowth of contaminating cells from a dissociated EB limiting viability. Patch clamp recordings showed electrical maturation of these cells over 3 weeks *in vitro*, progressing from a non-spiking phenotype to firing trains of APs. Additionally, the light-evoked currents in these cells increased over time in culture, and elicited AP firing equivalent to activity generated through direct electrical stimulation.

While successful, these cultures were hard to standardise, with varying degrees of clumping and sizes of aggregates generated by the hanging drop method used to combine the separate cell populations. These variations may be responsible for some of the variations in electrophysiological responses obtained from MNs in these cultures, as most aggregates appeared to spread out across the substrate before extending neurites and symmetry breaking, possibly leading to variable maturation times. It may be possible to counter this by forming the aggregates in microwell culture plates as opposed to hanging drop culture, enabling more uniformly sized aggregates to be made. It would also be worth investigating the ideal ratio of astrocytes to neurons in these cultures, especially considering the variation in astrocyte/neuron ratios between different CNS regions and between species *in vivo* (Azevedo et al., 2009; Herculano-Houzel, 2011).

The final culture format tested was to plate MACS-sorted MNs on monolayers of MACS-sorted astrocytes. This condition provided the neurotrophic benefits of co-culture with astrocytes, while also improving the reproducibility of the cultures. Long-term survival of MNs was seen over 4 weeks, with improved morphological and electrical maturation. MNs fired APs earlier in this format than in aggregates, possibly due to earlier symmetry breaking and neurite extension, key initial steps in neuronal differentiation, due to not having to first migrate out of an aggregate, allowing earlier differentiation of electrical properties (Inagaki et al., 2011; da Silva and Dotti, 2002). The cell soma of most MNs in these cultures were observed to grow in size over time, and along with the continued extension of axons and dendrites contributed to the

steadily increasing membrane resistance measured during patch clamp recordings. It would be interesting to quantify this increase in size to see if it correlates with electrical maturation and whether a maximum size is reached.

Comparing the electrophsiological results obtained for ES cell-derived MNs in this study with reported properties of endogenous spinal MNs reveals a similarity in activity and passive properties. ESC-MNs fire repetitive trains of APs at relatively high frequency as seen *in vivo*, have a typical resting membrane potential and a comparable but higher membrane capacitance when compared to mouse spinal MNs (Carlin et al., 2000; Mitra and Brownstone, 2012; Sernagor and O'Donovan, 1991). ESC-MNs even displayed the characteristic spike-frequency adaptation seen in *in vivo* MNs, where initial APs have a higher frequency than successive APs during a sustained depolarisation, thought to improve muscle fibre recruitment at the beginning of an impulse, as seen in figures 3.12, 3.13 and 3.21 (Miles et al., 2005). Mature *in vivo* mouse spinal lumbar MNs however show a much faster AP and lower voltage threshold than found in this study, which may reflect further maturation is needed *in vitro* to achieve maximal functionality, or possibly reflect differences in MN identity (Mitra and Brownstone, 2012). While the finding reported here that the AP voltage threshold decreases while the current threshold increases over time in culture initially seems counter-intuitive, this could be explained by changes in ionic channel number or density during maturation. This would alter the membrane resistance, and especially an increase in potassium channels would increase the current threshold without dramatically influencing the voltage threshold. It would therefore be interesting to monitor changes in expression level and membrane recruitment of the key voltage-gated ion channels to determine if this explains the maturing electrophysiological phenotype.

My results are also similar to previous reports of properties ESC-MNs in vitro, again with similar but higher membrane capacitance, resting membrane potential and firing frequencies (Miles et al., 2004). The higher values found in this study may be explained by the longer culture time and therefore greater maturation of MNs in this study, as a trend towards steadily increasing

membrane capacitance and AP frequency was seen during maturation. As previous studies have suggested that ESC-MNs derived via this differentiation protocol tend to produce Lhx3 positive "medial motor column" MNs, it would be interesting to determine if the MNs generated in this study have the same identity, or more closely align to another motor column (Soundararajan et al., 2006). It would also be beneficial to test the responses of these cells to exogenous neurotransmitters such as glutamate, GABA and glycine, as well as demonstrating inhibition of AP firing and synaptic activity by tetrodotoxin and curare respectively, both to confirm responsiveness to these agents, and to allow greater comparison to previously published studies (Miles et al., 2004).

Another factor that may influence electrical maturation is the development of the axon initial segment (AIS). As mentioned in Results chapter 3.3.4, the AIS is a specialised region of the proximal axon found in most neurons that functions as the initiation point for action potential firing. To investigate if the acquisition of AP firing behaviour was related to AIS formation, I carried out immunocytochemistry using antibodies against AIS markers. While the antibody against the most common marker, the scaffold protein Ankyrin G, did not work in ES cell-derived MNs, this may be due to the fixation sensitive nature of this antibody. Repeating this staining with a shorter fixation step, a different fixative agent, or even a less concentrated paraformaldehyde solution may resolve this issue. It is highly unlikely that the AIS of ES cell-derived MNs do not contain Ankyrin G, as previous studies have shown Ankyrin G present in the AIS of somatic MNs in mice, and that it is key to organising this structure *in vivo* (Duflocq et al., 2011; Hedstrom et al., 2007; Le Bras et al., 2014).

Another antibody was used as a marker of the AIS for this study, phosphorylated I kappaB alpha (pIκBα). Constitutive NF-kappaB signalling has been documented in mammalian central nervous system (CNS) neurons, and has been specifically implicated in neuronal polarity acquisition and AIS development (Sanchez-Ponce et al., 2008; Schultz et al., 2006). Activated I kappaB kinase (IKK), phosphorylated p65 and pIκBα have all been shown to be enriched at the AIS, and loss of

pIκBα leads to impaired axon outgrowth and a failure to cluster Ankyrin G and form an AIS in cultured hippocampal neurons (Sanchez-Ponce et al., 2008; Schultz et al., 2006). However, despite these findings, pIκBα labelling has still been observed at the AIS of IκBα-KO mice, and was shown to be unnecessary for AIS assembly, indicating that the labelling is likely due to cross-reactivity with a phosphorylated epitope of a protein associated with the AIS cytoskeleton (Buffington et al., 2012).

The pIκBα antibody was first used alongside anti-Ankyrin G in rat hippocampal cultures to confirm specific labelling of the AIS. pIκBα labelling was then found to be specifically enriched in a proximal region of a single neurite in each MN studied in ES cell-derived MN cultures, revealing the presence of an AIS in these cells. Interestingly, an AIS was visible as early as 3 DIV in ES cell-derived MNs, prior to AP firing and electrical maturation. This may be due to the complex nature of a mature AIS, which is composed of scaffolding proteins, cell adhesion molecules, modulatory proteins, a unique extra-cellular matrix (ECM), and many voltage gated ion channels (Ogawa and Rasband, 2008). The observed discrepancy between AIS formation and electrophysiological maturity may be accounted for by the initial accumulation of scaffolding proteins early in development giving rise to pIκBα labelling, with later ion channel clustering required for functional properties and AP initiation. It is also possible that the specialised ECM is required for electrical maturity, and takes longer to establish than the intracellular components.

It would be interesting to investigate these possibilities through direct labelling of voltage gated sodium and potassium channels to reveal the time course of AIS development in these cells, and determine if this correlates with acquisition of mature functional properties. The influence of the ECM on electrophysiological maturation could be investigated by inhibiting its formation or degrading it using an enzyme such as chondroitinase ABC, either from initial plating or more acutely during culture.

It would also be worth investigating the plasticity of the AIS in these cells, as recent reports have shown the AIS to be a key structure involved in the modulation of excitability in neurons, both

via changes in length and position (Grubb and Burrone, 2010b; Kuba et al., 2006). This cell line is particularly suited to hyper-excitability studies, due to the stable expression of a Channelrhodopsin-2 transgene, allowing non-intrusive excitation via photostimulation. It could also be possible to generate an ES cell line with a fluorescently tagged Ankyrin G protein, to allow live imaging of AIS development and modulation.

6.2 Establishing *in vitro* muscle culture

6.2.1 Establishing ESC-derived muscle

A major goal of stem cell research is the reliable generation of specialised, differentiated cells from pluripotent stem cells for use in disease modelling or therapy. While reliable protocols for the generation of many types of differentiated somatic cells have been established, including the protocol to generate spinal motor neurons used in this study, a protocol to generate skeletal muscle using exogenous factors or small molecules has remained elusive.

An alternative strategy to produce specific cell lineages from stem cells has been to drive differentiation using inducible transgenes to force the population towards a particular cell fate. Multiple studies have reported some level of success using this strategy to generate skeletal muscle, including forced expression of the paired box genes Pax3 or Pax7, and the myogenic transcription factor Myod1 (Darabi et al., 2008b; Skoglund et al., 2014; Tanaka et al., 2013). Another approach has been to FACS sort differentiating cells for early markers of the paraxial and lateral mesoderm lineages, such as the α-receptor for platelet-derived growth factor (PDGF-αR) and vascular endothelial growth factor receptor-2 (VEGFR-2) (Darabi et al., 2008b; Sakurai et al., 2008).

As initial attempts to generate skeletal muscle using a doxycycline-inducible Pax3 stem cell line were not successful in our lab, I generated a doxycycline-inducible *Myod1* murine ES cell line. This strategy was chosen due to the well documented ability of this myogenic regulatory factor (MRF) to force conversion of multiple differentiated cell types including fibroblasts and chondroblasts into the muscle lineage, and the observed strength of this transcription factor in epigenetic reprogramming (Choi et al., 1990; Hirai et al., 2011). Additionally, *Myod1* has been shown to directly up-regulate the expression of multiple other myogenic genes including *Pax7* and M*yogenin* (Gianakopoulos et al., 2011). A second construct to generate a doxycycline-inducible *Myf5* transgene was also generated as a back-up strategy, as these transcription

factors appear somewhat functionally redundant in myogenesis, with only a double-knockout resulting in loss of muscle formation, while a single knockout leads to compensatory up-regulation of the remaining transcription factor (Rudnicki et al., 1992, 1993).

Induction of Myod1 expression in murine ES cells via doxycycline following two days of embryoid body differentiation resulted in clear expression of myosin heavy chain (MHC), a definitive marker of terminal muscle differentiation. No MHC was detected in un-induced controls. In addition to expression of this lineage marker, the morphology of the doxycycline-induced cells changed to an elongated spindle shape, characteristic of proliferative myoblasts. While conversion to myoblasts was not 100% efficient, recent advances in epigenetics may provide a strategy to increase the efficiency of Myod1-driven differentiation. It has been shown that in human ES cells, forced expression of the SWI/SWF component BAF60C facilitates Myod1 positioning and chromatin remodelling at target sites, epigenetically committing the cells to the myogenic lineage (Albini et al., 2013). A similar strategy could be used in conjunction with forced Myod1 expression in ES cells to enhance the myogenic differentiation, and produce a more uniform skeletal muscle culture. Recent advances in our understanding of the contribution of other signalling factors such as Wnt and Fgf to the generation of paraxial mesoderm, as well as screens to identify small molecules and pathways that drive myogenesis, present further opportunities to produce stem cell-derived muscle without the need for transgenic strategies in the near future (Gouti et al., 2014; Xu et al., 2013a). The results presented here confirm the conversion of the murine ES cells to the myogenic lineage, and the clone with the best morphology and most specific MHC expression was selected for further characterisation and optimisation.

6.2.2 MACS-sortable ESC-derived muscle

To further refine ES cell-derived muscle culture, and greatly increase the reproducibility and reliability of the resulting cells, a MACS-sortable transgene was inserted to enable purification of the desired cell type. The tol-2 transposable element was chosen to enable stable genomic

integration of the transgene, and due to the lack of target site specificity and high efficiency of this technique in vertebrate cells compared to other systems (Balciunas et al., 2006; Kawakami and Noda, 2004). The cell-surface marker CD14 was chosen as the MACS-target marker due to previous success using this transgene to sort other types of ESC-derived differentiated cells (Machado et al., 2014). The myogenin promoter was selected to drive specific expression of the CD14 transgene for MACS, as myogenin is expressed downstream of Myod1 and only after commitment to myogenesis (Berkes and Tapscott, 2005; Rudnicki and Jaenisch, 1995).

Successfully transfected clones were selected via hygromycin resistance conferred by a hygromycin resistance cassette 5' to the CD14 transgene in the tol-2 construct. A sub-clone with strong specific expression of CD14 in muscle cells with clear myoblast morphology was chosen for all further studies. Due to the random nature of tol-2 integration in the genome, it was necessary to map the insertion site of the transgene via inverse PCR mapping. As only the 5' end of the tol-2 construct (Tol2R) returned a reliable result, with the expected primer binding sites and 5' end of the tol-2R element running into genomic DNA, further repeats of the inverse PCR protocol should be carried out to confirm this initial result, and investigate the possibility of multiple insertions. The 5' tol-2 element was found integrated into the *Tanc1* gene on chromosome 2, a relatively poorly characterised gene encoding a 200 kDa ankyrin-repeat containing scaffolding protein localised to the post-synaptic density of neurons (Suzuki et al., 2005). While this insertion may result in loss of one copy of this gene, no obvious influence on MN function or viability was observed in this cell line, indicating that a single allele of *Tanc1* is sufficient for the normal functioning of MNs.

MACS-sorting of this sub-clone revealed clear enrichment of the MHC-positive (Mf20) population, and depletion of non-MHC expression cells from the eluate. Conversely, there was noticeable depletion of MHC-positive cells from the flow-through fraction, indicating successful purification of the myogenic population. These results were further confirmed with flow cytometry and over multiple repeats, confirming the reliability of this sorting method and the

stable expression of the CD14 transgene over multiple passages. While some contamination of the eluate with non-MHC expressing cells was still seen, this is expected in MACS sorting, and is likely due to residual cell aggregation or clumping after chemical dissociation. We have also observed from ES cell-derived MN MACS sorts that some cells in the eluate that do not initially express markers of lineage commitment do go on to terminall differentiate 1-2 days following the sort, indicating that expression of the CD14 transgene precedes terminal marker expression (unpublished observations). This may also be occurring in the ES cell-derived muscle differentiation, with the myogenin promoter used in the transgene becoming active prior to the endogenous *myogenin* gene or MHC expression.

It may be possible to improve the quality or efficiency of the MACS sorting protocol by pre-sorting the differentiated cells for markers of paraxial mesoderm such as the PDGF-α receptor, restricting the CD14 MACS-sort to mesodermal progenitors, and therefore eliminating many of the potential contaminating cells (Darabi et al., 2008b; Sakurai et al., 2008). To reduce the impact of any contaminating cells remaining, 5'-fluoro-2'-deoxyuridine (5-FdU) was added to the eluate for the first 2 days of *in vitro* culture to prevent proliferation. However, even with this treatment, some proliferative cells were still observed. Longer or repeated 5-FdU treatment may be necessary to prevent this, or use of alternative anti-proliferative agents such as arabinofuranosyl cytidine (Ara-C).

6.2.3 Characterisation of ESC-derived muscle

Immunostaining of ES cell-derived myoblasts 1 day post-MACS revealed expression of multiple muscle-specific proteins, indicating complete conversion to the myogenic lineage. Additionally, the positive labelling using the My32 antibody is of particular interest, as this antibody is specific for an isotype of MHC found only in fast skeletal muscle, as opposed to cardiac or smooth muscle (Havenith et al., 1990). These results suggest that induction of *Myod1* expression is sufficient in itself to induce the full genetic program for fast skeletal myogenesis, via interaction with other MRFs and epigenetic remodelling. However, not all cells in doxycycline-induced conditions

showed conversion to myoblasts, similar to results seen with transfection of *Myod1* into some cell lines including HeLa cells (Weintraub et al., 1989). This may be due to epigenetic changes and commitment to other lineages during the embryoid body phase of differentiation, or the lack of certain Myod1 cofactors, such as E box proteins or MEF2 proteins. Forced expression of BAF60C may improve the efficiency of myoblast formation as mentioned previously, by facilitating Myod1 positioning and chromatin remodelling at target sites key to the myogenic program (Albini et al., 2013).

While the generation of ES cell-derived myoblasts was relatively successful using this method, long-term *in vitro* culture of these cells remains problematic. Long-term viability was poor on multiple culture substrates and media formulations, despite similar conditions allowing long-term culture of primary chick skeletal myoblasts. One possible reason is the lack of necessary survival factors or media supplements required specifically by murine myoblasts. Use of mouse embryonic extract instead of chick embryonic extract may resolve this issue. An alternative explanation may be the lack of a supportive environment, including the lack of other tissues typically found *in vivo*, such as the connective tissue, fibroblasts, endothelial cells or adipose cells, similar to the lack of astrocytes in the initial MN cultures. Indeed, defects in connective tissue transcription factor expression have been linked to musculoskeletal defects such as Holt-Oran syndrome, revealing the importance of this tissue for proper muscle development (Hasson et al., 2010). Additionally, the physical conditions of the culture may be a limiting factor; this is especially relevant due to the serendipitous long-term culture achieved by a floating aggregate of murine ES cell-derived myoblasts that fused to form myotubes with visible sarcomeres after 6 weeks *in vitro*. This result indicates that a 3-dimensional culture format may be necessary for improved long-term survival and maturation of murine skeletal muscle.

Use of different substrate materials and culture conditions, including 3D culture, has been reported previously, with varying levels of success and reproducibility. While the matrigel substrate used in this study provided reproducible muscle development and allowed MN

innervation and NMJ formation, incorporating collagen, fibrin or PDMS based substrates into 3D culture systems seems to provide improved tissue architecture, myofiber alignment and fusion, and increased reproducibility (Bian et al., 2009; Martin et al., 2015; Smith et al., 2012). Another advantage of such systems includes the ability to monitor and assess the biomechanics and force generation of resultant cultures, allowing more direct measurement of muscle function and contractile force (Martin et al., 2015; Ramade et al., 2014).

While the stem cell-derived transgenic myoblasts described in this study show many key characteristics of skeletal muscle found in vivo, including expression of fast skeletal muscle-specific myosin heavy chain isotypes, expression of *Myogenin* and *M-Cadherin* as well as fusion to form multinucleated myotubes displaying a striated F-actin cytoskeleton and functional contractions and synapses with MNs, they are perhaps not reflective of true *in vivo* development. As these cells are forced into the myogenic lineage by overexpression of a *Myod1* transgene, based on previous studies showing the importance of this transcription factor for muscle differentiation, they are effectively trans-fated from the non-somitic mesoderm-like tissue found in growing embryoid bodie (Choi et al., 1990; Hollenberg et al., 1993; Tapscott et al., 1988). This may result in a compromised myogenic lineage with a conflicting transcriptome that is not an accurate representation of endogenous skeletal muscle, and may even explain the poor long-term survival observed *in vitro*. A better stem-cell derived model of skeletal muscle has been developed recently, using only exogenous signalling factors to drive differentiation into the myogenic lineage via a pre-somitic mesoderm-like fate that recapitulates primary and secondary myogenesis that even gives rise to *Pax7* positive satellite cells, not seen in previous stem cell-derived muscle cultures (Chal et al., 2015). Incorporation of myoblasts generated by this directed differentiation into 3D culture substrates may therefore provide the best current *in vitro* model for studying skeletal muscle development and neuromuscular circuit formation, and co-culture with the optogenetic stem cell-derived MNs described here would enable great advances in *in vitro* modelling of neuromuscular circuits.

6.2.4 ESC-derived muscle activity

Manual measurement of the displacement of visual landmarks in short time-lapse movies of ES cell-derived muscle cultures enabled analysis of contractile activity. Spontaneous activity was seen in both fused myotubes and individual myoblasts, however fused cultures produced much larger displacements. While beyond the scope of this investigation, developing a more thorough and preferably automated analysis using multiple reference points from the movie would likely improve the characterisation of this phenotype significantly. Additionally, adding artificial reference points to be used in the analysis could significantly improve the reproducibility and consistency of the data, such as coloured or fluorescent beads embedded in a flexible culture substrate or directly in the culture itself. If analysis could be automated, it could also be preferable to install a camera inside the incubator, allowing collection of activity data over long periods of time and in a preferable environment, compared to the relatively short movies manually filmed in a non-sterile, not atmospherically controlled microscope room.

Unfortunately, due to the poor long-term viability of ES cell-derived muscle cultures, analysis of activity at later developmental time points or in co-culture with MNs was not possible in this study. Improvements the survival of the cultures *in vitro* via any of the strategies outlined previously may allow a better characterisation of ES cell-derived muscle development and activity. Of particular interested would be successful 3D culture, as a 3D muscle culture between defined flexible anchor points (similar to tendons *in* vitro) would allow direct measurement of the displacement of these anchor points.

6.2.5 Establishing chick primary skeletal muscle culture

As an alternative synaptic target for ES cell-derived MNs, chick primary muscle (CPM) culture was chosen due to the well-established protocols and relative ease and cheap cost of production (Caplan, 1976; Gerstenfeld et al., 1984). Initial testing of culture substrates and media revealed that chick embryo extract (CEE) was a necessary supplement for long-term survival, morphology and viability. Conversely, the matrigel concentration used to coat the substrate, and the

different substrates themselves did not significantly impact CPM morphology or viability. As with ES cell-derived cultures, contaminating proliferative cells quickly overgrew cultures, limiting long-term survival. Pre-plating the dissociated cells for 30 minutes and harvesting the suspended fraction reduced the number of contaminating cells, as contaminating fibroblasts adhere to the surface much more readily than skeletal myoblasts. Following this, treatment with 5-FdU for the first 2 days of culture also greatly limited the influence of proliferative cells on these cultures, but was still not sufficient to prevent eventual overgrowth beyond 4 weeks.

As the substrate material had little impact on culture viability, all experimental CPM cultures were grown on glass coverslips, standardising the preparation of these cultures with MN cultures, and allows confocal microscopy of the samples. One disadvantage of this format is the inability to grow 3D cultures on coverslips, which may be more representative of *in vivo* muscle development. The standard concentration of cells used was 1 million per 18mm coverslip, as this gave the most consistent monolayer culture over repeated cultures.

Similar to results with ES cell-derived myoblasts, CPM expressed markers of terminal muscle differentiation, including positive labelling with the My32 antibody, revealing fast skeletal muscle specific MHC. While low level staining was observed using the myogenin antibody F5D, it is likely this was non-specific background staining, likely due to the species specific nature of this antibody, which only recognises mammalian myogenin protein (Wright et al., 1991); http://dshb.biology.uiowa.edu/myogenin). While the mCadherin staining was also very weak and possibly non-specific background staining, this may also be due to species selectivity. To better characterise these cultures, it would be desirable to test the expression of more myogenic lineage markers, such as desmin, chick myogenin and α-actinin. Additionally, the presence of mesodermal progenitors or satellite cells in these cultures could be investigated using antibodies against Pax 3 and 7, which were not found in murine ES cell-derived muscle cultures.

6.3 Modelling Neuromuscular Circuits *In Vitro*

6.3.1 ESC-derived muscle/EB co-culture

Co-culture of ES cell-derived myoblasts with unsorted EBs resulted in outgrowth of neurites from EBs into the surrounding muscle tissue after 1 DIV and spontaneous contractile activity in the muscle after 3 DIV. While the strength of this contractile activity was not noticeably different to spontaneous activity in pure ES cell-derived muscle cultures, there was a noticeable increase in fused myotubes compared to unfused myoblasts in the co-cultures. This observation indicates that co-culture with MNs may accelerate myoblast fusion, and would be worth repeating the experiment with quantification of this phenotype to further investigate this possibility. It would also be interesting to determine if any effect of the MNs on the muscle at early time points (such as accelerated fusion or contractile activity) is via synaptic signalling or alternatively is a result of non-specific spontaneous release of neurotransmitters, similar to suggestions that CNS circuits mature in response to non-synaptic neurotransmitter release (Andreae and Burrone, 2014). This could be achieved by blocking MN-muscle synapse function using α-bungarotoxin, effectively silencing this mode of signalling.

Another observation from these cultures is that multiple different patterns of activity were seen in different myotubes, even within the same culture. If MN activity is driving this activity, this may be due to variable input from the MNs, or variable contraction thresholds in the muscle; this could be confirmed by patch clamp experiments to correlate muscle contraction with the firing patterns of the innervating MN. However, if this variable contractile activity is independent of MN innervation, it may be due to the presence of different sub-types of muscle, normal variations in spontaneous activity or possibly some other unforeseen heterogeneity or culture artefact. Further work is needed to clarify this phenomenon.

Stimulation of these co-cultures with blue light resulted in light-evoked contractions as early as 4 DIV, indicating the presence of functional synapses at this stage. Light-evoked activity was

reliable, and slightly stronger than spontaneous contractions, suggesting a stronger calcium response in the post-synaptic muscle target compared to spontaneous activity. No light-evoked activity was seen in pure ES cell-derived muscle cultures, confirming this behaviour is due to the ChR2 transgene in the MN population. Light-evoked contractions were only observed in myotubes physically close to EBs however, suggesting that MN axons did not reach the edges of the coverslip after 12 DIV. Light-evoked activity was much weaker at 12 DIV, suggesting a decrease in the viability of the cultures by this time point, also reflected in the poor morphology of the cultures seen after 14 DIV. Interestingly, this decrease in light-evoked activity reflects the procession of some *in vivo* neuromuscular diseases where breakdown of the NMJ precedes MN cell death (Fischer et al., 2004; Frey et al., 2000; Murray et al., 2008). As there is also much lower spontaneous activity at this time point, it is likely that myotube death is also a contributing factor in this culture condition.

Immunocytochemistry of these co-cultures at 14 DIV revealed concentrations of α-bungarotoxin-labelled acetylcholine receptors closely opposed to GFP positive axons, suggesting the presence of synapses or NMJs. However, no clear NMJs with complex morphology were seen in ES cell-derived myoblast/MN co-cultures at this time point. As the functional data indicates a significant decrease in viability by 12 DIV, it is possible that the majority of NMJs have broken down by 14 DIV. It would be worth repeating these cultures and investigating α-bungarotoxin staining at 3-5 DIV, when clear light-evoked activity is seen. While more MN/muscle synapses may be visible at earlier time points, it is unlikely that NMJs with complex morphology will be observed this early in the co-culture, as the maturation of the synapse takes up to 2 weeks *in vivo* (Personius and Balice-Gordon, 2001; Sanes and Lichtman, 1999).

6.3.2 Primary Chick Skeletal Muscle/Embroid Body Co-Culture

In co-cultures of chick primary muscle with EBs, multiple YFP-positive neurites could be seen extending out of the EB aggregates within the first week of culture. While processes radiated out from each EB throughout the surrounding myotubes, in many areas they aligned with muscle

fibres, suggesting some level of recognition that the CPM is a target structure. In most cases there were multiple neurites making contact with each myotube near the EB, suggesting that there may be intense competition for space or functional synapses between the MNs in the aggregate.

Photostimulation resulted in light-evoked contractions at all time points up to 4 weeks *in vitro*, that peaked in strength at 20 DIV. Evoked activity was much stronger than spontaneous activity which was also observed in these cultures. The most spontaneous activity was observed at 12 DIV, which could possibly represent a phase of reinforcement or stabilisation of immature synapses which then mature to form functional NMJs by 20 DIV, reflected by the strong stimulus evoked activity at this time point. By 26 DIV however, both the spontaneous and stimulus evoked activity and was significantly lower, and visual observation revealed overgrowth of the cultures by contaminating proliferative cells, despite treatment with 5-FdU after initial plating. This decrease in contractile strength may be a reflection of the declining viability of the cultures at this stage, possibly due to competition with contaminating cells for nutrients or build-up of waste products past sustainable levels. Improved elimination of these contaminating cells from the culture preparation may prevent premature death of these co-cultures, enabling NMJ maturation to be followed over a longer time period.

While fusion of myoblasts to form multinucleated myotubes and sarcomeric structure was seen in muscle in both EB co-cultures and CPM only cultures, NMJs with a complex, pretzel-shaped morphology were only observed in EB co-cultures from 14 DIV onwards. This observation suggests that the maturation of simple acetylcholine receptor clusters into the large, complex structures associated with NMJs is dependent on MN input, while fusion of myoblasts and development of sarcomeres is MN independent. This finding supports observations from skeletal myogenesis *in vivo*, where pre-patterned AChR clusters are found on multinucleated myofibres prior to the arrival of MN axons, but the formation of morphologically and functionally

mature NMJs requires neuronal activity and signalling factors from the axon terminal (Darabid et al., 2014; Yang et al., 2001).

Immunocytochemistry of CPM/EB co-cultures revealed the co-localisation of α-bungarotoxin with synaptophysin, a maker of pre-synaptic terminals, supporting the presence of functional synapses between MNs and muscle at these sites. While labelling for choline acetyl-transferase (ChAT), a common marker of cholinergic synapses, was not clearly opposed to α-bungarotoxin puncta (Figure 5.21), the staining produced by this antibody was poor, with high levels of background labelling. Repeating this staining with fresh antibody for ChAT may give a clearer result. Labelling the MN axons with anti-GFP revealed very clear innervation of α-bungarotoxin positive synapses, with direct overlap of GFP positive axon terminals with acetylcholine receptor complexes in multiple cases. These results reveal the formation of functional, functionally mature, cholinergic NMJs in these co-cultures, with direct control over activity possible via photostimulation of a ChR2 transgene expressed in the MN population.

6.3.3 Primary Chick Skeletal Muscle/AsNAs Co-Culture

While the use of unsorted EBs as a source of ES cell-derived MNs for co-culture with muscle enables viable, functional neuromuscular circuits that mature and form NMJs *in vitro*, the presence of many uncharacterised and proliferative contaminating cells from the EB results in a relatively poorly controlled and unreproducible model system. To improve upon this model, MACS-sorted MNs and astrocytes were combined via hanging drop culture to form well characterised astro-neural aggregates (AsNAs) for co-culture. As previous experiments showed little to no spontaneous activity in MNs cultured in this format, blue-light stimulation was used to induce neural activity in these co-cultures, to encourage functional synapse maturation.

Chronically photostimulated AsNAs co-cultures show a similar maturation profile to EB co-culture, however they had a higher peak contractile strength, and achieved this peak earlier, at 12 DIV. This result indicates that specific MN driven activity may reinforces developing synapses, and strengthen post-synaptic responses in the myotube population. On the other hand, non-

chronically stimulated co-cultures showed significantly weaker light-evoked contractions (Figure 5.33), suggesting the impaired development and maturation of NMJs when MN activity is low or absent. These results support findings from *in vivo* studies of neuromuscular development, which show that NMJ maturation is impaired in mouse models of spinal muscular atrophy, which have reduced MN activity (Kong et al., 2009). Imposing inactivity on otherwise healthy MNs using tetrodotoxin or spinal hemisection also results in remodelling of NMJs at fast-type muscle fibres, revealing a requirement for continued activity to maintain NMJ integrity (Prakash et al., 1999).

Confirmation that light-evoked muscle contraction was driven by acetylcholine release at NMJs was provided by blocking acetylcholine receptors in live co-cultures using α-bungarotoxin, a competitive and irreversible nicotinic acetylcholine receptor antagonist. After incubation with the toxin for 30 minutes at room temperature virtually all muscle activity ceased, and blue-light photostimulation could no longer illicit a contractile response. It would be interesting to repeat this experiment with patch clamp data from the MN population to confirm that MN activity was unaffected, and α-bungarotoxin treatment results in specific inhibition of neurotransmitter-dependent contractile activity. Another method to show this effect would be to block neurotransmitter release using botulinum toxin, which would be predicted to cause a similar effect on contractile activity as seen with α-bungarotoxin.

As the activity of the MNs in these co-cultures (and indirectly the activity of the muscle) can be controlled via photostimulation, an interesting extension to this work would be to investigate the effect of different stimulation patterns on the cultures. As the muscle used here is skeletal muscle, long-duration stimulation should result in tetanus, which would not occur in the case of cardiac muscle, due to the longer refractory periods in that muscle type (Henderson et al., 1971). It may also be possible to use light-driven activity to “train” the muscle, resulting in stronger contractions and larger myofibres over time *in vitro*. Also, as the fast/slow subtype identity of mature skeletal muscle is partially dependent on MN activity patterns *in vivo*, it may be possible

to convert the muscle population *in vitro* to a slow muscle identity using only light-evoked activity patterns (Pette and Staron, 2000).

Analysis of NMJ formation via immunocytochemistry revealed the presence of synapses at all time points in co-cultures, with large mature NMJs seen at 21 and 28 DIV. Similar to EB/CPM co-cultures, no large post-synaptic endplates were seen in CPM only controls, reinforcing the idea that MN activity is required for NMJ development and maturation. Further strengthening this idea is that more NMJs were observed in chronically stimulated co-cultures, and more synapses were occupied by GFP positive MN axons in the stimulated condition. Even fewer "NMJs" were seen in unstimulated controls, indicating that even relatively silent axons provide some level of signalling to support synapse formation and stabilisation. It would be interesting to further test this hypothesis by preventing neurotransmitter release in a chronically stimulated co-culture (e.g. by botulinum toxin) to determine if the supportive effect on NMJ development is neurotransmitter dependent, or alternatively via another mechanism.

While chronically stimulated co-cultures had slightly larger NMJs on average, this difference was not statistically significant, and possibly due to expected variation, especially due to the relatively low number of cultures analysed for this data set (Figure 5.42). A more typical analysis of NMJ formation would be to analyse only those structures which show co-localisation between pre-synaptic and post-synaptic components, for example synaptophysin and α-bungarotoxin labelling respectively. While this data was included in the analysis reported here (Fig.5.40 and 5.41), in order to allow comparison with muscle-only control cultures a measure not including pre-synaptic components was necessary. For this reason, a NMJ was classified as any α-bungarotoxin labelled structure with an area larger than 150μm. This value was found to exclude the vast majority of staining artefacts, and appeared most physiologically relevant in co-cultures – structures smaller than this were never innervated. Interestingly, other studies have reported a similar minimum size for NMJ development *in vivo*, indicating this may be a reliable indicator of post-synaptic specialisation (Sleigh et al., 2014a, 2014b). This definition does however open

the possibility of analysing post-synaptic clusters of acetylcholine receptors that could never be functionally innervated, or possibly large staining artefacts caused by aggregations of primary or secondary antibody.

Unexpectedly, the percentage of NMJs with a "complex" morphology was slightly higher in non-chronically stimulated co-cultures, however this difference is due to the lower total number of NMJs in this condition, as chronically stimulated co-cultures had more NMJs with complex morphology in total (Figure 5.43). Pure CPM controls had smaller NMJs and never showed complex morphology, again reinforcing the idea that NMJ development and maturation is MN dependent.

The distinction of simple vs complex NMJ morphology was based upon observations of NMJ maturation seen *in vivo*, where throughout post-natal development, NMJs mature from a simple ovoid plaque shape to a structurally complex "pretzel-like" morphology by gradual accumulation of perforations in the post-synaptic endplate (Marques et al., 2000; Sanes and Lichtman, 2001). This transition is a gradual process, however in this study only two states were defined, "simple" or "complex", where simple represents an ovoid plaque morphology, whilst a NMJ was deemed complex if at least one perforation was observed in its structure (see figure 6.1 for examples). While these criteria are relatively easy to determine, they do not capture the full range of morphological maturation that these specialised synapses undergo, and could be open to error due to imaging or labelling artefacts.

In addition to the influence of MNs on NMJ maturation shown here, multiple studies have shown the influence of MNs on muscle development *in vivo* and vice-versa. Perhaps most strikingly, loss of MN innervation in development leads to poor AChR patterning, and loss of MNs in adults leads to changes in fibre type composition, muscle atrophy and eventual degeneration, a situation clearly seen in motor neuron diseases and nerve injury (Aravamudan et al., 2006; Ohira et al., 2006; Yang et al., 2001; Yohn et al., 2008). Meanwhile, trophic factors produced by muscles have been shown to influence MN survival, sprouting and axon pathfinding. For

instance, overexpression of GDNF in muscle can cause hyperinnervation of NMJs by MNs, and has been shown to improve functional recovery after nerve injury (Glat et al., 2016; Kablar and Belliveau, 2005; Nguyen et al., 1998). Other neurotrophins, including neurotrophin-3 (NT3), have also been shown to promote MN survival (Angka and Kablar, 2007; Funakoshi et al., 1995).

This co-culture system could therefore serve as a suitable assay to investigate these MN-muscle interactions during development and maturation. The survival, functionality and morphology of both MN and muscle components could be assessed in co-culture versus monoculture, and the maturation and morphology of motor end plates in particular could be assessed. Preliminary results from this study suggest that co-culture with MNs leads to more numerous, larger and more morphologically mature post-synaptic specialisations on the myofibers, supporting the previously mentioned findings from *in vivo* experiments. Development of more controlled co-cultures, for example in microfluidic devices, would allow easier assessment of MN survival, myoblast fusion index and synapse formation than was feasible in the relatively large mixed co-cultures described in this study. Finally, use of all stem cell-derived components in the co-culture would allow easy manipulation of growth factor expression, as transgenes could be inserted to drive overexpression of GDNF or NT-3 in the muscle lineage for example, to investigate the effect on MN survival and innervation.

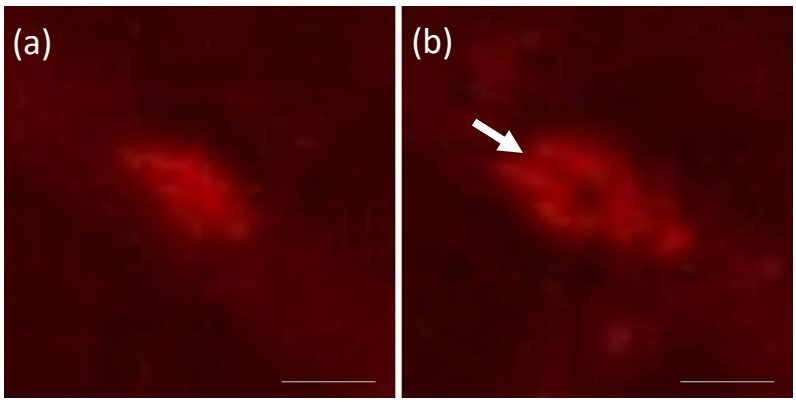

Figure 6.1 Defining neuromuscular junction morphology. Representative examples of a "simple" **(a)** and "complex" **(b)** NMJ respectively labelled with α-bungarotoxin. Note the clear perforation (white arrow) on one side in the "complex" NMJ, characteristic of NMJs seen *in vivo.* Examples taken from different regions of the same myofibre in a CPM/EB co-culture at 14 DIV. Scale bar = 10µm.

6.3.4 Incorporation of CPM/AsNAs co-cultures into a microfluidic device

With one of the ultimate goals of directed stem cell differentiation into specific cell types of clinical interest being the ability to model the development and/or disease of these tissues *in vitro*, I attempted to develop a basic microfluidic culture assay that would allow effective separation of the MN and muscle components while still enabling axon growth, synapse formation and MN driven muscle activity. Lacking the time or resources to develop a purpose built microfluidic device for this project, I adapted an Ibidi 3D chemotaxis slide for MN/muscle co-culture.

This simple device allowed physical separation of the neural cells from the myoblasts, yet allowed axon growth across the small intervening space. Additionally, due to the small size and clear plastic used in these slides, direct imaging of spontaneous muscle contraction was possible, enabling quantification of muscle activity. This data provides a basic proof of principle of the use of stem cells in an *in vitro* microfluidic neuromuscular assay. Further development of this technology, with specially designed materials and reagents, could transform this method into a reliable, reproducible high-throughput screen assay for neuromuscular circuit development and disease.

6.4 Extensions and Conclusions

This thesis describes the production and development of a broad range of cellular and molecular tools brought together to investigate neuromuscular circuit formation and maturation *in vitro*. With further optimisation and refinement, the assays developed here could be used in a wide variety of investigations ranging from basic developmental biology to genetic and pharmacological screens.

One major attraction of using stem cells for *in vitro* models of biological systems or disease is the ability to rapidly and efficiently introduce stable genetic modifications into cells lines. In this study we took advantage of this to introduce MACS-sortable markers, differentiation factors and an optogenetic tool allowing non-invasive control over MN activity. An interesting extension to this work currently being developed in our lab is the introduction of genetically encoded fluorescent reporters of activity, or GECIs (genetically encoded calcium indicators). The most well-known of these, G-CAMP, has been used in multiple neuronal systems to non-invasively study neural activity with high temporal precision. The recent development of GECIs with shifted spectral properties (R-GECO, red; B-GECO, blue) open up opportunities to combine these tools, potentially allowing simultaneous activity visualisation in separate cell lines or populations (Zhao et al., 2011). We hope to incorporate R-GECO into the MN cell line used in this work, and B-GECO into the iMyoD MACS-sortable muscle cell line, enabling visual monitoring of activity from both lineages in live *in vitro* co-cultures. This data should provide a dynamic and detailed insight into the activity of these cultures throughout development, and in response to external stimuli, drugs or further genetic modifications.

Another potential use of stable genetic modification is the incorporation of fluorescently tagged proteins, or other reporter constructs. The generation of a GFP-tagged Ankyrin G transgene for example should allow the visualisation of AIS formation in live cultures, providing a more thorough insight into the development of this structure. Fluorescently labelled post-synaptic proteins or even acetylcholine receptors could be introduced into the ES cell-derived muscle line

to enable live visualisation of synapse formation and maturation. While many other strategies using fluorescent reporters could be generated for specific biological questions, both of the strategies mentioned above would complement the data presented in this study, and facilitate a deeper investigation into the development of these vital sub-cellular structures *in vitro*.

Further extensions to this ES cell based assay include the introduction of specific disease-associated genes to model disease mechanisms and progression *in vitro*. Disease genes can be separately and stably introduced to any of the populations generated from ES cells, including the MNs, skeletal muscle or the astrocytes. Preliminary work on MNs and astrocytes expressing mutant superoxide dismutase 1 (SOD1), implicated in amyotrophic lateral sclerosis (ALS), have already returned promising results showing increased MN cell death in culture. Any neuromuscular disease with an identified genetic component could potentially be studied using this strategy, as introduction of disease genes into the muscle lineage would also open up opportunities to investigate muscular dystrophies including Duchenne muscular dystrophy, myotonias such as myotonia congenita, and familial periodic paralysis (Rideout et al., 2002; Suetterlin et al., 2014; Trollet et al., 2009).

Finally, opportunities to further improve and optimise this *in vitro* culture system remain. Recent advances in our understanding of the external signals and factors directing myogenesis enable the possibility of directed differentiation of ES cells into the skeletal myogenic lineage without the use of transgenes or other genetic or epigenetic modifications (Gouti et al., 2014; Xu et al., 2013b). As mentioned previously, 3D co-culture of MNs and muscle may significantly improve myofibre and NMJ morphology and viability, while also allowing more accurate assessment of contractile properties. Another area of interest in our lab has been the differentiation and culture of oligodendrocytes from ES cells (Stevenson, D., unpublished thesis, 2015). Incorporation of these specialised ensheathing glia into neuromuscular co-cultures could allow investigation of myelination, and myelination disorders. Other absent populations include as muscle connective tissue from ESC-derived muscle cultures, and perisynaptic Schwann cells,

which have been shown to be important for NMJ maturation (see Chapter 1.2.3), from both CPM and ESC-derived muscle cultures. The lack of muscle connective tissue may partly the reduced viability of the ESC-derived myofibres compared to primary myofibres, and incorporation of these cells may improve survival of ESC-derived muscle and enable long-term *in vitro* culture. The inclusion of these supporting cell types would also contribute to the accuracy of the model in terms of replicating the *in vivo* situation, improving the reliability of results obtained from this system. Finally, the use of microfluidic devices to form separate cell chambers representing different *in vivo* environments, for example a "CNS" with astrocytes and MNs and a "muscle target" with myoblasts, separated by a chamber containing oligodendrocytes, could also allow separate experimental manipulation of the different populations and culture environments, facilitating investigation of the contribution of each cell type to development and disease.

References

Agalliu, D., Takada, S., Agalliu, I., McMahon, A.P., and Jessell, T.M. (2009). Motor neurons with axial muscle projections specified by Wnt4/5 signaling. Neuron *61*, 708–720.

Albini, S., Coutinho, P., Malecova, B., Giordani, L., Savchenko, A., Forcales, S.V., and Puri, P.L. (2013). Epigenetic reprogramming of human embryonic stem cells into skeletal muscle cells and generation of contractile myospheres. Cell Rep. *3*, 661–670.

Aleckovic, M., and Simón, C. (2008). Is teratoma formation in stem cell research a characterization tool or a window to developmental biology? Reprod. Biomed. Online *17*, 270–280.

Alvarez, C.V., Garcia-Lavandeira, M., Garcia-Rendueles, M.E.R., Diaz-Rodriguez, E., Garcia-Rendueles, A.R., Perez-Romero, S., Vila, T.V., Rodrigues, J.S., Lear, P.V., and Bravo, S.B. (2012). Defining stem cell types: understanding the therapeutic potential of ESCs, ASCs, and iPS cells. J. Mol. Endocrinol. *49*, R89–R111.

Ambros, V. (2004). The functions of animal microRNAs. Nature *431*, 350–355.

Anderson, K., Potter, A., Baban, D., and Davies, K.E. (2003). Protein expression changes in spinal muscular atrophy revealed with a novel antibody array technology. Brain J. Neurol. *126*, 2052–2064.

Andreae, L.C., and Burrone, J. (2014). The role of neuronal activity and transmitter release on synapse formation. Curr. Opin. Neurobiol. *27*, 47–52.

Angka, H.E., and Kablar, B. (2007). Differential responses to the application of exogenous NT-3 are observed for subpopulations of motor and sensory neurons depending on the presence of skeletal muscle. Dev. Dyn. Off. Publ. Am. Assoc. Anat. *236*, 1193–1202.

Aravamudan, B., Mantilla, C.B., Zhan, W.-Z., and Sieck, G.C. (2006). Denervation effects on myonuclear domain size of rat diaphragm fibers. J. Appl. Physiol. Bethesda Md 1985 *100*, 1617–1622.

Arber, S., Han, B., Mendelsohn, M., Smith, M., Jessell, T.M., and Sockanathan, S. (1999). Requirement for the homeobox gene Hb9 in the consolidation of motor neuron identity. Neuron *23*, 659–674.

Arpke, R.W., Darabi, R., Mader, T.L., Zhang, Y., Toyama, A., Lonetree, C.-L., Nash, N., Lowe, D.A., Perlingeiro, R.C.R., and Kyba, M. (2013). A new immuno-, dystrophin-deficient model, the NSG-mdx(4Cv) mouse, provides evidence for functional improvement following allogeneic satellite cell transplantation. Stem Cells Dayt. Ohio *31*, 1611–1620.

Asgari, S., Moslem, M., Bagheri-Lankarani, K., Pournasr, B., Miryounesi, M., and Baharvand, H. (2013). Differentiation and transplantation of human induced pluripotent stem cell-derived hepatocyte-like cells. Stem Cell Rev. *9*, 493–504.

Aumailley, M., Bruckner-Tuderman, L., Carter, W.G., Deutzmann, R., Edgar, D., Ekblom, P., Engel, J., Engvall, E., Hohenester, E., Jones, J.C.R., et al. (2005). A simplified laminin nomenclature. Matrix Biol. J. Int. Soc. Matrix Biol. *24*, 326–332.

Azevedo, F.A.C., Carvalho, L.R.B., Grinberg, L.T., Farfel, J.M., Ferretti, R.E.L., Leite, R.E.P., Jacob Filho, W., Lent, R., and Herculano-Houzel, S. (2009). Equal numbers of neuronal and

nonneuronal cells make the human brain an isometrically scaled-up primate brain. J. Comp. Neurol. *513*, 532–541.

Baba, H., Nakahira, K., Morita, N., Tanaka, F., Akita, H., and Ikenaka, K. (1997). GFAP gene expression during development of astrocyte. Dev. Neurosci. *19*, 49–57.

Bajard, L., Relaix, F., Lagha, M., Rocancourt, D., Daubas, P., and Buckingham, M.E. (2006). A novel genetic hierarchy functions during hypaxial myogenesis: Pax3 directly activates Myf5 in muscle progenitor cells in the limb. Genes Dev. *20*, 2450–2464.

Balciunas, D., Wangensteen, K.J., Wilber, A., Bell, J., Geurts, A., Sivasubbu, S., Wang, X., Hackett, P.B., Largaespada, D.A., McIvor, R.S., et al. (2006). Harnessing a high cargo-capacity transposon for genetic applications in vertebrates. PLoS Genet. *2*, e169.

Barnes, A.P., and Polleux, F. (2009). Establishment of axon-dendrite polarity in developing neurons. Annu. Rev. Neurosci. *32*, 347–381.

Baron, W., Metz, B., Bansal, R., Hoekstra, D., and de Vries, H. (2000). PDGF and FGF-2 signaling in oligodendrocyte progenitor cells: regulation of proliferation and differentiation by multiple intracellular signaling pathways. Mol. Cell. Neurosci. *15*, 314–329.

Bartel, D.P. (2004). MicroRNAs: genomics, biogenesis, mechanism, and function. Cell *116*, 281–297.

Baum, C., Kustikova, O., Modlich, U., Li, Z., and Fehse, B. (2006). Mutagenesis and oncogenesis by chromosomal insertion of gene transfer vectors. Hum. Gene Ther. *17*, 253–263.

Bel-Vialar, S., Itasaki, N., and Krumlauf, R. (2002). Initiating Hox gene expression: in the early chick neural tube differential sensitivity to FGF and RA signaling subdivides the HoxB genes in two distinct groups. Dev. Camb. Engl. *129*, 5103–5115.

Benezra, R., Davis, R.L., Lockshon, D., Turner, D.L., and Weintraub, H. (1990). The protein Id: a negative regulator of helix-loop-helix DNA binding proteins. Cell *61*, 49–59.

Benraiss, A., and Goldman, S.A. (2011). Cellular therapy and induced neuronal replacement for Huntington's disease. Neurother. J. Am. Soc. Exp. Neurother. *8*, 577–590.

Ben-Yair, R., Kahane, N., and Kalcheim, C. (2003). Coherent development of dermomyotome and dermis from the entire mediolateral extent of the dorsal somite. Dev. Camb. Engl. *130*, 4325–4336.

Berendse, M., Grounds, M.D., and Lloyd, C.M. (2003). Myoblast structure affects subsequent skeletal myotube morphology and sarcomere assembly. Exp. Cell Res. *291*, 435–450.

Berkes, C.A., and Tapscott, S.J. (2005). MyoD and the transcriptional control of myogenesis. Semin. Cell Dev. Biol. *16*, 585–595.

Bian, W., Liau, B., Badie, N., and Bursac, N. (2009). Mesoscopic hydrogel molding to control the 3D geometry of bioartificial muscle tissues. Nat. Protoc. *4*, 1522–1534.

Bibikova, M., Laurent, L.C., Ren, B., Loring, J.F., and Fan, J.-B. (2008). Unraveling epigenetic regulation in embryonic stem cells. Cell Stem Cell *2*, 123–134.

Binder, L.I., Frankfurter, A., and Rebhun, L.I. (1985). The distribution of tau in the mammalian central nervous system. J. Cell Biol. *101*, 1371–1378.

Bishop, D.L., Misgeld, T., Walsh, M.K., Gan, W.-B., and Lichtman, J.W. (2004). Axon branch removal at developing synapses by axosome shedding. Neuron *44*, 651–661.

Black, B.L., and Olson, E.N. (1998). Transcriptional control of muscle development by myocyte enhancer factor-2 (MEF2) proteins. Annu. Rev. Cell Dev. Biol. *14*, 167–196.

Blackburn, D., Sargsyan, S., Monk, P.N., and Shaw, P.J. (2009). Astrocyte function and role in motor neuron disease: a future therapeutic target? Glia *57*, 1251–1264.

Blackwell, T.K., and Weintraub, H. (1990). Differences and similarities in DNA-binding preferences of MyoD and E2A protein complexes revealed by binding site selection. Science *250*, 1104–1110.

Bladt, F., Riethmacher, D., Isenmann, S., Aguzzi, A., and Birchmeier, C. (1995). Essential role for the c-met receptor in the migration of myogenic precursor cells into the limb bud. Nature *376*, 768–771.

Bober, E., Franz, T., Arnold, H.H., Gruss, P., and Tremblay, P. (1994). Pax-3 is required for the development of limb muscles: a possible role for the migration of dermomyotomal muscle progenitor cells. Dev. Camb. Engl. *120*, 603–612.

Borovski, T., De Sousa E Melo, F., Vermeulen, L., and Medema, J.P. (2011). Cancer stem cell niche: the place to be. Cancer Res. *71*, 634–639.

Boyden, E.S., Zhang, F., Bamberg, E., Nagel, G., and Deisseroth, K. (2005). Millisecond-timescale, genetically targeted optical control of neural activity. Nat. Neurosci. *8*, 1263–1268.

Braun, T., Rudnicki, M.A., Arnold, H.H., and Jaenisch, R. (1992). Targeted inactivation of the muscle regulatory gene Myf-5 results in abnormal rib development and perinatal death. Cell *71*, 369–382.

Brennan, T.J., and Olson, E.N. (1990). Myogenin resides in the nucleus and acquires high affinity for a conserved enhancer element on heterodimerization. Genes Dev. *4*, 582–595.

Brenner, M., Kisseberth, W.C., Su, Y., Besnard, F., and Messing, A. (1994). GFAP promoter directs astrocyte-specific expression in transgenic mice. J. Neurosci. Off. J. Soc. Neurosci. *14*, 1030–1037.

Brill, M.S., Lichtman, J.W., Thompson, W., Zuo, Y., and Misgeld, T. (2011). Spatial constraints dictate glial territories at murine neuromuscular junctions. J. Cell Biol. *195*, 293–305.

Briscoe, J., and Ericson, J. (2001). Specification of neuronal fates in the ventral neural tube. Curr. Opin. Neurobiol. *11*, 43–49.

Briscoe, J., Pierani, A., Jessell, T.M., and Ericson, J. (2000). A homeodomain protein code specifies progenitor cell identity and neuronal fate in the ventral neural tube. Cell *101*, 435–445.

Brons, I.G.M., Smithers, L.E., Trotter, M.W.B., Rugg-Gunn, P., Sun, B., Chuva de Sousa Lopes, S.M., Howlett, S.K., Clarkson, A., Ahrlund-Richter, L., Pedersen, R.A., et al. (2007). Derivation of pluripotent epiblast stem cells from mammalian embryos. Nature *448*, 191–195.

Brown, C.R., Butts, J.C., McCreedy, D.A., and Sakiyama-Elbert, S.E. (2014). Generation of v2a interneurons from mouse embryonic stem cells. Stem Cells Dev. *23*, 1765–1776.

Bryson, J.B., Machado, C.B., Crossley, M., Stevenson, D., Bros-Facer, V., Burrone, J., Greensmith, L., and Lieberam, I. (2014). Optical control of muscle function by transplantation of stem cell-derived motor neurons in mice. Science *344*, 94–97.

Buckingham, M. (2006). Myogenic progenitor cells and skeletal myogenesis in vertebrates. Curr. Opin. Genet. Dev. *16*, 525–532.

Buehr, M., Meek, S., Blair, K., Yang, J., Ure, J., Silva, J., McLay, R., Hall, J., Ying, Q.-L., and Smith, A. (2008). Capture of authentic embryonic stem cells from rat blastocysts. Cell *135*, 1287–1298.

Buffelli, M., Busetto, G., Cangiano, L., and Cangiano, A. (2002). Perinatal switch from synchronous to asynchronous activity of motoneurons: link with synapse elimination. Proc. Natl. Acad. Sci. U. S. A. *99*, 13200–13205.

Buffelli, M., Burgess, R.W., Feng, G., Lobe, C.G., Lichtman, J.W., and Sanes, J.R. (2003). Genetic evidence that relative synaptic efficacy biases the outcome of synaptic competition. Nature *424*, 430–434.

Buffington, S.A., Sobotzik, J.M., Schultz, C., and Rasband, M.N. (2012). IκBα is not required for axon initial segment assembly. Mol. Cell. Neurosci. *50*, 1–9.

Burden, S.J. (1993). Synapse-specific gene expression. Trends Genet. TIG *9*, 12–16.

Burgess, R.W., Nguyen, Q.T., Son, Y.J., Lichtman, J.W., and Sanes, J.R. (1999). Alternatively spliced isoforms of nerve- and muscle-derived agrin: their roles at the neuromuscular junction. Neuron *23*, 33–44.

Burke, R.E., Levine, D.N., Tsairis, P., and Zajac, F.E. (1973). Physiological types and histochemical profiles in motor units of the cat gastrocnemius. J. Physiol. *234*, 723–748.

Burkhardt, M.F., Martinez, F.J., Wright, S., Ramos, C., Volfson, D., Mason, M., Garnes, J., Dang, V., Lievers, J., Shoukat-Mumtaz, U., et al. (2013). A cellular model for sporadic ALS using patient-derived induced pluripotent stem cells. Mol. Cell. Neurosci. *56*, 355–364.

Burton, P.M. (2008). Insights from diploblasts; the evolution of mesoderm and muscle. J. Exp. Zoolog. B Mol. Dev. Evol. *310*, 5–14.

Caplan, A.I. (1976). A simplified procedure for preparing myogenic cells for culture. J. Embryol. Exp. Morphol. *36*, 175–181.

Carlin, K.P., Jiang, Z., and Brownstone, R.M. (2000). Characterization of calcium currents in functionally mature mouse spinal motoneurons. Eur. J. Neurosci. *12*, 1624–1634.

Chal, J., Oginuma, M., Al Tanoury, Z., Gobert, B., Sumara, O., Hick, A., Bousson, F., Zidouni, Y., Mursch, C., Moncuquet, P., et al. (2015). Differentiation of pluripotent stem cells to muscle fiber to model Duchenne muscular dystrophy. Nat. Biotechnol. *33*, 962–969.

Chamberlain, S.J., Chen, P.-F., Ng, K.Y., Bourgois-Rocha, F., Lemtiri-Chlieh, F., Levine, E.S., and Lalande, M. (2010). Induced pluripotent stem cell models of the genomic imprinting disorders Angelman and Prader-Willi syndromes. Proc. Natl. Acad. Sci. U. S. A. *107*, 17668–17673.

Chandrasekhar, A. (2004). Turning heads: development of vertebrate branchiomotor neurons. Dev. Dyn. Off. Publ. Am. Assoc. Anat. *229*, 143–161.

Chen, G., and Quinn, L.S. (1992). Partial characterization of skeletal myoblast mitogens in mouse crushed muscle extract. J. Cell. Physiol. *153*, 563–574.

Chen, J., Billings, S.E., and Nishimune, H. (2011). Calcium channels link the muscle-derived synapse organizer laminin β2 to Bassoon and CAST/Erc2 to organize presynaptic active zones. J. Neurosci. Off. J. Soc. Neurosci. *31*, 512–525.

Chen, J.-F., Tao, Y., Li, J., Deng, Z., Yan, Z., Xiao, X., and Wang, D.-Z. (2010). microRNA-1 and microRNA-206 regulate skeletal muscle satellite cell proliferation and differentiation by repressing Pax7. J. Cell Biol. *190*, 867–879.

Choe, A., Phun, H.Q., Tieu, D.D., Hu, Y.H., and Carpenter, E.M. (2006). Expression patterns of Hox10 paralogous genes during lumbar spinal cord development. Gene Expr. Patterns GEP *6*, 730–737.

Choi, J., Costa, M.L., Mermelstein, C.S., Chagas, C., Holtzer, S., and Holtzer, H. (1990). MyoD converts primary dermal fibroblasts, chondroblasts, smooth muscle, and retinal pigmented epithelial cells into striated mononucleated myoblasts and multinucleated myotubes. Proc. Natl. Acad. Sci. U. S. A. *87*, 7988–7992.

Cinnamon, Y., Ben-Yair, R., and Kalcheim, C. (2006). Differential effects of N-cadherin-mediated adhesion on the development of myotomal waves. Dev. Camb. Engl. *133*, 1101–1112.

Clark, K.A., McElhinny, A.S., Beckerle, M.C., and Gregorio, C.C. (2002). Striated muscle cytoarchitecture: an intricate web of form and function. Annu. Rev. Cell Dev. Biol. *18*, 637–706.

Cooke, P.H., Kargacin, G., Craig, R., Fogarty, K., and Fay, F.S. (1987). Molecular structure and organization of filaments in single, skinned smooth muscle cells. Prog. Clin. Biol. Res. *245*, 1–25.

Cowan, C.A., Klimanskaya, I., McMahon, J., Atienza, J., Witmyer, J., Zucker, J.P., Wang, S., Morton, C.C., McMahon, A.P., Powers, D., et al. (2004). Derivation of embryonic stem-cell lines from human blastocysts. N. Engl. J. Med. *350*, 1353–1356.

Darabi, R., Gehlbach, K., Bachoo, R.M., Kamath, S., Osawa, M., Kamm, K.E., Kyba, M., and Perlingeiro, R.C.R. (2008a). Functional skeletal muscle regeneration from differentiating embryonic stem cells. Nat. Med. *14*, 134–143.

Darabi, R., Gehlbach, K., Bachoo, R.M., Kamath, S., Osawa, M., Kamm, K.E., Kyba, M., and Perlingeiro, R.C.R. (2008b). Functional skeletal muscle regeneration from differentiating embryonic stem cells. Nat. Med. *14*, 134–143.

Darabi, R., Pan, W., Bosnakovski, D., Baik, J., Kyba, M., and Perlingeiro, R.C.R. (2011a). Functional myogenic engraftment from mouse iPS cells. Stem Cell Rev. *7*, 948–957.

Darabi, R., Santos, F.N.C., Filareto, A., Pan, W., Koene, R., Rudnicki, M.A., Kyba, M., and Perlingeiro, R.C.R. (2011b). Assessment of the myogenic stem cell compartment following transplantation of Pax3/Pax7-induced embryonic stem cell-derived progenitors. Stem Cells Dayt. Ohio *29*, 777–790.

Darabi, R., Arpke, R.W., Irion, S., Dimos, J.T., Grskovic, M., Kyba, M., and Perlingeiro, R.C.R. (2012). Human ES- and iPS-derived myogenic progenitors restore DYSTROPHIN and improve contractility upon transplantation in dystrophic mice. Cell Stem Cell *10*, 610–619.

Darabid, H., Arbour, D., and Robitaille, R. (2013). Glial cells decipher synaptic competition at the mammalian neuromuscular junction. J. Neurosci. Off. J. Soc. Neurosci. *33*, 1297–1313.

Darabid, H., Perez-Gonzalez, A.P., and Robitaille, R. (2014). Neuromuscular synaptogenesis: coordinating partners with multiple functions. Nat. Rev. Neurosci. *15*, 703–718.

Dasen, J.S., and Jessell, T.M. (2009). Hox networks and the origins of motor neuron diversity. Curr. Top. Dev. Biol. *88*, 169–200.

Dasen, J.S., Liu, J.-P., and Jessell, T.M. (2003). Motor neuron columnar fate imposed by sequential phases of Hox-c activity. Nature *425*, 926–933.

Dasen, J.S., Tice, B.C., Brenner-Morton, S., and Jessell, T.M. (2005). A Hox regulatory network establishes motor neuron pool identity and target-muscle connectivity. Cell *123*, 477–491.

DeChiara, T.M., Bowen, D.C., Valenzuela, D.M., Simmons, M.V., Poueymirou, W.T., Thomas, S., Kinetz, E., Compton, D.L., Rojas, E., Park, J.S., et al. (1996). The receptor tyrosine kinase MuSK is required for neuromuscular junction formation in vivo. Cell *85*, 501–512.

Dessaud, E., McMahon, A.P., and Briscoe, J. (2008). Pattern formation in the vertebrate neural tube: a sonic hedgehog morphogen-regulated transcriptional network. Dev. Camb. Engl. *135*, 2489–2503.

Dewil, M., dela Cruz, V.F., Van Den Bosch, L., and Robberecht, W. (2007). Inhibition of p38 mitogen activated protein kinase activation and mutant SOD1(G93A)-induced motor neuron death. Neurobiol. Dis. *26*, 332–341.

Diamant, N.E. (1997). Neuromuscular mechanisms of primary peristalsis. Am. J. Med. *103*, 40S – 43S.

Dietrich, S., Abou-Rebyeh, F., Brohmann, H., Bladt, F., Sonnenberg-Riethmacher, E., Yamaai, T., Lumsden, A., Brand-Saberi, B., and Birchmeier, C. (1999). The role of SF/HGF and c-Met in the development of skeletal muscle. Dev. Camb. Engl. *126*, 1621–1629.

Diez del Corral, R., and Storey, K.G. (2004). Opposing FGF and retinoid pathways: a signalling switch that controls differentiation and patterning onset in the extending vertebrate body axis. BioEssays News Rev. Mol. Cell. Dev. Biol. *26*, 857–869.

Dobrowolny, G., Aucello, M., Rizzuto, E., Beccafico, S., Mammucari, C., Boncompagni, S., Bonconpagni, S., Belia, S., Wannenes, F., Nicoletti, C., et al. (2008). Skeletal muscle is a primary target of SOD1G93A-mediated toxicity. Cell Metab. *8*, 425–436.

Dubrulle, J., and Pourquié, O. (2004). fgf8 mRNA decay establishes a gradient that couples axial elongation to patterning in the vertebrate embryo. Nature *427*, 419–422.

Dudanova, I., Gatto, G., and Klein, R. (2010). GDNF acts as a chemoattractant to support ephrinA-induced repulsion of limb motor axons. Curr. Biol. CB *20*, 2150–2156.

Duflocq, A., Chareyre, F., Giovannini, M., Couraud, F., and Davenne, M. (2011). Characterization of the axon initial segment (AIS) of motor neurons and identification of a para-AIS and a juxtapara-AIS, organized by protein 4.1B. BMC Biol. *9*, 66.

Dupuis, L., and Loeffler, J.-P. (2009). Neuromuscular junction destruction during amyotrophic lateral sclerosis: insights from transgenic models. Curr. Opin. Pharmacol. *9*, 341–346.

Echelard, Y., Epstein, D.J., St-Jacques, B., Shen, L., Mohler, J., McMahon, J.A., and McMahon, A.P. (1993). Sonic hedgehog, a member of a family of putative signaling molecules, is implicated in the regulation of CNS polarity. Cell *75*, 1417–1430.

Edmondson, D.G., Lyons, G.E., Martin, J.F., and Olson, E.N. (1994). Mef2 gene expression marks the cardiac and skeletal muscle lineages during mouse embryogenesis. Dev. Camb. Engl. *120*, 1251–1263.

Epstein, J.A., Shapiro, D.N., Cheng, J., Lam, P.Y., and Maas, R.L. (1996). Pax3 modulates expression of the c-Met receptor during limb muscle development. Proc. Natl. Acad. Sci. U. S. A. *93*, 4213–4218.

Estrella, N.L., Desjardins, C.A., Nocco, S.E., Clark, A.L., Maksimenko, Y., and Naya, F.J. (2015). MEF2 transcription factors regulate distinct gene programs in mammalian skeletal muscle differentiation. J. Biol. Chem. *290*, 1256–1268.

Evans, M.J., and Kaufman, M.H. (1981). Establishment in culture of pluripotential cells from mouse embryos. Nature *292*, 154–156.

Favero, M., Busetto, G., and Cangiano, A. (2012). Spike timing plays a key role in synapse elimination at the neuromuscular junction. Proc. Natl. Acad. Sci. U. S. A. *109*, E1667–E1675.

Fenno, L., Yizhar, O., and Deisseroth, K. (2011). The development and application of optogenetics. Annu. Rev. Neurosci. *34*, 389–412.

Fetcho, J.R. (1987). A review of the organization and evolution of motoneurons innervating the axial musculature of vertebrates. Brain Res. *434*, 243–280.

Filareto, A., Parker, S., Darabi, R., Borges, L., Iacovino, M., Schaaf, T., Mayerhofer, T., Chamberlain, J.S., Ervasti, J.M., McIvor, R.S., et al. (2013). An ex vivo gene therapy approach to treat muscular dystrophy using inducible pluripotent stem cells. Nat. Commun. *4*, 1549.

Filbin, M.E., and Kieft, J.S. (2009). Toward a structural understanding of IRES RNA function. Curr. Opin. Struct. Biol. *19*, 267–276.

Fischer, L.R., Culver, D.G., Tennant, P., Davis, A.A., Wang, M., Castellano-Sanchez, A., Khan, J., Polak, M.A., and Glass, J.D. (2004). Amyotrophic lateral sclerosis is a distal axonopathy: evidence in mice and man. Exp. Neurol. *185*, 232–240.

Fontes, A., and Lakshmipathy, U. (2013). Advances in genetic modification of pluripotent stem cells. Biotechnol. Adv. *31*, 994–1001.

Fox, M.A., Sanes, J.R., Borza, D.-B., Eswarakumar, V.P., Fässler, R., Hudson, B.G., John, S.W.M., Ninomiya, Y., Pedchenko, V., Pfaff, S.L., et al. (2007). Distinct target-derived signals organize formation, maturation, and maintenance of motor nerve terminals. Cell *129*, 179–193.

Francius, C., Harris, A., Rucchin, V., Hendricks, T.J., Stam, F.J., Barber, M., Kurek, D., Grosveld, F.G., Pierani, A., Goulding, M., et al. (2013). Identification of multiple subsets of ventral interneurons and differential distribution along the rostrocaudal axis of the developing spinal cord. PloS One *8*, e70325.

Frey, D., Schneider, C., Xu, L., Borg, J., Spooren, W., and Caroni, P. (2000). Early and selective loss of neuromuscular synapse subtypes with low sprouting competence in motoneuron diseases. J. Neurosci. Off. J. Soc. Neurosci. *20*, 2534–2542.

Friese, A., Kaltschmidt, J.A., Ladle, D.R., Sigrist, M., Jessell, T.M., and Arber, S. (2009). Gamma and alpha motor neurons distinguished by expression of transcription factor Err3. Proc. Natl. Acad. Sci. U. S. A. *106*, 13588–13593.

Funakoshi, H., Belluardo, N., Arenas, E., Yamamoto, Y., Casabona, A., Persson, H., and Ibáñez, C.F. (1995). Muscle-derived neurotrophin-4 as an activity-dependent trophic signal for adult motor neurons. Science *268*, 1495–1499.

Funanage, V.L., Schroedl, N.A., Moses, P.A., Smith, S.M., Kirwin, J.J., and Hartzell, C.R. (1989). Hemin enhances differentiation and maturation of cultured regenerated skeletal myotubes. J. Cell. Physiol. *141*, 591–597.

Garrido, J.J., Giraud, P., Carlier, E., Fernandes, F., Moussif, A., Fache, M.-P., Debanne, D., and Dargent, B. (2003). A targeting motif involved in sodium channel clustering at the axonal initial segment. Science *300*, 2091–2094.

Garver, T.D., Ren, Q., Tuvia, S., and Bennett, V. (1997). Tyrosine phosphorylation at a site highly conserved in the L1 family of cell adhesion molecules abolishes ankyrin binding and increases lateral mobility of neurofascin. J. Cell Biol. *137*, 703–714.

Gautam, M., Noakes, P.G., Mudd, J., Nichol, M., Chu, G.C., Sanes, J.R., and Merlie, J.P. (1995). Failure of postsynaptic specialization to develop at neuromuscular junctions of rapsyn-deficient mice. Nature *377*, 232–236.

Gautam, M., Noakes, P.G., Moscoso, L., Rupp, F., Scheller, R.H., Merlie, J.P., and Sanes, J.R. (1996). Defective neuromuscular synaptogenesis in agrin-deficient mutant mice. Cell *85*, 525–535.

Gensler, S., Sander, A., Korngreen, A., Traina, G., Giese, G., and Witzemann, V. (2001). Assembly and clustering of acetylcholine receptors containing GFP-tagged epsilon or gamma subunits: selective targeting to the neuromuscular junction in vivo. Eur. J. Biochem. FEBS *268*, 2209–2217.

Gerstenfeld, L.C., Crawford, D.R., Boedtker, H., and Doty, P. (1984). Expression of type I and III collagen genes during differentiation of embryonic chicken myoblasts in culture. Mol. Cell. Biol. *4*, 1483–1492.

Ghysen, A. (2003). The origin and evolution of the nervous system. Int. J. Dev. Biol. *47*, 555–562.

Gianakopoulos, P.J., Mehta, V., Voronova, A., Cao, Y., Yao, Z., Coutu, J., Wang, X., Waddington, M.S., Tapscott, S.J., and Skerjanc, I.S. (2011). MyoD directly up-regulates premyogenic mesoderm factors during induction of skeletal myogenesis in stem cells. J. Biol. Chem. *286*, 2517–2525.

Glaser, T., Perez-Bouza, A., Klein, K., and Brüstle, O. (2005). Generation of purified oligodendrocyte progenitors from embryonic stem cells. FASEB J. Off. Publ. Fed. Am. Soc. Exp. Biol. *19*, 112–114.

Glat, M.J., Benninger, F., Barhum, Y., Ben-Zur, T., Kogan, E., Steiner, I., Yaffe, D., and Offen, D. (2016). Ectopic Muscle Expression of Neurotrophic Factors Improves Recovery After Nerve Injury. J. Mol. Neurosci. MN *58*, 39–45.

Gluzman, Y. (1981). SV40-transformed simian cells support the replication of early SV40 mutants. Cell *23*, 175–182.

Gómez-Gaviro, M.V., Lovell-Badge, R., Fernández-Avilés, F., and Lara-Pezzi, E. (2012). The vascular stem cell niche. J Cardiovasc. Transl. Res. *5*, 618–630.

Gossett, L.A., Kelvin, D.J., Sternberg, E.A., and Olson, E.N. (1989). A new myocyte-specific enhancer-binding factor that recognizes a conserved element associated with multiple muscle-specific genes. Mol. Cell. Biol. *9*, 5022–5033.

Gould, T.W., Buss, R.R., Vinsant, S., Prevette, D., Sun, W., Knudson, C.M., Milligan, C.E., and Oppenheim, R.W. (2006a). Complete dissociation of motor neuron death from motor dysfunction by Bax deletion in a mouse model of ALS. J. Neurosci. Off. J. Soc. Neurosci. *26*, 8774–8786.

Gould, T.W., Buss, R.R., Vinsant, S., Prevette, D., Sun, W., Knudson, C.M., Milligan, C.E., and Oppenheim, R.W. (2006b). Complete dissociation of motor neuron death from motor dysfunction by Bax deletion in a mouse model of ALS. J. Neurosci. Off. J. Soc. Neurosci. *26*, 8774–8786.

Gould, T.W., Yonemura, S., Oppenheim, R.W., Ohmori, S., and Enomoto, H. (2008). The neurotrophic effects of glial cell line-derived neurotrophic factor on spinal motoneurons are restricted to fusimotor subtypes. J. Neurosci. Off. J. Soc. Neurosci. *28*, 2131–2146.

Goulding, D., Bullard, B., and Gautel, M. (1997). A survey of in situ sarcomere extension in mouse skeletal muscle. J. Muscle Res. Cell Motil. *18*, 465–472.

Gouti, M., Tsakiridis, A., Wymeersch, F.J., Huang, Y., Kleinjung, J., Wilson, V., and Briscoe, J. (2014). In vitro generation of neuromesodermal progenitors reveals distinct roles for wnt signalling in the specification of spinal cord and paraxial mesoderm identity. PLoS Biol. *12*, e1001937.

Grifone, R., Demignon, J., Houbron, C., Souil, E., Niro, C., Seller, M.J., Hamard, G., and Maire, P. (2005). Six1 and Six4 homeoproteins are required for Pax3 and Mrf expression during myogenesis in the mouse embryo. Dev. Camb. Engl. *132*, 2235–2249.

Grifone, R., Demignon, J., Giordani, J., Niro, C., Souil, E., Bertin, F., Laclef, C., Xu, P.-X., and Maire, P. (2007). Eya1 and Eya2 proteins are required for hypaxial somitic myogenesis in the mouse embryo. Dev. Biol. *302*, 602–616.

Gros, J., Scaal, M., and Marcelle, C. (2004). A two-step mechanism for myotome formation in chick. Dev. Cell *6*, 875–882.

Gros, J., Manceau, M., Thomé, V., and Marcelle, C. (2005). A common somitic origin for embryonic muscle progenitors and satellite cells. Nature *435*, 954–958.

Grubb, M.S., and Burrone, J. (2010a). Building and maintaining the axon initial segment. Curr. Opin. Neurobiol. *20*, 481–488.

Grubb, M.S., and Burrone, J. (2010b). Activity-dependent relocation of the axon initial segment fine-tunes neuronal excitability. Nature *465*, 1070–1074.

Guenther, M.G., Frampton, G.M., Soldner, F., Hockemeyer, D., Mitalipova, M., Jaenisch, R., and Young, R.A. (2010). Chromatin structure and gene expression programs of human embryonic and induced pluripotent stem cells. Cell Stem Cell *7*, 249–257.

Guo, X., Das, M., Rumsey, J., Gonzalez, M., Stancescu, M., and Hickman, J. (2010). Neuromuscular junction formation between human stem-cell-derived motoneurons and rat skeletal muscle in a defined system. Tissue Eng. Part C Methods *16*, 1347–1355.

Gutman, C.R., Ajmera, M.K., and Hollyday, M. (1993). Organization of motor pools supplying axial muscles in the chicken. Brain Res. *609*, 129–136.

Haase, G., Dessaud, E., Garcès, A., de Bovis, B., Birling, M., Filippi, P., Schmalbruch, H., Arber, S., and deLapeyrière, O. (2002). GDNF acts through PEA3 to regulate cell body positioning and muscle innervation of specific motor neuron pools. Neuron *35*, 893–905.

Hanna, J., Wernig, M., Markoulaki, S., Sun, C.-W., Meissner, A., Cassady, J.P., Beard, C., Brambrink, T., Wu, L.-C., Townes, T.M., et al. (2007). Treatment of sickle cell anemia mouse model with iPS cells generated from autologous skin. Science *318*, 1920–1923.

Hasson, P., DeLaurier, A., Bennett, M., Grigorieva, E., Naiche, L.A., Papaioannou, V.E., Mohun, T.J., and Logan, M.P.O. (2010). Tbx4 and tbx5 acting in connective tissue are required for limb muscle and tendon patterning. Dev. Cell *18*, 148–156.

Hasty, P., Bradley, A., Morris, J.H., Edmondson, D.G., Venuti, J.M., Olson, E.N., and Klein, W.H. (1993). Muscle deficiency and neonatal death in mice with a targeted mutation in the myogenin gene. Nature *364*, 501–506.

Havenith, M.G., Visser, R., Schrijvers-van Schendel, J.M., and Bosman, F.T. (1990). Muscle fiber typing in routinely processed skeletal muscle with monoclonal antibodies. Histochemistry *93*, 497–499.

Heanue, T.A., Davis, R.J., Rowitch, D.H., Kispert, A., McMahon, A.P., Mardon, G., and Tabin, C.J. (2002). Dach1, a vertebrate homologue of Drosophila dachshund, is expressed in the developing eye and ear of both chick and mouse and is regulated independently of Pax and Eya genes. Mech. Dev. *111*, 75–87.

Hedstrom, K.L., Xu, X., Ogawa, Y., Frischknecht, R., Seidenbecher, C.I., Shrager, P., and Rasband, M.N. (2007). Neurofascin assembles a specialized extracellular matrix at the axon initial segment. J. Cell Biol. *178*, 875–886.

Heidelberger, C., Chaudhuri, N.K., Danneberg, P., Mooren, D., Griesbach, L., Duschinsky, R., Schnitzer, R.J., Pleven, E., and Scheiner, J. (1957). Fluorinated pyrimidines, a new class of tumour-inhibitory compounds. Nature *179*, 663–666.

Henderson, A.H., Forman, R., Brutsaert, D.L., and Sonnenblick, E.H. (1971). Tetanic contraction in mammalian cardiac muscle. Cardiovasc. Res. *Suppl 1*, 96–100.

Henderson, C.E., Phillips, H.S., Pollock, R.A., Davies, A.M., Lemeulle, C., Armanini, M., Simmons, L., Moffet, B., Vandlen, R.A., Simpson LC corrected to Simmons, L., et al. (1994). GDNF: a potent survival factor for motoneurons present in peripheral nerve and muscle. Science *266*, 1062–1064.

Herculano-Houzel, S. (2011). Not all brains are made the same: new views on brain scaling in evolution. Brain. Behav. Evol. *78*, 22–36.

Hirai, H., Verma, M., Watanabe, S., Tastad, C., Asakura, Y., and Asakura, A. (2010). MyoD regulates apoptosis of myoblasts through microRNA-mediated down-regulation of Pax3. J. Cell Biol. *191*, 347–365.

Hirai, H., Tani, T., Katoku-Kikyo, N., Kellner, S., Karian, P., Firpo, M., and Kikyo, N. (2011). Radical acceleration of nuclear reprogramming by chromatin remodeling with the transactivation domain of MyoD. Stem Cells Dayt. Ohio *29*, 1349–1361.

Hochbaum, D.R., Zhao, Y., Farhi, S.L., Klapoetke, N., Werley, C.A., Kapoor, V., Zou, P., Kralj, J.M., Maclaurin, D., Smedemark-Margulies, N., et al. (2014). All-optical electrophysiology in mammalian neurons using engineered microbial rhodopsins. Nat. Methods *11*, 825–833.

Hollenberg, S.M., Cheng, P.F., and Weintraub, H. (1993). Use of a conditional MyoD transcription factor in studies of MyoD trans-activation and muscle determination. Proc. Natl. Acad. Sci. U. S. A. *90*, 8028–8032.

Hollyday, M., and Jacobson, R.D. (1990). Location of motor pools innervating chick wing. J. Comp. Neurol. *302*, 575–588.

Holowacz, T., Zeng, L., and Lassar, A.B. (2006). Asymmetric localization of numb in the chick somite and the influence of myogenic signals. Dev. Dyn. Off. Publ. Am. Assoc. Anat. *235*, 633–645.

Hosoyama, T., McGivern, J.V., Van Dyke, J.M., Ebert, A.D., and Suzuki, M. (2014). Derivation of myogenic progenitors directly from human pluripotent stem cells using a sphere-based culture. Stem Cells Transl. Med. *3*, 564–574.

Huizinga, J.D., and Lammers, W.J.E.P. (2009). Gut peristalsis is governed by a multitude of cooperating mechanisms. Am. J. Physiol. Gastrointest. Liver Physiol. *296*, G1–G8.

Hunt, C.C., and Kuffler, S.W. (1951). Further study of efferent small-nerve fibers to mammalian muscle spindles; multiple spindle innervation and activity during contraction. J. Physiol. *113*, 283–297.

Hwang, Y., Suk, S., Lin, S., Tierney, M., Du, B., Seo, T., Mitchell, A., Sacco, A., and Varghese, S. (2013). Directed in vitro myogenesis of human embryonic stem cells and their in vivo engraftment. PloS One *8*, e72023.

Iacovino, M., Bosnakovski, D., Fey, H., Rux, D., Bajwa, G., Mahen, E., Mitanoska, A., Xu, Z., and Kyba, M. (2011). Inducible cassette exchange: a rapid and efficient system enabling conditional gene expression in embryonic stem and primary cells. Stem Cells Dayt. Ohio *29*, 1580–1588.

Inagaki, N., Toriyama, M., and Sakumura, Y. (2011). Systems biology of symmetry breaking during neuronal polarity formation. Dev. Neurobiol. *71*, 584–593.

Irion, S., Nostro, M.C., Kattman, S.J., and Keller, G.M. (2008). Directed differentiation of pluripotent stem cells: from developmental biology to therapeutic applications. Cold Spring Harb. Symp. Quant. Biol. *73*, 101–110.

Itskovitz-Eldor, J., Schuldiner, M., Karsenti, D., Eden, A., Yanuka, O., Amit, M., Soreq, H., and Benvenisty, N. (2000). Differentiation of human embryonic stem cells into embryoid bodies compromising the three embryonic germ layers. Mol. Med. Camb. Mass *6*, 88–95.

Izrael, M., Zhang, P., Kaufman, R., Shinder, V., Ella, R., Amit, M., Itskovitz-Eldor, J., Chebath, J., and Revel, M. (2007). Human oligodendrocytes derived from embryonic stem cells: Effect of noggin on phenotypic differentiation in vitro and on myelination in vivo. Mol. Cell. Neurosci. *34*, 310–323.

Jacob, J., and Briscoe, J. (2003). Gli proteins and the control of spinal-cord patterning. EMBO Rep. *4*, 761–765.

Jaworski, A., and Burden, S.J. (2006). Neuromuscular synapse formation in mice lacking motor neuron- and skeletal muscle-derived Neuregulin-1. J. Neurosci. Off. J. Soc. Neurosci. *26*, 655–661.

Je, H.S., Yang, F., Ji, Y., Potluri, S., Fu, X.-Q., Luo, Z.-G., Nagappan, G., Chan, J.P., Hempstead, B., Son, Y.-J., et al. (2013). ProBDNF and mature BDNF as punishment and reward signals for synapse elimination at mouse neuromuscular junctions. J. Neurosci. Off. J. Soc. Neurosci. *33*, 9957–9962.

Jo, S.A., Zhu, X., Marchionni, M.A., and Burden, S.J. (1995). Neuregulins are concentrated at nerve-muscle synapses and activate ACh-receptor gene expression. Nature *373*, 158–161.

Jokic, N., Gonzalez de Aguilar, J.-L., Pradat, P.-F., Dupuis, L., Echaniz-Laguna, A., Muller, A., Dubourg, O., Seilhean, D., Hauw, J.-J., Loeffler, J.-P., et al. (2005). Nogo expression in muscle correlates with amyotrophic lateral sclerosis severity. Ann. Neurol. *57*, 553–556.

Jung, H., Lacombe, J., Mazzoni, E.O., Liem, K.F., Grinstein, J., Mahony, S., Mukhopadhyay, D., Gifford, D.K., Young, R.A., Anderson, K.V., et al. (2010). Global control of motor neuron topography mediated by the repressive actions of a single hox gene. Neuron *67*, 781–796.

Kablar, B., and Belliveau, A.C. (2005). Presence of neurotrophic factors in skeletal muscle correlates with survival of spinal cord motor neurons. Dev. Dyn. Off. Publ. Am. Assoc. Anat. *234*, 659–669.

Kablar, B., Asakura, A., Krastel, K., Ying, C., May, L.L., Goldhamer, D.J., and Rudnicki, M.A. (1998). MyoD and Myf-5 define the specification of musculature of distinct embryonic origin. Biochem. Cell Biol. Biochim. Biol. Cell. *76*, 1079–1091.

Kahane, N., Ben-Yair, R., and Kalcheim, C. (2007). Medial pioneer fibers pattern the morphogenesis of early myoblasts derived from the lateral somite. Dev. Biol. *305*, 439–450.

Kanarek, N., and Ben-Neriah, Y. (2012). Regulation of NF-κB by ubiquitination and degradation of the IκBs. Immunol. Rev. *246*, 77–94.

Kania, A., and Jessell, T.M. (2003). Topographic motor projections in the limb imposed by LIM homeodomain protein regulation of ephrin-A:EphA interactions. Neuron *38*, 581–596.

Kanning, K.C., Kaplan, A., and Henderson, C.E. (2010). Motor neuron diversity in development and disease. Annu. Rev. Neurosci. *33*, 409–440.

Kassar-Duchossoy, L., Gayraud-Morel, B., Gomès, D., Rocancourt, D., Buckingham, M., Shinin, V., and Tajbakhsh, S. (2004). Mrf4 determines skeletal muscle identity in Myf5:Myod double-mutant mice. Nature *431*, 466–471.

Kaushal, S., Schneider, J.W., Nadal-Ginard, B., and Mahdavi, V. (1994). Activation of the myogenic lineage by MEF2A, a factor that induces and cooperates with MyoD. Science *266*, 1236–1240.

Kawakami, K., and Noda, T. (2004). Transposition of the Tol2 element, an Ac-like element from the Japanese medaka fish Oryzias latipes, in mouse embryonic stem cells. Genetics *166*, 895–899.

Kawakami, K., Shima, A., and Kawakami, N. (2000). Identification of a functional transposase of the Tol2 element, an Ac-like element from the Japanese medaka fish, and its transposition in the zebrafish germ lineage. Proc. Natl. Acad. Sci. U. S. A. *97*, 11403–11408.

Kessaris, N., Pringle, N., and Richardson, W.D. (2001). Ventral neurogenesis and the neuron-glial switch. Neuron *31*, 677–680.

Kim, N., and Burden, S.J. (2008). MuSK controls where motor axons grow and form synapses. Nat. Neurosci. *11*, 19–27.

Kim, N., Stiegler, A.L., Cameron, T.O., Hallock, P.T., Gomez, A.M., Huang, J.H., Hubbard, S.R., Dustin, M.L., and Burden, S.J. (2008). Lrp4 is a receptor for Agrin and forms a complex with MuSK. Cell *135*, 334–342.

Kmita, M., and Duboule, D. (2003). Organizing axes in time and space; 25 years of colinear tinkering. Science *301*, 331–333.

Knight, D., Tolley, L.K., Kim, D.K., Lavidis, N.A., and Noakes, P.G. (2003). Functional analysis of neurotransmission at beta2-laminin deficient terminals. J. Physiol. *546*, 789–800.

Kole, M.H.P., Ilschner, S.U., Kampa, B.M., Williams, S.R., Ruben, P.C., and Stuart, G.J. (2008). Action potential generation requires a high sodium channel density in the axon initial segment. Nat. Neurosci. *11*, 178–186.

Komar, A.A., Mazumder, B., and Merrick, W.C. (2012). A new framework for understanding IRES-mediated translation. Gene *502*, 75–86.

Kong, L., Wang, X., Choe, D.W., Polley, M., Burnett, B.G., Bosch-Marcé, M., Griffin, J.W., Rich, M.M., and Sumner, C.J. (2009). Impaired synaptic vesicle release and immaturity of neuromuscular junctions in spinal muscular atrophy mice. J. Neurosci. Off. J. Soc. Neurosci. *29*, 842–851.

Kramer, E.R., Knott, L., Su, F., Dessaud, E., Krull, C.E., Helmbacher, F., and Klein, R. (2006). Cooperation between GDNF/Ret and ephrinA/EphA4 signals for motor-axon pathway selection in the limb. Neuron *50*, 35–47.

Kuba, H., Ishii, T.M., and Ohmori, H. (2006). Axonal site of spike initiation enhances auditory coincidence detection. Nature *444*, 1069–1072.

Kubo, T., Randolph, M.A., Gröger, A., and Winograd, J.M. (2009). Embryonic stem cell-derived motor neurons form neuromuscular junctions in vitro and enhance motor functional recovery in vivo. Plast. Reconstr. Surg. *123*, 139S – 48S.

Kurosawa, H. (2007). Methods for inducing embryoid body formation: in vitro differentiation system of embryonic stem cells. J. Biosci. Bioeng. *103*, 389–398.

Lagha, M., Kormish, J.D., Rocancourt, D., Manceau, M., Epstein, J.A., Zaret, K.S., Relaix, F., and Buckingham, M.E. (2008). Pax3 regulation of FGF signaling affects the progression of embryonic progenitor cells into the myogenic program. Genes Dev. *22*, 1828–1837.

Landmesser, L. (1978). The distribution of motoneurones supplying chick hind limb muscles. J. Physiol. *284*, 371–389.

Landmesser, L.T. (2001). The acquisition of motoneuron subtype identity and motor circuit formation. Int. J. Dev. Neurosci. Off. J. Int. Soc. Dev. Neurosci. *19*, 175–182.

Lane, S.W., Williams, D.A., and Watt, F.M. (2014). Modulating the stem cell niche for tissue regeneration. Nat. Biotechnol. *32*, 795–803.

Lasorella, A., Benezra, R., and Iavarone, A. (2014). The ID proteins: master regulators of cancer stem cells and tumour aggressiveness. Nat. Rev. Cancer *14*, 77–91.

Lassar, A.B., Paterson, B.M., and Weintraub, H. (1986). Transfection of a DNA locus that mediates the conversion of 10T1/2 fibroblasts to myoblasts. Cell *47*, 649–656.

Lassar, A.B., Buskin, J.N., Lockshon, D., Davis, R.L., Apone, S., Hauschka, S.D., and Weintraub, H. (1989). MyoD is a sequence-specific DNA binding protein requiring a region of myc homology to bind to the muscle creatine kinase enhancer. Cell *58*, 823–831.

Latvanlehto, A., Fox, M.A., Sormunen, R., Tu, H., Oikarainen, T., Koski, A., Naumenko, N., Shakirzyanova, A., Kallio, M., Ilves, M., et al. (2010). Muscle-derived collagen XIII regulates maturation of the skeletal neuromuscular junction. J. Neurosci. Off. J. Soc. Neurosci. *30*, 12230–12241.

Le Bras, B., Fréal, A., Czarnecki, A., Legendre, P., Bullier, E., Komada, M., Brophy, P.J., Davenne, M., and Couraud, F. (2014). In vivo assembly of the axon initial segment in motor neurons. Brain Struct. Funct. *219*, 1433–1450.

Lemaillet, G., Walker, B., and Lambert, S. (2003). Identification of a conserved ankyrin-binding motif in the family of sodium channel alpha subunits. J. Biol. Chem. *278*, 27333–27339.

Lemercier, C., To, R.Q., Carrasco, R.A., and Konieczny, S.F. (1998). The basic helix-loop-helix transcription factor Mist1 functions as a transcriptional repressor of myoD. EMBO J. *17*, 1412–1422.

Lemons, D., and McGinnis, W. (2006). Genomic evolution of Hox gene clusters. Science *313*, 1918–1922.

Li, M., Suzuki, K., Kim, N.Y., Liu, G.-H., and Izpisua Belmonte, J.C. (2014). A cut above the rest: targeted genome editing technologies in human pluripotent stem cells. J. Biol. Chem. *289*, 4594–4599.

Li, X.-J., Du, Z.-W., Zarnowska, E.D., Pankratz, M., Hansen, L.O., Pearce, R.A., and Zhang, S.-C. (2005). Specification of motoneurons from human embryonic stem cells. Nat. Biotechnol. *23*, 215–221.

Liem, K.F., Tremml, G., and Jessell, T.M. (1997). A role for the roof plate and its resident TGFbeta-related proteins in neuronal patterning in the dorsal spinal cord. Cell *91*, 127–138.

Liem, K.F., Jessell, T.M., and Briscoe, J. (2000). Regulation of the neural patterning activity of sonic hedgehog by secreted BMP inhibitors expressed by notochord and somites. Dev. Camb. Engl. *127*, 4855–4866.

Lin, J.H., Saito, T., Anderson, D.J., Lance-Jones, C., Jessell, T.M., and Arber, S. (1998). Functionally related motor neuron pool and muscle sensory afferent subtypes defined by coordinate ETS gene expression. Cell *95*, 393–407.

Lin, L.F., Doherty, D.H., Lile, J.D., Bektesh, S., and Collins, F. (1993). GDNF: a glial cell line-derived neurotrophic factor for midbrain dopaminergic neurons. Science *260*, 1130–1132.

Lin, Q., Schwarz, J., Bucana, C., and Olson, E.N. (1997). Control of mouse cardiac morphogenesis and myogenesis by transcription factor MEF2C. Science *276*, 1404–1407.

Lindvall, O. (2012). Dopaminergic neurons for Parkinson's therapy. Nat. Biotechnol. *30*, 56–58.

Liu, J.-P. (2006). The function of growth/differentiation factor 11 (Gdf11) in rostrocaudal patterning of the developing spinal cord. Dev. Camb. Engl. *133*, 2865–2874.

Liu, J.P., Laufer, E., and Jessell, T.M. (2001). Assigning the positional identity of spinal motor neurons: rostrocaudal patterning of Hox-c expression by FGFs, Gdf11, and retinoids. Neuron *32*, 997–1012.

Liu, L., Luo, G.-Z., Yang, W., Zhao, X., Zheng, Q., Lv, Z., Li, W., Wu, H.-J., Wang, L., Wang, X.-J., et al. (2010). Activation of the imprinted Dlk1-Dio3 region correlates with pluripotency levels of mouse stem cells. J. Biol. Chem. *285*, 19483–19490.

Livet, J., Sigrist, M., Stroebel, S., De Paola, V., Price, S.R., Henderson, C.E., Jessell, T.M., and Arber, S. (2002). ETS gene Pea3 controls the central position and terminal arborization of specific motor neuron pools. Neuron *35*, 877–892.

Longley, D.B., Harkin, D.P., and Johnston, P.G. (2003). 5-fluorouracil: mechanisms of action and clinical strategies. Nat. Rev. Cancer *3*, 330–338.

Lu, J., Webb, R., Richardson, J.A., and Olson, E.N. (1999). MyoR: a muscle-restricted basic helix-loop-helix transcription factor that antagonizes the actions of MyoD. Proc. Natl. Acad. Sci. U. S. A. *96*, 552–557.

Lu, J., McKinsey, T.A., Zhang, C.L., and Olson, E.N. (2000). Regulation of skeletal myogenesis by association of the MEF2 transcription factor with class II histone deacetylases. Mol. Cell *6*, 233–244.

Lund, E., and Dahlberg, J.E. (2006). Substrate selectivity of exportin 5 and Dicer in the biogenesis of microRNAs. Cold Spring Harb. Symp. Quant. Biol. *71*, 59–66.

Luo, W., Nie, Q., and Zhang, X. (2013). MicroRNAs involved in skeletal muscle differentiation. J. Genet. Genomics Yi Chuan Xue Bao *40*, 107–116.

Machado, C.B., Kanning, K.C., Kreis, P., Stevenson, D., Crossley, M., Nowak, M., Iacovino, M., Kyba, M., Chambers, D., Blanc, E., et al. (2014). Reconstruction of phrenic neuron identity in embryonic stem cell-derived motor neurons. Dev. Camb. Engl. *141*, 784–794.

MacIntosh, B.R., Gardiner, P.F., and McComas, A.J. (2006). Skeletal Muscle: Form and Function (Human Kinetics).

Manuel, M., and Zytnicki, D. (2011). Alpha, beta and gamma motoneurons: functional diversity in the motor system's final pathway. J. Integr. Neurosci. *10*, 243–276.

Marieb, E.N., and Hoehn, K. (2010). Human Anatomy & Physiology (Benjamin Cummings).

Marques, M.J., Conchello, J.A., and Lichtman, J.W. (2000). From plaque to pretzel: fold formation and acetylcholine receptor loss at the developing neuromuscular junction. J. Neurosci. Off. J. Soc. Neurosci. *20*, 3663–3675.

Martin, G.R. (1981). Isolation of a pluripotent cell line from early mouse embryos cultured in medium conditioned by teratocarcinoma stem cells. Proc. Natl. Acad. Sci. U. S. A. *78*, 7634–7638.

Martin, J.F., Schwarz, J.J., and Olson, E.N. (1993). Myocyte enhancer factor (MEF) 2C: a tissue-restricted member of the MEF-2 family of transcription factors. Proc. Natl. Acad. Sci. U. S. A. *90*, 5282–5286.

Martin, J.F., Miano, J.M., Hustad, C.M., Copeland, N.G., Jenkins, N.A., and Olson, E.N. (1994). A Mef2 gene that generates a muscle-specific isoform via alternative mRNA splicing. Mol. Cell. Biol. *14*, 1647–1656.

Martin, N.R.W., Passey, S.L., Player, D.J., Mudera, V., Baar, K., Greensmith, L., and Lewis, M.P. (2015). Neuromuscular Junction Formation in Tissue-Engineered Skeletal Muscle Augments Contractile Function and Improves Cytoskeletal Organization. Tissue Eng. Part A *21*, 2595–2604.

McKinsey, T.A., Zhang, C.L., and Olson, E.N. (2001). Control of muscle development by dueling HATs and HDACs. Curr. Opin. Genet. Dev. *11*, 497–504.

McPherron, A.C., Lawler, A.M., and Lee, S.J. (1999). Regulation of anterior/posterior patterning of the axial skeleton by growth/differentiation factor 11. Nat. Genet. *22*, 260–264.

Miles, G.B., Yohn, D.C., Wichterle, H., Jessell, T.M., Rafuse, V.F., and Brownstone, R.M. (2004). Functional properties of motoneurons derived from mouse embryonic stem cells. J. Neurosci. Off. J. Soc. Neurosci. *24*, 7848–7858.

Miles, G.B., Dai, Y., and Brownstone, R.M. (2005). Mechanisms underlying the early phase of spike frequency adaptation in mouse spinal motoneurones. J. Physiol. *566*, 519–532.

Miller, G. (2009). Origins. On the origin of the nervous system. Science *325*, 24–26.

Milner, L.D., and Landmesser, L.T. (1999). Cholinergic and GABAergic inputs drive patterned spontaneous motoneuron activity before target contact. J. Neurosci. Off. J. Soc. Neurosci. *19*, 3007–3022.

Misgeld, T., Kummer, T.T., Lichtman, J.W., and Sanes, J.R. (2005). Agrin promotes synaptic differentiation by counteracting an inhibitory effect of neurotransmitter. Proc. Natl. Acad. Sci. U. S. A. *102*, 11088–11093.

Mitra, P., and Brownstone, R.M. (2012). An in vitro spinal cord slice preparation for recording from lumbar motoneurons of the adult mouse. J. Neurophysiol. *107*, 728–741.

Molkentin, J.D., Black, B.L., Martin, J.F., and Olson, E.N. (1995). Cooperative activation of muscle gene expression by MEF2 and myogenic bHLH proteins. Cell *83*, 1125–1136.

Molofsky, A.V., Kelley, K.W., Tsai, H.-H., Redmond, S.A., Chang, S.M., Madireddy, L., Chan, J.R., Baranzini, S.E., Ullian, E.M., and Rowitch, D.H. (2014). Astrocyte-encoded positional cues maintain sensorimotor circuit integrity. Nature *509*, 189–194.

Moore, K.A., and Lemischka, I.R. (2006). Stem cells and their niches. Science *311*, 1880–1885.

Moretti, A., Bellin, M., Welling, A., Jung, C.B., Lam, J.T., Bott-Flügel, L., Dorn, T., Goedel, A., Höhnke, C., Hofmann, F., et al. (2010). Patient-specific induced pluripotent stem-cell models for long-QT syndrome. N. Engl. J. Med. *363*, 1397–1409.

Murray, L.M., Comley, L.H., Thomson, D., Parkinson, N., Talbot, K., and Gillingwater, T.H. (2008). Selective vulnerability of motor neurons and dissociation of pre- and post-synaptic pathology at the neuromuscular junction in mouse models of spinal muscular atrophy. Hum. Mol. Genet. *17*, 949–962.

Murry, C.E., and Keller, G. (2008). Differentiation of embryonic stem cells to clinically relevant populations: lessons from embryonic development. Cell *132*, 661–680.

Nabeshima, Y., Hanaoka, K., Hayasaka, M., Esumi, E., Li, S., Nonaka, I., and Nabeshima, Y. (1993). Myogenin gene disruption results in perinatal lethality because of severe muscle defect. Nature *364*, 532–535.

Nagel, G., Szellas, T., Huhn, W., Kateriya, S., Adeishvili, N., Berthold, P., Ollig, D., Hegemann, P., and Bamberg, E. (2003). Channelrhodopsin-2, a directly light-gated cation-selective membrane channel. Proc. Natl. Acad. Sci. U. S. A. *100*, 13940–13945.

Naya, F.J., and Olson, E. (1999). MEF2: a transcriptional target for signaling pathways controlling skeletal muscle growth and differentiation. Curr. Opin. Cell Biol. *11*, 683–688.

Ng, H.-H., and Surani, M.A. (2011). The transcriptional and signalling networks of pluripotency. Nat. Cell Biol. *13*, 490–496.

Nguyen, Q.T., Parsadanian, A.S., Snider, W.D., and Lichtman, J.W. (1998). Hyperinnervation of neuromuscular junctions caused by GDNF overexpression in muscle. Science *279*, 1725–1729.

Nichols, J., and Smith, A. (2009). Naive and primed pluripotent states. Cell Stem Cell *4*, 487–492.

Nishimune, H., Sanes, J.R., and Carlson, S.S. (2004). A synaptic laminin-calcium channel interaction organizes active zones in motor nerve terminals. Nature *432*, 580–587.

Nishimune, H., Valdez, G., Jarad, G., Moulson, C.L., Müller, U., Miner, J.H., and Sanes, J.R. (2008). Laminins promote postsynaptic maturation by an autocrine mechanism at the neuromuscular junction. J. Cell Biol. *182*, 1201–1215.

Nishiyama, A., Komitova, M., Suzuki, R., and Zhu, X. (2009). Polydendrocytes (NG2 cells): multifunctional cells with lineage plasticity. Nat. Rev. Neurosci. *10*, 9–22.

Niwa, H., Burdon, T., Chambers, I., and Smith, A. (1998). Self-renewal of pluripotent embryonic stem cells is mediated via activation of STAT3. Genes Dev. *12*, 2048–2060.

Noakes, P.G., Gautam, M., Mudd, J., Sanes, J.R., and Merlie, J.P. (1995). Aberrant differentiation of neuromuscular junctions in mice lacking s-laminin/laminin beta 2. Nature *374*, 258–262.

Nordström, U., Maier, E., Jessell, T.M., and Edlund, T. (2006). An early role for WNT signaling in specifying neural patterns of Cdx and Hox gene expression and motor neuron subtype identity. PLoS Biol. *4*, e252.

Norton, J.D., Deed, R.W., Craggs, G., and Sablitzky, F. (1998). Id helix-loop-helix proteins in cell growth and differentiation. Trends Cell Biol. *8*, 58–65.

Novitch, B.G., Chen, A.I., and Jessell, T.M. (2001). Coordinate regulation of motor neuron subtype identity and pan-neuronal properties by the bHLH repressor Olig2. Neuron *31*, 773–789.

Ogawa, Y., and Rasband, M.N. (2008). The functional organization and assembly of the axon initial segment. Curr. Opin. Neurobiol. *18*, 307–313.

Ohira, Y., Yoshinaga, T., Ohara, M., Kawano, F., Wang, X.D., Higo, Y., Terada, M., Matsuoka, Y., Roy, R.R., and Edgerton, V.R. (2006). The role of neural and mechanical influences in maintaining normal fast and slow muscle properties. Cells Tissues Organs *182*, 129–142.

Okita, K., Ichisaka, T., and Yamanaka, S. (2007). Generation of germline-competent induced pluripotent stem cells. Nature *448*, 313–317.

Okita, K., Nakagawa, M., Hyenjong, H., Ichisaka, T., and Yamanaka, S. (2008). Generation of mouse induced pluripotent stem cells without viral vectors. Science *322*, 949–953.

Olivera-Martinez, I., Coltey, M., Dhouailly, D., and Pourquié, O. (2000). Mediolateral somitic origin of ribs and dermis determined by quail-chick chimeras. Dev. Camb. Engl. *127*, 4611–4617.

Ozasa, S., Kimura, S., Ito, K., Ueno, H., Ikezawa, M., Matsukura, M., Yoshioka, K., Araki, K., Yamamura, K., Abe, K., et al. (2007). Efficient conversion of ES cells into myogenic lineage using the gene-inducible system. Biochem. Biophys. Res. Commun. *357*, 957–963.

Pan, Z., Kao, T., Horvath, Z., Lemos, J., Sul, J.-Y., Cranstoun, S.D., Bennett, V., Scherer, S.S., and Cooper, E.C. (2006). A common ankyrin-G-based mechanism retains KCNQ and NaV channels at electrically active domains of the axon. J. Neurosci. Off. J. Soc. Neurosci. *26*, 2599–2613.

Pecho-Vrieseling, E., Sigrist, M., Yoshida, Y., Jessell, T.M., and Arber, S. (2009). Specificity of sensory-motor connections encoded by Sema3e-Plxnd1 recognition. Nature *459*, 842–846.

Pera, M.F., and Tam, P.P.L. (2010). Extrinsic regulation of pluripotent stem cells. Nature *465*, 713–720.

Personius, K.E., and Balice-Gordon, R.J. (2001). Loss of correlated motor neuron activity during synaptic competition at developing neuromuscular synapses. Neuron *31*, 395–408.

Pette, D., and Staron, R.S. (2000). Myosin isoforms, muscle fiber types, and transitions. Microsc. Res. Tech. *50*, 500–509.

Pfaff, S.L., Mendelsohn, M., Stewart, C.L., Edlund, T., and Jessell, T.M. (1996). Requirement for LIM homeobox gene Isl1 in motor neuron generation reveals a motor neuron-dependent step in interneuron differentiation. Cell *84*, 309–320.

Ponomareva, O.N., Ma, H., Vock, V.M., Ellerton, E.L., Moody, S.E., Dakour, R., Chodosh, L.A., and Rimer, M. (2006). Defective neuromuscular synaptogenesis in mice expressing constitutively active ErbB2 in skeletal muscle fibers. Mol. Cell. Neurosci. *31*, 334–345.

Prakash, Y.S., Miyata, H., Zhan, W.Z., and Sieck, G.C. (1999). Inactivity-induced remodeling of neuromuscular junctions in rat diaphragmatic muscle. Muscle Nerve *22*, 307–319.

Prasad, A., and Hollyday, M. (1991). Development and migration of avian sympathetic preganglionic neurons. J. Comp. Neurol. *307*, 237–258.

Price, S.R., De Marco Garcia, N.V., Ranscht, B., and Jessell, T.M. (2002). Regulation of motor neuron pool sorting by differential expression of type II cadherins. Cell *109*, 205–216.

Proske, U., and Gandevia, S.C. (2009). The kinaesthetic senses. J. Physiol. *587*, 4139–4146.

Przyborski, S.A. (2005). Differentiation of human embryonic stem cells after transplantation in immune-deficient mice. Stem Cells Dayt. Ohio *23*, 1242–1250.

Puri, P.L., Avantaggiati, M.L., Balsano, C., Sang, N., Graessmann, A., Giordano, A., and Levrero, M. (1997). p300 is required for MyoD-dependent cell cycle arrest and muscle-specific gene transcription. EMBO J. *16*, 369–383.

Ramade, A., Legant, W.R., Picart, C., Chen, C.S., and Boudou, T. (2014). Microfabrication of a platform to measure and manipulate the mechanics of engineered microtissues. Methods Cell Biol. *121*, 191–211.

Ramiya, V.K., Maraist, M., Arfors, K.E., Schatz, D.A., Peck, A.B., and Cornelius, J.G. (2000). Reversal of insulin-dependent diabetes using islets generated in vitro from pancreatic stem cells. Nat. Med. *6*, 278–282.

Ransom, B.R., and Ransom, C.B. (2012). Astrocytes: multitalented stars of the central nervous system. Methods Mol. Biol. Clifton NJ *814*, 3–7.

Reddy, L.V., Koirala, S., Sugiura, Y., Herrera, A.A., and Ko, C.P. (2003). Glial cells maintain synaptic structure and function and promote development of the neuromuscular junction in vivo. Neuron *40*, 563–580.

Relaix, F., Rocancourt, D., Mansouri, A., and Buckingham, M. (2005). A Pax3/Pax7-dependent population of skeletal muscle progenitor cells. Nature *435*, 948–953.

Rideout, W.M., Hochedlinger, K., Kyba, M., Daley, G.Q., and Jaenisch, R. (2002). Correction of a genetic defect by nuclear transplantation and combined cell and gene therapy. Cell *109*, 17–27.

Riechmann, V., van Crüchten, I., and Sablitzky, F. (1994). The expression pattern of Id4, a novel dominant negative helix-loop-helix protein, is distinct from Id1, Id2 and Id3. Nucleic Acids Res. *22*, 749–755.

Riethmacher, D., Sonnenberg-Riethmacher, E., Brinkmann, V., Yamaai, T., Lewin, G.R., and Birchmeier, C. (1997). Severe neuropathies in mice with targeted mutations in the ErbB3 receptor. Nature *389*, 725–730.

da Rocha, S.T., Edwards, C.A., Ito, M., Ogata, T., and Ferguson-Smith, A.C. (2008). Genomic imprinting at the mammalian Dlk1-Dio3 domain. Trends Genet. TIG *24*, 306–316.

Rogister, B., Ben-Hur, T., and Dubois-Dalcq, M. (1999). From neural stem cells to myelinating oligodendrocytes. Mol. Cell. Neurosci. *14*, 287–300.

van Rooij, E., Quiat, D., Johnson, B.A., Sutherland, L.B., Qi, X., Richardson, J.A., Kelm, R.J., and Olson, E.N. (2009). A family of microRNAs encoded by myosin genes governs myosin expression and muscle performance. Dev. Cell *17*, 662–673.

Rossant, J., and Cross, J.C. (2001). Placental development: lessons from mouse mutants. Nat. Rev. Genet. *2*, 538–548.

Rouaux, C., Panteleeva, I., René, F., Gonzalez de Aguilar, J.-L., Echaniz-Laguna, A., Dupuis, L., Menger, Y., Boutillier, A.-L., and Loeffler, J.-P. (2007). Sodium valproate exerts neuroprotective effects in vivo through CREB-binding protein-dependent mechanisms but does not improve survival in an amyotrophic lateral sclerosis mouse model. J. Neurosci. Off. J. Soc. Neurosci. *27*, 5535–5545.

Rowitch, D.H., and Kriegstein, A.R. (2010). Developmental genetics of vertebrate glial-cell specification. Nature *468*, 214–222.

Rudnicki, M.A., and Jaenisch, R. (1995). The MyoD family of transcription factors and skeletal myogenesis. BioEssays News Rev. Mol. Cell. Dev. Biol. *17*, 203–209.

Rudnicki, M.A., Braun, T., Hinuma, S., and Jaenisch, R. (1992). Inactivation of MyoD in mice leads to up-regulation of the myogenic HLH gene Myf-5 and results in apparently normal muscle development. Cell *71*, 383–390.

Rudnicki, M.A., Schnegelsberg, P.N., Stead, R.H., Braun, T., Arnold, H.H., and Jaenisch, R. (1993). MyoD or Myf-5 is required for the formation of skeletal muscle. Cell *75*, 1351–1359.

Ryan, T., Liu, J., Chu, A., Wang, L., Blais, A., and Skerjanc, I.S. (2012). Retinoic acid enhances skeletal myogenesis in human embryonic stem cells by expanding the premyogenic progenitor population. Stem Cell Rev. *8*, 482–493.

Saarma, M. (2000). GDNF - a stranger in the TGF-beta superfamily? Eur. J. Biochem. FEBS *267*, 6968–6971.

Sakurai, H., Okawa, Y., Inami, Y., Nishio, N., and Isobe, K. (2008). Paraxial mesodermal progenitors derived from mouse embryonic stem cells contribute to muscle regeneration via differentiation into muscle satellite cells. Stem Cells Dayt. Ohio *26*, 1865–1873.

Samson, A.O., and Levitt, M. (2008). Inhibition mechanism of the acetylcholine receptor by alpha-neurotoxins as revealed by normal-mode dynamics. Biochemistry (Mosc.) *47*, 4065–4070.

Sanchez-Ponce, D., Tapia, M., Muñoz, A., and Garrido, J.J. (2008). New role of IKK alpha/beta phosphorylated I kappa B alpha in axon outgrowth and axon initial segment development. Mol. Cell. Neurosci. *37*, 832–844.

Sandrock, A.W., Dryer, S.E., Rosen, K.M., Gozani, S.N., Kramer, R., Theill, L.E., and Fischbach, G.D. (1997). Maintenance of acetylcholine receptor number by neuregulins at the neuromuscular junction in vivo. Science *276*, 599–603.

Sanes, J.R. (2003). The basement membrane/basal lamina of skeletal muscle. J. Biol. Chem. *278*, 12601–12604.

Sanes, J.R., and Lichtman, J.W. (1999). Development of the vertebrate neuromuscular junction. Annu. Rev. Neurosci. *22*, 389–442.

Sanes, J.R., and Lichtman, J.W. (2001). Induction, assembly, maturation and maintenance of a postsynaptic apparatus. Nat. Rev. Neurosci. *2*, 791–805.

Sarantitis, I., Papanastasopoulos, P., Manousi, M., Baikoussis, N.G., and Apostolakis, E. (2012). The cytoskeleton of the cardiac muscle cell. Hell. J. Cardiol. HJC Hellēnikē Kardiologikē Epitheōrēsē *53*, 367–379.

Schroedl, N.A., Funanage, V.L., Bacon, C.R., Smith, S.M., and Hartzell, C.R. (1988). Hemin increases aerobic capacity of cultured regenerating skeletal myotubes. Am. J. Physiol. *255*, C519–C525.

Schultz, C., König, H.-G., Del Turco, D., Politi, C., Eckert, G.P., Ghebremedhin, E., Prehn, J.H.M., Kögel, D., and Deller, T. (2006). Coincident enrichment of phosphorylated IkappaBalpha, activated IKK, and phosphorylated p65 in the axon initial segment of neurons. Mol. Cell. Neurosci. *33*, 68–80.

Schulz, T.C., Young, H.Y., Agulnick, A.D., Babin, M.J., Baetge, E.E., Bang, A.G., Bhoumik, A., Cepa, I., Cesario, R.M., Haakmeester, C., et al. (2012). A scalable system for production of functional pancreatic progenitors from human embryonic stem cells. PloS One *7*, e37004.

Seale, P., Sabourin, L.A., Girgis-Gabardo, A., Mansouri, A., Gruss, P., and Rudnicki, M.A. (2000). Pax7 is required for the specification of myogenic satellite cells. Cell *102*, 777–786.

Seipel, K., and Schmid, V. (2005). Evolution of striated muscle: jellyfish and the origin of triploblasty. Dev. Biol. *282*, 14–26.

Seipel, K., and Schmid, V. (2006). Mesodermal anatomies in cnidarian polyps and medusae. Int. J. Dev. Biol. *50*, 589–599.

de la Serna, I.L., Carlson, K.A., and Imbalzano, A.N. (2001). Mammalian SWI/SNF complexes promote MyoD-mediated muscle differentiation. Nat. Genet. *27*, 187–190.

Sernagor, E., and O'Donovan, M.J. (1991). Whole-cell patch clamp recordings from rhythmically active motoneurons in the isolated spinal cord of the chick embryo. Neurosci. Lett. *128*, 211–216.

Shah, V., Drill, E., and Lance-Jones, C. (2004). Ectopic expression of Hoxd10 in thoracic spinal segments induces motoneurons with a lumbosacral molecular profile and axon projections to the limb. Dev. Dyn. Off. Publ. Am. Assoc. Anat. *231*, 43–56.

Sharma, K., Sheng, H.Z., Lettieri, K., Li, H., Karavanov, A., Potter, S., Westphal, H., and Pfaff, S.L. (1998). LIM homeodomain factors Lhx3 and Lhx4 assign subtype identities for motor neurons. Cell *95*, 817–828.

Sharp, L., and Trivedi, J.R. (2014). Treatment and management of neuromuscular channelopathies. Curr. Treat. Options Neurol. *16*, 313.

Shieh, P.B. (2013). Muscular dystrophies and other genetic myopathies. Neurol. Clin. *31*, 1009–1029.

da Silva, J.S., and Dotti, C.G. (2002). Breaking the neuronal sphere: regulation of the actin cytoskeleton in neuritogenesis. Nat. Rev. Neurosci. *3*, 694–704.

Simone, C., Forcales, S.V., Hill, D.A., Imbalzano, A.N., Latella, L., and Puri, P.L. (2004). p38 pathway targets SWI-SNF chromatin-remodeling complex to muscle-specific loci. Nat. Genet. *36*, 738–743.

Singhal, N., and Martin, P.T. (2011). Role of extracellular matrix proteins and their receptors in the development of the vertebrate neuromuscular junction. Dev. Neurobiol. *71*, 982–1005.

Si-Tayeb, K., Noto, F.K., Sepac, A., Sedlic, F., Bosnjak, Z.J., Lough, J.W., and Duncan, S.A. (2010). Generation of human induced pluripotent stem cells by simple transient transfection of plasmid DNA encoding reprogramming factors. BMC Dev. Biol. *10*, 81.

Skoglund, G., Lainé, J., Darabi, R., Fournier, E., Perlingeiro, R., and Tabti, N. (2014). Physiological and ultrastructural features of human induced pluripotent and embryonic stem cell-derived skeletal myocytes in vitro. Proc. Natl. Acad. Sci. U. S. A. *111*, 8275–8280.

Sleigh, J.N., Burgess, R.W., Gillingwater, T.H., and Cader, M.Z. (2014a). Morphological analysis of neuromuscular junction development and degeneration in rodent lumbrical muscles. J. Neurosci. Methods *227*, 159–165.

Sleigh, J.N., Grice, S.J., Burgess, R.W., Talbot, K., and Cader, M.Z. (2014b). Neuromuscular junction maturation defects precede impaired lower motor neuron connectivity in Charcot-Marie-Tooth type 2D mice. Hum. Mol. Genet. *23*, 2639–2650.

Small, J.V. (1995). Structure-function relationships in smooth muscle: the missing links. BioEssays News Rev. Mol. Cell. Dev. Biol. *17*, 785–792.

Smith, A.S.T., Passey, S., Greensmith, L., Mudera, V., and Lewis, M.P. (2012). Characterization and optimization of a simple, repeatable system for the long term in vitro culture of aligned myotubes in 3D. J. Cell. Biochem. *113*, 1044–1053.

Smith, I.W., Mikesh, M., Lee, Y. il, and Thompson, W.J. (2013). Terminal Schwann cells participate in the competition underlying neuromuscular synapse elimination. J. Neurosci. Off. J. Soc. Neurosci. *33*, 17724–17736.

Song, A.-H., Wang, D., Chen, G., Li, Y., Luo, J., Duan, S., and Poo, M.-M. (2009). A selective filter for cytoplasmic transport at the axon initial segment. Cell *136*, 1148–1160.

Sonnenblick, E.H., and Stam, A.C. (1969). Cardiac muscle: activation and contraction. Annu. Rev. Physiol. *31*, 647–674.

Soundararajan, P., Miles, G.B., Rubin, L.L., Brownstone, R.M., and Rafuse, V.F. (2006). Motoneurons derived from embryonic stem cells express transcription factors and develop phenotypes characteristic of medial motor column neurons. J. Neurosci. Off. J. Soc. Neurosci. *26*, 3256–3268.

Spicer, D.B., Rhee, J., Cheung, W.L., and Lassar, A.B. (1996). Inhibition of myogenic bHLH and MEF2 transcription factors by the bHLH protein Twist. Science *272*, 1476–1480.

Staron, R.S. (1997). Human skeletal muscle fiber types: delineation, development, and distribution. Can. J. Appl. Physiol. Rev. Can. Physiol. Appliquée *22*, 307–327.

Stewart, C.L., Kaspar, P., Brunet, L.J., Bhatt, H., Gadi, I., Köntgen, F., and Abbondanzo, S.J. (1992). Blastocyst implantation depends on maternal expression of leukaemia inhibitory factor. Nature *359*, 76–79.

Stifani, N. (2014). Motor neurons and the generation of spinal motor neuron diversity. Front. Cell. Neurosci. *8*, 293.

Suetterlin, K., Männikkö, R., and Hanna, M.G. (2014). Muscle channelopathies: recent advances in genetics, pathophysiology and therapy. Curr. Opin. Neurol. *27*, 583–590.

Suzuki, T., Li, W., Zhang, J.-P., Tian, Q.-B., Sakagami, H., Usuda, N., Usada, N., Kondo, H., Fujii, T., and Endo, S. (2005). A novel scaffold protein, TANC, possibly a rat homolog of Drosophila rolling pebbles (rols), forms a multiprotein complex with various postsynaptic density proteins. Eur. J. Neurosci. *21*, 339–350.

Tajbakhsh, S., and Buckingham, M. (2000). The birth of muscle progenitor cells in the mouse: spatiotemporal considerations. Curr. Top. Dev. Biol. *48*, 225–268.

Takahashi, K., and Yamanaka, S. (2006). Induction of pluripotent stem cells from mouse embryonic and adult fibroblast cultures by defined factors. Cell *126*, 663–676.

Takahashi, K., Tanabe, K., Ohnuki, M., Narita, M., Ichisaka, T., Tomoda, K., and Yamanaka, S. (2007). Induction of pluripotent stem cells from adult human fibroblasts by defined factors. Cell *131*, 861–872.

Tanaka, A., Woltjen, K., Miyake, K., Hotta, A., Ikeya, M., Yamamoto, T., Nishino, T., Shoji, E., Sehara-Fujisawa, A., Manabe, Y., et al. (2013). Efficient and reproducible myogenic differentiation from human iPS cells: prospects for modeling Miyoshi Myopathy in vitro. PloS One *8*, e61540.

Tapia, J.C., Wylie, J.D., Kasthuri, N., Hayworth, K.J., Schalek, R., Berger, D.R., Guatimosim, C., Seung, H.S., and Lichtman, J.W. (2012). Pervasive synaptic branch removal in the mammalian neuromuscular system at birth. Neuron *74*, 816–829.

Tapscott, S.J. (2005). The circuitry of a master switch: Myod and the regulation of skeletal muscle gene transcription. Dev. Camb. Engl. *132*, 2685–2695.

Tapscott, S.J., Davis, R.L., Thayer, M.J., Cheng, P.F., Weintraub, H., and Lassar, A.B. (1988). MyoD1: a nuclear phosphoprotein requiring a Myc homology region to convert fibroblasts to myoblasts. Science *242*, 405–411.

Tedesco, F.S., Gerli, M.F.M., Perani, L., Benedetti, S., Ungaro, F., Cassano, M., Antonini, S., Tagliafico, E., Artusi, V., Longa, E., et al. (2012). Transplantation of genetically corrected human iPSC-derived progenitors in mice with limb-girdle muscular dystrophy. Sci. Transl. Med. *4*, 140ra89.

Tesar, P.J., Chenoweth, J.G., Brook, F.A., Davies, T.J., Evans, E.P., Mack, D.L., Gardner, R.L., and McKay, R.D.G. (2007). New cell lines from mouse epiblast share defining features with human embryonic stem cells. Nature *448*, 196–199.

Thomson, J.A., Itskovitz-Eldor, J., Shapiro, S.S., Waknitz, M.A., Swiergiel, J.J., Marshall, V.S., and Jones, J.M. (1998). Embryonic stem cell lines derived from human blastocysts. Science *282*, 1145–1147.

Thomson, S.R., Wishart, T.M., Patani, R., Chandran, S., and Gillingwater, T.H. (2012). Using induced pluripotent stem cells (iPSC) to model human neuromuscular connectivity: promise or reality? J. Anat. *220*, 122–130.

Tosney, K.W., and Landmesser, L.T. (1985). Growth cone morphology and trajectory in the lumbosacral region of the chick embryo. J. Neurosci. Off. J. Soc. Neurosci. *5*, 2345–2358.

Tremblay, P., and Gruss, P. (1994). Pax: genes for mice and men. Pharmacol. Ther. *61*, 205–226.

Trollet, C., Athanasopoulos, T., Popplewell, L., Malerba, A., and Dickson, G. (2009). Gene therapy for muscular dystrophy: current progress and future prospects. Expert Opin. Biol. Ther. *9*, 849–866.

Tucker, K.L., Meyer, M., and Barde, Y.-A. (2001). Neurotrophins are required for nerve growth during development. Nat. Neurosci. *4*, 29–37.

Ullian, E.M., Christopherson, K.S., and Barres, B.A. (2004). Role for glia in synaptogenesis. Glia *47*, 209–216.

Ulloa, F., and Briscoe, J. (2007). Morphogens and the control of cell proliferation and patterning in the spinal cord. Cell Cycle Georget. Tex *6*, 2640–2649.

Umbach, J.A., Adams, K.L., Gundersen, C.B., and Novitch, B.G. (2012). Functional neuromuscular junctions formed by embryonic stem cell-derived motor neurons. PloS One *7*, e36049.

Valenzuela, D.M., Stitt, T.N., DiStefano, P.S., Rojas, E., Mattsson, K., Compton, D.L., Nuñez, L., Park, J.S., Stark, J.L., and Gies, D.R. (1995). Receptor tyrosine kinase specific for the skeletal muscle lineage: expression in embryonic muscle, at the neuromuscular junction, and after injury. Neuron *15*, 573–584.

Vallstedt, A., Muhr, J., Pattyn, A., Pierani, A., Mendelsohn, M., Sander, M., Jessell, T.M., and Ericson, J. (2001). Different levels of repressor activity assign redundant and specific roles to Nkx6 genes in motor neuron and interneuron specification. Neuron *31*, 743–755.

VanSaun, M., and Werle, M.J. (2000). Matrix metalloproteinase-3 removes agrin from synaptic basal lamina. J. Neurobiol. *43*, 140–149.

VanSaun, M., Herrera, A.A., and Werle, M.J. (2003). Structural alterations at the neuromuscular junctions of matrix metalloproteinase 3 null mutant mice. J. Neurocytol. *32*, 1129–1142.

Vasyutina, E., Stebler, J., Brand-Saberi, B., Schulz, S., Raz, E., and Birchmeier, C. (2005). CXCR4 and Gab1 cooperate to control the development of migrating muscle progenitor cells. Genes Dev. *19*, 2187–2198.

Vock, V.M., Ponomareva, O.N., and Rimer, M. (2008). Evidence for muscle-dependent neuromuscular synaptic site determination in mammals. J. Neurosci. Off. J. Soc. Neurosci. *28*, 3123–3130.

Voog, J., and Jones, D.L. (2010). Stem cells and the niche: a dynamic duo. Cell Stem Cell *6*, 103–115.

Vrieseling, E., and Arber, S. (2006). Target-induced transcriptional control of dendritic patterning and connectivity in motor neurons by the ETS gene Pea3. Cell *127*, 1439–1452.

Walsh, M.K., and Lichtman, J.W. (2003). In vivo time-lapse imaging of synaptic takeover associated with naturally occurring synapse elimination. Neuron *37*, 67–73.

Wang, S., Bates, J., Li, X., Schanz, S., Chandler-Militello, D., Levine, C., Maherali, N., Studer, L., Hochedlinger, K., Windrem, M., et al. (2013). Human iPSC-derived oligodendrocyte progenitor cells can myelinate and rescue a mouse model of congenital hypomyelination. Cell Stem Cell *12*, 252–264.

Wasserman, W.W., and Fickett, J.W. (1998). Identification of regulatory regions which confer muscle-specific gene expression. J. Mol. Biol. *278*, 167–181.

Weatherbee, S.D., Anderson, K.V., and Niswander, L.A. (2006). LDL-receptor-related protein 4 is crucial for formation of the neuromuscular junction. Dev. Camb. Engl. *133*, 4993–5000.

Weingarten, M.D., Lockwood, A.H., Hwo, S.Y., and Kirschner, M.W. (1975). A protein factor essential for microtubule assembly. Proc. Natl. Acad. Sci. U. S. A. *72*, 1858–1862.

Weintraub, H., Tapscott, S.J., Davis, R.L., Thayer, M.J., Adam, M.A., Lassar, A.B., and Miller, A.D. (1989). Activation of muscle-specific genes in pigment, nerve, fat, liver, and fibroblast cell lines by forced expression of MyoD. Proc. Natl. Acad. Sci. U. S. A. *86*, 5434–5438.

Weintraub, H., Davis, R., Tapscott, S., Thayer, M., Krause, M., Benezra, R., Blackwell, T.K., Turner, D., Rupp, R., and Hollenberg, S. (1991). The myoD gene family: nodal point during specification of the muscle cell lineage. Science *251*, 761–766.

Wen, H., and Brehm, P. (2010). Paired patch clamp recordings from motor-neuron and target skeletal muscle in zebrafish. J. Vis. Exp. JoVE.

Wichterle, H., Lieberam, I., Porter, J.A., and Jessell, T.M. (2002). Directed differentiation of embryonic stem cells into motor neurons. Cell *110*, 385–397.

Williams, R.L., Hilton, D.J., Pease, S., Willson, T.A., Stewart, C.L., Gearing, D.P., Wagner, E.F., Metcalf, D., Nicola, N.A., and Gough, N.M. (1988). Myeloid leukaemia inhibitory factor maintains the developmental potential of embryonic stem cells. Nature *336*, 684–687.

Wilmut, I., Schnieke, A.E., McWhir, J., Kind, A.J., and Campbell, K.H. (1997). Viable offspring derived from fetal and adult mammalian cells. Nature *385*, 810–813.

Wilson, L., and Maden, M. (2005). The mechanisms of dorsoventral patterning in the vertebrate neural tube. Dev. Biol. *282*, 1–13.

Wilting, J., Papoutsi, M., Schneider, M., and Christ, B. (2000). The lymphatic endothelium of the avian wing is of somitic origin. Dev. Dyn. Off. Publ. Am. Assoc. Anat. *217*, 271–278.

Wolpowitz, D., Mason, T.B., Dietrich, P., Mendelsohn, M., Talmage, D.A., and Role, L.W. (2000). Cysteine-rich domain isoforms of the neuregulin-1 gene are required for maintenance of peripheral synapses. Neuron *25*, 79–91.

Wright, W.E., Binder, M., and Funk, W. (1991). Cyclic amplification and selection of targets (CASTing) for the myogenin consensus binding site. Mol. Cell. Biol. *11*, 4104–4110.

Wu, H., Xiong, W.C., and Mei, L. (2010). To build a synapse: signaling pathways in neuromuscular junction assembly. Dev. Camb. Engl. *137*, 1017–1033.

Wyatt, R.M., and Balice-Gordon, R.J. (2003). Activity-dependent elimination of neuromuscular synapses. J. Neurocytol. *32*, 777–794.

Wyllie, A.H. (1997). Apoptosis: an overview. Br. Med. Bull. *53*, 451–465.

Xu, C., Tabebordbar, M., Iovino, S., Ciarlo, C., Liu, J., Castiglioni, A., Price, E., Liu, M., Barton, E.R., Kahn, C.R., et al. (2013a). A zebrafish embryo culture system defines factors that promote vertebrate myogenesis across species. Cell *155*, 909–921.

Xu, C., Tabebordbar, M., Iovino, S., Ciarlo, C., Liu, J., Castiglioni, A., Price, E., Liu, M., Barton, E.R., Kahn, C.R., et al. (2013b). A zebrafish embryo culture system defines factors that promote vertebrate myogenesis across species. Cell *155*, 909–921.

Yaffe, D., and Saxel, O. (1977). Serial passaging and differentiation of myogenic cells isolated from dystrophic mouse muscle. Nature *270*, 725–727.

Yampolsky, P., Pacifici, P.G., Lomb, L., Giese, G., Rudolf, R., Röder, I.V., and Witzemann, V. (2010). Time lapse in vivo visualization of developmental stabilization of synaptic receptors at neuromuscular junctions. J. Biol. Chem. *285*, 34589–34596.

Yang, X., Arber, S., William, C., Li, L., Tanabe, Y., Jessell, T.M., Birchmeier, C., and Burden, S.J. (2001). Patterning of muscle acetylcholine receptor gene expression in the absence of motor innervation. Neuron *30*, 399–410.

Yang, Y., Ogawa, Y., Hedstrom, K.L., and Rasband, M.N. (2007). betaIV spectrin is recruited to axon initial segments and nodes of Ranvier by ankyrinG. J. Cell Biol. *176*, 509–519.

Yee, S.P., and Rigby, P.W. (1993). The regulation of myogenin gene expression during the embryonic development of the mouse. Genes Dev. *7*, 1277–1289.

Yin, H., Price, F., and Rudnicki, M.A. (2013). Satellite cells and the muscle stem cell niche. Physiol. Rev. *93*, 23–67.

Ying, Q.-L., Wray, J., Nichols, J., Batlle-Morera, L., Doble, B., Woodgett, J., Cohen, P., and Smith, A. (2008). The ground state of embryonic stem cell self-renewal. Nature *453*, 519–523.

Yohn, D.C., Miles, G.B., Rafuse, V.F., and Brownstone, R.M. (2008). Transplanted mouse embryonic stem-cell-derived motoneurons form functional motor units and reduce muscle atrophy. J. Neurosci. Off. J. Soc. Neurosci. *28*, 12409–12418.

Yusuf, F., Rehimi, R., Dai, F., and Brand-Saberi, B. (2005). Expression of chemokine receptor CXCR4 during chick embryo development. Anat. Embryol. (Berl.) *210*, 35–41.

Yusuf, F., Rehimi, R., Moroşan-Puopolo, G., Dai, F., Zhang, X., and Brand-Saberi, B. (2006). Inhibitors of CXCR4 affect the migration and fate of CXCR4+ progenitors in the developing limb of chick embryos. Dev. Dyn. Off. Publ. Am. Assoc. Anat. *235*, 3007–3015.

Zapata, A.G. (2013). Bone-marrow stroma: A source of mesenchymal stem cells for cell therapy. Stem Cells Reprod. Med. Basic Sci. Ther. Potential 140.

Zhang, H., Robinson, N., Wu, C., Wang, W., and Harrington, M.A. (2010). Electrophysiological properties of motor neurons in a mouse model of severe spinal muscular atrophy: in vitro versus in vivo development. PloS One *5*, e11696.

Zhang, H., Wu, C.-Y., Wang, W., and Harrington, M.A. (2011). Interneuronal synapses formed by motor neurons appear to be glutamatergic. Neuroreport *22*, 809–813.

Zhang, H.-M., Robinson, N., Gómez-Curet, I., Wang, W., and Harrington, M.A. (2009). Neuronal and network activity in networks of cultured spinal motor neurons. Neuroreport *20*, 849–854.

Zhao, X., Li, W., Lv, Z., Liu, L., Tong, M., Hai, T., Hao, J., Guo, C., Ma, Q., Wang, L., et al. (2009). iPS cells produce viable mice through tetraploid complementation. Nature *461*, 86–90.

Zhao, Y., Araki, S., Wu, J., Teramoto, T., Chang, Y.-F., Nakano, M., Abdelfattah, A.S., Fujiwara, M., Ishihara, T., Nagai, T., et al. (2011). An expanded palette of genetically encoded Ca^{2+} indicators. Science *333*, 1888–1891.

Zhu, Z., and Miller, J.B. (1997). MRF4 can substitute for myogenin during early stages of myogenesis. Dev. Dyn. Off. Publ. Am. Assoc. Anat. *209*, 233–241.

Appendix A

Gene targeting strategy to create ChR2-myc ES cell line

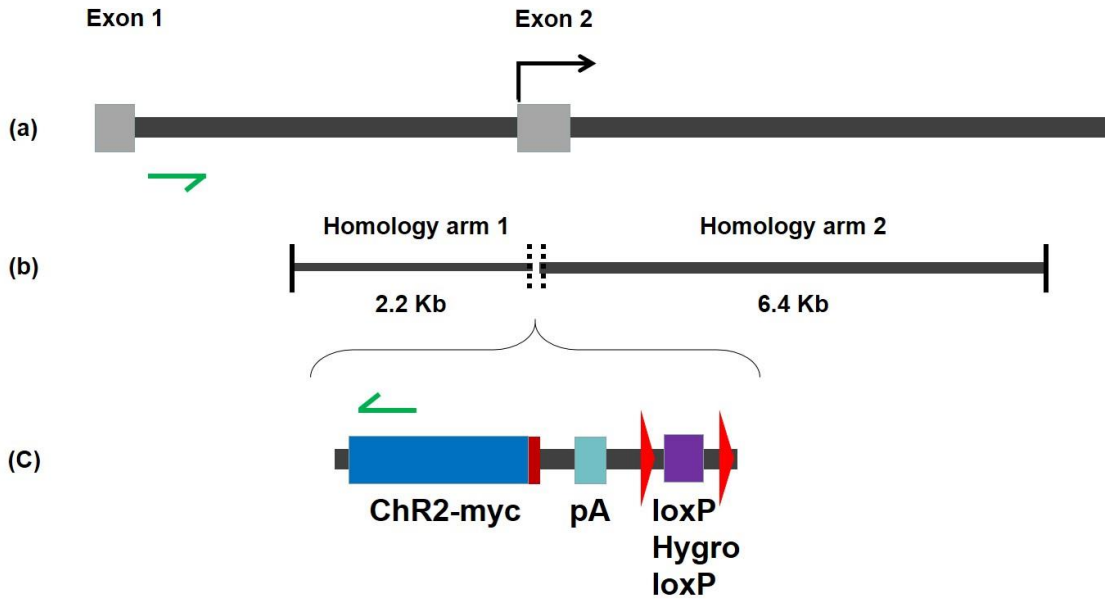

Appendix A Gene targeting strategy to generate a ChR2-myc knock-in at the endogenous *Mapt* locus. The ChR2-myc murine ES cell line described in this thesis was generated by Dr. Ivo Lieberam by insertion of a ChR2-myc construct downstream of the endogenous tau (*Mapt)* promoter via a gene targeting approach using homologous recombination. The ChR2-myc expression cassette **(c)** was inserted between two homology arms (**b**; kind gift from Silvia Arber) to regions upstream and downstream of exon 2 of the endogenous *Mapt* gene **(a)**. The homology arms were designed to recombine at exon 2 as this exon contains the start ATG codon of *Mapt*, and exon 1 is non-coding. A successful recombination event therefore replaces exon 2, including the endogenous start codon, with the desired expression cassette. The expression cassette consisted of the ChR2 gene fused to the short myc tag, followed by the bovine growth hormone poly-A (pA) and a floxed Hygromycin resistance gene to allow antibiotic resistance selection of desired ESC colonies. Successful integration of the construct into the *Mapt* locus was confirmed by long-distance PCR. The forward primer (CCTGAGTTCAAATCCCCAGAAAC) was designed to bind to a site upstream of the small homology arm in the endogenous *Mapt* gene, while the reverse primer (GTGTCCTGTGGCAAGGTAGAGC) binding site is situated in the ChR2 gene, ensuring a PCR product is only generated in the case of a successful integration event.

Appendix B

Data tables for NMJs and muscle contraction

	Monolayer	Myoblast
Average	14.122	3.435
Standard Dev.	3.470	1.172
SEM	0.496	0.040

Table A1 Spontaneous contractile activity recorded in ESC-derived muscle after 4 DIV. Average displacement caused by contractile events in fused monolayer cultures against mononuclear myoblasts. Monolayer n = 3; Myoblast n = 2. Dev. = Deviation, SEM = Standard error of the mean.

	4 DIV		12 DIV	
	+ Stim	- Stim	+ Stim	- Stim
Average	15.687	6.311	7.751	1.322
Standard Dev.	7.990	3.943	1.995	0.893
SEM	1.598	0.123	0.399	0.0812

Table A2 Spontaneous and light-evoked contractile activity recorded in ESC-derived muscle/EB co-cultures after 4 and 12 DIV. Average displacement caused by contractile events. +Stim indicates events in response to a short, manual blue-light photostimulus. DIV = Days *in* vitro. 4 DIV n = 5/3; 12 DIV n = 4/4. Dev. = Deviation, SEM = Standard error of the

	5 DIV		12 DIV	
	+ Stim	- Stim	+ Stim	- Stim
Average	23.871	3.185	32.323	28.483
Standard Dev.	5.484	2.204	10.333	11.797
SEM	1.371	0.441	1.722	0.843

	20 DIV		26 DIV	
	+ Stim	- Stim	+ Stim	- Stim
Average	93.874	17.259	32.924	12.366
Standard Dev.	69.185	11.852	18.993	3.361
SEM	4.070	0.790	1.357	0.224

Table A3 Spontaneous and light-evoked contractile activity recorded in chick primary skeletal muscle/EB co-cultures. Average displacement caused by contractile events. +Stim indicates events in response to a short, manual blue-light photostimulus. DIV = Days *in* vitro. 5 DIV n = 2/2; 12 DIV n = 2/2; 20 DIV n = 4/4; 26 DIV n = 2/3. Dev. = Deviation, SEM = Standard

	3 DIV		6 DIV	
	+ Stim	- Stim	+ Stim	- Stim
Average	11.651	0	164.926	34.901
Standard Dev.	3.149	0	91.184	50.562
SEM	1.575	0	22.796	3.160

	12 DIV		20 DIV	
	+ Stim	- Stim	+ Stim	- Stim
Average	252.970	23.7192	195.960	20.042
Standard Dev.	21.767	6.765	98.036	13.617
SEM	5.442	0.294	14.005	0.332

Table A4 Spontaneous and light-evoked contractile activity recorded in chronically photostimulated chick primary skeletal muscle/Astro-neural aggregate co-cultures. Average displacement caused by contractile events. +Stim indicates events in response to a short, manual blue-light photostimulus. DIV = Days *in* vitro. 5 DIV n = 2/2; 12 DIV n = 2/2; 20 DIV n = 4/4; 26 DIV n = 2/3. Dev. = Deviation, SEM = Standard error of the mean.

	3 DIV		6 DIV	
	+ Stim	- Stim	+ Stim	- Stim
Average	N/A	N/A	N/A	N/A
Standard Dev.	N/A	N/A	N/A	N/A
SEM	N/A	N/A	N/A	N/A

	14 DIV		21 DIV	
	+ Stim	- Stim	+ Stim	- Stim
Average	32.034	6.734	22.757	2.257
Standard Dev.	12.111	3.857	20.773	0.319
SEM	2.422	0.771	2.308	0.160

Table A5 Spontaneous and light-evoked contractile activity recorded in non-chronically stimulated chick primary skeletal muscle/Astro-neural aggregate co-cultures. Average displacement caused by contractile events. All cultures from 3 and 6 DIV were contaminated, and no data could be obtained. +Stim indicates events in response to a short, manual blue-light photostimulus. DIV = Days *in* vitro. 14 DIV n = 2/2; 21 DIV n = 3/2. Dev. = Deviation, SEM = Standard error of the mean.

	3 DIV		6 DIV	
	+ Stim	- Stim	+ Stim	- Stim
Average	0	2.628	0	1.698
Standard Dev.	0	4.551	0	2.217
SEM	0	1.138	0	0.317

	12 DIV		20 DIV	
	+ Stim	- Stim	+ Stim	- Stim
Average	25.752	25.282	7.242	16.386
Standard Dev.	14.716	27.088	2.924	9.331
SEM	4.905	0.903	0.731	0.467

Table A6 Spontaneous and light-evoked contractile activity recorded in chronically photostimulated chick primary skeletal muscle control cultures. Average displacement caused by contractile events. No response was seen in 3 or 6 DIV cultures in response to photostimulation. +Stim indicates events in response to a short, manual blue-light photostimulus. DIV = Days *in* vitro. 3 DIV n = 2/2; 6 DIV n = 3/3; 12 DIV n = 3/5; 20 DIV n = 4/4. Dev. = Deviation, SEM = Standard error of the mean.

	3 DIV		6 DIV	
	+ Stim	- Stim	+ Stim	- Stim
Average	0	2.628	0	1.698
Standard Dev.	0	4.551	0	2.217
SEM	0	1.138	0	0.317

	14 DIV		21 DIV	
	+ Stim	- Stim	+ Stim	- Stim
Average	25.752	25.282	7.242	16.386
Standard Dev.	14.716	27.088	2.924	9.331
SEM	4.905	0.903	0.731	0.467

Table A7 Spontaneous and light-evoked contractile activity recorded in in non-chronically stimulated chick primary skeletal muscle control cultures. Average displacement caused by contractile events. No response was seen in 3 or 6 DIV cultures in response to photostimulation.+Stim indicates events in response to a short, manual blue-light photostimulus. DIV = Days *in* vitro. 3 DIV n = 2/2; 6 DIV n = 3/3; 14 DIV n = 1/1; 21 DIV n = 4/4. Dev. = Deviation, SEM = Standard error of the mean.

7 DIV	CC + Stim	CC - Stim	Control + Stim	Control - Stim
N =	4	3	3	4
No. NMJs	32	3	0	1
No. Innervated	18	3	0	0
No. Partial	9	0	0	0
No. Complex Morphology	0	0	0	0
Average NMJ Area	223.705	220.589	0	157.170
St Dev	71.798	89.801	0	0
SEM	2.244	29.934	0	0
Average No. NMJs	8	1	0	0.250
Average No. Innervated	6.750	1	0	0

Table A8 Average number, morphology and size of NMJs in 7 DIV CPM/AsNAs co-cultures, with and without chronic photostimulation. +Stim indicates chronic stimulation, -Stim means no chronic stimulation. CC = Co-culture, control = CPM only. DIV = Days *in* vitro. Dev. = Deviation, SEM = Standard error of the mean.

14 DIV	CC + Stim	CC - Stim	Control + Stim	Control - Stim
N =	4	5	3	3
No. NMJs	23	15	1	2
No. Inervated	7	9	0	0
No. Partial	7	2	0	0
No. Complex Morphology	2	2	0	0
Average NMJ Area	299.255	276.638	176.471	153.034
St Dev	138.683	95.969	0	0
SEM	6.030	6.3980	0	0
Average No. NMJs	5.750	3	0.333	0.667
Average No. Innervated	3.5	2.2	0	0

Table A8 Average number, morphology and size of NMJs in 14 DIV CPM/AsNAs co-cultures, with and without chronic photostimulation. +Stim indicates chronic stimulation, -Stim means no chronic stimulation. CC = Co-culture, control = CPM only. DIV = Days *in* vitro. Dev. = Deviation, SEM = Standard error of the mean.

21 DIV	CC + Stim	CC - Stim	Control + Stim	Control - Stim
N =	5	6	3	3
No. NMJs	24	14	4	4
No. Inervated	18	3	0	0
No. Partial	5	2	0	0
No. Complex Morphology	5	4	0	0
Average NMJ Area	378.012	263.920	162.685	285.387
St Dev	259.753	168.194	8.499	165.091
SEM	10.823	12.014	2.125	41.273
Average No. NMJs	4.8	2.333	1.3333	1.333
Average No. Innervated	4.6	0.833	0	0

Table A8 Average number, morphology and size of NMJs in 21 DIV CPM/AsNAs co-cultures, with and without chronic photostimulation. +Stim indicates chronic stimulation, -Stim means no chronic stimulation. CC = Co-culture, control = CPM only. DIV = Days *in* vitro. Dev. = Deviation, SEM = Standard error of the mean.

28 DIV	CC + Stim	CC - Stim	Control + Stim	Control - Stim
N =	6	5	3	3
No. NMJs	37	14	4	3
No. Inervated	21	3	0	0
No. Partial	4	4	0	0
No. Complex Morphology	4	4	0	0
Average NMJ Area	321.884	291.493	160.617	175.552
St Dev	191.180	133.654	6.280	20.179
SEM	5.167	9.547	1.570	6.726
Average No. NMJs	6.167	2.8	1.333	1
Average No. Innervated	4.167	1.4	0	0

Table A8 Average number, morphology and size of NMJs in 28 DIV CPM/AsNAs co-cultures, with and without chronic photostimulation. +Stim indicates chronic stimulation, -Stim means no chronic stimulation. CC = Co-culture, control = CPM only. DIV = Days *in* vitro. Dev. = Deviation, SEM = Standard error of the mean.

Appendix C

Published Papers

REPORTS

Optical Control of Muscle Function by Transplantation of Stem Cell–Derived Motor Neurons in Mice

J. Barney Bryson,[1] Carolina Barcellos Machado,[2]* Martin Crossley,[2]* Danielle Stevenson,[2]* Virginie Bros-Facer,[1] Juan Burrone,[2] Linda Greensmith,[1,3]†‡ Ivo Lieberam[2]†‡

Damage to the central nervous system caused by traumatic injury or neurological disorders can lead to permanent loss of voluntary motor function and muscle paralysis. Here, we describe an approach that circumvents central motor circuit pathology to restore specific skeletal muscle function. We generated murine embryonic stem cell–derived motor neurons that express the light-sensitive ion channel channelrhodopsin-2, which we then engrafted into partially denervated branches of the sciatic nerve of adult mice. These engrafted motor neurons not only reinnervated lower hind-limb muscles but also enabled their function to be restored in a controllable manner using optogenetic stimulation. This synthesis of regenerative medicine and optogenetics may be a successful strategy to restore muscle function after traumatic injury or disease.

Electrical stimulation of motor axons within peripheral nerves has been known to induce muscle contraction since Luigi Galvani's early experiments. In more recent times, phrenic nerve pacing has been used clinically to control the function of the diaphragm, the major muscle involved in respiration, in some patients with high-level spinal cord injury (*1*) or amyotrophic lateral sclerosis (ALS) (*2*). However, peripheral nerves are composed of efferent motor axons as well as afferent sensory axons (which are unaffected in ALS). Functional electrical stimulation, which stimulates nerves indiscriminately, can thus cause considerable discomfort (*3*). Furthermore, functional electrical stimulation is ineffective if axon integrity is compromised because of injury or degenerative disease. Other strategies to replace lost motor neurons within the central nervous system include the use of embryonic stem cells (ESCs), but ESC-derived neurons do not always integrate into adult brain and spinal cord circuitry (*4*) and have difficulty overcoming molecular inhibitors of neuronal outgrowth (*5*) and extending axons across the barrier between the central and peripheral nervous system to reach the appropriate muscles (*6*).

It has previously been shown that motor neurons derived from ESCs can be engrafted into a peripheral nerve environment and successfully reinnervate denervated muscle (*7*). However, these engrafted cells are not connected to the descending inputs within the central nervous system that normally control motor function; therefore, their neural activity must be regulated by an artificial control system. Such engrafted ESC-derived motor neurons can be electrically stimulated (*7*), but this approach stimulates endogenous as well as engrafted neurons. In transgenic mice that express the light-sensitive ion channel channelrhodopsin-2 (ChR2) (*8*, *9*) in endogenous motor neurons, it has been shown that the axons of these ChR2 motor neurons can be recruited by optical stimulation in a physiological and graded fashion, resulting in optogenetic control of muscle function (*10*). It has also been shown that viral expression of ChR2 in motor neurons of adult rats can enable optical stimulation of muscle function (*11*). In this study, we tested whether expression of ChR2 in ESC-derived motor neurons engrafted into a denervated peripheral nerve (i) confers optically regulated control of muscle function, without interfering with endogenous motor signals or afferent sensory axons, and (ii) enables physiological recruitment of motor units.

We generated genetically modified ESC-derived motor neurons that express both ChR2, to enable

[1]Sobell Department of Motor Neuroscience and Movement Disorders, University College London (UCL) Institute of Neurology, London, UK. [2]Medical Research Council (MRC) Centre for Developmental Neurobiology, King's College London, Guy's Hospital Campus, London, UK. [3]MRC Centre for Neuromuscular Diseases, UCL Institute of Neurology, London, UK.

*These authors contributed equally to this work.
†These authors contributed equally to this work.
‡Corresponding author. E-mail: l.greensmith@ucl.ac.uk (L.G.); ivo.lieberam@kcl.ac.uk (I.L.)

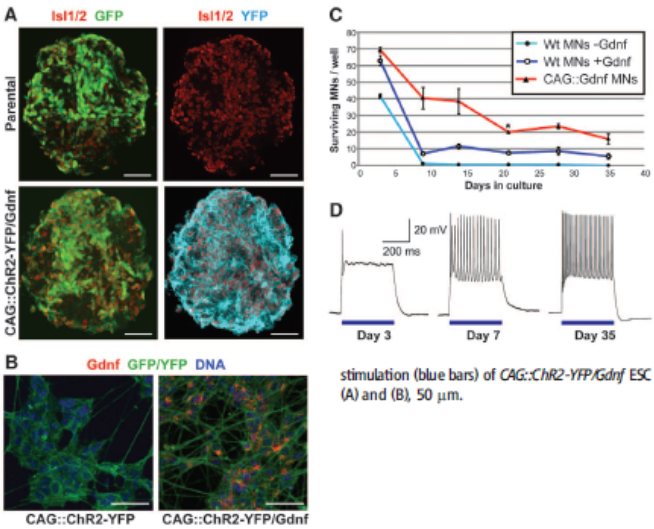

Fig. 1. Expression of Gdnf in ChR2 motor neurons enhances survival and enables them to mature electrically in vitro. (**A**) Embryoid bodies derived from *CAG::ChR2-YFP/Gdnf* transgenic ESCs and parental controls stained for the pan-motor neuron marker Isl1/2. GFP and YFP signals were detected by direct fluorescence. (**B**) Confocal images of MACS-sorted ESC motor neurons derived from *CAG::ChR2-YFP* (MACS, magnetic-activated cell sorting) and *CAG::ChR2-YFP/Gdnf* ESCs immunostained for Gdnf and GFP/YFP. (**C**) Survival analysis of sorted *CAG::ChR2-YFP* and *CAG::ChR2-YFP/Gdnf* ESC motor neurons (MNs) (200 cells per well) plated on ESC astrocytes at indicated time points. *CAG::ChR2-YFP* motor neurons were cultured with (10 ng/ml) or without recombinant Gdnf (two replicates, analysis of variance with Bonferroni correction, $*P < 0.25$). Error bars indicate SEM. One representative of three separate experiments is shown. Wt, wild type. (**D**) Optogenetic stimulation (blue bars) of *CAG::ChR2-YFP/Gdnf* ESC motor neurons cultured on ESC astrocytes. Scale bars in (A) and (B), 50 μm.

optical stimulation, as well as glial-derived neurotrophic factor (Gdnf), a neurotrophic factor that promotes long-term motor neuron survival (see supplementary materials and methods). To develop such ESCs suitable for in vivo engraftment of ESC motor neurons, we stably transfected an established mouse ESC clonal cell line that already carried the motor neuron–specific reporter *Hb9::CD14-IRES-GFP* (GFP, green fluorescent protein) (*12*) with a photoreceptor transgene that is expressed regardless of cell type, *CAG::ChR2-YFP* (YFP, yellow fluorescent protein), and with the neurotrophin-expressing *CAG::Gdnf* transgene. Embryoid bodies derived from *CAG:ChR2-YFP/Gdnf* ESCs, which express ChR2-YFP in all cells including motor neurons (Fig. 1A), were differentiated in vitro using an established protocol (*13*, *14*). *CAG::ChR2-YFP/Gdnf* motor neurons also produce Gdnf (Fig. 1B), which improves their long-term survival in vitro (Fig. 1C). When cultured on an ESC-derived astrocyte feeder layer (fig. S1), ChR2 motor neurons mature electrically over a period of 35 days, until they fire trains of action potentials in response to optical stimulation and closely resemble adult motor neuron activity patterns induced by electrical stimulation (*15*) (Fig. 1D and fig. S2).

After developing these ChR2 motor neurons, we next established an in vivo model to assess the feasibility of restoring muscle function with optical control of the engrafted cells, using the sciatic nerve. Muscle denervation was induced by sciatic nerve ligation in adult mice. This procedure results in a complete initial denervation, followed by limited regeneration of endogenous axons through the ligation site, thereby creating a partially denervated environment resembling the partial muscle denervation of early-stage ALS (fig. S3). Three days postligation, embryoid bodies containing ChR2 motor neurons were engrafted distal to the ligation into the tibial and common peroneal branches of the sciatic nerve. Histological analysis revealed that the engrafted ChR2 motor neurons not only survive for at least 35 days in the peripheral nerve environment (Fig. 2A), but also mature morphologically to resemble adult spinal motor neurons and express the mature motor neuron marker choline acetyltransferase (Fig. 2B). Immunodetection of ChR2-YFP, using an antibody to GFP, demonstrates that ChR2 is localized to the membrane of motor neurons, whereas direct detection of GFP versus YFP fluorescent signals reveals that Hb9-driven GFP expression is virtually absent in ChR2 motor neurons that have matured in vivo for 35 days (figs. S4 and S5). Additionally, ChR2 motor neurons extended large numbers of axons (Fig. 2C) distally toward both anterior [tibialis anterior (TA) and extensor digitorum longus (EDL)] and posterior [triceps surae (TS)] lower hind-limb muscles when grafted into the specific branches of the sciatic nerve that innervate these muscles. Engrafted ChR2 motor neuron axons, which grow alongside regenerating endogenous (YFP-negative) motor axons, are mostly myelinated (Fig. 2D). Histological analysis also revealed robust reinnervation of muscle fibers by ChR2 motor neurons, although the neuromuscular junctions exhibited hallmarks of inactivity, including poly-innervation as well as collateral and terminal axonal sprouting (*16*) (Fig. 2E), most likely because these motor neurons were inactive

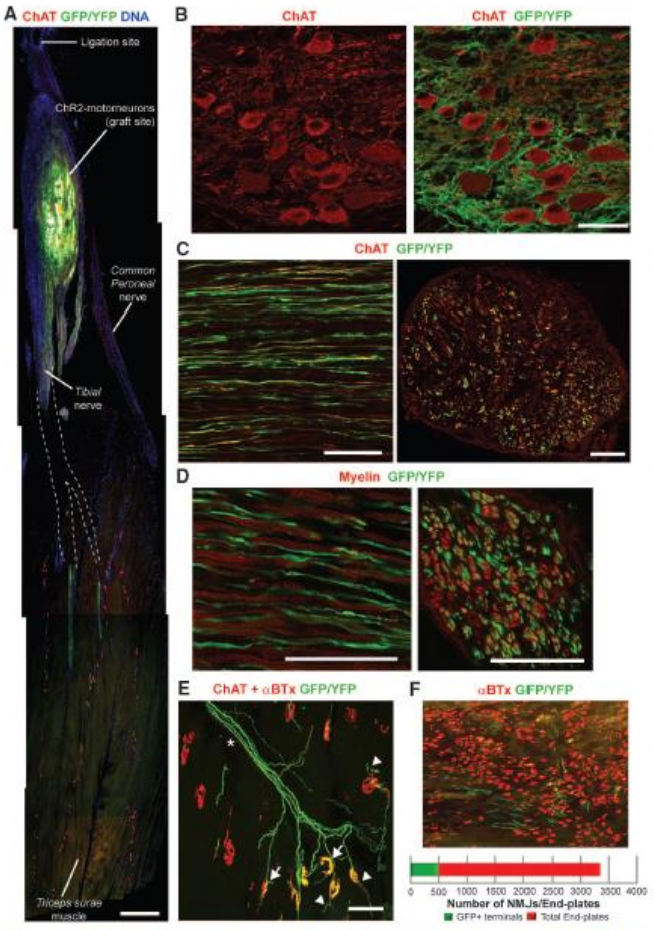

Fig. 2. Robust axonal growth and reinnervation of distal muscles after engraftment of ChR2 motor neurons. (**A**) Image montage of a whole nerve and muscle section showing ChR2 motor neuron cell bodies at the graft site and axon projection (dashed lines indicate approximate trajectory). Scale bar, 500 μm. (**B**) Confocal image of engrafted ChR2 motor neurons immunolabeled for choline acetyltransferase (ChAT; left image) and GFP and/or YFP (merged image at right). Scale bar, 50 μm. (**C**) Confocal image of longitudinal and transverse common peroneal nerve sections showing both ChR2 motor neurons and endogenous axons. Scale bar, 50 μm. (**D**) Confocal images of engrafted ChR2 motor neuron axons showing myelination. Scale bar, 50 μm. (**E**) Confocal z-stack of ChR2 motor neuron axon terminals innervating multiple neuromuscular junctions within the TS muscle. Arrows indicate preterminal collateral sprouting, arrowheads denote terminal sprouting, and the asterisk indicates an endogenous motor axon. Scale bar, 50 μm. (**F**) Two-dimensional projection image of a TS muscle showing proportion of neuromuscular junctions (NMJs) innervated by engrafted ChR2 motor neurons, relative to the total number of end plates present [labeled with α-bungarotoxin (αBTx)]. Quantification is shown below. Representative images shown here are compiled from $n = 4$ engrafted nerves from three separate experiments.

in vivo until stimulated by the external optical signal. Nevertheless, quantification of all end plates within a whole TS muscle revealed that 14.7% were innervated by YFP-positive ChR2 motor neurons axons after 35 days (Fig. 2F). Moreover, we observed YFP-positive neuromuscular junctions in both fast-twitch and slow-twitch regions of the TS, indicating that ChR2 motor neurons can innervate different muscle types. Therefore, this time point (35 days) was used in subsequent experiments to establish whether the transplanted ChR2 motor neurons were indeed functional and responsive to optical stimuli in vivo.

In anesthetized animals, we used isometric muscle tension physiology to examine the contractile responses elicited from TA, EDL, and TS (data summarized in table S1) muscles after optical stimulation of the exposed sciatic nerve using finely controlled pulses of 470-nm blue light generated by a light-emitting diode (LED) unit and delivered via a light-guide to the graft site (Fig. 3A and movie S1). Short-duration (14-ms) light pulses were able to induce submaximal twitch contractions in muscles innervated by transplanted ChR2 motor neurons (Fig. 3B), whereas high-frequency illumination (40 to 80 Hz) induced tetanic muscle contraction (Fig. 3C) that can be repeated in a highly reproducible manner (Fig. 3D). Quantification of these contractile responses demonstrated that the ratio of tetanic to twitch force was 3.09 ± 0.52 and 2.34 ± 0.33 for TA and EDL muscles, respectively (Fig. 3E), similar to normal values in uninjured animals.

Because nerve ligation enables regeneration of some endogenous motor axons, it was possible to directly compare the properties of these endogenous axons with those of the grafted ChR2 motor neurons by electrical nerve stimulation, which activates both populations of axons. This comparison demonstrated that the proportionate increase between twitch and tetanic stimuli after electrical stimulation was similar to that of optical stimulation [3.07 ± 0.5 and 2.96 ± 0.3 for TA and EDL muscles, respectively) (table S1)], although maximal force generation induced by optical stimulation of ChR2 motor neurons was weaker in comparison with electrical recruitment of both ChR2-expressing and endogenous motor neurons (12.2% of electrically induced force for TA and 12.3% for EDL). It is likely that this reduced force output of muscle fibers innervated by ChR2 motor neurons reflects the 35-day period of inactivity preceding optical stimulation, as indicated by the findings of the histological analysis of these muscles, which showed the presence of axonal sprouting and poly-innervated end plates, characteristic features of inactive muscles (*16*). Sustained optical stimulation in vivo would probably lead to reinforcement of these neuromuscular junctions and a corresponding increase in force output. Analysis of muscle contractile characteristics also revealed that the latency to peak twitch contraction from initiation of the electrical trigger to the LED unit, or direct stimulation of the nerve, was identical for both optical and electrical stimulation (Fig. 3F). This finding indicates that the nerve conduction velocities were similar for both types of stimulation and supports the histological findings showing that axons of ChR2 motor

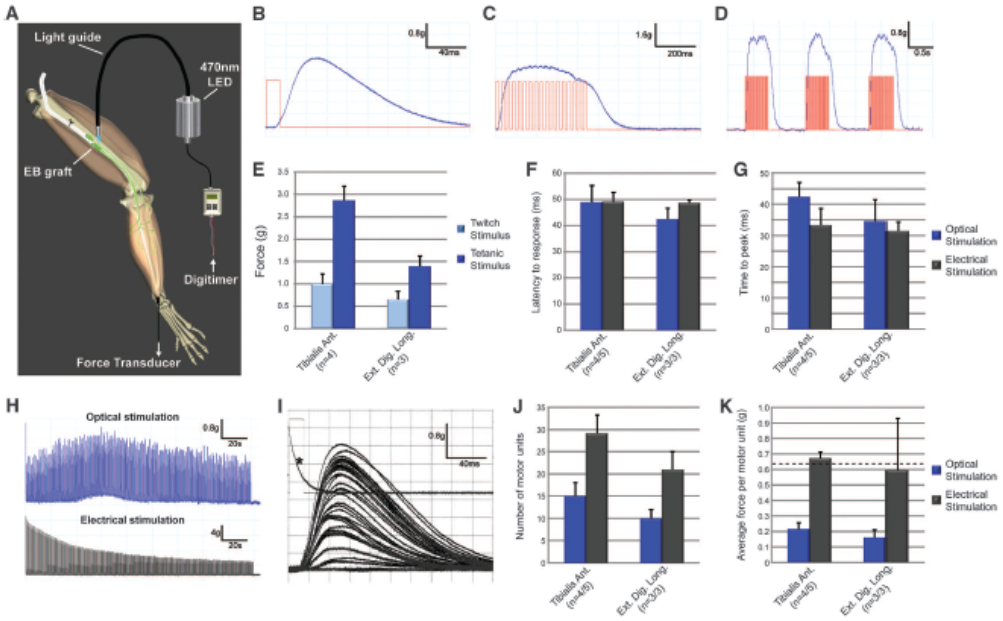

Fig. 3. Restoration of muscle function, in a controlled manner, using optical stimulation of engrafted ChR2 motor neurons in vivo. (**A**) Schematic showing optical stimulation and isometric muscle tension recordings. EB, embryoid body. Representative twitch (**B**), tetanic (**C**), and repetitive tetanic (**D**) contraction traces obtained from the TA muscle, induced by optical stimulation. Blue line, muscle force; red line, electrical trigger signals sent to the LED unit. (**E**) Quantification of twitch and tetanic contraction of TA and EDL muscles. Time to peak contractile force, from initiation of the electrical trigger to the LED unit (**F**) or from the initiation of muscle contraction (**G**), is shown alongside direct electrical nerve stimulation (*n* values represent optical/electrical stimulation, respectively, compiled from four separate experiments). (**H**) Representative fatigue traces from TA muscles (different animals) produced by optical (top) or electrical (bottom) stimulation for 180 s. (**I**) Representative TA muscle optical stimulation motor-unit number estimate trace. The asterisk indicates square-wave trigger voltage to the LED unit and oscilloscope trigger. (**J**) Motor-unit number quantification of TA and EDL muscles after optical versus electrical stimulation. (**K**) Analysis of average motor-unit force. The dashed line indicates the normal EDL value. All error bars indicate SEM.

neurons are myelinated (Fig. 2D). Additionally, the contraction rate—that is, the time from initiation of muscle contraction to peak contraction—was also very similar (Fig. 3G) for both forms of stimulation. Repetitive trains of optical or electrical stimuli (40 Hz, 250-ms duration, every 1 s) were delivered for a period of 180 s to investigate the fatigue characteristics of the reinnervated muscles, which normally have a fast-twitch, fatigable phenotype. The results showed that muscle fibers innervated by grafted ChR2 motor neurons were fatigue-resistant, in contrast to muscle fibers activated by electrical stimulation (Fig. 3H). Again, this probably reflects the prolonged period of inactivity of ChR2 motor neurons before optical stimulation.

Simultaneous activation of all motor neurons innervating a specific muscle would result in inefficient spasmodic contraction and muscle fatigue. It is therefore important that motor neurons are recruited physiologically, according to their activation threshold, to generate a graded muscle contraction that is proportionate to the intended force output. Activation threshold is normally determined by motor neuron soma size (*17*), but in the case of optogenetic activation of motor neurons, axonal diameter and intermodal distance are also important factors (*10*, *18*). With this in mind, it was important to determine whether grafted ChR2 motor neurons could also be recruited in a graded manner by optical stimulation to induce physiological motor-unit recruitment, where smaller motor units are recruited before larger motor units. To test this, the illumination intensity of the LED was varied from 0.8 to 8 mW/mm^2, which resulted in stochastic increases in muscle contractile force, demonstrating that different motor units could be recruited according to their optical activation threshold (Fig. 3I). This technique also enabled us to count the number of individual motor units innervating a given muscle, which for the TA muscle was 15 ± 3.03. Furthermore, by comparing optical and electrical nerve stimulation, we found that grafted ChR2 motor neurons accounted for ~50% of all motor units (Fig. 3J). Moreover, the motor-unit counts enabled us to calculate the average motor-unit force (Fig. 3K), which, after optical stimulation, was found to be 0.21 ± 0.04 g and 0.16 ± 0.05 g for TA and EDL muscles, respectively. Combined recruitment of endogenous and ChR2 motor neuron axons by electrical stimulation resulted in average motor-unit force values of 0.67 ± 0.04 g and 0.59 ± 0.34 g for TA and EDL muscles, respectively, consistent with normal motor-unit force (0.62 g).

In this study, we show that ChR2 motor neurons can be successfully transplanted into a peripheral nerve, where they can survive and extend axons that not only replace lost endogenous motor axons but also reinnervate denervated muscle fibers. Moreover, these transplanted ChR2 motor neurons can be selectively activated by 470-nm light, in a controlled manner to produce graded muscle contractions. Major challenges still remain before this approach can be established as an effective clinical intervention: These obstacles include the development of an implantable optical stimulator, such as that shown by Towne *et al.* (*11*), and a means to encapsulate the grafted cells. Additionally, incorporation of sensitive, red-shifted channelrhodopsin variants, such as ReaChR (*19*), rather than ChR2 would abrogate potential cellular toxicity associated with short-wavelength light (*20*).

These results show that through the use of a synthesis of regenerative medicine and optogenetics, it is possible to restore specific motor nerve functions. Although this study is largely a proof-of-principle study, it is possible that with further development this strategy may be of use in conditions where muscle function is lost—for example, after traumatic injury or neurodegenerative disease.

References and Notes

1. W. W. Glenn, M. L. Phelps, *Neurosurgery* **17**, 974–984 (1985).
2. R. P. Onders *et al.*, *Surg. Endosc.* **23**, 1433–1440 (2009).
3. B. Gernandt, *Acta Physiol. Scand.* **12**, 255–260 (1946).
4. S. C. Zhang, *J. Hematother. Stem Cell Res.* **12**, 625–634 (2003).
5. M. T. Filbin, *Nat. Rev. Neurosci.* **4**, 703–713 (2003).
6. J. M. Harper *et al.*, *Proc. Natl. Acad. Sci. U.S.A.* **101**, 7123–7128 (2004).
7. D. C. Yohn, G. B. Miles, V. F. Rafuse, R. M. Brownstone, *J. Neurosci.* **28**, 12409–12418 (2008).
8. G. Nagel *et al.*, *Proc. Natl. Acad. Sci. U.S.A.* **100**, 13940–13945 (2003).
9. E. S. Boyden, F. Zhang, E. Bamberg, G. Nagel, K. Deisseroth, *Nat. Neurosci.* **8**, 1263–1268 (2005).
10. M. E. Llewellyn, K. R. Thompson, K. Deisseroth, S. L. Delp, *Nat. Med.* **16**, 1161–1165 (2010).
11. C. Towne, K. L. Montgomery, S. M. Iyer, K. Deisseroth, S. L. Delp, *PLOS ONE* **8**, e72691 (2013).
12. C. B. Machado *et al.*, *Development* **141**, 784–794 (2014).
13. H. Wichterle, I. Lieberam, J. A. Porter, T. M. Jessell, *Cell* **110**, 385–397 (2002).
14. M. Peljto, J. S. Dasen, E. O. Mazzoni, T. M. Jessell, H. Wichterle, *Cell Stem Cell* **7**, 355–366 (2010).
15. L. Carrascal, J. L. Nieto-Gonzalez, W. E. Cameron, B. Torres, P. A. Nunez-Abades, *Brain Res. Brain Res. Rev.* **49**, 377–387 (2005).
16. W. J. Thompson, *Cell. Mol. Neurobiol.* **5**, 167–182 (1985).
17. E. Henneman, *Science* **126**, 1345–1347 (1957).
18. J. Tønnesen, *Behav. Brain Res.* **255**, 35–43 (2013).
19. J. Y. Lin, P. M. Knutsen, A. Muller, D. Kleinfeld, R. Y. Tsien, *Nat. Neurosci.* **16**, 1499–1508 (2013).
20. P. E. Hockberger *et al.*, *Proc. Natl. Acad. Sci. U.S.A.* **96**, 6255–6260 (1999).

Acknowledgments: We thank T. Keck, D. Kullman, and G. Schiavo for constructive feedback on the manuscript and the Thierry Latran Foundation for supporting this study. I.L. is funded by the Medical Research Council (G0900585), the Biotechnology and Biological Sciences Research Council (G1001234), King's Health Partners, and the Association Française contre les Myopathies. L.G. is the Graham Watts Senior Research Fellow, funded by The Brain Research Trust, and is supported by the European Community's Seventh Framework Programme (FP7/2007-2013). J.B. is a Wellcome Trust Investigator. The data reported in this paper are tabulated in the supplementary materials. We declare no conflicts of interest. I.L., C.B.M., M.C., and D.S. developed and characterized ESCs, prepared EBs, and purified motor neurons; M.C. and J.B. performed in vitro physiology; J.B.B. performed surgery, in vivo physiology, and histology and drafted the manuscript; V.B.-F. and D.S. assisted with surgery and histology; and L.G. and I.L. developed the original concept, designed and oversaw the study, and revised the manuscript.

Supplementary Materials

www.sciencemag.org/content/344/6179/94/suppl/DC1
Materials and Methods
Figs. S1 to S5
Table S1
References (*21*–*27*)
Movie S1

14 November 2013; accepted 5 March 2014
10.1126/science.1248523

Neuronal Control of *Drosophila* Walking Direction

Salil S. Bidaye,* Christian Machacek, Yang Wu,† Barry J. Dickson†‡

Most land animals normally walk forward but switch to backward walking upon sensing an obstacle or danger in the path ahead. A change in walking direction is likely to be triggered by descending "command" neurons from the brain that act upon local motor circuits to alter the timing of leg muscle activation. Here we identify descending neurons for backward walking in *Drosophila*—the MDN neurons. MDN activity is required for flies to walk backward when they encounter an impassable barrier and is sufficient to trigger backward walking under conditions in which flies would otherwise walk forward. We also identify ascending neurons, MAN, that promote persistent backward walking, possibly by inhibiting forward walking. These findings provide an initial glimpse into the circuits and logic that control walking direction in *Drosophila*.

Walking relies on the intrinsic rhythmic activity of local motor circuits within the central nervous system, called central pattern generators (CPGs). Such locomotor circuits have been documented in a number of species, including cats (*1*), rodents (*2*), crayfish (*3*), stick insects (*4*), and cockroaches (*5*). Proprioceptive feedback from leg mechanosensors ensures the accurate timing of each joint movement, but walking toward or away from specific targets requires descending signals from the brain. These descending inputs might act on CPGs to adjust the order, timing, or amplitude of individual leg movements (*6*, *7*). The nature and identity of these descending commands are poorly understood.

© 2014. Published by The Company of Biologists Ltd | Development (2014) 141, 784-794 doi:10.1242/dev.097188

RESEARCH ARTICLE

STEM CELLS AND REGENERATION

Reconstruction of phrenic neuron identity in embryonic stem cell-derived motor neurons

Carolina Barcellos Machado[1,*], Kevin C. Kanning[2], Patricia Kreis[1], Danielle Stevenson[1], Martin Crossley[1], Magdalena Nowak[1], Michelina Iacovino[3], Michael Kyba[3], David Chambers[1], Eric Blanc[1] and Ivo Lieberam[1,*]

ABSTRACT

Air breathing is an essential motor function for vertebrates living on land. The rhythm that drives breathing is generated within the central nervous system and relayed via specialised subsets of spinal motor neurons to muscles that regulate lung volume. In mammals, a key respiratory muscle is the diaphragm, which is innervated by motor neurons in the phrenic nucleus. Remarkably, relatively little is known about how this crucial subtype of motor neuron is generated during embryogenesis. Here, we used direct differentiation of motor neurons from mouse embryonic stem cells as a tool to identify genes that direct phrenic neuron identity. We find that three determinants, Pou3f1, Hoxa5 and Notch, act in combination to promote a phrenic neuron molecular identity. We show that Notch signalling induces Pou3f1 in developing motor neurons *in vitro* and *in vivo*. This suggests that the phrenic neuron lineage is established through a local source of Notch ligand at mid-cervical levels. Furthermore, we find that the cadherins Pcdh10, which is regulated by Pou3f1 and Hoxa5, and Cdh10, which is controlled by Pou3f1, are both mediators of like-like clustering of motor neuron cell bodies. This specific Pcdh10/Cdh10 activity might provide the means by which phrenic neurons are assembled into a distinct nucleus. Our study provides a framework for understanding how phrenic neuron identity is conferred and will help to generate this rare and inaccessible yet vital neuronal subtype directly from pluripotent stem cells, thus facilitating subsequent functional investigations.

KEY WORDS: Embryonic stem cell, Phrenic neuron, Transcriptional identity, Motor neuron differentiation

INTRODUCTION

Land vertebrates, including humans, use lungs to breathe air. The inspiratory and expiratory movements of the lungs are driven by a complex neural circuitry that consists of a central network in the brainstem that generates breathing rhythms and an output layer of motor neurons (MNs) that connect to respiratory muscles. These respiratory circuits develop prenatally and must become functional immediately after birth. Although significant progress has been made in understanding the central pattern generator itself (Champagnat et al., 2009; Fortin and Thoby-Brisson, 2009), relatively little is known about the formation of MNs that relay breathing rhythms from the CNS to the periphery. In mammals, respiration is driven by muscles that connect to the rib cage and thereby indirectly inflate and deflate the lungs. Arguably, the most important of these muscles is the diaphragm, which forms the boundary between the thoracic and abdominal cavities and contracts during inspiration. The diaphragm is innervated by the phrenic nucleus (PN), a population of MNs located in the mid-cervical spinal cord. During embryonic development, phrenic neurons emerge alongside other MNs from ventral progenitors (Arber et al., 1999; Briscoe et al., 2000; Thaler et al., 1999), send their axons through cervical ventral roots and then project caudally through the thoracic cavity to innervate the diaphragm muscle (Allan and Greer, 1997). We have only a partial understanding of the molecular cascade that establishes phrenic MN identity. It is, however, important that this pathway is defined as this would provide insights into how mammal-specific anatomical adaptations are patterned and allow us to model aspects of respiratory motor circuitry in neuronal cultures to study neuromuscular function and disease.

Spinal MNs segregate into distinct columns during embryogenesis. Each column connects to a specific set of muscles: the medial motor column (MMC) projects to epaxial muscles, the lateral motor column (LMC) innervates limb muscles (Lance-Jones and Landmesser, 1980; Tsuchida et al., 1994), and the hypaxial motor column (HMC) innervates body wall muscles (Dasen et al., 2003; Peljto and Wichterle, 2011). MNs acquire subtype transcriptional identities due to exposure to locally restricted morphogens (Marshall et al., 1992). For example, the expression of the MMC determinants Lhx3 and Lhx4 is sustained by floor plate-derived Wnt4 and Wnt5 (Agalliu et al., 2009). Likewise, brachial LMC fate depends on overlapping, segmentally restricted gradients of retinoic acid and Fgfs (Liu et al., 2001), which induce Hox6 paralogues and the accessory factor Foxp1 in presumptive LMC neurons in register with forelimbs (Dasen et al., 2008; Dasen et al., 2003). The HMC, by contrast, appears to lack specific determinants and might represent a ground state of MNs. Phrenic neurons are thought to be derivatives of the HMC (Rousso et al., 2008).

Some candidate determinants for early phrenic development have been identified, although their contribution to phrenic neuron specification is poorly understood: the transcription factor (TF) Pou3f1 is enriched in phrenic neurons, and *Pou3f1* deficiency in mice leads to disorganisation of the PN (Bermingham et al., 1996). Absence of mid-cervical Hox5 paralogues affects the maintenance of phrenic neurons, but not their initial specification (Philippidou et al., 2012). Lastly, Foxp1 appears to negatively regulate the phrenic MN lineage, since *Foxp1* mutants have increased numbers of phrenic MNs (Rousso et al., 2008). What is largely lacking at this point is an understanding of which potential effector genes are downstream of these factors, how these and other determinants interact and, in the case of Pou3f1, how the expression of the factor itself is initiated.

[1]MRC Centre for Developmental Neurobiology, King's College London, London SE1 1UL, UK. [2]Motor Neuron Center, Columbia University, New York, NY 10032, USA. [3]Lillehei Heart Institute, University of Minnesota, Minneapolis, MN 55455, USA.

*Authors for correspondence (carolina.barcellos_machado@kcl.ac.uk; ivo.lieberam@kcl.ac.uk)

Received 16 April 2013; Accepted 20 November 2013

Development (2014) doi:10.1242/dev.097188

MN development can be recapitulated *in vitro* from mouse or human embryonic stem cells (ESCs), which will form functional spinal MNs under the appropriate culture conditions (Li et al., 2008; Miles et al., 2004; Wichterle et al., 2002). ESC-derivation of MNs depends on the same extrinsic and intrinsic cues that act during normal embryogenesis and has been repeatedly used to investigate subtype-specific developmental pathways in these cells (Jung et al., 2010; Peljto et al., 2010; Soundararajan et al., 2006). We set out to apply this approach to the acquisition of phrenic neuron identity.

To address how phrenic neuron fate is established in the developing spinal cord, we first identified candidate determinants in primary MNs sorted from mouse embryos, and then used a systematic *in vitro* gain-of-function (GOF) screening approach to test whether any given candidate approximates phrenic neuron transcriptional patterns when ectopically expressed in ESC-derived MNs (ESC-MNs). The aim was to define modules of effector genes downstream of the key determinants, as well as to understand how the determinants interact with each other. We found that the TFs Pou3f1, Hoxa5 and Notch intracellular domain (NICD) combine to regulate distinct sets of effector genes, which together comprise a large fraction of all phrenic neuron-specific genes. Moreover, expression of the receptors Cdh10, which is downstream of Pou3f1, or Pcdh10, a gene coordinately regulated by Hoxa5 and Pou3f1, is sufficient to mediate like-like clustering of MNs into aggregates *in vitro*, mimicking nucleus formation *in vivo*. Our findings suggest that local Notch-Delta interaction in the ventral spinal cord might be an early event in phrenic neuron specification and that a defined combination of intrinsic and/or extrinsic factors may be used to emulate phrenic neuron transcriptional identity and morphological features in MNs derived from pluripotent stem cells *in vitro*.

RESULTS

Isolation of phrenic neurons from E11.5 mouse embryos by flow cytometry

In the ventral embryonic spinal cord, phrenic neurons are generated alongside other MNs from ventral progenitors. To determine the transcriptional profile of embryonic phrenic neurons, and how they differ from other MNs, we isolated phrenic neurons from E11.5 *Hb9::GFP* mouse embryos. The genetic reporter labels axons and cell bodies of all spinal MNs (Wichterle et al., 2002). In cervical and thoracic trunk explants, the cell bodies of phrenic neurons were retrogradely labelled with the tracer TMR-dextran (Fig. 1A,B). Then, spinal cord segments C3-C5 were excised from the trunks, dissociated, and phrenic neurons were sorted as GFP$^+$ TMR$^+$ cells by flow cytometry (Fig. 1C). Immunohistochemistry confirmed that only Pou3f1$^+$ phrenic MNs in the medial-dorsal part of the ventral horn were TMR positive (Fig. 1B). As a control population, non-phrenic MNs were isolated from the same cell suspension. Given their segmental origin, these MNs are likely to represent a mix of MMC, HMC and LMC neurons (Peljto et al., 2010). A second control population of pure LMC neurons was isolated by retrograde labelling through the radial nerve (Fig. 1D,E). Following isolation by flow cytometry, genome-wide transcriptional patterns of phrenic neurons and the two control populations of MNs were determined using Affymetrix arrays.

Identification of phrenic neuron-specific genes

We next devised a scheme to systematically catalogue genes into groups based on their expression pattern in radial LMC MNs, phrenic MNs and non-phrenic control MNs derived from segments C3-C5, respectively. A logical value was attributed to each gene in

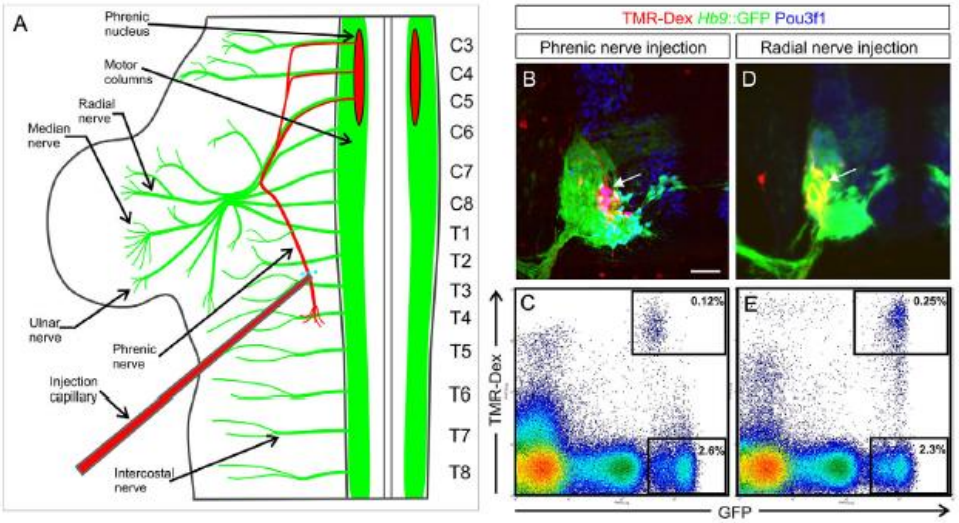

Fig. 1. Retrograde labelling and purification of mouse E11.5 embryonic phrenic MNs by flow cytometry. (A) The phrenic nerve was injected with TMR-dextran in *Hb9::GFP* trunk explants. Spinal segments are numbered according to the ventral roots that emerge from them (labels on right). C, cervical; T, thoracic. (B) Mid-cervical spinal cord transverse section: phrenic neurons (arrow) are labelled with TMR-dextran (red). The *Hb9::GFP* transgene labels all MNs; phrenic neurons co-express Pou3f1. Scale bar: 50 µm. (C) TMR$^+$ GFP$^+$ phrenic neurons and GFP$^+$ non-phrenic MNs were isolated from spinal cords (C3-C5 levels) by flow cytometry. (D) TMR$^+$ GFP$^+$ radial LMC neurons (arrow) in E11.5 cervical spinal cord (C6-C8 levels), following retrograde tracing through the radial nerve. (E) Purification of TMR$^+$ GFP$^+$ radial LMC neurons by flow cytometry.

Development (2014) doi:10.1242/dev.097188

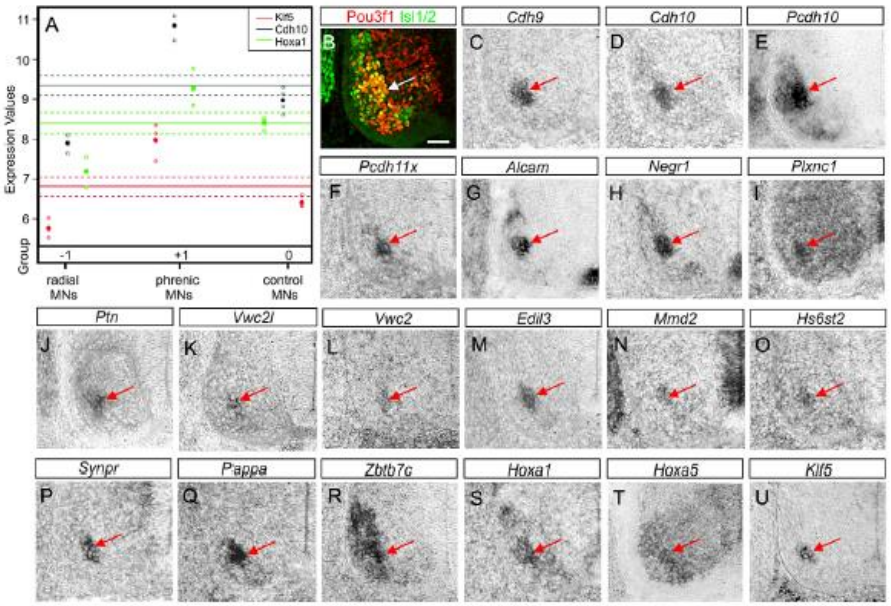

Fig. 2. Identification of genes enriched in phrenic neurons by Affymetrix array analysis. (A) Logical values were attributed to each gene in each cell type based on whether it is enriched (+1), within the mean (0) or depleted (−1). Three examples for genes enriched in phrenic neurons (*Klf5*, *Hoxa1*, *Cdh10*) are shown. Expression values are shown in $\log_2$ scale. (B) The PN is identified by expression of Pou3f1 and Isl1/2 in E11.5 mid-cervical spinal cords (arrow). Scale bar: 50 µm. (C-U) Candidate mRNAs are enriched in phrenic MNs. Red arrows indicate PN.

each cell population: genes expressed significantly above the mean across the three MN populations received the value +1, genes expressed significantly below the mean −1, and genes with expression levels above the 5th and below the 95th percentile around the mean received the value 0. *Hoxa1*, *Cdh10* and *Klf5* are examples of phrenic neuron-enriched genes with an expression value of −1 in radial MNs, +1 in phrenic MNs, and 0 in control MNs (Fig. 2A). This pattern can be described with the row vector [–1 +1 0].

A number of known MN subtype markers found in different groups of neurons suggest that our approach yields genuine expression patterns (Table 1). The MMC determinants *Lhx3* and *Lhx4* follow the pattern [–1 –1 +1] and are enriched in the C3-C5 control (Table 1), the only cell population with an MMC

Table 1. PN-enriched genes identified by Affymetrix array analysis

Enriched in PN	Examples for genes in group	Genes	Radial MNs	Phrenic MNs	Control MNs
No	*Dscam*	10	0	0	–1
No	*Gcnt2*	24	+1	0	–1
Yes	*Pappa*, *Alcam*	5	–1	+1	–1
Yes	***Tox***, *Pcdh10*, *Pcdh11x*	21	0	+1	–1
No	***Etv4***, ***Hoxc6***, *Cdh20*	78	0	–1	0
No	***Lhx1***, ***Hoxc8***, *Epha4*	63	+1	–1	0
No	***Hoxb6***, ***Hoxc5***	108	–1	0	0
No	***Etv6***, *Epha6*	277	+1	0	0
Yes	***Hoxa1***, ***Hoxa5***, *Cdh9*, *Cdh10*	173	–1	+1	0
Yes	***Arid5b***, ***Hey1***, ***Hey2***, *Plxnc1*	166	0	+1	0
No	***Lhx3***, ***Lhx4***	7	–1	–1	+1
No	***Runx2***	29	0	–1	+1
No	***Foxp1***, *Cdh7*	15	+1	–1	+1
No	***Hoxb5***, ***Nkx6-1***	52	–1	0	+1
No	***Rxrg***, ***Neurod1***	81	0	0	+1
No	***Hoxa4***, ***Pou3f1***, *Unc5c*	12	–1	+1	+1

PN-enriched genes are defined as (i) being significantly above the mean (+1) in phrenic neurons and (ii) within the 5th and 95th percentile around the mean or significantly below the mean (0 or −1, respectively) in the two control MN populations. Only selected genes are shown. Bold, TF; underlined, cadherin.

Development (2014) doi:10.1242/dev.097188

component. *Pou3f1*, one of the few established phrenic neuron markers (Bermingham et al., 1996; Rousso et al., 2008), is found both in phrenic neurons and C3-C5 control MNs. Subsequent expression analysis revealed that, at E11.5, *Pou3f1* is also expressed in a subset of MMC neurons (Fig. 2B; supplementary material Figs S3, S4), which explains the pattern that we observed. A second factor required for PN development, *Hoxa5* (Philippidou et al., 2012), is enriched in phrenic neurons as well. We were able to confirm phrenic neuron-specific expression for several candidate genes by *in situ* hybridisation (Fig. 2C-U). These genes fall into different functional categories and include cadherins (Fig. 2C-F), Ig superfamily receptors (Fig. 2G,H), BMP inhibitors (Fig. 2K,L), synaptic proteins (Fig. 2P) and TFs (Fig. 2R-U). The identification of phrenic MN-specific cadherins is significant, as adhesion molecules of this protein family are expressed in specific combinations on many, if not all, MN subsets. Cadherins mediate like-like clustering of MN cell bodies and drive the formation of topographic maps in the ventral spinal cord (Bello et al., 2012; Demireva et al., 2011; Price et al., 2002). In summary, we were able to identify a large number of genes potentially enriched in primary phrenic neurons and confirmed most of those analysed by histology.

An ESC-MN-based screening method for subtype determinants

To assess the efficacy of these genes to assign PN identity, we adapted the ESC-MN culture system such that we could perform GOF screens for multiple factors in purified MNs. We chose a mouse ESC clone that allows the efficient insertion of DOX-inducible transgenes by Cre/loxP-mediated cassette exchange (Iacovino et al., 2011) and equipped it with an additional MN-specific reporter transgene that allows magnetic enrichment of this cell type (Fig. 3A). During the initial phase of the project, we used ESCs carrying an *Hb9::CD2-GFP* MN-specific reporter (supplementary material Fig. S5, Table S2). To optimise the sorting procedure, we generated an ESC subclone that carries the *Hb9::CD14-IRES-GFP* transgene (supplementary material Fig. S1), which resulted in an improved signal-to-background ratio (Fig. 3B) and sorting efficiency. The GFP MN reporter tightly correlates with the endogenous embryonic MN marker Isl1/2 (Fig. 3C,D), and, following MACS, yielded large numbers (10^5-10^6) of viable, enriched ESC-MNs (Fig. 3B,E-G). Furthermore, we were able to induce the expression of candidate transgenes with DOX in culture, as shown here for the candidate factor Pou3f1 (Fig. 3H,I).

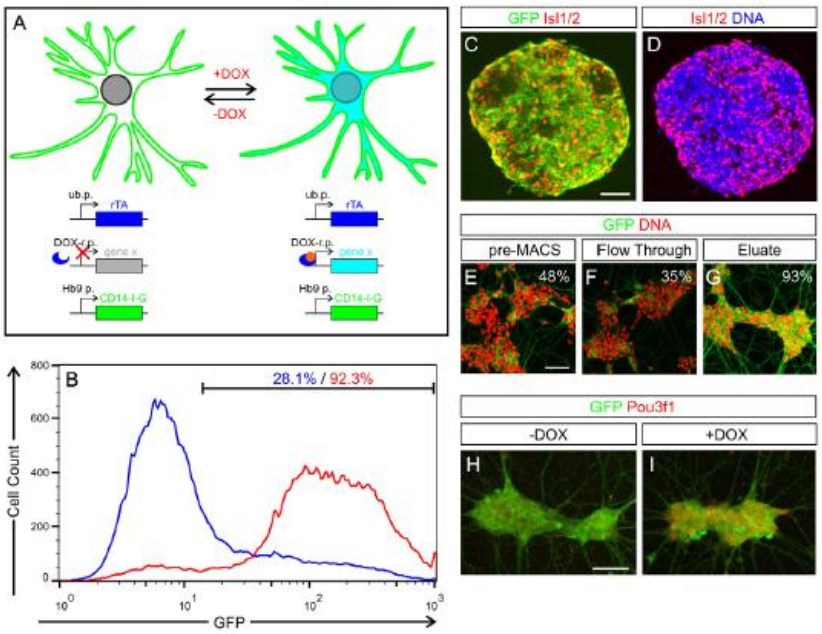

Fig. 3. Inducible expression of candidate phrenic determinants in sorted ESC-derived MNs. (A) GOF screen experimental setup for the identification of PN-specific transcriptional patterns. ESC-MNs were differentiated *in vitro*, isolated from mixed cultures with an MN-specific *Hb9::CD14-IRES-GFP* reporter gene and induced to express a given candidate gene with DOX. rTA, reverse Tet transactivator; ub.p., ubiquitous promoter; DOX-r.p., DOX-responsive promoter; Hb9 p., *Hb9* promoter. (B) Flow cytometry analysis of ESC-MNs enrichment by anti-CD14 MACS. Blue, pre-MACS cell suspension (dissociated EBs); red, anti-CD14-enriched MACS eluate. (C,D) GFP reporter and Isl1/2 expression in day 6 EBs differentiated from *Hb9::CD14-IRES-GFP* ESCs. (E-G) GFP-labelled MNs were enriched by anti-CD14 MACS and cultured (G), compared with the input (E) or the flowthrough (F). Percentage: GFP$^+$ cells. (H,I) DOX induction of iPou3f1 ESC-MNs cultured for 24 hours. Scale bars: 50 µm.

Development (2014) doi:10.1242/dev.097188

We next examined the subtype composition of parental ESC-MNs to determine the baseline identity in our assay. Primary mid-cervical MNs belong to three distinct subsets: HMC, MMC and PN (supplementary material Fig. S3A-G). When we compared the phenotypes of ESC-MNs with *in vivo* MNs, we found that they mostly belonged to the Pou3f1$^-$ Lhx3$^-$ HMC and the Pou3f1$^-$ Lhx3$^+$ or Pou3f1$^+$ Lhx3$^+$ MMC subsets, with only a small percentage of Pou3f1$^+$ Lhx3$^-$ phrenic-like neurons (supplementary material Fig. S3H-L), consistent with an earlier study (Peljto et al., 2010). The percentage of ESC-MNs with an MMC phenotype declines between day 5 and day 6 (supplementary material Fig. S3L). This might be explained by the fact that all MN progenitors express Lhx3 initially, but only MNs committed to the MMC fate sustain its expression (Sharma et al., 1998). The MN subtype composition does not depend on the ESC clone used in this study, as we have detected similar ratios of MN subtypes in cultures differentiated from a second, independently derived ESC clone (supplementary material Fig. S3M).

Our analysis of genes enriched in primary phrenic neurons pinpointed a cluster of known and putative TFs that would be good candidates as determinants of PN identity (Table 1; supplementary material Table S1). In cases in which two closely related genes were isolated, only one gene was investigated further. Our transcriptional profile also identified Notch signalling as a potential key player in this process, as we found that Notch targets, such as *Hey1* and *Hey2* (Table 1), are enriched in phrenic neurons. Furthermore, we included a dominant-negative mutant form of Lhx3 (DNLhx3) (West et al., 2004) because DNLhx3 suppresses Lhx3 target genes and might inhibit this key MMC determinant (Agalliu et al., 2009). *Vwc2* was the only non-TF chosen for analysis, because it is a chordin-like BMP inhibitor and may modulate neural patterning. Finally, we selected *Hoxc6* and wild-type *Lhx3* as control TFs, as they represent known LMC and MMC determinants, respectively. We established 19 sets of ESC subclones carrying single candidate transgenes (supplementary material Table S2) and confirmed inducible candidate gene expression in embryoid bodies (EBs) (supplementary material Fig. S6).

Reconstruction of PN-specific transcriptional patterns in ESC-MNs

To address whether candidate determinants promote transcriptional profiles associated with phrenic neurons when ectopically expressed in ESC-MNs, we differentiated transgenic ESCs into MNs in EB cultures. MNs were magnetically sorted from dissociated EBs on day 5 and induced to express the transgene with DOX during the subsequent 30 hour culture period. In some experiments with Notch constructs, the ESC-MNs were only induced for the last 10 hours to limit the effect of the transgenes. RNA of ESC-MNs derived from two independent subclones for each candidate gene was isolated, and gene expression profiles determined using Affymetrix arrays. The expression data are represented as a scatter plot in Fig. 4, in which the number of PN-enriched genes (supplementary material Table S4) repressed/induced (*y*-axis) is plotted against all genes repressed/induced by a given candidate factor (*x*-axis). The mean value for each transgene is represented by two data points, one for repression (lower left quadrant) and one for induction (upper right quadrant). We would like to point out that the terms repression and induction do not necessarily imply a direct genetic interaction, as we measure mRNA levels and not promoter binding.

Thus, the lower the *y*/*x* ratio for repression (*R*-ratio) and the higher the *y*/*x* ratio for induction (*I*-ratio) the more the transcriptional pattern evoked by a transgene approximates that of primary phrenic neurons. The *P*-values obtained using a hypergeometric distribution for over-representation of induced or repressed genes (supplementary material Table S5) provide a very similar picture to that offered by the *R*- and *I*-ratios, except that these results are more difficult to visualise.

Of all candidate determinants tested, ESC-MNs overexpressing Pou3f1 showed the most specific induction of PN-enriched genes (*I*-

Fig. 4. Identification of TFs that control parts of the PN-specific transcriptional pattern. MACS-sorted ESC-MNs were induced to express candidate determinants, and their transcriptional profiles were examined by Affymetrix array analysis. In the scatter plot, the number of PN-specific genes induced/repressed (*y*-axis) is plotted against the number of all genes induced/repressed (*x*-axis) by a given candidate factor or combination thereof. The diagonal line represents a robust fit through all the points shown, both induced and repressed.

ratio=0.3; Fig. 4, upper right quadrant), whereas not a single specific gene is repressed (*R*-ratio=0). The genes upregulated by Pou3f1 include the confirmed PN-specific genes *Cdh9*, *Cdh10* and *Pcdh11x* (Fig. 2C,D,F). NICD, when DOX-induced for the last 10 hours of ESC-MN culture, was identified as a second PN-candidate factor with a high *I*-ratio (0.102) and low *R*-ratio (0.05) (Fig. 4; supplementary material Fig. S7A). The set of PN-specific genes upregulated by iNICD includes *Vwc2l* (Fig. 2K) and is largely non-overlapping with that observed in inducible (i) Pou3f1 ESC-MNs (supplementary material Fig. S8A, Table S6), although a few target genes, such as *Hs6st2*, are shared. The timing and signal intensity of Notch activity appear to be critical, as iNICD expressed for 30 hours, or the attenuated mutant isoform iNERT (Schroeder et al., 2003) induced for 10 hours or 30 hours, do not evoke a PN-like pattern. iHoxc6, despite the absence of *Hoxc6* from primary phrenic neurons (Table 1), has a high *I*-ratio (0.109), yet also a high *R*-ratio (0.163) (supplementary material Fig. S7B). However, although iHoxc6 does induce 20 PN-enriched genes, including *Hoxa5* (supplementary material Table S6), it also upregulates two key LMC determinants, *Foxp1* (Dasen et al., 2008) and *Aldh1a2* (Sockanathan and Jessell, 1998) (supplementary material Table S7). Ectopic iHoxa5 expression in ESC-MNs, by contrast, does not induce these LMC markers, and positively regulates only three phrenic neuron-enriched genes, including *Ptn* (Fig. 2J; supplementary material Table S6). Thus, when activated in isolation, iHoxa5 does not emulate a PN transcriptional programme. Finally, iDNLhx3 does not evoke PN-like patterns (Fig. 4), but surprisingly shows the best *I*-ratio for LMC-like patterns (supplementary material Fig. S9, Tables S5, S7). This suggests that repression of Lhx3 targets unlocks parts of the LMC but not of the PN transcriptional programme in ESC-MNs.

Pou3f1 interacts with Hoxa5 to establish a phrenic-like transcriptional profile *in vitro*

To explore whether any of the candidate determinants interact to elicit PN-like transcriptional patterns, we combined the most promising candidate, Pou3f1, with Hoxa5, Hoxc6, Hoxa1 and DNLhx3 in an expression system that allows us to simultaneously induce two candidate genes in the same ESC-MNs (Bondue et al., 2011). In addition, we combined Pou3f1 with Lhx3 to investigate negative interactions, as we observed that Pou3f1 target genes, such as *Cdh9* and *Cdh10* (Fig. 2C,D), are restricted to the PN, whereas Pou3f1 itself is also expressed by a subpopulation of the MMC (supplementary material Figs S3, S4) (Rousso et al., 2008). Array analysis of double-transgenic ESC-MNs revealed that iPou3f1/iHoxa5 and iPou3f1/iHoxc6 DOX induction resulted in nearly identical *I*-ratios (0.158 versus 0.163; Fig. 4; supplementary material Fig. S7C). By contrast, the *R*-ratio for iPou3f1/iHoxa5 (0.032) indicates higher specificity than that for iPou3f1/iHoxc6 (0.069). As in the iHoxc6 single-transgenic ESC-MNs, iPou3f1/iHoxc6 expression upregulates the LMC determinants *Foxp1* and *Aldh1a2*, whereas iPou3f1/iHoxa5 expression does not (supplementary material Table S7). Interestingly, the number of PN-specific genes activated above the twofold threshold in iPou3f1/iHoxa5 ESC-MNs (22 genes) is higher than the sum of the two target gene sets in single transgenic MNs (12+3 genes), which suggests that several PN target genes, such as *Pcdh10*, require the combined activity of both determinants (supplementary material Table S6). Comparison of transcriptional patterns of iPou3f1 and iPou3f1/iLhx3 ESC-MNs shows that four of 12 iPou3f1-induced PN-specific targets, including *Cdh9*, are downregulated more than twofold by co-expression of Lhx3 (supplementary material Fig. S7D, Table S6). These findings provide evidence that Pou3f1 can interact with other determinants to regulate the activation of PN-specific target genes, and that both positive (Hoxa5) and negative (Lhx3) combinatorial interactions can be observed in ESC-MNs. Furthermore, Hoxa5 and Hoxc6, despite considerable overlap in their target genes (supplementary material Fig. S8B), differ in that Hoxc6 initiates LMC-like transcriptional patterns in ESC-MNs, whereas Hoxa5 does not.

In order to validate the transcriptional patterns observed by array analysis, we tested the expression of selected candidate genes in iYFP, iHoxa5, iNICD (10 hour pulse), iPou3f1 and iPou3f1/iHoxa5 ESC-MNs by qRT-PCR (supplementary material Table S8). The qRT-PCR expression data are largely consistent with the array data, although some additional target genes were detected. Crucially, the qRT-PCR analysis showed that NICD upregulates the PN determinant *Pou3f1*.

Notch signalling induces the PN determinant Pou3f1 in MNs *in vitro* and *in vivo*

Do the three positive phrenic determinants we identified simply act in parallel or is there a transcriptional hierarchy, i.e. does one of the candidate factors initiate phrenic neuron specification? As the qRT-PCR data suggested that NICD activity upregulates *Pou3f1*, we further examined a possible hierarchical relationship between the two factors. We compared EBs derived from the parental ESC line with those derived from iNERT ESCs, which express an attenuated, tamoxifen (4HT)-inducible version of NICD (Fig. 5A-F). Even in the absence of induction with DOX and 4HT, iNERT EBs contained a significantly higher proportion of both phrenic-like Pou3f1$^+$ Lhx3$^-$ MNs and MMC-like Pou3f1$^+$ Lhx3$^+$ MNs (Fig. 5G), without a change in total MN numbers. This increase is likely to be caused by low-level transgene expression/activity in the absence of added inducers, which is a common phenomenon seen in inducible genetic systems (Howe et al., 1995; Schroeder et al., 2003). Full induction of the iNERT transgene led to a decrease in the number of MNs (Fig. 5E,F), consistent with previous findings when NICD was overexpressed in spinal progenitors *in vivo* (Dias et al., 2012). We next examined whether Notch signalling is required for Pou3f1 expression in a subset of normal ESC-MNs. We treated developing EBs with γ-secretase inhibitors, which block ligand-dependent Notch activation (De Strooper et al., 1999). Both of the inhibitors that we tested decreased the percentage of Pou3f1$^+$ ESC-MNs by more than 90% (Fig. 5H-N), whereas they did not affect MN development in general. To test if Notch GOF upregulates additional PN markers, we examined the effect of a 10 hour pulse of DOX on the transcriptional patterns of iNICD EBs and cultured ESC-MNs, compared with normal controls. We found that NICD induces the PN-enriched genes *Synpr* (supplementary material Fig. S10), *Cdh9*, *Cdh10*, *Pcdh11x* and *Ptn* (supplementary material Table S8).

Given that Notch activity controls Pou3f1 in MNs *in vitro*, does the presence of a Notch ligand correlate with the appearance of Pou3f1$^+$ MNs *in vivo*? Analysis of mid-cervical ventral spinal cord revealed that at E10.5, which is when MNs emerge from the pMN domain, a cluster of *Dll4*-positive cells is located just dorsal of nascent Pou3f1$^+$ Isl1/2$^+$ MNs (Fig. 6A,B). Previous studies have mapped *Dll4* expression to the p2 progenitor domain (Del Barrio et al., 2007; Peng et al., 2007). Furthermore, Notch1 protein is detectable on the most immature, medial MNs, and Pou3f1 expression in MNs overlaps with that of the Notch target gene *Hey1* (supplementary material Fig. S11). At E11.5, Pou3f1$^+$ MNs have migrated laterally to settle in the PN and the MMC (Fig. 6D), a pattern that remains unchanged at E12.5 (Fig. 6G). *Dll4* expression, by contrast, is transient and not seen at later time points (Fig. 6E,H),

Development (2014) doi:10.1242/dev.097188

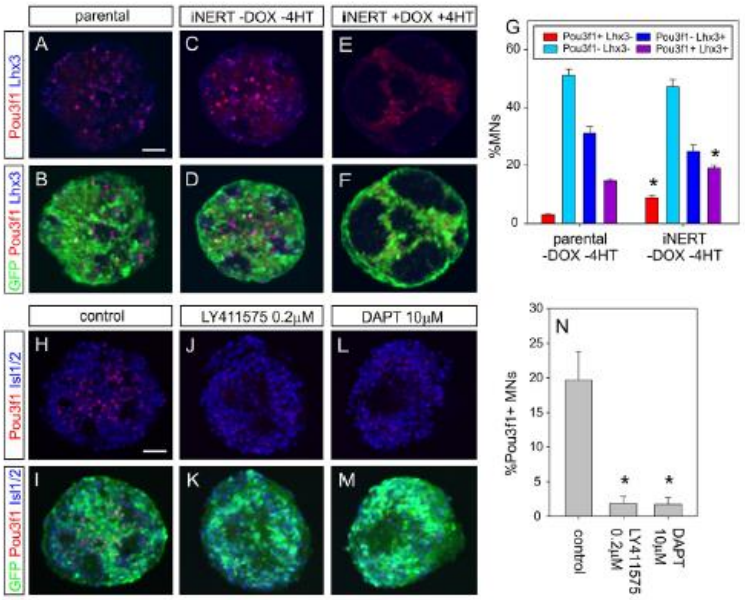

Fig. 5. Notch activation regulates Pou3f1 expression in ESC-derived MNs. (A-F) GFP, Lhx3 and Pou3f1 staining in day 6 EBs derived from parental H14IG#E3 ESCs and iNERT ESCs (without and with DOX/4HT induction). (G) Percentages of Pou3f1$^+$ Lhx3$^-$ (PN-like, red), Pou3f1$^-$ Lhx3$^-$ (HMC-like, light blue), Pou3f1$^-$ Lhx3$^+$ (dark blue) and Pou3f1$^+$ Lhx3$^+$ (purple) cells among ESC-derived GFP$^+$ MNs in day 6 EBs. The EBs were derived from ESC clones H14IG#E3 and iNERT without DOX/4HT induction. (H-M) GFP, Pou3f1 and Isl1/2 labelling in day 6 EBs. EBs were either differentiated according to the standard protocol (H,I) or treated the γ-secretase inhibitors LY411575 (J,K) or DAPT (L,M) from day 2 onwards. (N) Percentages of Pou3f1$^+$ MNs among all GFP$^+$ MNs in the absence or presence of γ-secretase inhibitor. Error bars indicate mean values from three independent experiments ± s.e.m. (G,N). *P<0.05 (paired Student's t-test). Scale bars: 50 μm.

except in blood vessels. The expression of the Pou3f1 target gene *Cdh10* is delayed compared with Pou3f1 itself and is first detected in the PN at E11.5 (Fig. 6C,F,I). The juxtaposition of Pou3f1 and *Dll4 in vivo* is mirrored by the pattern that we see in EBs, where patches of Pou3f1$^+$ Isl1/2$^+$ MNs are localised close to *Dll4*$^+$ non-MNs (Fig. 6J,K).

To examine whether Dll4 protein is capable of inducing Pou3f1 expression in primary MNs, we used whole embryo culture (WEC) (Osumi and Inoue, 2001) to ectopically express this Notch ligand in cervical spinal cords of intact mouse embryos. Owing to the timing of the WEC cultures, many non-MNs in close proximity to Isl1/2$^+$ MNs and ventral progenitors express the co-transfected reporter nGFP (Fig. 6L,N), whereas MNs themselves are mostly negative. Hence, any effect seen in MNs is likely to be non-cell-autonomous. Embryos developed normally in culture and formed a Pou3f1$^+$ PN (Fig. 6L-O). In DLL4-transfected embryos (Fig. 6L,M), but not in controls (Fig. 6N,O), the transfected side of the spinal cord contains significantly more MNs of phrenic phenotype (Fig. 6P). At the same time, the total number of MNs is unchanged (Fig. 6P), suggesting that ectopic expression of DLL4 does not expand MN progenitors. Taken together, these findings show that Pou3f1 induction in embryonic MNs is controlled by Notch signalling both in ESC-MNs and *in vivo*, and suggest that Delta-Notch interaction is involved in the acquisition of phrenic neuron identity.

The PN-specific receptors Cdh10 and Pcdh10 mediate cell clustering of ESC-MNs

A key event in early MN patterning is the aggregation of MNs of the same subtype into clusters/nuclei within the ventral horn. This like-like recognition of cell bodies is mediated by receptors of the cadherin family. Expression profiling of primary MNs suggested that the cadherins Cdh10 and Pcdh10 are highly enriched in the PN (Fig. 2D,E). To examine whether these potential effector genes are sufficient to drive specific MN clustering, we ectopically expressed Cdh10 or Pcdh10 in ESC-MNs and mixed them with RFP-labelled control ESC-MNs (Fig. 7A-C). Near-neighbour analysis revealed that iCdh10 MNs and iPcdh10 MNs, but not RFP$^-$ control MNs, segregated from RFP$^+$ control MNs in culture and formed nucleus-like aggregates (Fig. 7D-J).

DISCUSSION

The development of phrenic neurons, which drive respiration in mammals, requires the integration of positional signals to restrict their specification to mid-cervical segments of the spinal cord, where they emerge in register with myoblasts destined to form their target muscle, the diaphragm (Babiuk et al., 2003). We performed expression profiling in primary embryonic neurons followed by the reconstruction of phrenic-like transcriptional patterns in transgenic ESC-MNs to identify factors that combine

Development (2014) doi:10.1242/dev.097188

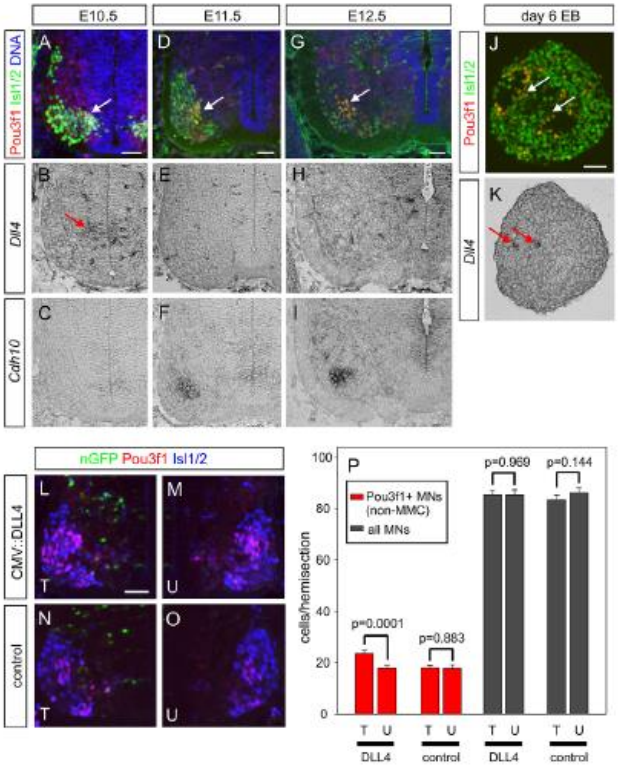

Fig. 6. The Notch ligand *Dll4* is expressed adjacent to nascent Pou3f1⁺ MNs and induces Pou3f1 in primary embryonic MNs. (A,D,G) Expression of Pou3f1 and the pan-MN marker Isl1/2 in E10.5, E11.5 and E12.5 mid-cervical spinal cord. Phrenic neurons are labelled by both markers (arrow). (B,E,H) Red arrow indicates *Dll4* expression at E10.5. At E11.5 and E12.5, few *Dll4*⁺ cells are visible, apart from blood vessels. (C,F,I) *Cdh10*, a Pou3f1 target gene, labels phrenic neurons at E11.5 and E12.5. (J) Day 6 EBs stained for Isl1/2 and Pou3f1; arrows indicate double-positive cells. (K) Expression of *Dll4* in small patches of day 6 EBs (arrows). The sections in J and K are adjacent. (L-O) Mid-cervical spinal cords of mouse embryos transfected with expression vectors for human DLL4 and nGFP (L,M) or mock and nGFP (N,O) at ~E9.75 and then allowed to develop in WEC for 40 hours. Sections were stained for nGFP, Isl1/2 and Pou3f1. (P) Analysis of mean numbers of Pou3f1⁺ Isl1/2⁺ MNs outside the MMC (red bars) and all Isl1/2⁺ MNs (black bars) in mid-cervical spinal cord hemi-sections of transfected embryos. Error bars indicate mean values from four (DLL4) or three (control) embryos ± s.e.m. (25 pairs of images each). *P*-values are by paired Student's *t*-test. Similar significances were obtained using the Mann-Whitney test and logistic regression. T, transfected side; U, untransfected side. Scale bars: 50 µm.

to establish PN identity along the dorsoventral and anteroposterior axes of the spinal cord. We found that three factors, Pou3f1, Hoxa5 and Notch, interact to control sets of putative PN-specific effector genes: Hoxa5 only evokes PN-like transcriptional patterns when combined with Pou3f1, and Notch signalling is upstream of Pou3f1. The latter interaction was observed both in ESC-MNs and in spinal cords of intact mouse embryos. Thus, our study suggests that Delta-Notch signalling at the dorsal margin of the nascent motor columns has to intersect with Hox5-dependent mid-cervical segmental identity for phrenic neurons to develop (Fig. 8). Given that NICD controls *Pou3f1*, why is there only a limited overlap between their target genes in ESC-MNs (supplementary material Fig. S8A)? The most likely explanation for this is the short time frame of iNICD induction (10 hours), which is sufficient to upregulate *Pou3f1* itself (supplementary material Table S8) but not second-order Pou3f1 targets. Based on co-expression assays in ESC-MNs, we also predict that Lhx3 is a negative regulator of phrenic identity in Pou3f1⁺ MMC neurons. In addition to transcriptional determinants, we identified and validated several sets of putative PN effector genes downstream of these regulators of PN identity. Many of these genes are regulated in a modular fashion by single factors, whereas others require the combined activity of two determinants.

The aggregation of MNs that connect to the same target muscle into nuclei and motor pools is a key event in early MN development and depends on MN subtype-specific expression of cadherins (Bello et al., 2012; Demireva et al., 2011; Price et al., 2002). This establishes a topographic map of MN cell bodies within the ventral horn and ensures that functionally related MNs receive the same sensory synaptic input (Sürmeli et al., 2011), as well as facilitating the formation of electrical synapses between MNs to coordinate activity (Personius et al., 2007). We found that the phrenic neuron-enriched receptors Cdh10, which is regulated by Pou3f1, and Pcdh10 (Hirano et al., 1999), which is regulated by Hoxa5 and Pou3f1, mediate like-like clustering of ESC-MN cell bodies *in vitro* (Fig. 7, Fig. 8C) and may contribute to the aggregation of phrenic neurons into the PN, probably in concert with other adhesion molecules.

Our findings on PN specification in ESC-MNs suggest that the coordinated expression of cadherins and other effector genes in phrenic neurons depends on the combinatorial activity of at least three positive and one negative determinant. Nevertheless, our understanding of PN gene regulation remains incomplete. For example, we do not know how the PN-enriched receptor genes *Alcam* and *Plxnc1* are regulated. There are a number of possible explanations for the limitations to our approach: (1) additional,

Development (2014) doi:10.1242/dev.097188

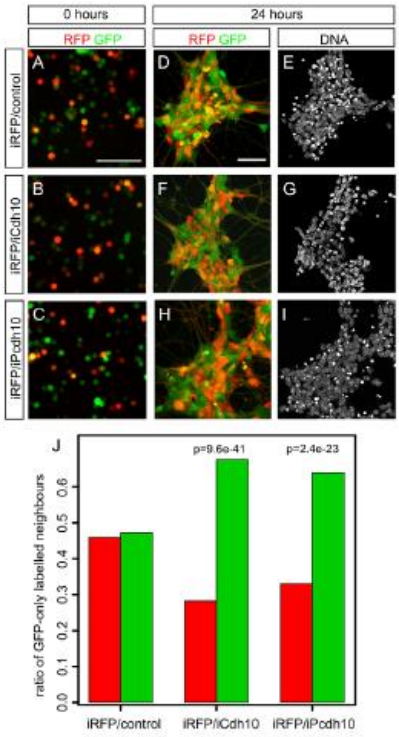

Fig. 7. The PN-specific cadherins Cdh10 and Pcdh10 mediate specific clustering of ESC-MNs. (A-C) GFP-only and RFP$^+$ GFP$^+$ ESC-MNs are randomly mixed at 0 hours. (D-I) Mixed cultures of GFP-only and RFP$^+$ GFP$^+$ ESC-MNs aggregate within 24 hours. (J) Analysis of like-like clustering of ESC-MNs in mixed cultures (24 hours) by near-neighbour analysis. Bar colours indicate the label of the central cell: red, RFP$^+$ GFP$^+$ control MNs; green, GFP-only control, iCdh10 or iPcdh10 MNs. *P*-values were calculated based on the generalised linear model with random effects. The chart shows pooled data from three independent experiments. Eight to ten cell clusters per condition (2267 MNs total) were scored. Scale bars: 50 µm.

unknown transcriptional determinants might positively regulate additional sets of PN-selective genes; (2) ESC-MNs might contain more negative regulators, which mask aspects of induced PN identity; (3) peripheral cues encountered by outgrowing phrenic axons might control some PN target genes, and these cues would not be present *in vitro*; (4) some of the PN-enriched genes that are not yet confirmed by histology could be false positives, in particular those in the least stringent [0 +1 0] group (supplementary material Table S4).

The two cervical Hox genes *Hoxa5* and *Hoxc6* evoked strikingly similar transcriptional patterns when overexpressed in ESC-MNs as single transgenes (supplementary material Fig. S8B) or combined with Pou3f1 (supplementary material Table S7), consistent with the fact that different cervical Hox proteins can bind to the same consensus DNA site (Pellerin et al., 1994). Co-expression of iPou3f1 plus iHoxa5 revealed combinatorial effects, and the overall PN specificity of the pattern is higher than that of iPou3f1 plus iHoxc6. Crucially, iHoxc6 and iPou3f1 plus iHoxc6, but not iHoxa5 and iPou3f1 plus iHoxa5, induce the TF *Foxp1*. This key LMC determinant, which largely depends on Hox6 expression *in vivo* (Dasen et al., 2008; Lacombe et al., 2013), suppresses PN identity when ectopically expressed in cervical MNs (Rousso et al., 2008). Thus, the combination of iPou3f1 plus iHoxc6 induces an LMC-type programme that is similar to that of the PN, yet at the same time is incompatible with PN identity. An *in vivo* correlate to the *Foxp1*-positive iPou3f1/iHoxc6 ESC-MNs indeed exists: ulnar motor pools, which are caudal LMC subpopulations that innervate distal limb muscles in mice (Lacombe et al., 2013), and anatomically related flexor carpi ulnaris MNs in chick (Dasen et al., 2005) co-express Pou3f1 and Hoxc6 during its initial specification. Despite their different identities, aspects of the subtype-specific genetic programmes are shared between the PN and ulnar MNs, as both populations selectively express the Pou3f1 target genes *Cdh9* and *Cdh10* (Fig. 2B-D; supplementary material Fig. S12).

MN subtype identity has been linked to Notch signalling: in *Gde2* (*Gdpd5*) null mutant mice, which have increased levels of activated Notch, MNs show a marked shift in columnar subtype composition (Sabharwal et al., 2011). Intriguingly, in their study, Notch affects MN fate at the level of progenitor cells. We first observe Pou3f1 upregulation in Isl1/2$^+$ postmitotic MNs (Fig. 6A). Nevertheless, we do not know whether Notch induction of this key PN determinant occurs before or after cell cycle exit. Delta-Notch interaction as a mechanism to diversify V2a/V2b spinal interneurons appears to be conserved between fish, birds and mammals (Batista et al., 2008; Del Barrio et al., 2007; Peng et al., 2007). There are two scenarios of how the ancestral Dll4$^+$ territory in the p2 progenitor domain, which drives this process, might relate to the emergence of the PN during mammalian evolution. In the first scenario, Dll4 expression might have acquired a novel role in establishing the mammal-specific PN. This would imply that phrenic neurons arose from cervical HMC neurons, which were respecified by Delta-Notch signalling, as the diaphragm evolved from cervical hypaxial muscle (Perry et al., 2010). Alternatively, the PN might be an evolutionary modification of an ancestral LMC subset that predates mammals. Hirasawa and Kuratani recently proposed that the diaphragm originated from limb muscle associated with the pectoral girdle (Hirasawa and Kuratani, 2013). If this scenario is correct, then phrenic neurons might have evolved from a Pou3f1$^+$ LMC subset that lost its brachial Hox code due to a duplication of two cervical segments coupled with a caudal shift in brachial identity, an event that might have occurred during early mammalian phylogeny (Hirasawa and Kuratani, 2013). This view is supported by the fact that, in mammals, there are two Pou3f1$^+$ MN subsets spaced by about two segments at cervical levels, one rostral of the LMC (the PN) and one caudal within the LMC (ulnar MNs).

In this study, we have demonstrated that MN derivation from ESCs is a viable screening tool to systematically dissect developmental pathways. Our experimental strategy was based on initially identifying candidate determinants in sorted primary embryonic neurons by transcriptional profiling and then validating the factors in the ESC-derived equivalent of these *ex vivo* cells. Both a highly reductionist approach (genome-wide expression analysis in ESC-MNs) and the more complex, heterogeneous EB culture system provided insights into how a network of TFs interact to establish PN identity. Similar ESC-based screens could be undertaken for other cell types that are difficult to access in large numbers. We think that the derivation of MNs from pluripotent stem cells will mature into

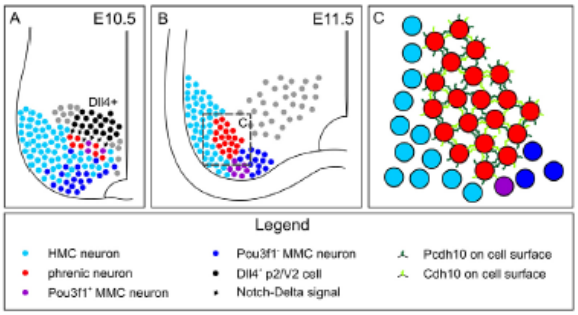

Fig. 8. Model of Delta/Notch induction of phrenic neuron identity. (A) At E10.5, Dll4-positive p2 progenitors and V2 interneurons are located immediately dorsal of nascent MNs. MNs committed to MMC or HMC fate adjacent to Dll4$^+$ territory fate are exposed to Notch signalling and upregulate the phrenic neuron determinant Pou3f1. Other Notch ligands expressed in the embryonic spinal cord might also contribute to this process. (B) Following their specification by Delta/Notch, Pou3f1$^+$ phrenic neurons migrate laterally and settle into a medial position next to the HMC. (C) The Pou3f1 targets Cdh10 and Pcdh10 mediate like-like clustering of phrenic MNs and contribute to the formation of the PN.

a powerful tool to investigate not only prenatal developmental programmes, but also subtype-dependent features of adult MN function and connectivity, complementing existing animal models. Our long-term aim is to assemble adult-like phrenic ESC-MNs, as well as other defined cell types, into artificial neuromuscular circuits to simulate aspects of respiratory motor function in health and disease *in vitro*. The progress towards understanding embryonic phrenic neuron identity reported here will allow us to extend the investigation to later steps of neuronal maturation and circuit formation.

MATERIALS AND METHODS

Summary

Embryonic phrenic neurons were labelled by injecting a retrograde tracer (TMR-dextran) into the phrenic nerve in E11.5 trunk explants derived from mouse embryos carrying the *Hb9::GFP* transgene (Wichterle et al., 2002). Explants were cultured in an oxygenated bath for 2 hours and then dissociated with papain, and TMR$^+$ GFP$^+$ phrenic neurons, as well as GFP$^+$ control MNs, isolated by flow cytometry (Fig. 1A-C). In separate experiments, radial LMC neurons were retrogradely labelled and isolated using the same methodology. Gene expression profiles of sorted primary MNs were determined by Affymetrix array analysis.

MNs were directly differentiated *in vitro* from mouse ESCs as described (Peljto et al., 2010). Briefly, A2.lox ESCs (Iacovino et al., 2011) carrying the MN-specific, magnetically sortable reporter genes *Hb9::CD2GFP* or *Hb9::CD14-IRES-GFP* (supplementary material Fig. S1) were grown for 2 days as EBs, induced with 1 µM retinoic acid and 0.5 µM smoothened agonist (SAG), and dissociated on day 5. MNs were then isolated by magnetically activated cell sorting (MACS). MACS-purified ESC-MNs were cultured for 30 hours on Matrigel, and the expression of PN-specific candidate genes (supplementary material Tables S1, S2) was induced with doxycycline (DOX). Then, transcriptional profiles of ESC-MNs were determined by Affymetrix array analysis and qRT-PCR (Spandidos et al., 2010) (supplementary material Table S3). ESC-MNs expressing the neutral transgene YFP were used as the baseline, as the DOX-inducible Cre recombinase present in the parental ESC line triggers a DNA damage response in MNs (supplementary material Fig. S2).

Detailed protocols are available in supplementary Materials and Methods.

Acknowledgements

We thank Tom Jessell and Andrew Lumsden for support and encouragement; Noriko Osumi and Yoko Arai for advice on WECs; Ira Schieren, Kaity Miao and Fazal Oozeer for expert technical assistance; Jeremy Dasen, Fiona Watt, Robert Knight, Linda Greensmith, Christopher E. Henderson, QueeLim Ch'ng, Stephen Price and Anthony Graham for comments on the manuscript; Chris G. Tan for sharing unpublished observations; and Austin Smith, Esteban O. Mazzoni, Hynek Wichterle, Koichi Kawakami, Cedric Blainpain, Dafe A. Uwanogho, Shinji Hirano, Ursula Just, Malcolm Logan, Linda Greensmith, Matthew Grist, Uwe Drescher and Simon J. Rhodes for providing reagents.

Competing interests

The authors declare no competing financial interests.

Author contributions

C.B.M., I.L., M.N., K.C.K. and P.K. generated DNA constructs. C.B.M., I.L., P.K., D.S., M.C. and M.N. established and characterised ESC subclones. C.B.M. and I.L. derived MNs from ESCs, MACS sorted them and analysed them by flow cytometry and microscopy. M.I. and M.K. contributed the A2lox.Cre ESC clone prior to its publication. I.L. isolated primary MN populations from embryos and D.C. determined their transcriptional patterns. K.C.K. contributed to the original concept of the study. E.B. developed the strategy for large-scale comparison of transcriptional patterns and performed statistical analysis. C.B.M., E.B. and I.L. wrote the manuscript and assembled the figures. I.L. developed the original concept, designed and oversaw the study.

Funding

Personnel and work were supported by the Medical Research Council [grant G0900585, I.L.]. Additional funding was provided by the Thierry Latran Foundation (I.L.); the Biotechnology and Biological Sciences Research Council [grant G1001234, I.L. and Britta Eickholt, KCL/Charité, Berlin, Germany]; Project ALS (K.C.K.) and the Tow Foundation (K.C.K.). K.C.K. was the recipient of a Kirschstein-NRSA Fellowship from NINDS, National Institutes of Health. Deposited in PMC for immediate release.

Supplementary material

Supplementary material available online at
http://dev.biologists.org/lookup/suppl/doi:10.1242/dev.097188/-/DC1

References

Agalliu, D., Takada, S., Agalliu, I., McMahon, A. P. and Jessell, T. M. (2009). Motor neurons with axial muscle projections specified by Wnt4/5 signaling. *Neuron* **61**, 708-720.

Allan, D. W. and Greer, J. J. (1997). Embryogenesis of the phrenic nerve and diaphragm in the fetal rat. *J. Comp. Neurol.* **382**, 459-468.

Arber, S., Han, B., Mendelsohn, M., Smith, M., Jessell, T. M. and Sockanathan, S. (1999). Requirement for the homeobox gene Hb9 in the consolidation of motor neuron identity. *Neuron* **23**, 659-674.

Babiuk, R. P., Zhang, W., Clugston, R., Allan, D. W. and Greer, J. J. (2003). Embryological origins and development of the rat diaphragm. *J. Comp. Neurol.* **455**, 477-487.

Batista, M. F., Jacobstein, J. and Lewis, K. E. (2008). Zebrafish V2 cells develop into excitatory CiD and Notch signalling dependent inhibitory VeLD interneurons. *Dev. Biol.* **322**, 263-275.

Bello, S. M., Millo, H., Rajebhosale, M. and Price, S. R. (2012). Catenin-dependent cadherin function drives divisional segregation of spinal motor neurons. *J. Neurosci.* **32**, 490-505.

Bermingham, J. R., Jr, Scherer, S. S., O'Connell, S., Arroyo, E., Kalla, K. A., Powell, F. L. and Rosenfeld, M. G. (1996). Tst-1/Oct-6/SCIP regulates a unique step in peripheral myelination and is required for normal respiration. *Genes Dev.* **10**, 1751-1762.

Bondue, A., Tännler, S., Chiapparo, G., Chabab, S., Ramialison, M., Paulissen, C., Beck, B., Harvey, R. and Blanpain, C. (2011). Defining the earliest step of cardiovascular progenitor specification during embryonic stem cell differentiation. *J. Cell Biol.* **192**, 751-765.

Briscoe, J., Pierani, A., Jessell, T. M. and Ericson, J. (2000). A homeodomain protein code specifies progenitor cell identity and neuronal fate in the ventral neural tube. *Cell* **101**, 435-445.

Champagnat, J., Morin-Surun, M. P., Fortin, G. and Thoby-Brisson, M. (2009). Developmental basis of the rostro-caudal organization of the brainstem respiratory rhythm generator. *Philos. Trans. R. Soc. B* **364**, 2469-2476.
Dasen, J. S., Liu, J. P. and Jessell, T. M. (2003). Motor neuron columnar fate imposed by sequential phases of Hox-c activity. *Nature* **425**, 926-933.
Dasen, J. S., Tice, B. C., Brenner-Morton, S. and Jessell, T. M. (2005). A Hox regulatory network establishes motor neuron pool identity and target-muscle connectivity. *Cell* **123**, 477-491.
Dasen, J. S., De Camilli, A., Wang, B., Tucker, P. W. and Jessell, T. M. (2008). Hox repertoires for motor neuron diversity and connectivity gated by a single accessory factor, FoxP1. *Cell* **134**, 304-316.
De Strooper, B., Annaert, W., Cupers, P., Saftig, P., Craessaerts, K., Mumm, J. S., Schroeter, E. H., Schrijvers, V., Wolfe, M. S., Ray, W. J. et al. (1999). A presenilin-1-dependent gamma-secretase-like protease mediates release of Notch intracellular domain. *Nature* **398**, 518-522.
Del Barrio, M. G., Taveira-Marques, R., Muroyama, Y., Yuk, D. I., Li, S., Wines-Samuelson, M., Shen, J., Smith, H. K., Xiang, M., Rowitch, D. et al. (2007). A regulatory network involving Foxn4, Mash1 and delta-like 4/Notch1 generates V2a and V2b spinal interneurons from a common progenitor pool. *Development* **134**, 3427-3436.
Demireva, E. Y., Shapiro, L. S., Jessell, T. M. and Zampieri, N. (2011). Motor neuron position and topographic order imposed by β- and γ-catenin activities. *Cell* **147**, 641-652.
Dias, T. B., Yang, Y. J., Ogai, K., Becker, T. and Becker, C. G. (2012). Notch signaling controls generation of motor neurons in the lesioned spinal cord of adult zebrafish. *J. Neurosci.* **32**, 3245-3252.
Fortin, G. and Thoby-Brisson, M. (2009). Embryonic emergence of the respiratory rhythm generator. *Respir. Physiol. Neurobiol.* **168**, 86-91.
Hirano, S., Yan, Q. and Suzuki, S. T. (1999). Expression of a novel protocadherin, OL-protocadherin, in a subset of functional systems of the developing mouse brain. *J. Neurosci.* **19**, 995-1005.
Hirasawa, T. and Kuratani, S. (2013). A new scenario of the evolutionary derivation of the mammalian diaphragm from shoulder muscles. *J. Anat.* **222**, 504-517.
Howe, J. R., Skryabin, B. V., Belcher, S. M., Zerillo, C. A. and Schmauss, C. (1995). The responsiveness of a tetracycline-sensitive expression system differs in different cell lines. *J. Biol. Chem.* **270**, 14168-14174.
Iacovino, M., Bosnakovski, D., Fey, H., Rux, D., Bajwa, G., Mahen, E., Mitanoska, A., Xu, Z. and Kyba, M. (2011). Inducible cassette exchange: a rapid and efficient system enabling conditional gene expression in embryonic stem and primary cells. *Stem Cells* **29**, 1580-1588.
Jung, H., Lacombe, J., Mazzoni, E. O., Liem, K. F., Jr, Grinstein, J., Mahony, S., Mukhopadhyay, D., Gifford, D. K., Young, R. A., Anderson, K. V. et al. (2010). Global control of motor neuron topography mediated by the repressive actions of a single hox gene. *Neuron* **67**, 781-796.
Lacombe, J., Hanley, O., Jung, H., Philippidou, P., Surmeli, G., Grinstein, J. and Dasen, J. S. (2013). Genetic and functional modularity of Hox activities in the specification of limb-innervating motor neurons. *PLoS Genet.* **9**, e1003184.
Lance-Jones, C. and Landmesser, L. (1980). Motoneurone projection patterns in the chick hind limb following early partial reversals of the spinal cord. *J. Physiol.* **302**, 581-602.
Li, X. J., Hu, B. Y., Jones, S. A., Zhang, Y. S., Lavaute, T., Du, Z. W. and Zhang, S. C. (2008). Directed differentiation of ventral spinal progenitors and motor neurons from human embryonic stem cells by small molecules. *Stem Cells* **26**, 886-893.
Liu, J. P., Laufer, E. and Jessell, T. M. (2001). Assigning the positional identity of spinal motor neurons: rostrocaudal patterning of Hox-c expression by FGFs, Gdf11, and retinoids. *Neuron* **32**, 997-1012.
Marshall, H., Nonchev, S., Sham, M. H., Muchamore, I., Lumsden, A. and Krumlauf, R. (1992). Retinoic acid alters hindbrain Hox code and induces transformation of rhombomeres 2/3 into a 4/5 identity. *Nature* **360**, 737-741.
Miles, G. B., Yohn, D. C., Wichterle, H., Jessell, T. M., Rafuse, V. F. and Brownstone, R. M. (2004). Functional properties of motoneurons derived from mouse embryonic stem cells. *J. Neurosci.* **24**, 7848-7858.
Osumi, N. and Inoue, T. (2001). Gene transfer into cultured mammalian embryos by electroporation. *Methods* **24**, 35-42.
Peljto, M. and Wichterle, H. (2011). Programming embryonic stem cells to neuronal subtypes. *Curr. Opin. Neurobiol.* **21**, 43-51.
Peljto, M., Dasen, J. S., Mazzoni, E. O., Jessell, T. M. and Wichterle, H. (2010). Functional diversity of ESC-derived motor neuron subtypes revealed through intraspinal transplantation. *Cell Stem Cell* **7**, 355-366.
Pellerin, I., Schnabel, C., Catron, K.M. and Abate, C. (1994). Hox proteins have different affinities for a consensus DNA site that correlate with the positions of their genes on the hox cluster. *Mol. Cell. Biol.* **14**, 4532-4545.
Peng, C. Y., Yajima, H., Burns, C. E., Zon, L. I., Sisodia, S. S., Pfaff, S. L. and Sharma, K. (2007). Notch and MAML signaling drives Scl-dependent interneuron diversity in the spinal cord. *Neuron* **53**, 813-827.
Perry, S. F., Similowski, T., Klein, W. and Codd, J. R. (2010). The evolutionary origin of the mammalian diaphragm. *Respir. Physiol. Neurobiol.* **171**, 1-16.
Personius, K. E., Chang, Q., Mentis, G. Z., O'Donovan, M. J. and Balice-Gordon, R. J. (2007). Reduced gap junctional coupling leads to uncorrelated motor neuron firing and precocious neuromuscular synapse elimination. *Proc. Natl. Acad. Sci. USA* **104**, 11808-11813.
Philippidou, P., Walsh, C. M., Aubin, J., Jeannotte, L. and Dasen, J. S. (2012). Sustained Hox5 gene activity is required for respiratory motor neuron development. *Nat. Neurosci.* **15**, 1636-1644.
Price, S. R., De Marco Garcia, N. V., Ranscht, B. and Jessell, T. M. (2002). Regulation of motor neuron pool sorting by differential expression of type II cadherins. *Cell* **109**, 205-216.
Rousso, D. L., Gaber, Z. B., Wellik, D., Morrisey, E. E. and Novitch, B. G. (2008). Coordinated actions of the forkhead protein Foxp1 and Hox proteins in the columnar organization of spinal motor neurons. *Neuron* **59**, 226-240.
Sabharwal, P., Lee, C., Park, S., Rao, M. and Sockanathan, S. (2011). GDE2 regulates subtype-specific motor neuron generation through inhibition of Notch signaling. *Neuron* **71**, 1058-1070.
Schroeder, T., Kohlhof, H., Rieber, N. and Just, U. (2003). Notch signaling induces multilineage myeloid differentiation and up-regulates PU.1 expression. *J. Immunol.* **170**, 5538-5548.
Sharma, K., Sheng, H. Z., Lettieri, K., Li, H., Karavanov, A., Potter, S., Westphal, H. and Pfaff, S. L. (1998). LIM homeodomain factors Lhx3 and Lhx4 assign subtype identities for motor neurons. *Cell* **95**, 817-828.
Sockanathan, S. and Jessell, T. M. (1998). Motor neuron-derived retinoid signaling specifies the subtype identity of spinal motor neurons. *Cell* **94**, 503-514.
Soundararajan, P., Miles, G. B., Rubin, L. L., Brownstone, R. M. and Rafuse, V. F. (2006). Motoneurons derived from embryonic stem cells express transcription factors and develop phenotypes characteristic of medial motor column neurons. *J. Neurosci.* **26**, 3256-3268.
Spandidos, A., Wang, X., Wang, H. and Seed, B. (2010). PrimerBank: a resource of human and mouse PCR primer pairs for gene expression detection and quantification. *Nucleic Acids Res.* **38**, D792-D799.
Sürmeli, G., Akay, T., Ippolito, G. C., Tucker, P. W. and Jessell, T. M. (2011). Patterns of spinal sensory-motor connectivity prescribed by a dorsoventral positional template. *Cell* **147**, 653-665.
Thaler, J., Harrison, K., Sharma, K., Lettieri, K., Kehrl, J. and Pfaff, S. L. (1999). Active suppression of interneuron programs within developing motor neurons revealed by analysis of homeodomain factor HB9. *Neuron* **23**, 675-687.
Tsuchida, T., Ensini, M., Morton, S. B., Baldassare, M., Edlund, T., Jessell, T. M. and Pfaff, S. L. (1994). Topographic organization of embryonic motor neurons defined by expression of LIM homeobox genes. *Cell* **79**, 957-970.
West, B. E., Parker, G. E., Savage, J. J., Kiratipranon, P., Toomey, K. S., Beach, L. R., Colvin, S. C., Sloop, K. W. and Rhodes, S. J. (2004). Regulation of the follicle-stimulating hormone beta gene by the LHX3 LIM-homeodomain transcription factor. *Endocrinology* **145**, 4866-4879.
Wichterle, H., Lieberam, I., Porter, J. A. and Jessell, T. M. (2002). Directed differentiation of embryonic stem cells into motor neurons. *Cell* **110**, 385-397.